On the physics of polariton interactions

THÈSE N^{O} 6877 (2016)

PRÉSENTÉE LE 22 JANVIER 2016
À LA FACULTÉ DES SCIENCES DE BASE
LABORATOIRE D'OPTOÉLECTRONIQUE QUANTIQUE
PROGRAMME DOCTORAL EN PHOTONIQUE

ÉCOLE POLYTECHNIQUE FÉDÉRALE DE LAUSANNE

POUR L'OBTENTION DU GRADE DE DOCTEUR ÈS SCIENCES

PAR

Naotomo TAKEMURA

acceptée sur proposition du jury:

Prof. J.-E. Moser, président du jury
Prof. B. M. J. Deveaud, Dr M. Portella Oberli, directeurs de thèse
Prof. S. Savasta, rapporteur
Prof. S. Cundiff, rapporteur
Prof. A. Imamoglu, rapporteur

ÉCOLE POLYTECHNIQUE
FÉDÉRALE DE LAUSANNE

Suisse
2015

Acknowledgements

I would like to thank all people who supported this work.

First of all, I am very grateful to my supervisor Benoît Deveaud for giving me the opportunity to investigate the wonderful world of polariton physics. He has been a great supervisor and given me the freedom in his lab. I was always inspired and learned a lot through discussions with him. I would also like to thank a lot co-supervisor Portella Oberli Marcia. This thesis would not have been possible without her endless supports and fruitful physics discussions.

I warmly thank the members of my thesis jury, Steven Cundiff, Salvatore Savasta, Atac Imamoglu and Jacques-Edouard Moser for accepting my thesis through the careful reading and providing critical remarks.

I am also grateful to have the opportunity to work with Stéphane Trebaol and Anderson Mitchell David in both lab and office. They taught me many experimental, theoretical, and communication skills during my PhD days. I owe many results of my work to their supports and discussions. I deeply thank Oberli Daniel, Michiel Wouters, Yoan Léger and Verena Kohnle for stimulating discussions, theoretical contributions, and a transfer of knowledges. I would like to thank technical and IT staffs Roger Rochat, Yoan and Damian Trolliet, Nicolas Leiser, and Florence Hagen for their invaluable supports.

I am also very happy that I spent four years with wonderful colleagues of LOEQ, Adiyatullin Albert, Liu Wei, Navadeh Toupchi Morteza, Ouellet-Plamondon Claudéric, Hezam Mahmoud, Jabeen Fauzia, Jacopin Gwénolé Jean, Sallen Grégory Chilpéric, Morier-Genoud François, Rita Spano, Francesco Manni, Gabriele Grosso, Hadis Abbaspour, and Mehran Shahmohammadi. I really enjoyed a fantastic time with them not only in the office, but also during lunch and coffee times.

Many thanks to our secretary, Rouiller Claire-Lyse for her warm supports and kindness. From finding an apartment to administrative issues, I owe my comfortable life in Lausanne largely to her.

Finally, I would like to sincerely thank my friends and family for their endless support and encouragement.

Lausanne, 10 Dec 2015 N. T.

Abstract

An exciton-polariton is a quasi-particle that emerges from the strong coupling between an exciton and a photon. Recently, the studies of the exciton-polariton have been receiving a great deal of attention in terms of both fundamental physics and potential applications. The very small polariton effective mass and the interactions brought respectively by the photon and excitonic content of polaritons enable a wide range of interesting physical phenomena including the realization of Bose-Einstein condensate, superfluidity, and quantum vortices. In addition to the interest in the basic physics, several device applications of semiconductor microcavities such as polariton switching, bistability, and stochastic resonance have also been proposed. In these researches, the interactions between exciton-polaritons, which is a source of nolinearity, are central. In this thesis, we explore the various aspects of the polariton interactions in semiconductor microcavities.

We employ nonlinear spectroscopies as experimental techniques and compare our experimental results with different theoretical models. Firstly, we study lower-lower (upper-upper) polariton self-interactions and lower-upper polariton cross interactions. The self- and cross-interactions are identified in four-wave mixing two-dimensional Fourier spectra, which are followed by theoretical analyses based on a third-order perturbation theory and on a non-perturbative simulation of Gross-Pitaevskii equations. Secondly, using pump-probe spectroscopy, we measure the spin dependent nature of exciton-polariton interactions, which is called spinor interaction. The two spin projections of exciton-polaritons give rise to a spin anisotropy of the polariton interactions. In particular, we show that the polariton interactions with anti-parallel spins presents a scattering resonance behavior via an exciton molecule (biexciton), which we call polaritonic Feshbach resonance. The measurements of the spinor polariton interactions are compared with numerical simulations based on spinor Gross-Pitaevskii equations including the exciton-biexciton coupling. Finally, we explore the decoherence effect induced by the interaction of polaritons. Focusing on the delay dependence of the experimental pump-probe spectra, we find that the excitation induced dephasing (EID) plays an important role in the dynamics of exciton-polaritons. The delay dependence of the pump-probe spectra clearly probes that the coherent and incoherent parts of excitons temporally behave in a different way. These experimental features can be well reproduced only with the excitonic Bloch equations (EBE) approach, which is a theoretical framework that can include the incoherent population of excitons. In the last part of this thesis, a future perspective of the research is discussed while showing preliminary experimental results of pump-probe spectroscopy with a spectrally narrowband pump pulse.

Key words: semiconductor microcavity, exciton-polariton, biexciton, nonlinear optics, nonlinear spectroscopy, heterodyne spectral interferometry, time- and spectral-resolved pump and probe and four-wave mixing, two-dimensional Fourier transform spectroscopy, light-matter interaction, spinor interaction, Feshbach resonance, excitation induced dephasing, decoherence.

Résumé

Un exciton-polariton est une quasi-particule qui provient du couplage fort entre un exciton et un photon. Depuis quelques années, l'exciton-polariton est l'objet d'une intense recherche à la fois en termes de physique fondamentale et d'applications potentielle. Leur masse effective très légère, et la possibilité d'interactions amenée par la composante excitonique des polaritons permettent des recherches sur des phénomènes physiques très variées comme la réalisation de condensats de Bose-Einstein, la superfluidité, et les vortex quantiques. En plus de leur intérêt pour la physique de base, plusieurs applications pratiques des microcavités semi-conductrices ont également été proposées. Par exemple, la commutation, la bistabilité et la résonance stochastique sont des possibilités très intéressantes. Dans ces recherches, l'interaction entre l'exciton-polariton, qui est la source des non-linéarités, est au cœur du fonctionnement du système. Cette thèse est consacrée à l'étude des divers aspects de l'interaction entre polaritons dans les microcavités semiconductrices.

Nous utilisons la spectroscopie non-linéaire comme technique expérimentale et nous comparons nos résultats expérimentaux avec différents modèles théoriques. Dans un premier temps, nous étudions l'auto-interaction entre deux polaritons bas (polaritons hauts) et l'interaction mutuelle entre polaritons bas et hauts. L'auto interaction et l'interaction mutuelle sont identifiées dans les spectres à deux dimensions, qui sont corroborés par des analyses théoriques de perturbation développées jusqu' à l'ordre 3 et une simulation non-perturbative d'équations de Gross-Pitaevskii. Dans un deuxième temps, au moyen d'expériences de spectroscopie pompe-sonde, nous mesurons la dépendance en spin des interactions entre exciton-polaritons, qui s'appelle l'interaction spinor. L'existence des deux états de spin des polaritons contribue à une anisotropie de spin de leurs interactions. En particulier, nous montrons que l'interaction entre polaritons avec spins anti-parallèles présente une résonance via une molécule excitonique (biexciton), que nous appelons la résonance de Feshbach polaritonique. Les mesures de l'interaction de spin entre polaritons sont comparées avec des simulations numériques avec les équations de Gross-Pitaevskii en spin, qui considèrent le couplage entre un exciton et un biexciton. Finalement, nous explorons les effets de décohérence induits par l'interaction entre polaritons. Nous nous concentrons sur la dépendance en fonction du délai de spectres pompe-sonde et démontrons que le dephasage induit par l'excitation (l'excitation induced dephasing (EID)) joue un rôle important dans la dynamique des polaritons. La dépendance temporelle des spectres pompe-sonde montre clairement que les parties cohérente et incohérente des excitons sont temporellement dissociés. Ces résultats expérimentaux ne peuvent être bien reproduits qu'avec les équations de Bloch excitoniques (EBE), ce qui est un cadre théorique qui permet d'inclure la population incohérente des excitons. Dans la dernière partie de cette thèse, une perspective d'avenir sur les recherches est discutée avec des résultats expérimentaux préliminaires d'une expérience pompe-sonde utilisant une impulsion de pompe spectralement étroite.

Mots clefs : microcavité semi-conducteur, exciton-polariton, biexciton, nonlinéarité optique, spectroscopie non linéaire, interférométrie hétérodyne, pompe et sonde, mélange à quatre ondes, spectroscopie bidimensionnelle à transformée de Fourier, interaction lumière-matière, spinor interaction, résonance de Feshbach, excitation induced dephasing, décohérence.

Contents

Acknowledgements **i**

Abstract (English/Français) **iii**

1 Introduction **1**

2 Microcavity polaritons **5**
2.1 Bands in direct gap III-V semiconductor 5
2.2 Excitons 7
2.3 Photon confinement in microcavity 9
2.4 Photon mass due to the cavity confinement 10
2.5 Strong-coupling between exciton and photon 11

3 Theoretical framework **15**
3.1 Exciton-photon basis (local mode) 15
3.1.1 Exciton-photon Hamiltonian 15
3.1.2 Equations of motion in exciton-photon basis 17
3.2 Polariton basis (normal mode) 18
3.2.1 Diagonalization in momentum-space 18
3.2.2 Polariton basis in real-space 21
3.2.3 Interaction Hamiltonians in polariton basis (polariton-polariton interactions) 24
3.2.4 Equation of motion of lower-polariton 25
3.3 Spin-dependent interactions 26

4 Experimental setup and technique **29**
4.1 High-quality GaAs based semiconductor microcavity 29
4.2 Pump-probe excitation configuration 31
4.3 Heterodyne Pump-probe and four-wave mixing technique 32

5 Two-dimensional Fourier Transform (2DFT) spectroscopy of polaritons **39**
5.1 Concept of 2DFT spectroscopy 39
5.2 Experimental configuration and numerical process for 2DFT of polaritons . . . 40
5.3 Experimental results and perturbative analysis 43
5.3.1 2DFT spectrum of one-quantum regime $|S_{1\mathrm{Q}}(\epsilon_t, \epsilon_\tau)|$ 44

5.3.2 2DFT spectrum of two-quantum regime $|S_{2Q}(\epsilon_t, \epsilon_\tau)|$ 50
5.4 Numerical simulation and detailed study of 2DFT spectra 53
5.4.1 Different interaction contributions 55
5.4.2 Fine structures inside peak groups 57
5.4.3 2DFT spectrum at a negative (δ=-2 meV) and positive (δ=2.7 meV) cavity detuning 61
5.4.4 Comparison with experiments 65
5.5 Conclusion 66

6 Spinor polariton interaction 69
6.1 Experimental setup for pump-probe experiment 70
6.2 Pump-probe spectrum and polariton interaction 71
6.3 Experimental results: energy shifts vs cavity detuning 73
6.3.1 Polariton interaction with parallel spins 73
6.3.2 Polariton interaction with anti-parallel spins 74
6.4 Theoretical model 75
6.4.1 A. Parallel spin polariton interaction 77
6.4.2 B. Anti-parallel spin polariton interaction 79
6.5 Lower-polariton interaction constants 81
6.5.1 Lower-polariton interaction constants α_1 and α_2 82
6.6 Polariton Feshbach resonance 86
6.6.1 Concept of Feshbach resonance 86
6.6.2 Measurements and model 88
6.6.3 delay dependence 94
6.7 Conclusion 96

7 Effect of dephasing in pump-probe spectroscopy 97
7.1 Experimental setup for pump-probe experiment 97
7.2 Excitonic Bloch equations (EBE) 99
7.3 Experimental results and analysis based on EBE 101
7.3.1 Experimental results 101
7.3.2 Details of simulations 102
7.3.3 Comparison between experiments and simulation 105
7.4 The effect of dephasing 109
7.4.1 Pump-probe spectra in coherent limit 109
7.4.2 Dynamics of population and polarization 110
7.5 Discussion 111
7.5.1 Dephasing mechanism 111
7.5.2 Relation between EBE and two reservoirs model 112
7.6 Conclusion 113

8 Future perspective 115

9 Conclusion **121**

10 Appendix A: Phase correction **123**
10.1 Phase correction after an acquisition sequence 123
10.2 Phase correction for 2DFT 125

11 Appendix B: Third-order perturbation theory of 2DFT spectroscopy **127**
11.1 one-quantum regime (negative delay) 130
11.2 two-quantum regime (positive delay) 134

12 Appendix C: Giant oscillator strength model **139**
12.0.1 Hamiltonian 139
12.0.2 Lower-polariton basis 141
12.0.3 Feshbach resonance 143
12.0.4 Summary 144

Bibliography **153**

Curriculum Vitae **155**

1 Introduction

Light-matter interaction has always been an exciting area in physics. In particular, it is well known that the quantum physics was born from Planck's investigation of the black body radiation spectrum (1900). After the construction of quantum mechanics, our understanding of the light-matter interaction progressed explosively. In terms of basic science, the quantization of light paved the way to the establishment of quantum electrodynamics (QED) and quantum optics. In parallel to the development of fundamental physics, the 20th century witnessed various important inventions concerning the light-matter interaction. Among them, the most important one might be the invention of "light amplification by stimulated emission of radiation (LASER)" by Schawlow and Townes (1957). The laser is the first realization of a bright “coherent" light source. The first generation of lasers are “gas lasers", which use atomic or molecular gases such as helium–neon and CO_2 as gain materials. One of the next important steps in the history of lasers is the development of "light emitting diode" (LED) followed by “semiconductor laser". Since the semiconductor laser is easy to implement with reasonably simple technology, it acquired a wide range of applications and plays crucial roles in our daily life. Furthermore, the advancement of the semiconductor optics technologies opened the way to a solid-state based manipulation of the light-matter interaction in a single quantum state, which has been traditionally investigated in atoms, molecules, and ions. In this thesis, we study the physics of semiconductor strongly interacting with light.

Recent advancements of semiconductor growth technologies made it possible to realize a system called “semiconductor microcavity". The semiconductor microcavity is a hybrid system composed of quantum wells and distributed Bragg reflectors (DBRs). This type of nano-structure is employed in a laser called “vertical-cavity surface-emitting laser (VCSEL)", which already found its way to commercial applications. VCSELs are working in a regime where the light and matter are weakly interacting (weak coupling). What is going on if we increase the light-matter interaction by making the light confinement more tight? The first strong coupling between a semiconductor and light in a high quality semiconductor microcavity was identified by Weisbuch and co-authors [1]. In the strong coupling regime, the dipole in a quantum well (excitons) and highly confined photon form quasi-particles called “polaritons". The dipole in a quantum well is a hydrogen-like particle, the “exciton", composed of an electron and a hole. Thus, the polariton in a semiconductor microcavity is the superposition state of exciton and photons, which is refereed to as “exciton-polariton". Exciton-polaritons possess mutual interactions originating from the excitonic content and the photonic content allows a readout as well as an input of properties respectively from a light emission and an excitation. These features make the semiconductor microcavity an attractive tool to investigate nonlinear quantum optics including parametric amplification [2, 3, 4, 5, 6], bistability [7], and optical switching [8, 9].

In addition to the interest in nonlinear optical applications, the exciton-polariton in semiconductor microcavities has recently raised a large attention as a playground to investigate interacting quantum fluids. One of the striking achievements is the Bose-Einstein condensation of exciton-polaritons [10, 11], which was followed by the observations of collective quantum phenomena such as polariton superfluidity [12], quantum vortices [13], and, Bogoliubov dispersion [14, 15, 16]. Moreover, the spin degree of freedom of exciton-polariton leads to spinor interactions. Especially, the spin anisotropic nature of polaritons is the origin of a wide range of nonlinear effects such as stimulated spin dynamics of polaritons [17, 18], the transport of spin polarized polaritons [19], the optical spin Hall effect [20, 21, 22], the generation of polarization vortices [23, 24] and half quantum vortices [25], and the spontaneous polarization buildup polariton condensates [26]. The spinor interaction also inspired device applications of exciton-polaritons such as multistability [27, 28, 29] and polariton switching [8, 9], spin stochastic resonance [30].

Although the physics of exciton-polaritons has been very actively investigated, there exist a lot of basic questions left unanswered. For instance, the polariton mode has two branches lower and upper polaritons. Usually, most of the theoretical and experimental activities are focused only on the lower-polariton. The physical properties of the upper-polariton branch has not been investigated intensively. In the viewpoint of many-body physics, in a low density electron-hole phase, which is the regime we investigate with the high quality semiconductor microcavity in strong-coupling condition, a bosonized exciton picture is known to be a good starting point [31, 32]. It is important to notice that once we consider the interaction between excitons, the complex Coulomb correlation effect plays an important role [33], which makes the dynamical description of low-density excitons (polariton) nontrivial. For example, bound exciton molecules called biexcitons plays a dominant role in the spinor polariton interactions [34, 35]. This is in contrast to the case of VCSELs, which are operating in the high density regime, thus the Coulomb correlation effects are screened and Semiconductor-Bloch equation based on a fermionic electron-hole picture describes the dynamics very well [36]. For describing the dynamics of exciton-polaritons, a meanfield analysis based on a nonlinear Schrödinger equation is enjoying a wide range of success [37]. Since the nonlinear Schrödinger is formally same as the Gross-Pitaevskii equation in atomic Bose-Einstein condensates, it is easy to find close analogies between the exciton-polaritons and degenerate bosonic gases. At the same time, the deviation of the polariton dynamics from the Gross-Pitaevskii equation is an interesting subject in order to go beyond the meanfied description of many-body quantum fluids. As a first step in this direction, we focus on a dephasing effect on exciton-polaritons.

In this thesis, we attempt to answer these questions via non-linear optical methods: pump-probe and four-wave mixing spectroscopies. Non-linear spectroscopy is indeed a very powerful method in semiconductor microcavities, because we can directly excite exciton-polaritons using coherent laser sources and readout them via spectroscopic detection. The lower and upper-polariton interaction is probed by two-dimensional Fourier transform (2DFT) spectroscopy, while the spinor interactions and dephasing effects are investigated through the pump-probe spectroscopy. The sample we investigate is a high quality GaAs-based microcavity [38]. The thesis is organized in the following way.

Chapter 2 gives a brief review of semiconductor microcavities. We present the basic concepts of excitons in a direct gap GaAs semiconductor and of semiconductor microcavity composed of a single quantum well and distributed Bragg reflectors (DBRs). The idea of the strong-coupling between excitons and photons and the emergence of the polaritons are also addressed in this section.

Chapter 3 is devoted to theoretical description of exciton-polaritons. We introduce an interacting bosonic exciton-photon Hamiltonian as a starting point, which is partly diagonalized by the introduction of a polariton basis Hamiltonian. Both for the exciton-photon and polariton basis, we obtain the equations of motions: excitonic Bloch equations (EBE) and Gross-Pitaevskii equations (GPE). In the last section of this chapter, we discuss Hamiltonians and equations of motions including the biexciton state.

In Chapter 4, the experimental setup is explained. We address the properties of the GaAs-based microcavity sample and optical setup including an excitation scheme and a heterodyne detection technique. In particular, the principle of the heterodyne detection technique is described in detail, which is important mainly for the two-dimensional Fourier transform spectroscopy.

The subject of Chapter 5 is the investigation of the polariton interactions through two-dimensional Fourier transform (2DFT) spectroscopy. Using 2DFT, we can selectively identify the lower-lower and the upper-upper polariton self-interactions, as well as the lower-upper cross interaction in two-dimensional spectra. The 2DFT spectra are analysed by a third-order perturbation theory and “non-perturbative" Gross-Pitaevskii equations. We discuss the physics behind the obtained 2DFT spectra by comparing the experiments and simulations.

In Chapter 6, we study the spinor polariton interactions using polarization dependent pump-probe spectroscopy. The sign and strength of the polariton interactions with parallel and anti-parallel spins are directly measured from the energy shift of the probe spectra. The important role of the biexciton in polaritons with anti-parallel spins is addressed. Finally, we discuss the modification of the polariton spinor interaction via a scattering resonance with biexciton called “polaritonic Feshbach resonance". The experimental data are analysed with the Gross-Pitaevskii equations including the biexciton effect.

Chapter 7 addresses the importance of the role of the dephasing effect in exciton-polaritons, which is usually neglected in a coherent limit description. The dephasing processes trigger the decoherence of excitons. We probe the signatures of incoherent excitons through the delay dependence of the pump-probe spectroscopy. In order to understand the physics, we perform numerical simulation based on excitonic Bloch equations (EBEs), which explicitly take into account the incoherent population of excitons. The experimental results are well reproduced by EBEs only when the dephasing is included.

Chapter 8 is a future perspective, where we overview the next directions of the experiment such as a pump-probe spectroscopy with narrow spectral band pulse. In addition to this, we discuss the possibility of a theory that can include both incoherent exciton and biexciton effects. Finally, we address a concluding remark in Chapter 9.

The subject of Appendix A is the phase correction process, which is important experimental technique in 2DFT spectroscopy. The detailed derivation of the third-order perturbation theory and a double-sided Feynman diagram technique is provided in Appensix B. In Appendix C, we discuss a biexciton formation process called “giant oscillator strength model". This model is of a different type compared to the biexciton creation model employed in Chapter 6.

2 Microcavity polaritons

In this chapter, we briefly review the properties of semiconductor microcavities. The semiconductor microcavities are the systems that couple quantum-well excitons and microcavity photons. In the first section, we explain the basics of a direct gap GaAs semiconductor and excitonic quasiparticles. In the next section, we introduce a microcavity composed of distributed Bragg reflectors (DBRs), which allows the confinement of photons. Finally, we discuss GaAs based semiconductor microcavity which we study in this thesis.

2.1 Bands in direct gap III-V semiconductor

In this section, we consider the band structure and photon absorption of a direct gap semiconductor such as GaAs [39, 40].

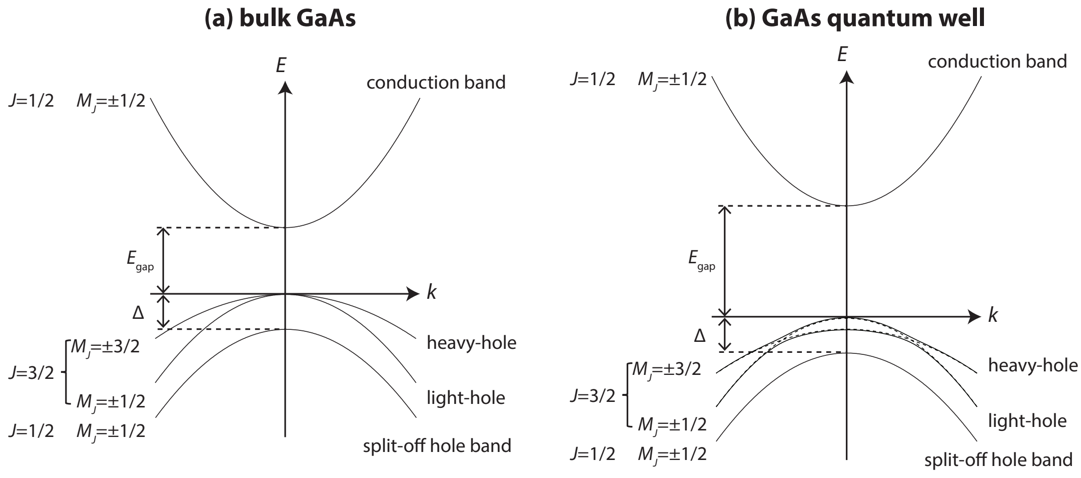
(a) bulk GaAs

(b) GaAs quantum well

Figure 2.1: Scheme of the band structure of GaAs based semiconductor. Energy-momentum dispersion of a bulk (a) and quantum well GaAs (b). The spin-orbit coupling makes the split-off hole band lower than the heavy and light-hole. In the quantum well, the confinement leads to a lift of the degeneracy between the light-hole and heavy-hole valence band.

The schematic of energy-momentum dispersion for small wave-vector k close to the Γ point is presented in Fig. 2.1. As is shown in Fig 2.1, in a direct gap semiconductor, the energy minimum of the conduction band and the energy maximum of the valence band have the same momentum $k = 0$. Therefore, a direct gap semiconductor can directly absorb and emit photons. On the other hand, in an indirect gap semiconductor such as Si, since the conduction band energy minimum and the valence band energy maximum have different momenta, for this transition both photon absorption and emission require phonon processes for conserving momenta. Figure 2.1 shows that the valence band has a more complex structure than the conduction band. This is because the valence and conduction bands originate respectively from p- and s-like atomic states. The top of the valence band consists of three bands. The heavy- and light-hole bands are degenerate at $k = 0$ in bulk GaAs (Fig. 2.1 (a)), while the energy of the split-off hole band is lowered due to the spin-orbit coupling.

Now let us consider two-dimensional confinement structure called a quantum well. A quantum well consists of the layers of different types of semiconductor materials grown on the top of a substrate crystal, for example, by molecular beam epitaxy (MBE) [39]. When the layer of a smaller energy gap semiconductor with a thickness comparable to the electron de Broglie wavelength is located between two semiconductors with a large energy gap, this structure realizes a well-type potential along the growth axis. Thus electrons and holes are confined inside the two-dimensional layer. In the quantum well, the degeneracy of the heavy- and light-hole no longer exists because of the difference of confinement energies of heavy- and light-hole (Fig. 2.1 (b)) [39, 40]. We notice that in a quantum well GaAs, around $k = 0$ the heavy-hole is lighter than the light-hole because of the avoided crossing of the two dispersion curves (See Fig. 2.1 (b)).

2.2 Excitons

Until now, we have neglected the Coulomb interaction of electrons and holes, however, the Coulomb interaction plays an important role in direct gap semiconductors mainly at a low temperature. Figure 2.2 presents the schematics of the light absorption of a bulk direct gap semiconductor. The sharp peaks are the signature of a quasi-particle called “exciton", which is composed of an electron and a hole bound by the Coulomb interaction. The photon absorption neglecting the Coulomb interaction is depicted as a dashed line in Fig. 2.2, which is proportional to $(E - E_{gap})^{1/2}$. The exciton behaves like a hydrogen atom. The exciton behaves as a bosonic quasiparticle, it can absorb and emit light.

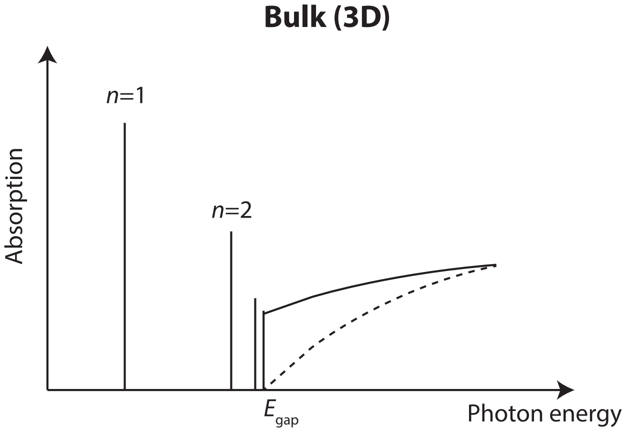

Figure 2.2: Schematic band edge absorption spectrum for a bulk direct gap semiconductor including the excitonic effect. The dashed line depicts the absorption without the excitonic effect.

Depending on the Bohr radius of excitons, we can classify them into two types: Wannier and Frenkel excitons. In Wannier excitons, electrons and holes are bound by a weak Coulomb force, thus its Bohr radius is larger than the lattice constant. This is the case in semiconductors such as GaAs, CdTe, GaN, ZnSe where the Coulomb interaction between electrons and holes is weakened by the dielectric screening. On the other hand, in Frenkel excitons, since electron and hole are tightly bound by a strong Coulomb interaction, its Bohr radius is smaller than the lattice constant. Frenkel excitons are observed in organic semiconductor where the dielectric constant is small. In this thesis, we focus only on Wannier excitons. In analogy with a hydrogen atom, the energy of exciton is given by [39]

$$E_n = E_{\text{gap}} - \frac{R_X}{n^2}. \tag{2.1}$$

R_X is the Rydberg energy of the exciton defined as

$$R_X = \frac{\mu}{m_0 \epsilon_r^2} R_H. \tag{2.2}$$

R_H is the Rydberg energy of the hydrogen atom (13.6 eV). μ and ϵ_r are respectively the exciton reduced mass and the material dielectric constant. m_0 is the free electron mass. Moreover, the Bohr radius of the bulk 3D exciton for $n = 1$ is given by

$$a_X^{3D} = \frac{m_0 \epsilon_r}{\mu} a_H. \tag{2.3}$$

a_H is the hydrogen Bohr radius (5.29×10^{-11} m). Similarly, in the two-dimensional quantum well, the 2D Bohr radius of exciton for $n = 1$ reads,

$$a_X^{2D} = \frac{m_0 \epsilon_r}{2\mu} a_H. \tag{2.4}$$

The Bohr radius of 2D exciton is smaller than that of 3D one, and the binding energy of exciton is larger in the two-dimensional quantum well than in the bulk semiconductor due to the confinement. The band gap energy E_{gap}, Rydberg energy R_X, and 3D Bohr radius a_X^{3D} of various direct band gap semiconductors are listed in Table. 2.1.

crystal	E_{gap} (eV)	R_X (meV)	a_X^{3D} (nm)
GaN	3.5	23	3.2
ZnSe	2.8	20	4.5
CdS	2.6	28	2.7
CdTe	1.6	12	6.7
GaAs	1.5	4.2	13

Table 2.1: Table of the band gap energy E_{gap}, Rydberg energy R_X, and 3D Bohr radius a_X of direct band gap semiconductors [39].

Another important aspect of the exciton is its spin structure. Since both electron and hole carry spins, the exciton displays a rich spin structure. Fig. 2.3 shows the schematics of the spin structure of electron and holes in GaAs based quantum wells. In our experiments, we are interested only in heavy-hole, we therefore focus on heavy-hole excitons. Depending on the spin configuration, a heavy-hole exciton has four spin states: dipole-active states $|J_z = \pm 1\rangle = |J_z^e = \pm 1/2, j_z^h = \mp 3/2\rangle$ and dipole-forbidden states $|J_z = \pm 2\rangle = |J_z^e = \pm 1/2, j_z^h = \pm 3/2\rangle$ [39, 41]. Here, J_z and $J_z^{e(h)}$ are respectively z-components of the total and electron (hole) spins. The z-direction is defined along the quantum well growth axis, which is perpendicular to the 2D layer. The states $|J_z = \pm 2\rangle$ are called dipole-forbidden because a photon has an angular momentum ± 1 and a single photon cannot excite $|J_z = \pm 2\rangle$. Therefore, in this thesis we deal only with the dipole-active states $|J_z = \pm 1\rangle$. The state $|J_z = +(-)1\rangle$ is coupled to a photon with a $\sigma^{+(-)}$ circular polarization. In the following, we call $|J_z = +(-)1\rangle$ simply as spin-up (-down) exciton. The spin states of excitons play an important role in the spin-dependent interaction of exciton-exciton interactions.

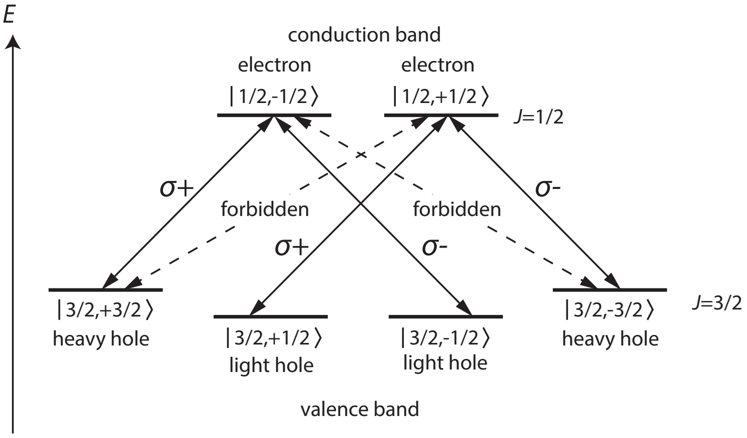

Figure 2.3: Selection rules for transitions under circularly polarized light in GaAs quantum wells. The heavy-hole and light-hole levels are non-degenerate due to the difference in confinement energies. The dashed lines represent forbidden transitions because these would require an angular momentum ±2.

2.3 Photon confinement in microcavity

In a semiconductor microcavity, a quantum well is sandwiched within two distributed Bragg reflectors (DBRs). A DBR is a stack of $\lambda/4$ thick semiconductor layers with two different refractive indices n_1 and n_2 ($n_2 > n_1$). n_1 and n_2 fulfil the Bragg interference condition,

$$n_1 L_1 = n_2 L_2 = \lambda_c/4. \tag{2.5}$$

L_1 and L_2 are respectively the thickness of the layers with refractive index n_1 and n_2. λ_c represents the center wavelength of the stop band of the DBR. Based on the transfer matrix method the DBR reflectivity R_{DBR} is calculated as

$$R_{\mathrm{DBR}} = \frac{n_0 n_2^{2N} - n_3 n_1^{2N}}{n_0 n_2^{2N} + n_3 n_1^{2N}}, \tag{2.6}$$

where N is the number of DBR pairs. n_0 and n_3 are respectively the refractive indices of a surrounding medium and substrate of DBR. The above equation indicates that the higher the contrast between the refractive indices of the two layers becomes, the larger the reflectivity that is obtained. The bandwidth of the stop-band $\delta\lambda_{\mathrm{DBR}}$ is given by

$$\delta\lambda_{\mathrm{DBR}} = \frac{4\lambda_c}{\pi} \arcsin\left(\frac{n_2 - n_1}{n_2 + n_1}\right). \tag{2.7}$$

This equation also indicates that the stop-band width increases as the contrast of two refractive indices becomes higher. The calculation of a DBR based on the transfer matrix method is presented in Fig. 2.4 [42]. For $R \simeq 1$,a cavity quality factor Q is defined as

$$Q = \frac{4}{1-R} \tag{2.8}$$

Using the relation $\gamma_c = E_c/Q$ ($E_c = hc/\lambda_c$), the photon decay rate γ_c is given by

$$\gamma_c = E_c \frac{1-R}{4}. \tag{2.9}$$

Since the photon lifetime of the cavity τ_c is defined as $\tau_c = \hbar/\gamma_c$, in order to obtain a longer photon lifetime, we need to increase the cavity quality factor Q (make the reflectivity R closer to unity).

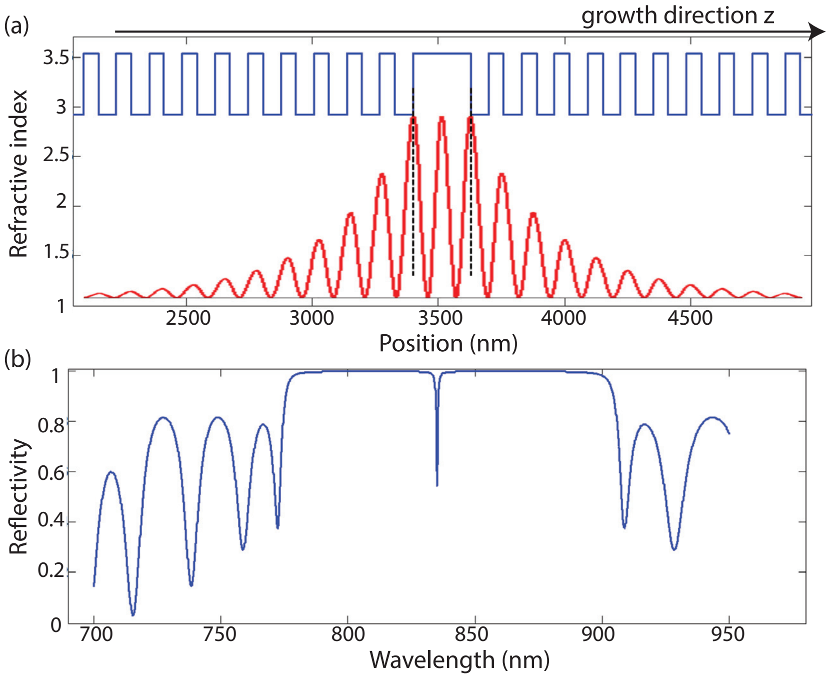

Figure 2.4: Transfer matrix calculation of an electric field intensity inside DBR mirrors and reflectivity from [42]. Given reflective index and calculated distribution of the electric field are presented respectively as a blue and red lines (a). Calculated reflectivity is shown in (b). The dip at 835 nm in the reflectivity is the cavity resonance.

2.4 Photon mass due to the cavity confinement

In this section, we will calculate the 2D energy-momentum dispersion and effective mass of a photon confined in DBR microcavity in the growth direction z (See Fig. 2.4 (a)). In general, the photon energy-momentum dispersion is given by

$$E = \frac{c}{n}\hbar|\boldsymbol{k}| = \frac{c}{n}\hbar\sqrt{k_z^2 + \boldsymbol{k}_\parallel^2}. \tag{2.10}$$

k_z represents the momentum of a photon along the axis of the cavity confinement z, while $\boldsymbol{k}_\parallel$ is the momentum vector parallel to the plane of the cavity defined as $\boldsymbol{k}_\parallel = (k_x, k_y)$. Since the photon is confined along the z-axis, k_z satisfies a resonance condition $k_z l_c = N\pi$, where l_c is the cavity length and N is a positive integer. Equation. 2.10 is rewritten as

$$\begin{aligned} E &= \frac{c}{n}\hbar\left(\frac{N\pi}{l_c}\right)\sqrt{1+\left(\frac{l_c}{N\pi}\right)^2 \boldsymbol{k}_\parallel^2} \\ &\simeq \frac{c}{n}\hbar\left(\frac{N\pi}{l_c}\right) + \frac{c}{2n}\hbar\left(\frac{l_c}{N\pi}\right)\boldsymbol{k}_\parallel^2 \\ &= \frac{2\pi c\hbar}{\lambda_c} + \frac{\hbar^2\boldsymbol{k}_\parallel^2}{2\frac{n^2 h}{c\lambda_c}} \\ &= E_c + \frac{\hbar^2\boldsymbol{k}_\parallel^2}{2m_c}. \end{aligned} \tag{2.11}$$

In the derivation of the above equation, we used another form of resonance condition $2nl_c = N\lambda_c$. The effective mass of a photon confined in the 1D microcavity m_c is defined as

$$m_c = \frac{n^2 h}{c\lambda_c}. \tag{2.12}$$

In conclusion, due to the confinement by a cavity, a photon acquires an effective mass and parabolic energy-momentum dispersion along the cavity plane. The effective mass is determined only by the refractive index and resonance wavelength of the cavity.

2.5 Strong-coupling between exciton and photon

By placing a quantum well at the anti-node of the cavity electric field, we can realize the coupling between a quantum well exciton and a cavity photon. If the coupling strength between the exciton and the photon is strong enough, two new eigenstates called “polaritons" appear, where the exciton and photon mode are no more eigenstates. The schematic of the polariton formation from the exciton-photon coupling is presented in Fig. 2.5. The polariton state with the lower energy is called “lower-polariton" and that with the higher energy is called “upper-polariton". The lower- and upper-polaritons respectively can be seen as the bonding and the anti-bonding molecular state composed of the exciton and photon. By defining the exciton ϵ_x, photon ϵ_c energy and exciton-photon coupling Ω, the lower $\epsilon_L(\boldsymbol{k}_\parallel)$ and upper

$\epsilon_U(\boldsymbol{k}_\parallel)$ polariton energies at $\boldsymbol{k}_\parallel = 0$ are respectively given by

$$\epsilon_{L,0} = \frac{1}{2}\left(\epsilon_x + \epsilon_c - \sqrt{(\epsilon_c - \epsilon_x)^2 + (2\Omega)^2}\right) \tag{2.13}$$

and

$$\epsilon_{U,0} = \frac{1}{2}\left(\epsilon_x + \epsilon_c + \sqrt{(\epsilon_c - \epsilon_x)^2 + (2\Omega)^2}\right) \tag{2.14}$$

The derivation of these equations will be addressed in the next chapter. Since, in reality both cavity photon and the exciton have a finite lifetime, phenomenologically we add decay rates to the energies of the photon and exciton as $\epsilon_x - i\gamma_x$ and $\epsilon_c - i\gamma_c$. When the energy of the photon state is equal to that of the exciton, $\epsilon_c = \epsilon_x$ (zero cavity detuning), the lower and upper-polariton energies read,

$$\epsilon'_{L,0} = \frac{1}{2}\left(2\epsilon_x - i(\gamma_x + \gamma_c) - \sqrt{(2\Omega)^2 - (\gamma_x - \gamma_c)^2}\right) \tag{2.15}$$

and

$$\epsilon'_{U,0} = \frac{1}{2}\left(2\epsilon_x - i(\gamma_x + \gamma_c) + \sqrt{(2\Omega)^2 - (\gamma_x - \gamma_c)^2}\right). \tag{2.16}$$

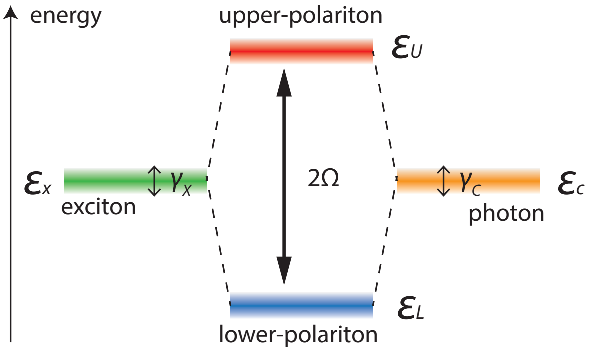

Figure 2.5: Strong-coupling between exciton and photon. If the exciton-photon coupling Ω is large enough compared to the decay rates of the exciton γ_x and photon γ_c, the normal-mode splitting gives rise to the lower and upper polariton modes.

If $2\Omega > |\gamma_x - \gamma_c|$, $\sqrt{(2\Omega)^2 - (\gamma_x - \gamma_c)^2}$ is a real value and the normal-mode splitting of the exciton and photon energy gives rise to the lower- and upper-polaritons. This condition is called "strong-coupling" regime. In addition to this, in order to observe a clear splitting, another condition $2\Omega > \gamma_x + \gamma_c$ should be required [43]. Meanwhile, if $2\Omega < |\gamma_x - \gamma_c|$, $\sqrt{(2\Omega)^2 - (\gamma_x - \gamma_c)^2}$ is an imaginary value and the energy splitting does not appear, instead, decay rates are enhanced. This condition is called "weak-coupling" regime, which is employed in VCSELs (Vertical-cavity surface-emitting lasers) [44]. In this thesis, we investigate the strong-coupling regime between excitons and photons. Namely, the semiconductor microcavity sample which we will study satisfies the two conditions: $2\Omega > |\gamma_x - \gamma_c|$ and $2\Omega > \gamma_x + \gamma_c$.

3 Theoretical framework

This chapter outlines the basic theoretical framework for describing the polariton dynamics in semiconductor microcavities. Firstly, we introduce the starting point: bosonic exciton Hamiltonian interacting with photons. Secondly, we will introduce two types of dynamical equations, excitonic Bloch and Gross-Pitaevskii equations. These two formalisms respectively describe the polariton dynamics with and without dephasing. Finally, we address the physics of the system and their dynamics, within the lower and upper-polariton basis Hamiltonian.

3.1 Exciton-photon basis (local mode)

3.1.1 Exciton-photon Hamiltonian

The starting point of the description of excitons as bosons is the following exciton-photon Hamiltonian without considering a spin degree of freedom [32]: $\hat{H} = \hat{H}_{\mathrm{lin}} + \hat{H}_{\mathrm{int}} + \hat{H}_{\mathrm{qm}}$. The linear coupling term $\hat{H}_{\mathrm{lin}}$ is given by

$$\hat{H}_{\mathrm{lin}} = \int d\mathbf{x} \left[\hat{\boldsymbol{\psi}}_x^\dagger (\epsilon_x - \frac{\hbar^2 \nabla^2}{2m_x}) \hat{\boldsymbol{\psi}}_x + \hat{\boldsymbol{\psi}}_c^\dagger (\epsilon_c - \frac{\hbar^2 \nabla^2}{2m_c}) \hat{\boldsymbol{\psi}}_c + \Omega (\hat{\boldsymbol{\psi}}_c^\dagger \hat{\boldsymbol{\psi}}_x + \hat{\boldsymbol{\psi}}_x^\dagger \hat{\boldsymbol{\psi}}_c) \right]. \tag{3.1}$$

The interacting Hamiltonian $\hat{H}_{\mathrm{int}}$ and $\hat{H}_{\mathrm{qm}}$ respectively read

$$\hat{H}_{\mathrm{int}} = \int d\mathbf{x} \left[\frac{1}{2} g \hat{\boldsymbol{\psi}}_x^\dagger \hat{\boldsymbol{\psi}}_x^\dagger \hat{\boldsymbol{\psi}}_x \hat{\boldsymbol{\psi}}_x - g_{\mathrm{pae}} (\hat{\boldsymbol{\psi}}_c^\dagger \hat{\boldsymbol{\psi}}_x^\dagger \hat{\boldsymbol{\psi}}_x \hat{\boldsymbol{\psi}}_x + \hat{\boldsymbol{\psi}}_x^\dagger \hat{\boldsymbol{\psi}}_x^\dagger \hat{\boldsymbol{\psi}}_x \hat{\boldsymbol{\psi}}_c) \right] \tag{3.2}$$

and

$$\hat{H}_{\mathrm{qm}} = \int d\mathbf{x}\, \Omega_{qm} (\hat{\boldsymbol{\psi}}_c^\dagger \boldsymbol{F} + \boldsymbol{F}^* \hat{\boldsymbol{\psi}}_c). \tag{3.3}$$

$\hat{\boldsymbol{\psi}}_{x(c)}$ and $\hat{\boldsymbol{\psi}}^{\dagger}_{x(c)}$ are exciton (photon) field annihilation and creation operators at position $\mathbf{x}$. They satisfy Bose commutation relations,

$$[\hat{\boldsymbol{\psi}}_{x(c)}(\mathbf{x}), \hat{\boldsymbol{\psi}}^{\dagger}_{x(c)}(\mathbf{x}')] = \delta(\mathbf{x}-\mathbf{x}') \tag{3.4}$$

and

$$[\hat{\boldsymbol{\psi}}^{(\dagger)}_{x(c)}(\mathbf{x}), \hat{\boldsymbol{\psi}}^{(\dagger)}_{x(c)}(\mathbf{x}')] = 0 \tag{3.5}$$

$\epsilon_{x(c)}$ and $m_{x(c)}$ respectively represent the eigenenergies and effective mass of exciton (photon). Ω is the Rabi coupling between excitons and photons inside the microcavity, which corresponds to half the energy of the splitting between the lower and upper-polariton branches at zero cavity detuning. Ω_{qm} in the Hamiltonian $\hat{H}_{\mathrm{qm}}$ represents a “quasi-mode coupling" between photons inside the microcavity $\hat{\boldsymbol{\psi}}_c$ and classical electric-fields outside the cavity $\boldsymbol{F}$. The interaction coefficients g and g_{pae} are introduced as contact interactions [45, 37]. The interaction g represents an exciton-exciton interaction associated with Coulomb exchange scattering [41]. The Coulomb exchange interaction is the Coulomb scattering that involves the exchange of an electron or an hole. This scattering arises from the cooperation of the fermionic nature of excitons and the Coulomb interaction. The exciton-exciton interaction term $\hat{\boldsymbol{\psi}}^{\dagger}_{x}\hat{\boldsymbol{\psi}}^{\dagger}_{x}\hat{\boldsymbol{\psi}}_{x}\hat{\boldsymbol{\psi}}_{x}$ is schematically shown in Fig. 3.1 (a).

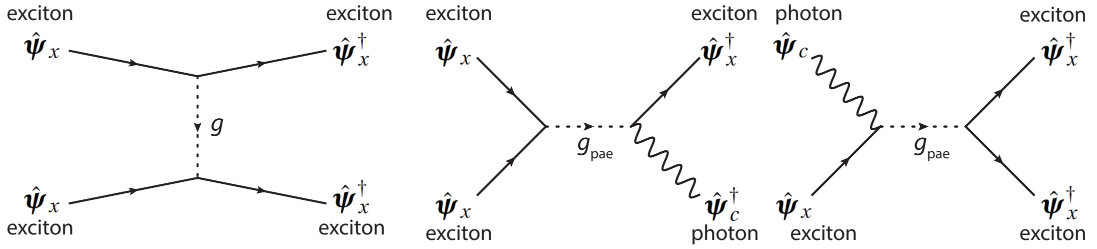
exciton
$\hat{\boldsymbol{\psi}}_x$
exciton
$\hat{\boldsymbol{\psi}}^{\dagger}_x$
g
$\hat{\boldsymbol{\psi}}_x$
exciton
$\hat{\boldsymbol{\psi}}^{\dagger}_x$
exciton
exciton
$\hat{\boldsymbol{\psi}}_x$
exciton
$\hat{\boldsymbol{\psi}}^{\dagger}_x$
g_{pae}
$\hat{\boldsymbol{\psi}}_x$
exciton
$\hat{\boldsymbol{\psi}}^{\dagger}_c$
photon
photon
$\hat{\boldsymbol{\psi}}_c$
exciton
$\hat{\boldsymbol{\psi}}^{\dagger}_x$
g_{pae}
$\hat{\boldsymbol{\psi}}_x$
exciton
$\hat{\boldsymbol{\psi}}^{\dagger}_x$
exciton

(a) exciton-exciton interaction g (b) photon-assisted exchange scattering g_{pae}

Figure 3.1: Schematic representation of the exciton-exciton interaction g (a) and photon-assisted exchange scattering g_{pae} (b) [46]. The solid and wavy lines respectively represent an exciton and a photon. The dashed lines are the interactions.

On the other hand, g_{pae} is called “photon-assisted exchanged scattering" [1]. The term $\hat{\boldsymbol{\psi}}^{\dagger}_{c}\hat{\boldsymbol{\psi}}^{\dagger}_{x}\hat{\boldsymbol{\psi}}_{x}\hat{\boldsymbol{\psi}}_{x}$ ($\hat{\boldsymbol{\psi}}^{\dagger}_{x}\hat{\boldsymbol{\psi}}^{\dagger}_{x}\hat{\boldsymbol{\psi}}_{x}\hat{\boldsymbol{\psi}}_{c}$) represents an annihilation (creation) of two excitons and creation (annihilation) of a pair of exciton and photon (See Fig. 3.1 (b)). Phenomenologically, this term reduces the Rabi coupling between exciton and cavity photon, which leads to a blue-shift of the lower-polariton and a red-shift of the upper-polariton.

---

[1] In many articles, this term is referred to as “phase-space filling".

3.1.2 Equations of motion in exciton-photon basis

In order to calculate the time evolution of the system, we derive the equations of motion of the operators $\hat{\boldsymbol{\psi}}_x$, $\hat{\boldsymbol{\psi}}_x^\dagger\hat{\boldsymbol{\psi}}_x$, and $\hat{\boldsymbol{\psi}}_c$ with the Heisenberg equation of motion $i\hbar\frac{d}{dt}\hat{\boldsymbol{\psi}} = [\hat{\boldsymbol{\psi}}, \hat{H}]$. Our objective is to obtain a closed set of equations of motion that consists of the expectation values $P(\mathbf{x},t) = \langle\hat{\boldsymbol{\psi}}_x\rangle$, $N(\mathbf{x},t) = \langle\hat{\boldsymbol{\psi}}_x^\dagger\hat{\boldsymbol{\psi}}_x\rangle$ and $E(\mathbf{x},t) = \langle\hat{\boldsymbol{\psi}}_c\rangle$. We refer to $P(\mathbf{x},t)$, $N(\mathbf{x},t)$ and $E(\mathbf{x},t)$ respectively as “polarization", “population", and “photon field". The interaction Hamiltonian H_{int} connects the term $\langle\hat{\boldsymbol{\psi}}_x\rangle$ to higher-order terms such as $\langle\hat{\boldsymbol{\psi}}_x\hat{\boldsymbol{\psi}}_x\rangle$ and $\langle\hat{\boldsymbol{\psi}}_x^\dagger\hat{\boldsymbol{\psi}}_x\hat{\boldsymbol{\psi}}_x\rangle$, which connect to next higher-order terms. This infinite chain is called a hierarchy problem. Therefore, we cut the hierarchy by assuming truncations: $\langle\hat{\boldsymbol{\psi}}_x^\dagger\hat{\boldsymbol{\psi}}_x\hat{\boldsymbol{\psi}}_x\rangle \simeq \langle\hat{\boldsymbol{\psi}}_x^\dagger\hat{\boldsymbol{\psi}}_x\rangle\langle\hat{\boldsymbol{\psi}}_x\rangle$, $\langle\hat{\boldsymbol{\psi}}_x^{\dagger\prime}\hat{\boldsymbol{\psi}}'_x\hat{\boldsymbol{\psi}}_x\rangle \simeq \langle\hat{\boldsymbol{\psi}}_x^{\dagger\prime}\hat{\boldsymbol{\psi}}'_x\rangle\langle\hat{\boldsymbol{\psi}}_x\rangle$, $\langle\hat{\boldsymbol{\psi}}_x\hat{\boldsymbol{\psi}}_x\rangle = 0$, and $\langle\hat{\boldsymbol{\psi}}_x^\dagger\hat{\boldsymbol{\psi}}'_x\hat{\boldsymbol{\psi}}'_x\rangle \simeq \langle\hat{\boldsymbol{\psi}}_x^\dagger\rangle\langle\hat{\boldsymbol{\psi}}'_x\hat{\boldsymbol{\psi}}'_x\rangle = 0$ [32]. Finally, from the Heisenberg equations of motion, we obtain excitonic Bloch equations (EBE):

$$
\begin{aligned}
&\text{EBE} \\
i\hbar\dot{N} &= -i\Gamma_x N - 2i(\Omega - 2g_{\text{pae}}N)\text{Im}[PE^*] \qquad (3.6) \\
i\hbar\dot{P} &= (\epsilon_x + g_0 N - i\gamma_x(N))P + (\Omega - 2g_{\text{pae}}N)E \qquad (3.7) \\
i\hbar\dot{E} &= (\epsilon_c - \frac{\hbar^2}{2m_c}\nabla^2 - i\gamma_c)E + (\Omega - g_{\text{pae}}N)P - f_{\text{ext}}. \qquad (3.8)
\end{aligned}
$$

In order to derive the above equations, we assumed that the exciton mass m_x is very large and we therefore neglected the momentum-dispersion of the exciton. $f_{ext}(= -\Omega_{qm}\boldsymbol{F})$ represents the excitation by the external electric field. γ_c represents photon decay rate from the cavity. Γ_x and $\gamma_x(N)$ are respectively the decay and dephasing rate of excitons. Γ_x and $\gamma_x(N)$ respectively correspond to the inverse of T_1 and T_2 time in atomic physics. The general form of $\gamma_x(N)$ is given by

$$\gamma_x(N) = \Gamma_x/2 + \gamma_x^* + g'N. \qquad (3.9)$$

γ_x^* is called pure dephasing. g' is the strength of excitation induced dephasing (EID) (also referred to as “collisional broadening"). If neither pure dephasing nor EID exist (γ_x^* and $g' = 0$), the time evolution of the population is uniquely determined by the polarization according to $N(\mathbf{x},t) = |P(\mathbf{x},t)|^2$. Actually, we can easily show that $|P(\mathbf{x},t)|^2 (= P(\mathbf{x},t)^* P(\mathbf{x},t))$ follows the same equation as Eq. 3.6 in case $\gamma_x(N) = \Gamma_x/2$. Thus, in the coherent limit, we can reduce the three coupled equations (EBE) to two coupled exciton-photon Gross-Pitaevskii equations (GPE):

$$
\begin{aligned}
&\text{exciton} - \text{photon GPE} \\
&i\hbar\dot{\psi_x} = (\epsilon_x + g_0|\psi_x|^2 - i\gamma_x)\psi_x + (\Omega - 2g_{\text{pae}}|\psi_x|^2)\psi_c \qquad (3.10) \\
&i\hbar\dot{\psi_c} = (\epsilon_c - \frac{\hbar^2}{2m_c}\nabla^2 - i\gamma_c)\psi_c + (\Omega - g_{\text{pae}}|\psi_x|^2)\psi_x - f_{\text{ext}}. \qquad (3.11)
\end{aligned}
$$

The symbols P and E are replaced respectively by ψ_x and ψ_c. In GPE, factorization $\langle \hat{\boldsymbol{\psi}}_x^\dagger \hat{\boldsymbol{\psi}}_x \rangle = \langle \hat{\boldsymbol{\psi}}_x^\dagger \rangle \langle \hat{\boldsymbol{\psi}}_x \rangle$ is assumed [37]. GPE has enjoyed a wide range of success for describing the dynamics of resonantly excited polariton and we will use GPE in this thesis for analysing the coherent aspects of polaritons. However, it is worth noting that in strict sense GPE holds only in coherent limit. In order to include the EID effect and calculate the polarization and population explicitly, EBE are necessary. In Chapter 7, we will describe femtosecond pump-probe spectroscopy results that require EBE and examine the difference between EBE and GPE in a detailed way.

3.2 Polariton basis (normal mode)

In the previous section, we described the system written in the exciton-photon basis. We can call excitons and photons local modes, because the nonlinearity originates from the “local" exciton-photon interaction ($\hat{H}_{\text{int}}$). Actually, the exciton-photon basis is a very useful basis for describing the strong non-linearity and incoherent effects associated with excitons. However, due to the strong coupling between exciton and photon Ω, excitons and photons are no more eigenstates of $\hat{H}_{\text{lin}}$. In this section, we introduce the new eigenstates, polaritons, which diagonalize exciton-photon linear coupling Hamiltonian $\hat{H}_{\text{lin}}$.

3.2.1 Diagonalization in momentum-space

Firstly, in order to rewrite $\hat{H}_{\text{lin}}$ in k-space, we use the relations

$$\hat{\psi}_{x(c)}(\mathbf{x}) = \sum_{\boldsymbol{k}} \frac{1}{\sqrt{V}} e^{i\boldsymbol{k}\cdot\mathbf{x}} \cdot \hat{a}_{x(c)}(\boldsymbol{k}). \tag{3.12}$$

and

$$F(\mathbf{x}) = \sum_{\boldsymbol{k}} \frac{1}{\sqrt{V}} e^{i\boldsymbol{k}\cdot\mathbf{x}} \cdot F_{\boldsymbol{k}}. \tag{3.13}$$

V is the volume occupied by excitons or photons. $\hat{a}_{x(c)}$ satisfies the bose commutation relations

$$[\hat{a}_{x(c)}(\boldsymbol{k}), \hat{a}^\dagger_{x(c)}(\boldsymbol{k}')] = \delta_{\boldsymbol{k},\boldsymbol{k}'} \tag{3.14}$$

and

$$[\hat{a}^{(\dagger)}_{x(c)}(\boldsymbol{k}), \hat{a}^{(\dagger)}_{x(c)}(\boldsymbol{k}')] = 0. \tag{3.15}$$

$\hat{H}_{\text{lin}}$ (Eq. 3.1) and $\hat{H}_{\text{qm}}$ (Eq. 3.3) in k-space are given by

$$\hat{H}_{\text{lin}} = \sum_{\boldsymbol{k}} \epsilon_x(\boldsymbol{k}) \hat{a}_x^\dagger(\boldsymbol{k}) \hat{a}_x(\boldsymbol{k}) + \epsilon_c(\boldsymbol{k}) \hat{a}_c^\dagger(\boldsymbol{k}) \hat{a}_c(\boldsymbol{k}) + \Omega \left(\hat{a}_c^\dagger(\boldsymbol{k}) \hat{a}_x(\boldsymbol{k}) + \hat{a}_x^\dagger(\boldsymbol{k}) \hat{a}_c(\boldsymbol{k}) \right) \tag{3.16}$$

and

$$\hat{H}_{\mathrm{qm}} = \sum_{\boldsymbol{k}} \Omega_{qm}(\hat{a}_c^{\dagger}(\boldsymbol{k})F_{\boldsymbol{k}} + F_{\boldsymbol{k}}^{*}\hat{a}_c(\boldsymbol{k})). \tag{3.17}$$

The energy-momentum dispersion $\epsilon_{x(c)}(\boldsymbol{k})$ is

$$\epsilon_{x(c)}(\boldsymbol{k}) = \epsilon_{x(c)} + \frac{\hbar^2 \boldsymbol{k}^2}{2m_{x(c)}}. \tag{3.18}$$

We introduce new operators $\hat{a}_L$ and $\hat{a}_U$ defined as

$$\begin{pmatrix} \hat{a}_x(\boldsymbol{k}) \\ \hat{a}_c(\boldsymbol{k}) \end{pmatrix} = \begin{pmatrix} X_{\boldsymbol{k}} & -C_{\boldsymbol{k}} \\ C_{\boldsymbol{k}} & X_{\boldsymbol{k}} \end{pmatrix} \begin{pmatrix} \hat{a}_L(\boldsymbol{k}) \\ \hat{a}_U(\boldsymbol{k}) \end{pmatrix}$$

or inversely

$$\begin{pmatrix} \hat{a}_L(\boldsymbol{k}) \\ \hat{a}_U(\boldsymbol{k}) \end{pmatrix} = \begin{pmatrix} X_{\boldsymbol{k}} & C_{\boldsymbol{k}} \\ -C_{\boldsymbol{k}} & X_{\boldsymbol{k}} \end{pmatrix} \begin{pmatrix} \hat{a}_x(\boldsymbol{k}) \\ \hat{a}_c(\boldsymbol{k}) \end{pmatrix}.$$

$\hat{a}_{L(U)}$ is the annihilation operator of lower (upper)-polariton. $X_{\boldsymbol{k}}$ and $C_{\boldsymbol{k}}$ are respectively called excitonic (photonic) and photonic (excitonic) Hopfield coefficients of lower (upper) polaritons. Their explicit forms are

$$X_{\boldsymbol{k}} = \sqrt{\frac{1}{2}\left(1 + \frac{\epsilon_c(\boldsymbol{k}) - \epsilon_x(\boldsymbol{k})}{\sqrt{(\epsilon_c(\boldsymbol{k}) - \epsilon_x(\boldsymbol{k}))^2 + (2\Omega)^2}}\right)} \tag{3.19}$$

and

$$C_{\boldsymbol{k}} = -\sqrt{\frac{1}{2}\left(1 - \frac{\epsilon_c(\boldsymbol{k}) - \epsilon_x(\boldsymbol{k})}{\sqrt{(\epsilon_c(\boldsymbol{k}) - \epsilon_x(\boldsymbol{k}))^2 + (2\Omega)^2}}\right)}. \tag{3.20}$$

$X_{\boldsymbol{k}}$ and $C_{\boldsymbol{k}}$ satisfy the relation: $|X_{\boldsymbol{k}}|^2 + |C_{\boldsymbol{k}}|^2 = 1$. The polariton operators satisfy the bosonic commutation relations: $[\hat{a}_{L(U)}(\boldsymbol{k}), \hat{a}^{\dagger}_{L(U)}(\boldsymbol{k}')] = \delta_{\boldsymbol{k},\boldsymbol{k}'}$ and $[\hat{a}_{L(U)}(\boldsymbol{k}), \hat{a}_{L(U)}(\boldsymbol{k}')] = 0$.

Using the polariton operator $\hat{a}_L$ and $\hat{a}_U$, $\hat{H}_{lin}$ can be diagonalized as

$$\hat{H}_{\mathrm{lin}} = \sum_{\boldsymbol{k}} \epsilon_L(\boldsymbol{k})\hat{a}_L^{\dagger}(\boldsymbol{k})\hat{a}_L(\boldsymbol{k}) + \epsilon_U(\boldsymbol{k})\hat{a}_U^{\dagger}(\boldsymbol{k})\hat{a}_U(\boldsymbol{k}). \tag{3.21}$$

The lower $\epsilon_L(\boldsymbol{k})$ and upper $\epsilon_U(\boldsymbol{k})$ polariton dispersions are given by

$$\epsilon_L(\boldsymbol{k}) = \frac{1}{2}\left(\epsilon_c(\boldsymbol{k}) + \epsilon_x(\boldsymbol{k}) - \sqrt{(\epsilon_c(\boldsymbol{k}) - \epsilon_x(\boldsymbol{k}))^2 + (2\Omega)^2}\right) \tag{3.22}$$

and

$$\epsilon_U(\boldsymbol{k}) = \frac{1}{2}\left(\epsilon_c(\boldsymbol{k}) + \epsilon_x(\boldsymbol{k}) + \sqrt{(\epsilon_c(\boldsymbol{k}) - \epsilon_x(\boldsymbol{k}))^2 + (2\Omega)^2}\right). \tag{3.23}$$

$\epsilon_L(\boldsymbol{k})$ and $\epsilon_U(\boldsymbol{k})$ are plotted in Fig. 3.2 for three different cavity detunings, $\delta = \epsilon_c - \epsilon_x$=-1, 0, and 1 meV. For the plot, the Rabi coupling 2Ω is chosen to be 3.26 meV and we assume that the exciton energy-momentum dispersion $\epsilon_x(\boldsymbol{k})$ is flat at 0 meV, because of the heavy mass of exciton.

The quasi-mode coupling Hamiltonian $\hat{H}_{\text{qm}}$ is rewritten as

$$\hat{H}_{\text{qm}} = \sum_{\boldsymbol{k}} \Omega^*_{L,\boldsymbol{k}} \hat{a}^\dagger_L(\boldsymbol{k}) F_{\boldsymbol{k}} + \Omega_{L,\boldsymbol{k}} F^*_{\boldsymbol{k}} \hat{a}_L(\boldsymbol{k}) + \Omega^*_{U,\boldsymbol{k}} \hat{a}^\dagger_U(\boldsymbol{k}) F_{\boldsymbol{k}} + \Omega_{U,\boldsymbol{k}} F^*_{\boldsymbol{k}} \hat{a}_U(\boldsymbol{k}). \tag{3.24}$$

$\hat{H}_{\text{qm}}$ in polariton basis indicates that lower (upper)-polaritons $\hat{a}_{L(U)}(\boldsymbol{k})$ is “weakly" coupled to the electric-field outside the cavity f_{ext} with the coupling strength $\Omega_{L(U)}$ defined as $\Omega_{L,\boldsymbol{k}} = \Omega_{\text{qm}} C_{\boldsymbol{k}}$ and $\Omega_{U,\boldsymbol{k}} = \Omega_{\text{qm}} X_{\boldsymbol{k}}$. This formalism is important when we apply a third-order perturbation theory to the strong-coupling system in Chapter. 5.

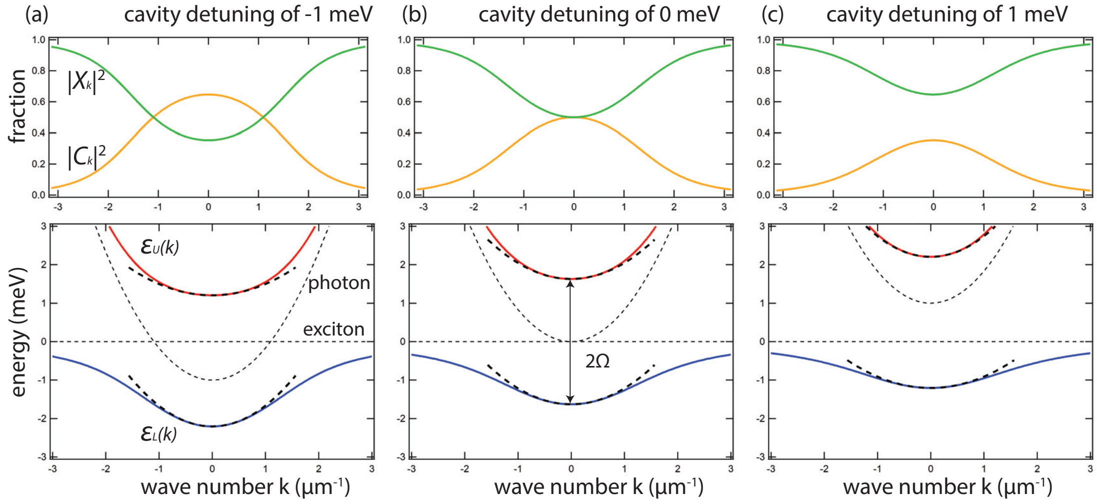

Figure 3.2: Hopfield coefficients and energy-momentum dispersions of the lower and upper polaritons for -1 (a), 0 (b), and 1 meV (c) cavity detunings. The dashed lines overlapped on the polariton energy-momentum dispersions are harmonic approximations to the polariton effective masses.

3.2.2 Polariton basis in real-space

If the momentum $\boldsymbol{k}$ is small, the lower and upper-polariton energy-momentum dispersion can be approximated as parabolic dispersion:

$$\epsilon_{L(U)}(\boldsymbol{k}) \simeq \epsilon_{L(U),0} + \frac{\hbar^2 \boldsymbol{k}^2}{2m_{L(U)}} \tag{3.25}$$

$\epsilon_{L(U),0}$ is defined as $\epsilon_{L(U),0} = \epsilon_{L(U)}(\mathbf{0})$. Using the Hopfield coefficients, the effective masses of lower and upper polariton are represented as

$$\frac{1}{m_{L(U)}} = \frac{|X_{\mathbf{0}}|^2}{m_{x(c)}} + \frac{|C_{\mathbf{0}}|^2}{m_{c(x)}} \tag{3.26}$$

In Fig. 3.2, the harmonic approximation of the polariton energy-momentum dispersion (Eq. 3.25) is overlapped on the exact ones, which shows that the harmonic approximation is a good approximation for small momentum values. Within this approximation, we can rewrite $\hat{H}_{\text{lin}}$ in real space under a simple form:

$$\begin{aligned}\hat{H}_{\text{lin}} + \hat{H}_{\text{qm}} \quad \simeq \quad & \int d\mathbf{x} \Big[\hat{\boldsymbol{\psi}}_L^\dagger (\epsilon_{L,0} - \frac{\hbar^2 \nabla^2}{2m_L}) \hat{\boldsymbol{\psi}}_L + \hat{\boldsymbol{\psi}}_U^\dagger (\epsilon_{U,0} - \frac{\hbar^2 \nabla^2}{2m_U}) \hat{\boldsymbol{\psi}}_U \\ & + \Omega_{L,0}^* \hat{\boldsymbol{\psi}}_L^\dagger \boldsymbol{F} + \Omega_{L,0} \boldsymbol{F}^* \hat{\boldsymbol{\psi}}_L + \Omega_{U,0}^* \hat{\boldsymbol{\psi}}_U^\dagger \boldsymbol{F} + \Omega_{U,0} \boldsymbol{F}^* \hat{\boldsymbol{\psi}}_U \Big] ,\end{aligned} \tag{3.27}$$

where $\Omega_{L(U),0} = \Omega_{L(U),\boldsymbol{k}}$ at $\boldsymbol{k} = 0$. $\hat{\boldsymbol{\psi}}_{L(U)}$ is connected to $\hat{\boldsymbol{\psi}}_{x(c)}$ as

$$\begin{pmatrix} \hat{\psi}_x(\mathbf{x}) \\ \hat{\psi}_c(\mathbf{x}) \end{pmatrix} = \begin{pmatrix} X_{\mathbf{0}} & -C_{\mathbf{0}} \\ C_{\mathbf{0}} & X_{\mathbf{0}} \end{pmatrix} \begin{pmatrix} \hat{\psi}_L(\mathbf{x}) \\ \hat{\psi}_U(\mathbf{x}) \end{pmatrix}$$

or inversely

$$\begin{pmatrix} \hat{\psi}_L(\mathbf{x}) \\ \hat{\psi}_U(\mathbf{x}) \end{pmatrix} = \begin{pmatrix} X_{\mathbf{0}} & C_{\mathbf{0}} \\ -C_{\mathbf{0}} & X_{\mathbf{0}} \end{pmatrix} \begin{pmatrix} \hat{\psi}_x(\mathbf{x}) \\ \hat{\psi}_c(\mathbf{x}) \end{pmatrix}.$$

With a cavity detuning defined as $\delta = \epsilon_c - \epsilon_x$

$$\epsilon_{L,0} = \frac{1}{2}\left(2\epsilon_x + \delta - \sqrt{\delta^2 + (2\Omega)^2}\right) \tag{3.28}$$

and

$$\epsilon_{U,0} = \frac{1}{2}\left(2\epsilon_x + \delta + \sqrt{\delta^2 + (2\Omega)^2}\right). \tag{3.29}$$

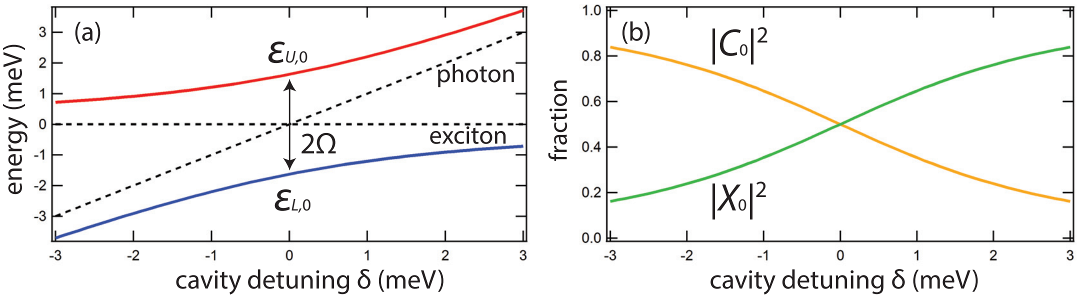

Figure 3.3: The lower $\epsilon_{L,0}$ and upper $\epsilon_{U,0}$ polariton energy at $\boldsymbol{k} = 0$ as a function of the cavity detuning (a). The excitonic (photonic) $|X_\mathbf{0}|^2$ and photonic (excitonic) fraction $|C_\mathbf{0}|^2$ of the lower (upper) -polariton as a function of the cavity detuning (b).

Similarly, $X_\mathbf{0}$ and $C_\mathbf{0}$ can be represented as

$$X_\mathbf{0} = \sqrt{\frac{1}{2}\left(1 + \frac{\delta}{\sqrt{\delta^2 + (2\Omega)^2}}\right)} \tag{3.30}$$

and

$$C_\mathbf{0} = -\sqrt{\frac{1}{2}\left(1 - \frac{\delta}{\sqrt{\delta^2 + (2\Omega)^2}}\right)}. \tag{3.31}$$

Figure 3.3 presents $|X_\mathbf{0}|^2$, $|C_\mathbf{0}|^2$, and $\epsilon_{L(U),0}$. At negative (positive) cavity detuning, the lower-polariton is photonic (excitonic) and the upper-polariton is exciton (photon) like.

Now, it is instructive to compare the present polariton model with the Jaynes-Cummings model, which models the strong-coupling between a two-level atom and photons [47]. In the present polariton model, since bosonic exciton and photon are considered as two harmonic oscillators, the eigenstates (normal modes) of the strong-coupling are also two harmonic oscillators (bosons). As is shown in Fig. 3.4 (a), all transitions between different polariton states always correspond either to the lower ϵ_L or the upper-polariton energy ϵ_U. The consequence is that the strong coupling between bosonic excitons and photon does not give rise to a non-linearity. Therefore, in order to introduce non-linearities in the polariton system, we need to consider the exciton-exciton interaction or photon-assisted exchange scattering term in $\hat{H}_\text{int}$. This has a striking contrast to the strong-coupling between a single two-level atom and photons (Jaynes-Cummings model). In the Jaynes-Cummings model (Fig. 3.4 (b)), the energy of normal-mode splitting depends on the number of photons as $2\sqrt{n}\Omega$. Thus, the energy ladder is not harmonic and there exists a non-linearity in the Jaynes-Cummings model. This originates from the fact that two-level system such as a single atom and quantum-dot is intrinsically optically non-linear because of its “fermionic" nature (“fermionic in a sense that two quanta cannot occupy the same excited state).

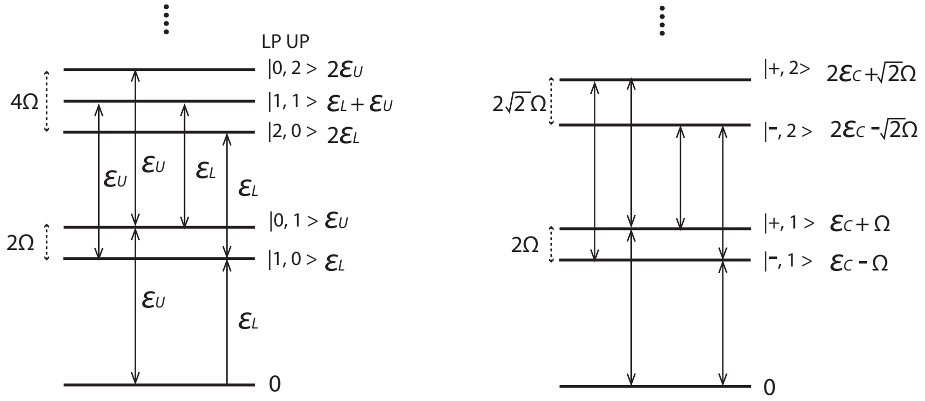
LP UP
|0, 2 > 2εU
|1, 1 > εL + εU
|2, 0 > 2εL
4Ω
εU
εU
εL
εL
|0, 1 > εU
|1, 0 > εL
2Ω
εU
εL
0
|+, 2> 2εC+√2Ω
|-, 2 > 2εC -√2Ω
2√2 Ω
|+, 1 > εC+ Ω
|-, 1 > εC - Ω
2Ω
0

(a) Bosonic exciton-photon coupling
(polariton model)

(b) Two-levels atom-photon coupling
(Jaynes-Cummings model)

Figure 3.4: Energy levels of polariton mode (a) and Jaynes-Cummings model (b). In the polariton model, all the ladder transition energies correspond to either ϵ_L or ϵ_U, therefore the system is linear. On the other hand, in the Jaynes-Cummings model, the ladder transition energies strongly depend on the level of the rang, which originates a optical nonlinearity.

3.2.3 Interaction Hamiltonians in polariton basis (polariton-polariton interactions)

The interaction Hamiltonian H_{int} is separated into the exciton-exciton and photon-assisted scattering term as $\hat{H}_{int} = \hat{H}_{xx} + \hat{H}_{\text{pae}}$. $\hat{H}_{xx}$ and $\hat{H}_{\text{pae}}$ are respectively

$$\hat{H}_{xx} = \int d\mathbf{x} \left[\frac{1}{2} g \hat{\boldsymbol{\psi}}_x^\dagger \hat{\boldsymbol{\psi}}_x^\dagger \hat{\boldsymbol{\psi}}_x \hat{\boldsymbol{\psi}}_x \right] \tag{3.32}$$

and

$$\hat{H}_{\text{pae}} = \int d\mathbf{x} \left[-g_{\text{pae}} (\hat{\boldsymbol{\psi}}_c^\dagger \hat{\boldsymbol{\psi}}_x^\dagger \hat{\boldsymbol{\psi}}_x \hat{\boldsymbol{\psi}}_x + \hat{\boldsymbol{\psi}}_x^\dagger \hat{\boldsymbol{\psi}}_x^\dagger \hat{\boldsymbol{\psi}}_x \hat{\boldsymbol{\psi}}_c) \right]. \tag{3.33}$$

Firstly we rewrite the interaction Hamiltonian associated with the exciton-exciton interaction term $\hat{H}_{xx}$ in polariton basis as

$$\hat{H}_{xx} = \int d\mathbf{x} \ [\ \frac{1}{2} g X_{\mathbf{0}}^4 \hat{\boldsymbol{\psi}}_L^\dagger \hat{\boldsymbol{\psi}}_L^\dagger \hat{\boldsymbol{\psi}}_L \hat{\boldsymbol{\psi}}_L \tag{xx a1}$$

$$+ \frac{1}{2} g |C_{\mathbf{0}}|^4 \hat{\boldsymbol{\psi}}_U^\dagger \hat{\boldsymbol{\psi}}_U^\dagger \hat{\boldsymbol{\psi}}_U \hat{\boldsymbol{\psi}}_U \tag{xx a2}$$

$$+ 2 g X_{\mathbf{0}}^2 |C_{\mathbf{0}}|^2 \hat{\boldsymbol{\psi}}_L^\dagger \hat{\boldsymbol{\psi}}_U^\dagger \hat{\boldsymbol{\psi}}_L \hat{\boldsymbol{\psi}}_U \tag{xx a3}$$

$$+ g X_{\mathbf{0}}^3 |C_{\mathbf{0}}| \hat{\boldsymbol{\psi}}_L^\dagger \hat{\boldsymbol{\psi}}_L^\dagger \hat{\boldsymbol{\psi}}_L \hat{\boldsymbol{\psi}}_U \tag{xx b1}$$

$$+ g X_{\mathbf{0}} |C_{\mathbf{0}}|^3 \hat{\boldsymbol{\psi}}_L^\dagger \hat{\boldsymbol{\psi}}_U^\dagger \hat{\boldsymbol{\psi}}_U \hat{\boldsymbol{\psi}}_U \tag{xx b2}$$

$$+ g X_{\mathbf{0}}^3 |C_{\mathbf{0}}| \hat{\boldsymbol{\psi}}_U^\dagger \hat{\boldsymbol{\psi}}_L^\dagger \hat{\boldsymbol{\psi}}_L \hat{\boldsymbol{\psi}}_L \tag{xx b3}$$

$$+ g X_{\mathbf{0}} |C_{\mathbf{0}}|^3 \hat{\boldsymbol{\psi}}_U^\dagger \hat{\boldsymbol{\psi}}_U^\dagger \hat{\boldsymbol{\psi}}_U \hat{\boldsymbol{\psi}}_L \tag{xx b4}$$

$$+ \frac{1}{2} g X_{\mathbf{0}}^2 |C_{\mathbf{0}}|^2 \hat{\boldsymbol{\psi}}_L^\dagger \hat{\boldsymbol{\psi}}_L^\dagger \hat{\boldsymbol{\psi}}_U \hat{\boldsymbol{\psi}}_U \tag{xx c1}$$

$$+ \frac{1}{2} g X_{\mathbf{0}}^2 |C_{\mathbf{0}}|^2 \hat{\boldsymbol{\psi}}_U^\dagger \hat{\boldsymbol{\psi}}_U^\dagger \hat{\boldsymbol{\psi}}_L \hat{\boldsymbol{\psi}}_L\ ]. \tag{xx c2}$$

Similarly, $\hat{H}_{\text{pae}}$ reads in the polariton basis,

$$\hat{H}_{\text{pae}} = \int d\mathbf{x} \ [\ 2 g_{\text{pae}} X_{\mathbf{0}}^3 |C_{\mathbf{0}}| \hat{\boldsymbol{\psi}}_L^\dagger \hat{\boldsymbol{\psi}}_L^\dagger \hat{\boldsymbol{\psi}}_L \hat{\boldsymbol{\psi}}_L \tag{pae a1}$$

$$- 2 g_{\text{pae}} X_{\mathbf{0}} |C_{\mathbf{0}}|^3 \hat{\boldsymbol{\psi}}_U^\dagger \hat{\boldsymbol{\psi}}_U^\dagger \hat{\boldsymbol{\psi}}_U \hat{\boldsymbol{\psi}}_U \tag{pae a2}$$

$$+ 4 g_{\text{pae}} X_{\mathbf{0}} |C_{\mathbf{0}}| (|C_{\mathbf{0}}|^2 - X_{\mathbf{0}}^2) \hat{\boldsymbol{\psi}}_L^\dagger \hat{\boldsymbol{\psi}}_U^\dagger \hat{\boldsymbol{\psi}}_L \hat{\boldsymbol{\psi}}_U \tag{pae a3}$$

$$- g_{\text{pae}} (X_{\mathbf{0}}^4 - 3 X_{\mathbf{0}}^2 |C_{\mathbf{0}}|^2) \hat{\boldsymbol{\psi}}_L^\dagger \hat{\boldsymbol{\psi}}_L^\dagger \hat{\boldsymbol{\psi}}_L \hat{\boldsymbol{\psi}}_U \tag{pae b1}$$

$$- g_{\text{pae}} (3 X_{\mathbf{0}}^2 |C_{\mathbf{0}}|^2 - |C_{\mathbf{0}}|^4) \hat{\boldsymbol{\psi}}_L^\dagger \hat{\boldsymbol{\psi}}_U^\dagger \hat{\boldsymbol{\psi}}_U \hat{\boldsymbol{\psi}}_U \tag{pae b2}$$

$$- g_{\text{pae}} (X_{\mathbf{0}}^4 - 3 X_{\mathbf{0}}^2 |C_{\mathbf{0}}|^2) \hat{\boldsymbol{\psi}}_U^\dagger \hat{\boldsymbol{\psi}}_L^\dagger \hat{\boldsymbol{\psi}}_L \hat{\boldsymbol{\psi}}_L \tag{pae b3}$$

$$- g_{\text{pae}} (3 X_{\mathbf{0}}^2 |C_{\mathbf{0}}|^2 - |C_{\mathbf{0}}|^4) \hat{\boldsymbol{\psi}}_U^\dagger \hat{\boldsymbol{\psi}}_U^\dagger \hat{\boldsymbol{\psi}}_U \hat{\boldsymbol{\psi}}_L \tag{pae b4}$$

$$+ \frac{1}{2} g_{\text{pae}} X_{\mathbf{0}} |C_{\mathbf{0}}| (|C_{\mathbf{0}}|^2 - X_{\mathbf{0}}^2) \hat{\boldsymbol{\psi}}_L^\dagger \hat{\boldsymbol{\psi}}_L^\dagger \hat{\boldsymbol{\psi}}_U \hat{\boldsymbol{\psi}}_U \tag{pae c1}$$

$$+ \frac{1}{2} g_{\text{pae}} X_{\mathbf{0}} |C_{\mathbf{0}}| (|C_{\mathbf{0}}|^2 - X_{\mathbf{0}}^2) \hat{\boldsymbol{\psi}}_U^\dagger \hat{\boldsymbol{\psi}}_U^\dagger \hat{\boldsymbol{\psi}}_L \hat{\boldsymbol{\psi}}_L\ ]. \tag{pae c2}$$

The exciton-exciton interaction g_0 works as a repulsive interaction both for lower and upper polaritons (See the signs of (xx a1) and (xx a2)). On the other hand, the photon-assisted exchange scattering is a repulsive (attractive) interaction for lower (upper) polariton interaction (See the signs of (pae a1) and (pae a2)). The terms (xx a3) and (pae a3) are mutual interaction between lower and upper-polariton, which contribute to the energy shift of a polariton branch induced by the other branch. These terms are interpreted as cross phase modulations [48]. When only the lower-polariton branch is excited, we neglect the terms that involve the upper-polariton operator. In this approximation, the Hamiltonian for the lower-polariton is given by [49]

$$\hat{H}_{\text{int,LP}} = \int d\mathbf{x} \left[\frac{1}{2} g X_{\mathbf{0}}^4 \hat{\boldsymbol{\psi}}_L^\dagger \hat{\boldsymbol{\psi}}_L^\dagger \hat{\boldsymbol{\psi}}_L \hat{\boldsymbol{\psi}}_L + 2 g_{\text{pae}} X_{\mathbf{0}}^3 |C_{\mathbf{0}}| \hat{\boldsymbol{\psi}}_L^\dagger \hat{\boldsymbol{\psi}}_L^\dagger \hat{\boldsymbol{\psi}}_L \hat{\boldsymbol{\psi}}_L \right] \tag{3.34}$$

3.2.4 Equation of motion of lower-polariton

The Hamiltonian for the lower polariton H_{LP} is

$$\begin{aligned} \hat{H}_{\text{LP}} &= \hat{H}_{\text{lin,LP}} + \hat{H}_{\text{int,LP}} + \hat{H}_{\text{qm,LP}} \\ &= \int d\mathbf{x} \Big[\hat{\boldsymbol{\psi}}_L^\dagger (\epsilon_{L,0} - \frac{\hbar^2 \nabla^2}{2 m_L}) \hat{\boldsymbol{\psi}}_L \\ &\quad + (\frac{1}{2} g X_{\mathbf{0}}^4 + 2 g_{\text{pae}} X_{\mathbf{0}}^3 |C_{\mathbf{0}}|) \hat{\boldsymbol{\psi}}_L^\dagger \hat{\boldsymbol{\psi}}_L^\dagger \hat{\boldsymbol{\psi}}_L \hat{\boldsymbol{\psi}}_L \\ &\quad + \Omega_{L,0}^* \hat{\boldsymbol{\psi}}_L^\dagger \boldsymbol{F} + \Omega_{L,0} \boldsymbol{F}^* \hat{\boldsymbol{\psi}}_L \Big]. \end{aligned} \tag{3.35}$$

$H_{\text{lin,LP}}$ and $H_{\text{qm,LP}}$ are respectively the linear Hamiltonian and the quasi-mode coupling of lower-polaritons. The Heisenberg equation of motion for the lower-polariton is obtained as

$$i\hbar \dot{\psi}_L = (\epsilon_L, 0 - \frac{\hbar^2}{2 m_L} \nabla^2 + g_{LP} |\psi_L|^2 - i \gamma_L) \psi_L - f_{\text{ext}}. \tag{3.36}$$

This is the commonly used Gross-Pitaevskii equation for lower-polaritons. ψ_L is the expectation value of the lower-polariton annihilation operator, $\psi_L = \langle \hat{\boldsymbol{\psi}}_L \rangle$. In order to derive this equation, we apply the coherent limit approximation as $\langle \hat{\boldsymbol{\psi}}_L^\dagger \hat{\boldsymbol{\psi}}_L \hat{\boldsymbol{\psi}}_L \rangle = \langle \hat{\boldsymbol{\psi}}_L^\dagger \rangle \langle \hat{\boldsymbol{\psi}}_L \rangle \langle \hat{\boldsymbol{\psi}}_L \rangle$. The term $f_{\text{ext}} = (-\Omega_{L,0}^* \boldsymbol{F})$ represents a driving term due to the electric-field outside the cavity. The lower-polariton interaction g_{LP} is given by

$$g_{LP} = g X_{\mathbf{0}}^4 + 4 g_{\text{pae}} X_{\mathbf{0}}^3 |C_{\mathbf{0}}|. \tag{3.37}$$

γ_L is the effective dephasing rate of the lower-polaritons defined as $\gamma_L = |X|^2 \gamma_x + |C|^2 \gamma_c$.

3.3 Spin-dependent interactions

Until now, we have neglected the spin-degree of freedom by assuming that only a single direction of spin configuration is involved. In this section, we consider the spin-dependence of the exciton-exciton interactions. As stated in the previous chapter, a quantum well exciton has two-spin projections: spin up and down. Moreover, there is a one-to-one correspondence between the spin of the exciton and the polarization of the cavity photon. An exciton with a spin-up (-down) $\hat{\boldsymbol{\psi}}_{x,\uparrow(\downarrow)}$ couples cavity photon with a $\sigma^{+(-)}$ polarization $\hat{\boldsymbol{\psi}}_{c,\uparrow(\downarrow)}$. In particular, when two excitons have opposite spins (spin-up and -down), an exciton molecule called “biexciton" can be formed. Defining the bosonic biexciton operator $\hat{\boldsymbol{\psi}}_B$, a spin-dependent Hamiltonian including biexciton coupling is given by [50]

$$\hat{H} = \hat{H}_{\text{lin}} + \hat{H}_{\text{int}} + \hat{H}_{\text{qm}}. \tag{3.38}$$

The three parts are respectively

$$\begin{aligned}\hat{H}_{\text{lin}} &= \sum_{\sigma=\{\uparrow\downarrow\}} \int d\mathbf{x} \Big[\hat{\boldsymbol{\psi}}^{\dagger}_{x,\sigma} (\epsilon_x - \frac{\hbar^2\nabla^2}{2m_x}) \hat{\boldsymbol{\psi}}_{x,\sigma} + \hat{\boldsymbol{\psi}}^{\dagger}_{c,\sigma} (\epsilon_c - \frac{\hbar^2\nabla^2}{2m_c}) \hat{\boldsymbol{\psi}}_{c,\sigma} + \epsilon_B \hat{\boldsymbol{\psi}}^{\dagger}_B \hat{\boldsymbol{\psi}}_B \\ &\quad + \Omega(\hat{\boldsymbol{\psi}}^{\dagger}_{c,\sigma} \hat{\boldsymbol{\psi}}_{x,\sigma} + \hat{\boldsymbol{\psi}}^{\dagger}_{x,\sigma} \hat{\boldsymbol{\psi}}_{c,\sigma}) \Big], \end{aligned} \tag{3.39}$$

$$\begin{aligned}\hat{H}_{\text{int}} &= \sum_{\sigma=\{\uparrow\downarrow\}} \int d\mathbf{x} [\, \frac{1}{2} g \hat{\boldsymbol{\psi}}^{\dagger}_{x,\sigma} \hat{\boldsymbol{\psi}}^{\dagger}_{x,\sigma} \hat{\boldsymbol{\psi}}_{x,\sigma} \hat{\boldsymbol{\psi}}_{x,\sigma} + \frac{1}{2} g_{+-} \hat{\boldsymbol{\psi}}^{\dagger}_{x,\sigma} \hat{\boldsymbol{\psi}}^{\dagger}_{x,-\sigma} \hat{\boldsymbol{\psi}}_{x,-\sigma} \hat{\boldsymbol{\psi}}_{x,\sigma} \\ &\quad + \frac{1}{2} g_{bx} (\hat{\boldsymbol{\psi}}_B \hat{\boldsymbol{\psi}}^{\dagger}_{x,\sigma} \hat{\boldsymbol{\psi}}^{\dagger}_{x,-\sigma} + \hat{\boldsymbol{\psi}}_{x,\sigma} \hat{\boldsymbol{\psi}}_{x,-\sigma} \hat{\boldsymbol{\psi}}^{\dagger}_B) \\ &\quad - g_{\text{pae}} (\hat{\boldsymbol{\psi}}^{\dagger}_{c,\sigma} \hat{\boldsymbol{\psi}}^{\dagger}_{x,\sigma} \hat{\boldsymbol{\psi}}_{x,\sigma} \hat{\boldsymbol{\psi}}_{x,\sigma} + \hat{\boldsymbol{\psi}}^{\dagger}_{x,\sigma} \hat{\boldsymbol{\psi}}^{\dagger}_{x,\sigma} \hat{\boldsymbol{\psi}}_{x,\sigma} \hat{\boldsymbol{\psi}}_{c,\sigma}) \,], \end{aligned} \tag{3.40}$$

and

$$\hat{H}_{\text{qm}} = \sum_{\sigma=\{\uparrow\downarrow\}} \int d\mathbf{x}\, \Omega_{qm} (\hat{\boldsymbol{\psi}}^{\dagger}_{c,\sigma} \boldsymbol{F}_{\sigma} + \boldsymbol{F}^{*}_{\sigma} \hat{\boldsymbol{\psi}}_{c,\sigma}). \tag{3.41}$$

here, the spin-dependent operators satisfy the following commutation relations,

$$[\hat{\boldsymbol{\psi}}_{x(c),\sigma}(\mathbf{x}), \hat{\boldsymbol{\psi}}^{\dagger}_{x(c),\sigma'}(\mathbf{x}')] = \delta_{\sigma,\sigma'} \delta(\mathbf{x}-\mathbf{x}') \tag{3.42}$$

and

$$[\hat{\boldsymbol{\psi}}^{(\dagger)}_{x(c),\sigma}(\mathbf{x}), \hat{\boldsymbol{\psi}}^{(\dagger)}_{x(c),\sigma'}(\mathbf{x}')] = 0. \tag{3.43}$$

The bosonic biexciton operator $\hat{\boldsymbol{\psi}}_B$ satisfies

$$[\hat{\boldsymbol{\psi}}_B(\mathbf{x}), \hat{\boldsymbol{\psi}}^{\dagger}_B(\mathbf{x}')] = \delta(\mathbf{x}-\mathbf{x}') \tag{3.44}$$

and

$$[\hat{\boldsymbol{\psi}}_B^{(\dagger)}(\mathbf{x}), \hat{\boldsymbol{\psi}}_B^{(\dagger)}(\mathbf{x}')] = 0. \tag{3.45}$$

The constants g_{+-} and g_{bx} respectively represent exciton-exciton interaction with anti-parallel spins and exciton-biexciton coupling. The exciton-biexciton coupling term represents the formation of biexciton from two-excitons with opposite spins as schematically shown in Fig. 3.5. It is worth noting that the photon-assisted exchange scattering occurs only between excitons and photons with parallel spins because it is originated from the fermionic nature of the excitons.

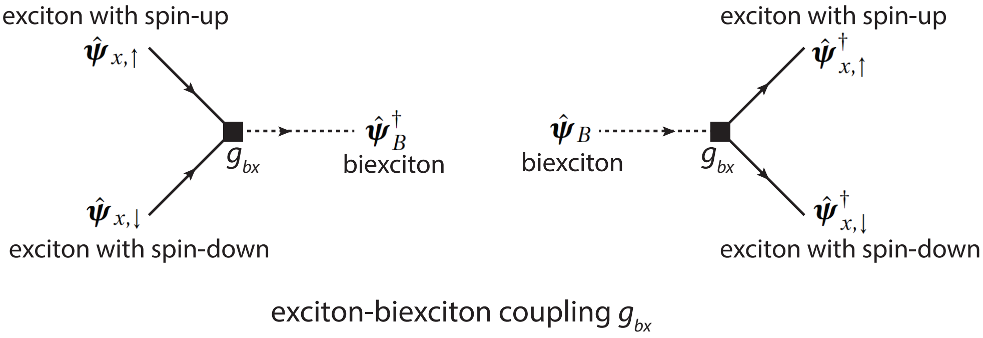
exciton with spin-up
$\hat{\boldsymbol{\psi}}_{x,\uparrow}$
g_{bx}
$\hat{\boldsymbol{\psi}}_B^\dagger$
biexciton
$\hat{\boldsymbol{\psi}}_{x,\downarrow}$
exciton with spin-down
exciton with spin-up
$\hat{\boldsymbol{\psi}}_{x,\uparrow}^\dagger$
$\hat{\boldsymbol{\psi}}_B$
biexciton
g_{bx}
$\hat{\boldsymbol{\psi}}_{x,\downarrow}^\dagger$
exciton with spin-down
exciton-biexciton coupling g_{bx}

Figure 3.5: Schematic representation of the exciton-biexciton coupling g_{bx}. The diagrams show that the coupling g_{bx} converts two excitons with opposite spins into a bound state biexciton and the opposite process.

With the Heisenberg equation of motion and coherent limit assumption, we obtain the equations of motion of the exciton, photon, and biexciton fields. Since the biexciton effect is a four-particle correlation, the inclusion of the incoherent effect of biexciton is theoretically extremely difficult. Therefore, here we consider only the coherent limit and rewrite the exciton, photon, and biexciton operator into c-numbers. Finally, the equations of motion read,

$$\begin{aligned} i\hbar\dot{\psi}_{x,\uparrow} &= (\epsilon_x + g|\psi_{x,\uparrow}|^2 + g_{+-}|\psi_{x,\downarrow}|^2 - i\gamma_x)\psi_{x,\uparrow} \\ &\quad + g_{bx}\psi_B\psi_{x,\downarrow}^* + (\Omega - 2g_{\text{pae}}|\psi_{x,\uparrow}|^2)\psi_{c,\uparrow} \qquad (3.46) \\ i\hbar\dot{\psi}_{c,\uparrow} &= (\epsilon_c - \frac{\hbar^2}{2m_c}\nabla^2 - i\gamma_c)\psi_{c,\uparrow} + (\Omega - g_{\text{pae}}|\psi_{x,\uparrow}|^2)\psi_{x,\uparrow} - f_{\text{ext},\uparrow} \qquad (3.47) \\ i\hbar\dot{\psi}_B &= (\epsilon_B - i\gamma_B)\psi_B + g_{bx}\psi_{x,\uparrow}\psi_{x,\downarrow}. \qquad (3.48) \end{aligned}$$

The equations of motion above indicate that g_{+-} contributes to the mean-energy shift induced by the exciton population with anti-parallel spins. Within the second-order Born approximation, the term g_{+-} is zero because of the lack of the Coulomb exchange interaction between excitons with opposite spins [41], but an inclusion of the higher-order scattering matrices results in a negative value of g_{+-} (the exciton continuum correlations) [51, 52, 53, 54]. Although the effect of exciton-biexciton coupling g_{bx} is not intuitive, g_{bx} has a significant contribution to the effective polariton interaction through a biexciton resonant scattering (Feshbach resonance) [50, 55, 56]. In order to investigate the effect of the biexciton on the lower-polariton, we rewrite the spin-dependent Hamiltonian and equations of motion into the lower-polariton basis.

$$\begin{aligned}
\hat{H}_{\text{int,LP}} &= \sum_{\sigma=\{\uparrow\downarrow\}} \int d\mathbf{x}\,[\,(\frac{1}{2} g X_{\mathbf{0}}^4 + 2 g_{\text{pae}} X_{\mathbf{0}}^3 |C_{\mathbf{0}}|)\hat{\boldsymbol{\psi}}^\dagger_{L,\sigma}\hat{\boldsymbol{\psi}}^\dagger_{L,\sigma}\hat{\boldsymbol{\psi}}_{L,\sigma}\hat{\boldsymbol{\psi}}_{x,\sigma} \\
&\quad + g_{+-} X_{\mathbf{0}}^4 \hat{\boldsymbol{\psi}}^\dagger_{L,\sigma}\hat{\boldsymbol{\psi}}^\dagger_{L,-\sigma}\hat{\boldsymbol{\psi}}_{L,-\sigma}\hat{\boldsymbol{\psi}}_{L,\sigma} \\
&\quad + \frac{1}{2} g_{bx} X_{\mathbf{0}}^2 (\hat{\boldsymbol{\psi}}_B \hat{\boldsymbol{\psi}}^\dagger_{L,\sigma}\hat{\boldsymbol{\psi}}^\dagger_{L,-\sigma} + \hat{\boldsymbol{\psi}}_{L,\sigma}\hat{\boldsymbol{\psi}}_{L,-\sigma}\hat{\boldsymbol{\psi}}^\dagger_B)\,]\,. \qquad (3.49)
\end{aligned}$$

The equations of motion of the lower-polariton considering the spin dependence and biexciton are written as

$$\begin{aligned}
i\hbar\dot{\psi}_{L,\uparrow} &= (\epsilon_{L,0} - \frac{\hbar^2}{2m_L}\nabla^2 + g_L|\psi_{L,\uparrow}|^2 + g_{L,+-} X_{\mathbf{0}}^4 |\psi_{L,\downarrow}|^2 - i\gamma_L)\psi_{L,\uparrow} \\
&\quad + g_{bx} X_{\mathbf{0}}^2 \psi_B \psi^*_{L,\downarrow} - f_{\text{ext},\uparrow} \qquad (3.50) \\
i\hbar\dot{\psi}_B &= (\epsilon_B - i\gamma_B)\psi_B + g_{bx} X_{\mathbf{0}}^2 \psi_{L,\uparrow}\psi_{L,\downarrow}. \qquad (3.51)
\end{aligned}$$

The scattering resonance and resulting enhancement of the polariton-polariton interaction occur when the lower-polariton's energy is close to the half of biexciton's energy. This is possible by changing the cavity detuning (see Eq. 5.3) and make the energy $2\epsilon_{L,0}$ close to ϵ_B. In Chapter 6, we will describe the details of the scattering resonance of the polaritons (polaritonic Feshbach resonance) with anti-parallel spins. Our experimental results indicate the existence of both g_{+-} and g_{bx}.

4 Experimental setup and technique

The details of the experimental set-up and measurement technique will be given in this chapter. In the first section, we will give details about the semiconductor microcavity sample used in this thesis. In the next section, the optical set-up for a non-linear optics experiments and heterodyne detection technique will be addressed.

4.1 High-quality GaAs based semiconductor microcavity

The sample used for the experiments in this thesis is a high-quality semiconductor microcavity composed of a single quantum well and two DBR mirrors. The sample was grown in the group of M. Ilegems by U. Oesterle at EPFL in 1998 [38]. The bottom mirror includes 26.5 pairs, while the top mirror has 20 pairs of DBRs. The quantum well is 8 nm $In_{0.04}Ga_{0.96}As$ quantum well and the DBR consists of GaAs/AlAs. Since light can be transmitted through the substrate of $In_{0.04}Ga_{0.96}As$ quantum well, we can employ a transmission measurement configuration. All our experiments are performed at the cryogenic temperature of 4 K.

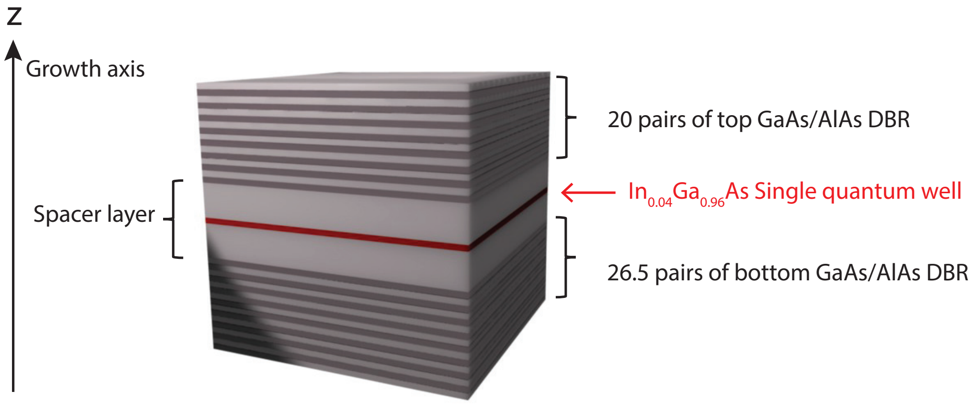
z
Growth axis
Spacer layer
20 pairs of top GaAs/AlAs DBR
$In_{0.04}Ga_{0.96}As$ Single quantum well
26.5 pairs of bottom GaAs/AlAs DBR

Figure 4.1: Schematic of semiconductor microcavity. The single $In_{0.04}Ga_{0.96}As$ quantum well (represented as a red colour) is sandwiched by two GaAs/AlAs DBRs

Since the sample is wedged during a sample growth process, we can tune the cavity resonance energy by changing the position of the laser spot over the sample. Therefore, by sweeping the position of the laser spot at zero incidence angle and observing the transmitted beam, we can obtain a cavity detuning dependence of the lower- and upper-polariton energies (Fig. 4.2 (a)). The 1s exciton energy is extracted as ϵ_x=1.4867 eV. The Rabi splitting energy at zero cavity detuning is about 2Ω =3.45 meV. In Fig. 4.2 (b), the energy-momentum dispersion of the lower and upper-polariton is shown. This figure is obtained at a zero cavity detuning with a non-resonant excitation by a continuous-wave helium-neon laser (1.96 eV) and a far-field image of a photo-luminescence.

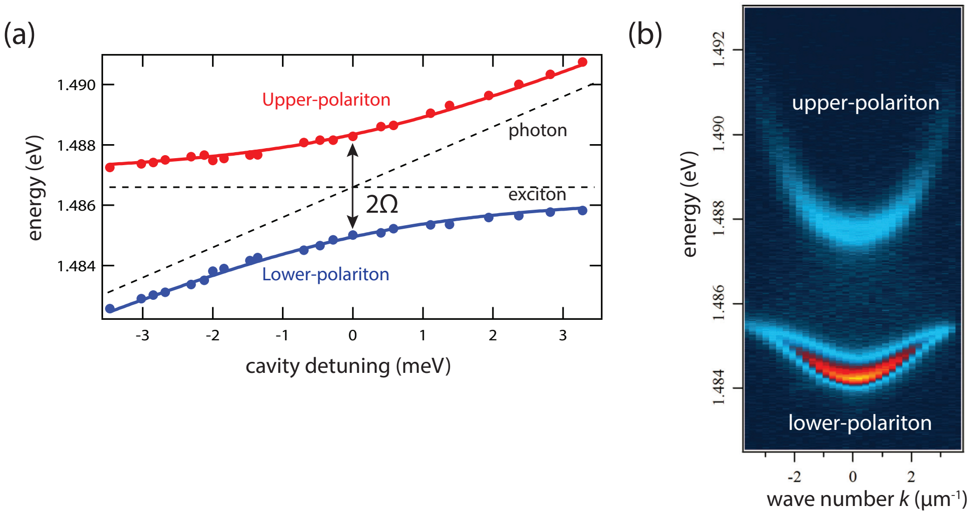

Figure 4.2: (a) The energies of the lower and upper-polaritons as a function of the cavity detuning. The splitting between the two branches at zero cavity detuning is about 3.45 meV. (b) The energy-momentum dispersion of the lower and upper-polariton obtained with a non-resonant excitation and far-field imaging of the photo-luminescence at zero cavity detuning from [42] (b).

4.2 Pump-probe excitation configuration

Figure. 4.3 is the scheme of the experimental setup. A Ti:sapphire laser TSUNAMI with a broadband few hundreds femtosecond pulse and 80 MHz repetition rate is used. The laser source is divided into three beams: k_1 (probe or trigger), k_2 (pump), and reference pulses with two acousto-optic modulator (AOM). The optical setup is divided into three parts: a pulse shaper, excitation of the sample, and detection of the signal. The pulse shaper reshapes the broadband pump pulse into a narrowband pulse, which is used to excite a single branch of polariton.

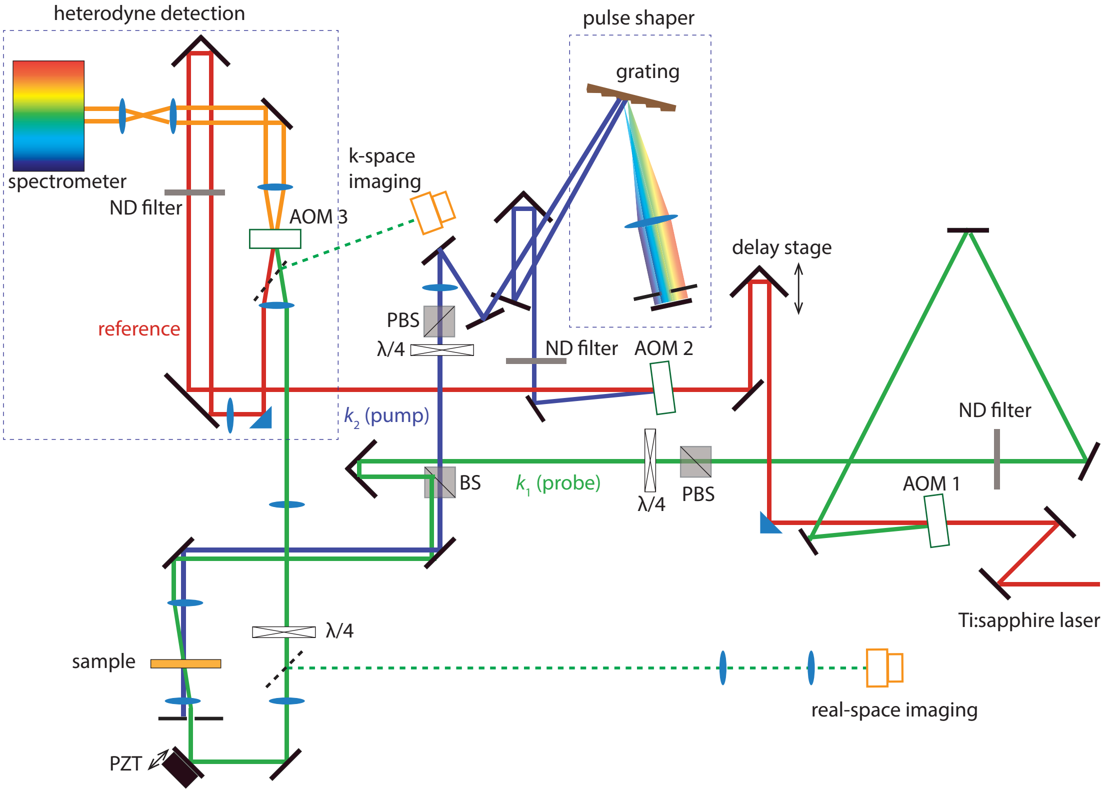
heterodyne detection
pulse shaper
grating
spectrometer
ND filter
AOM 3
k-space imaging
delay stage
reference
PBS
λ/4
ND filter
AOM 2
k_2 (pump)
ND filter
BS
k_1 (probe)
λ/4
PBS
AOM 1
λ/4
Ti:sapphire laser
sample
real-space imaging
PZT

Figure 4.3: Scheme of an experimental setup. The meanings of abbreviations are the following. **AOM**: acousto-optic modulator. **PZT**: piezo-electric device ,which blurs the mirror and introduce an artificial noise. **ND filter**: neutral density filter, which adjusts the intensity of beams. **BS**: beam splitter. **PBS**: polarization beam splitter, which extracts a linear component of an elliptic polarization. **λ/4**: quarter wave plate, which converts a linear polarization to $\sigma^{+(-)}$ circular polarization. Real and k-space imaging is used for alignments of the setup. A pulse shaping with the pulse shaper is used only when we excite a single polariton branch, otherwise, the slit of pulse shaper is opened and k_2 pulse width is same as that of k_1

For the excitation of the sample, a two-pulse configuration is employed (See the schematic in Fig. 4.4). The k_2 and k_1 pulses are respectively referred to as “pump" and “probe" in a pump-probe experiment (See Chapters 6 and 7). The wave-vector of the k_2 pulse is always zero ($k_2 = 0\ \mu\text{m}^{-1}$). Meanwhile, the wave-vector of k_1 pulse is tunable by changing the angle between the two pulses (See Fig. 4.4). The pulses k_1 and k_2 arrive on the sample at times t_{k_1} and t_{k_2} respectively. A time delay $\tau = t_{k_1} - t_{k_2}$ between the two pulses is called positive (negative) when the k_2 (k_1) pulse arrives before the k_1 (k_2) pulse. In the experiment, the delay τ is controlled by the delay stage in Fig. 4.3 with LabVIEW. All measurements are performed in the transmission configuration. In the pump-probe experiment, we spatially select the transmitted probe beam with a pinhole and sent it to the heterodyne detection path (Fig. 4.3). The polarization of the k_1 and k_2 pulses can be controlled by the $\lambda/4$ plates (shown in Fig. 4.3) in co- and counter-circular polarization configuration. In the two-pulses configuration with co-circular polarization, four-wave mixing signal (also referred to as “idler") appears with a wave vector k_{FWM} (Fig. 4.4). The four-wave mixing with this configuration is degenerate four-wave mixing, because the pulse k_2 (pump) is considered as two degenerate pulses with $k_2 = 0\ \mu\text{m}^{-1}$. Since, the momentum conservation must be satisfied, the momentum of the four-wave mixing signal is $k_{\text{FWM}} = 2k_2 - k_1 = -k_1\ \mu\text{m}^{-1}$. In the four-wave mixing experiment, similarly to the pump-probe one, the four-wave mixing signal is spatially selected with the pinhole and interfered with the reference beam for the heterodyne detection.

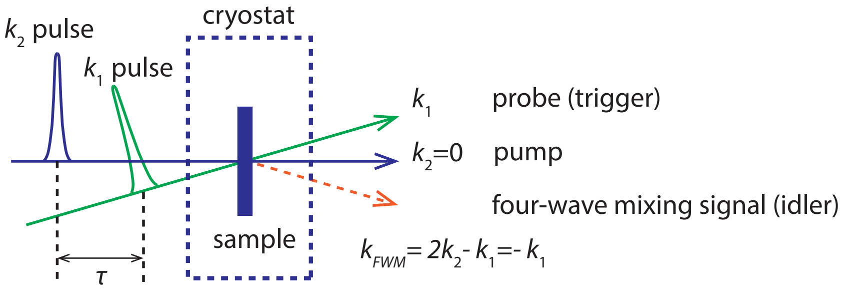

Figure 4.4: Scheme of the excitation of the sample and the probe and FWM signal directions. The delay τ represents the delay time between the k_1 and k_2 pulse. The wave vector of the FWM signal is given by $k_{\text{FWM}} = 2k_2 - k_1 = -k_1\ \mu\text{m}^{-1}$.

4.3 Heterodyne Pump-probe and four-wave mixing technique

Here, we describe the heterodyne measurement technique employed in both pump-probe and four-wave mixing experiments [57, 42, 16]. The idea of the heterodyne measurement is to interfere a signal electric field with a local oscillator and amplify it. The employment of the heterodyne technique has two advantages. Firstly, we can obtain both the amplitude and the phase of the measured electric fields. This is indispensable for two-dimensional Fourier transformation spectroscopy, which requires the phase information for the Fourier transformation. Secondly, since stray light does not interfere with the local oscillator, we can obtain a large signal to noise ratio using heterodyne measurements. This is very important because in a spatially degenerate pump-probe and four-wave mixing configuration, the heterodyne measurement is an efficient way to remove the strong pump beam transmission.

Firstly, in order to understand the heterodyne technique, we should recall that the femtosecond pulse can be considered as a frequency comb (See Fig. 4.5). Namely, in the energy axis, the laser pulse is an ensemble of continuous-wave lasers with an interval of 80 MHz. Since the pump and probe are up-converted by AOMs respectively with 75 MHz and 79 MHz from the reference, the combs of the k_2 (pump) and k_1 (probe) pulses are also shifted from that of the reference (See the inset of Fig. 4.5). Recalling the four-wave mixing in continuous-wave regime, the angular frequency of the four-wave mixing signal is given by $\omega_{FWM} = 2\omega_{pu} - \omega_{pr}$. Thus, the four-wave mixing signal is shifted with 71 MHz(=2×75 MHz -79 MHz) from the reference. It is important to notice that these shifts do not affect the envelope of pulses and the discussion of physics, because the pulse bandwidth (>10 meV) is much larger than the energy shift ($\sim 3.0\times10^{-4}$ meV) induced by the AOM.

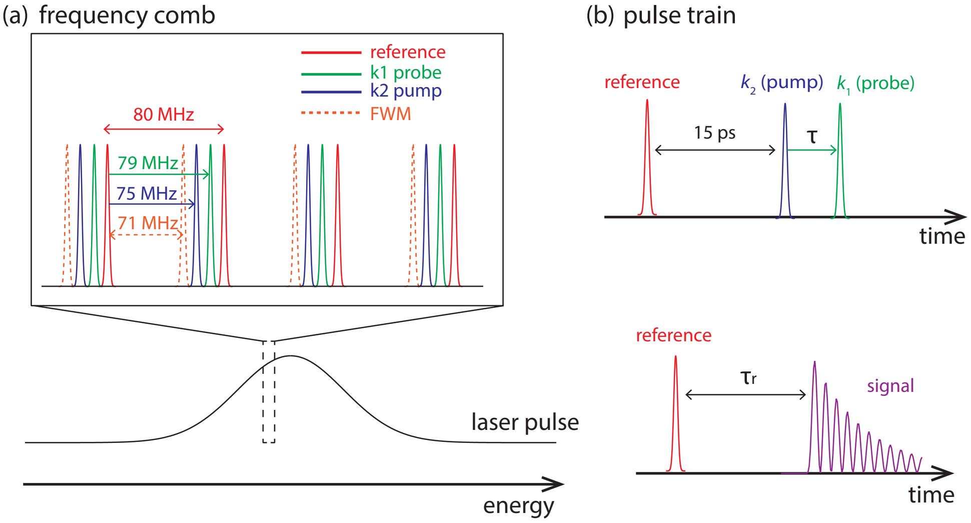

Figure 4.5: A broadband laser pulse can be considered as a frequency comb (a). In the inset, the combs of the reference, k_2, and k_1 pulse is drawn. The comb of k_2 and k_1 are shifted from that of the reference by AOM. The pulse train of the three beams is schematically shown in the upper part of (b). The lower part of (b) displays that the delay time between the reference and signal is defined as τ_r. The signal is FWM and probe respectively for FWM and pump-probe measurements.

The idea of the heterodyne detection has a close similarity to a homodyne one. While, a signal and reference (local oscillator) are mixed with beam splitter in the homodyne detection, the beam splitter is replaced with the acoustic-optical modulator (AOM) in our heterodyne detection scheme. We make use of AOM as a “frequency beam splitter" [58]. As shown in

Fig. 4.6, when the driving radio frequency of AOM corresponds to the difference of the input reference and signal frequencies, the two input beams are interfered with each other in the output ports. As shown in Fig. 4.6 (a), the principle of AOM is a diffraction of a laser beam by “a moving grating" driven by acoustic waves, which introduce a π phase shift between output channel A and B.

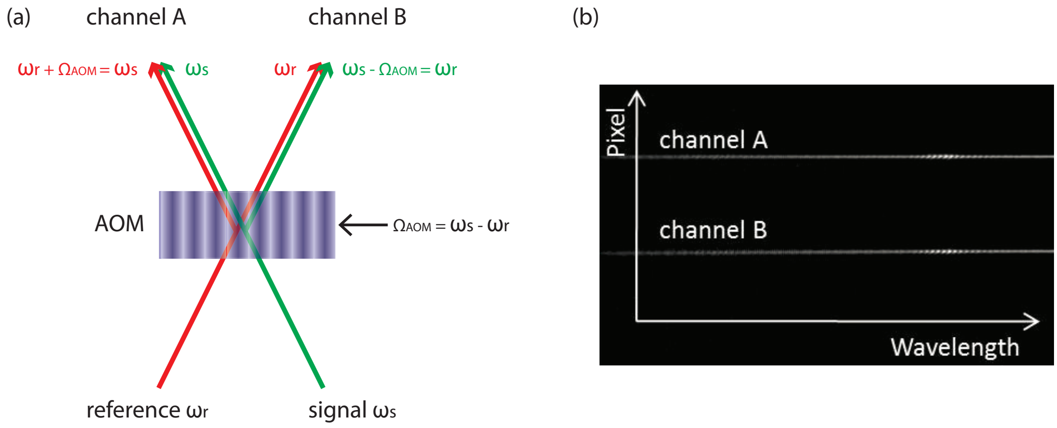

Figure 4.6: (a): Scheme of acoustic-optical modulator, which represents that two input modes are mixed in the output modes (channel A and B). AOM works as a “frequency beam splitter". (b): CCD image of the spectrum of the channel A and B. (interferogram)

signal	Ω_{AOM}
k_1 (probe)	79 MHz
k_2 (pump)	75 MHz
four-wave mixing	71 MHz

Table 4.1: Table of the driving frequencies Ω_{AOM} for AOM 3 (See Fig. 4.3) for detecting different signals.

Assuming that $E_s(\omega_s)$ and $E_r(\omega_r)$ are the complex amplitudes of input signal and reference respectively. Here, the input signal is the probe or four-wave mixing signal. Using an analogy with the beam splitter matrix in quantum optics, the output beams in channel A (E_A) and B (E_B) (See Fig. 4.6) are given by

$$\begin{pmatrix} E_A(\omega_s) \\ E_B(\omega_r) \end{pmatrix} = \begin{pmatrix} \sqrt{\eta} & -\sqrt{1-\eta} \\ \sqrt{1-\eta} & \sqrt{\eta} \end{pmatrix} \begin{pmatrix} E_s(\omega_s) \\ E_r(\omega_r) \end{pmatrix}.$$

Here, η is a number between 0 and 1, which is determined by the properties and gain of AOM. When the gain of AOM is turned off, η becomes 1 and the diffraction does not occur. The important character of this technique is that we can select the signal by choosing the rf frequency of the AOM, because the difference frequency between the signal and reference must be the same as the driving frequency of the AOM. Therefore, with this technique we can exclude the strong stray light coming from the pump beam. For example, in the case of pump-probe measurement, the AOM is driven with rf-frequency of 79 MHz, which corresponds to the modulation frequency of the probe. In Table. 4.1, we summarize rf-frequencies of the AOM for three different signals.

From now on, since the energy difference between ω_s and ω_r is very small compared to the energy scale of the physical phenomena which we investigate, we will discuss the heterodyne technique neglecting this difference. The complex amplitude of output channels A and B is a superposition of the signal and the reference as

$$E_A(\omega) = \sqrt{\eta}E_s(\omega) - \sqrt{1-\eta}E_r(\omega,\tau_r). \tag{4.1}$$

and

$$E_B(\omega) = \sqrt{1-\eta}E_s(\omega) + \sqrt{\eta}E_r(\omega,\tau_r). \tag{4.2}$$

Here, the delay τ_r in $E_r(\omega,\tau_r)$ represents the delay between the signal and reference pulses. Figure. 4.5 (b) presents pulse trains in our experiments. The probe pulse is fixed and the pump and reference pulses are moved simultaneously by the delay stage (See Fig. 4.3). The reference pulse arrives before the signal which is measured. The delay between the pump and reference pulse is kept around 15 ps. $E_r(\omega,\tau_r)$ is related to $E_s(\omega)(=E_s(\omega,0))$ as $E_r(\omega,\tau_r) = E_r(\omega)e^{i\omega\tau_r}$. The outputs channel A and B are transferred to a spectrometer, which records the amplitudes $I_A(\omega) = |E_A(\omega)|^2$ and $I_B(\omega) = |E_B(\omega)|^2$ as interferograms. The example of $I_A(\omega)$ and $I_B(\omega)$ is presented in Fig. 4.6 (b), where the term associated with the reference-signal delay $e^{i\omega\tau_r}$ gives rise to periodic interference fringes. The intensities $I_A(\omega)$ and $I_B(\omega)$ are calculated as

$$\begin{aligned} I_A(\omega) &= |E_A(\omega)|^2 \\ &= \eta|E_s(\omega)|^2 + (1-\eta)|E_r(\omega,\tau_r)|^2 - 2\sqrt{(1-\eta)\eta}\,\mathrm{Re}\left[E_s(\omega)\cdot E_r^*(\omega,\tau_r)\right] \end{aligned} \tag{4.3}$$

and

$$\begin{aligned} I_B(\omega) &= |E_B(\omega)|^2 \\ &= (1-\eta)|E_s(\omega)|^2 + \eta|E_r(\omega,\tau_r)|^2 + 2\sqrt{(1-\eta)\eta}\,\mathrm{Re}\left[E_s(\omega)\cdot E_r^*(\omega,\tau_r)\right]. \end{aligned} \tag{4.4}$$

In Eq. 4.3 and 4.4, the last term represents the interference term of the signal and reference. It is important that the phase information of the signal appears in the interference term as a relative phase to the reference. The first two terms are the intensities of the signal and reference respectively. The difference of the intensities between two channel $I_B(\omega) - I_A(\omega)$ is given by

$$\begin{aligned} I_B(\omega)-I_A(\omega) &= (1-2\eta)|E_s(\omega)|^2+(2\eta-1)|E_r(\omega,\tau_r)|^2+4\sqrt{(1-\eta)\eta}\,\mathrm{Re}\left[E_s(\omega)\cdot E_r^*(\omega,\tau_r)\right] \\ &= 2\mathrm{Re}\left[E_s(\omega)\cdot E_r^*(\omega,\tau_r)\right] \qquad (\text{if } \eta=0.5). \end{aligned} \tag{4.5}$$

As the above equation shows, if the intensity of the channel A and B are balanced, the subtraction $I_B(\omega)-I_A(\omega)$ includes only the interference term (balanced detection). However, in practice, the perfect balance is not easy. Therefore, in order to remove the residual intensity terms $|E_s(\omega)|^2$ and $|E_r(\omega)|^2$ from the subtraction $I_B(\omega)-I_A(\omega)$, we use the piezoelectric device (PZT) in Fig. 4.3. When we add an artificial phase noise to the signal with the piezoelectric actuator of the mirror (See PZT in Fig. 4.3), the interference term is averaged out and we can obtain only the intensity terms. In order to reconstruct the signal $E_s(\omega)$, firstly we perform the balanced detection and obtain $I_B(\omega)-I_A(\omega)$, then remove the residual intensity terms by using the PZT noise method. Neglecting the constants and defining a function $f(\omega)$ as

$$f(\omega)=E_s(\omega)\cdot E_r^*(\omega), \tag{4.6}$$

the extracted interference term I_{in} reads

$$\begin{aligned} I_{\mathrm{in}}(\omega) &= 2\mathrm{Re}\left[E_s(\omega)\cdot E_r^*(\omega,\tau_r)\right] \\ &= f(\omega)e^{i\omega\tau_r}+f^*(\omega)e^{-i\omega\tau_r}. \end{aligned} \tag{4.7}$$

The Fourier transformation of $I_{\mathrm{in}}(\omega)$ includes two time reversed parts as

$$\begin{aligned} \mathscr{F}\left[I_{\mathrm{in}}(\omega)\right](t) &= \widetilde{f}(t-\tau_r)+\widetilde{f}^*(t+\tau_r) \\ &= \widetilde{f}(t-\tau_r)+\widetilde{f}(-t-\tau_r). \end{aligned} \tag{4.8}$$

The function $\widetilde{f}(t)$ is the Fourier transformation of $f(\omega)$: $\widetilde{f}(t)=\mathscr{F}\left[f(\omega)\right](t)$. By applying a Heaviside function $\Theta(t)$, we obtain only $\widetilde{f}(t-\tau_r)$ term. Them, by removing the delay offset, we obtain $\widetilde{f}(t)$. The inverse Fourier transformation of $\widetilde{f}(t)$ is the convolution of the signal and reference $f(\omega)=E_s(\omega)\cdot E_r^*(\omega)$. If the spectrum profile of the reference is broad enough, $E_s(\omega)$ is written as $E_r(\omega)=|E_r|e^{i\phi_r}$. In this case, $f(\omega)$ reads, $E_s(\omega)|E_r|e^{i\phi_r}$. This means that finally, by obtaining $f(\omega)$ from the interferogram, we recover the signal $E_s(\omega)$ except for the absolute phase and absolute amplitude, which is written as

$$f(\omega)=e^{-i\omega_r\tau}\mathscr{F}^{-1}\left[\Theta(t)\mathscr{F}\left[I_{\mathrm{in}}(\omega)\right]\right]. \tag{4.9}$$

If we have the complete information of the reference pulse, we can obtain the signal as

$$E_s(\omega)=\frac{f(\omega)}{E_r^*(\omega)}. \tag{4.10}$$

However, we cannot know the amplitude and phase of $E_r^*(\omega)$, thus we need some assumptions for $E_r^*(\omega)$. Firstly, since the linewidth of the reference pulse ($\approx$15 meV) is much larger than the Rabi splitting (3.45 meV) in our sample, we assume that the reference pulse is broad enough and the amplitude does not have a frequency dependence: $|E_r^*(\omega)| = |E_r|$. Secondly, let us note the absolute phase of the reference does not affect the amplitude of the spectrum of the signal $|f(\omega)|^2 = |E_r| \cdot |E_s(\omega) e^{i\phi_r}|^2 \propto |E_s(\omega)|^2$, while it introduces a phase dependence to the real part of $f(\omega)$ as $\mathrm{Re}\left[f(\omega)\right] \propto |E_s(\omega)| \cdot \cos(\phi_s(\omega) + \phi_r)$. This is why we will present only amplitude of the experimental spectra, which is not affected by the absolute phase of the reference.

5 Two-dimensional Fourier Transform (2DFT) spectroscopy of polaritons

In this chapter, we discuss in detail two-dimensional Fourier Transform (2DFT) spectroscopy of polaritons [59]. Using 2DFT spectroscopy, we reveal two types of interactions between the polariton branches: lower-lower and upper-upper polariton self-interaction and lower-upper polariton cross interaction. Firstly, we describe an experimental configuration necessary for 2DFT. Secondly, we analyse the experimental 2DFT spectra based on third-order perturbation theory, where we introduce double-sided Feynman diagrams. The third-order perturbation theory is the simplest and intuitive description of 2DFT. Actually, the appearance of main peak groups in experimental 2DFT spectra can be explained with this theory. Finally, we compare experiments with “non-perturbative" numerical simulations based on lower- and upper-polariton basis Gross-Pitaevskii equations. We find that the full inclusion of the dispersion effects, which is usually neglected in the case of heavy particles such as exctions, is possible with this non-perturbative approach.

5.1 Concept of 2DFT spectroscopy

2DFT spectroscopy is a powerful tool to investigate coherent couplings and vibrational anharmonicities of molecular vibrational states [60, 61] and non-linear interaction between different exciton states in semiconductor [62, 63, 64, 65, 66]. One advantage of this technique is that we can know whether two oscillators are independent or coupled with a mutual anharmonicity from the existence of off-diagonal peak in two-dimensional spectrum. This is very difficult with a conventional one-dimensional (1D) spectroscopy. Additionally, we can associate each peak of the 2DFT spectrum with different Liouville-space pathway through double-sided Feynman diagrams [61, 67]. For example, let us consider two two-level systems with and without a mutual anharmonicity (non-linearity) as shown in Fig. 5.1. The two systems have transition energies ϵ_1 and ϵ_2. With a conventional one-dimensional spectroscopy we cannot distinguish two cases, because the spectra from both systems present two peaks at the resonance energies ϵ_1 and ϵ_2. On the other hand, in 2DFT spectrum, the two systems display a striking difference: namely, the effect of the anharmonicity results in the appearance of the off-diagonal peaks (See Fig. 5.1).

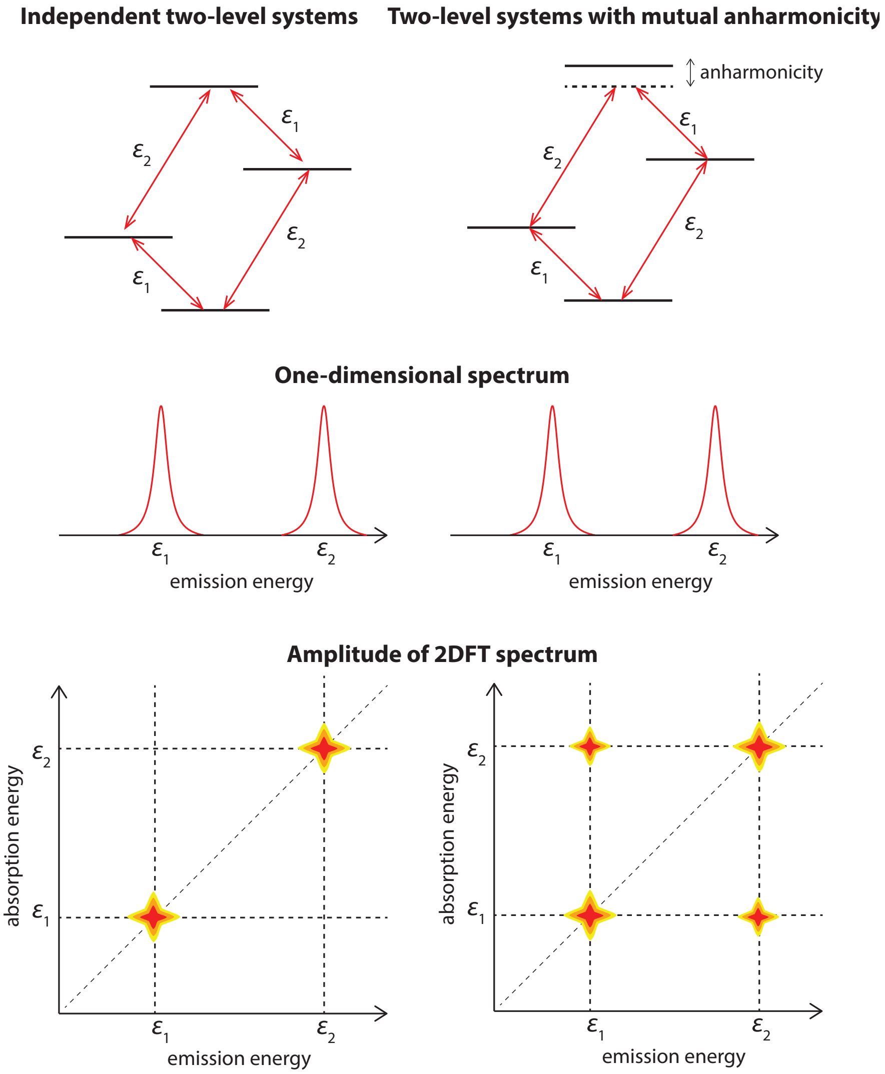
Independent two-level systems
Two-level systems with mutual anharmonicity
anharmonicity
ε1
ε2
ε2
ε1
One-dimensional spectrum
ε1
ε2
emission energy
ε1
ε2
emission energy
Amplitude of 2DFT spectrum
absorption energy
ε2
ε1
ε1
ε2
emission energy
absorption energy
ε2
ε1
ε1
ε2
emission energy

Figure 5.1: An Example of 2DFT spectroscopy scheme. Two-level systems with and without a mutual anharmonicity are considered. The transition energies are ϵ_1 and ϵ_2. While a conventional one-dimensional spectroscopy displays spectrum with two peaks at the energies ϵ_1 and ϵ_2 for both cases, 2DFT spectrum makes it possible to distinguish them based on the presence or absence of off-diagonal peaks.

5.2 Experimental configuration and numerical process for 2DFT of polaritons

For the 2DFT, two-pulses configuration stated in the Chapter 4 is employed. The k_2 and k_1 pulses respectively arrive on the sample in directions $|\boldsymbol{k}_1| = 0.96\ \mu\text{m}^{-1}$ and $\boldsymbol{k}_2$=0 μm^{-1} (See Fig. 5.2 (a)). We detect the four-wave mixing (FWM) signal in the direction $\boldsymbol{k}_{\text{FWM}} = 2\boldsymbol{k}_2 - \boldsymbol{k}_1 = -\boldsymbol{k}_1$. The pulses k_1 and k_2 arrive on the sample at times t_{k_1} and t_{k_2} respectively. A time delay

$\tau = t_{k_1} - t_{k_2}$ between two pulses is called positive (negative) when the k_2 (k_1) pulse arrives before the k_1 (k_2) pulse. The 2DFT experiments are performed in the low-density regime with k_1 and k_2 pulse intensities of 6.7×10^{12} photons pulse^{-1} cm^{-2}. The polarization of the two pulses are co-circular to avoid the possible effects of biexcitons [55, 56] (Chapter 6). The center energy of the pulse spectrum is set between the lower and upper polariton energies in order to excite the two branches with a similar intensity. Figure. 5.2 (b) presents the scheme of the polariton dispersion with k_1 and k_2 pulses and the k_{FWM} signal. The transmission spectra of k_2 and k_1 pulses are shown in 5.2 (c). The difference of the energy peaks of the k_1 and k_2 pulses is due to the polariton dispersion.

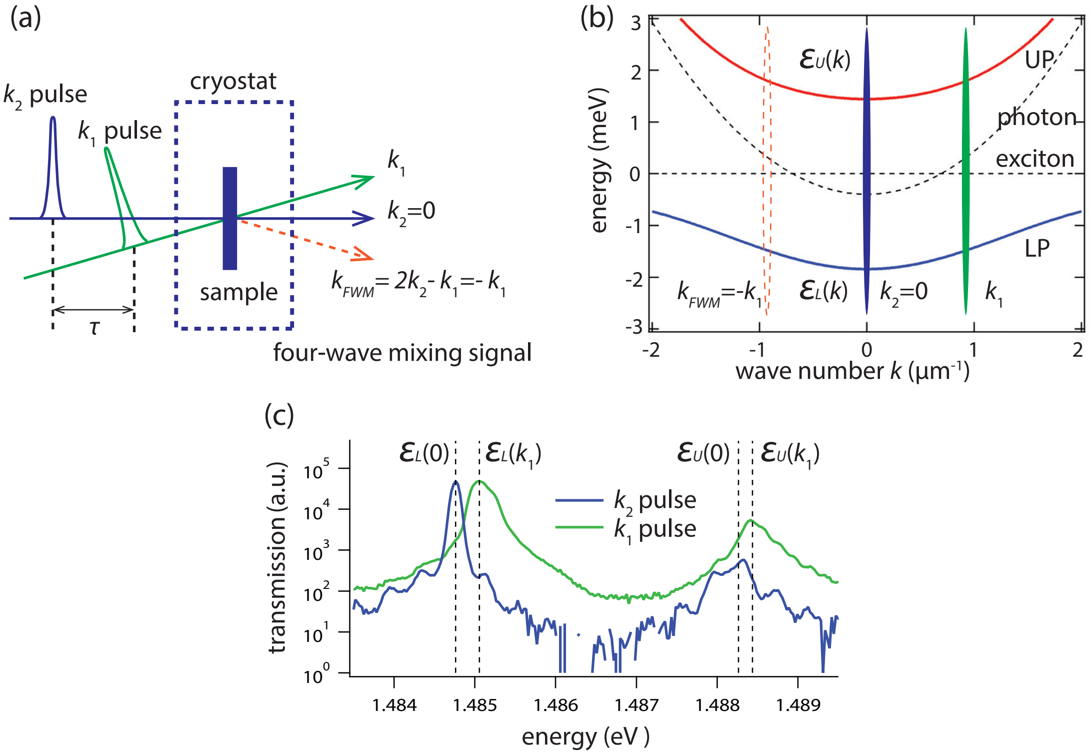

Figure 5.2: Scheme of excitation configuration and pulse sequence for 2DFT experiments (a). The lower- (LP) and upper-polariton (UP) energy-momentum dispersions at slight negative cavity detuning (δ=-0.38 meV) (b). The dashed black lines represent exciton and photon energy-momentum dispersion. Transmission spectra of the k_2 and k_1 beams (c). $\epsilon_L(k)$ and $\epsilon_U(k)$ are respectively lower and upper-polariton enegy at wave-vector k.

The heterodyne detection technique (See Chapter 4) allows us to record the electric field of the FWM signal $S(t,\tau)$ as a function of two independent time periods. The time τ is the delay time between the k_1 and k_2 pulses, while t is the real evolution time of the FWM signal after the arrival of the two pulses. An example of the FWM signal $S(t,\tau)$ is presented in Fig. 5.3 (b), which evidences the fact that the FWM signal appears after the incidence of the two pulses

(See Fig. 5.3 (a)).

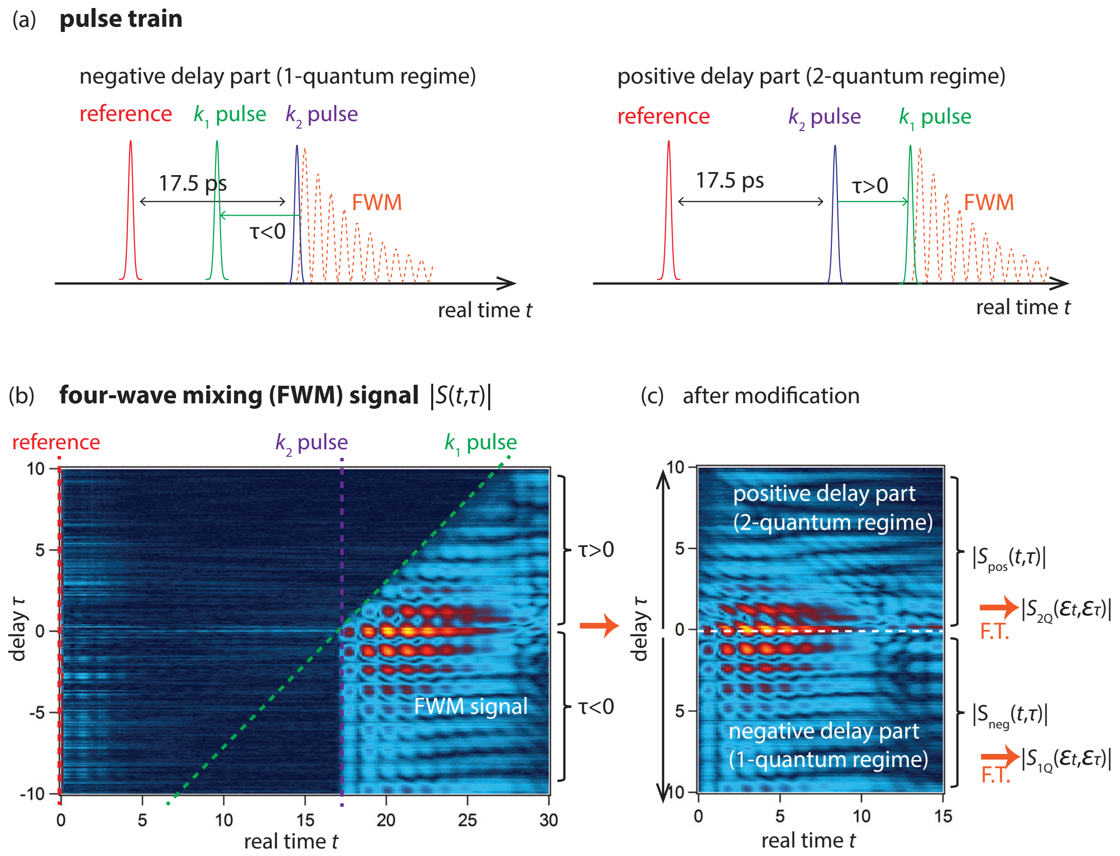

Figure 5.3: (a) Pulse trains for a negative ($\tau < 0$) and positive ($\tau > 0$) delays. FWM signal appears after the incident of two pulses. (b) The amplitude of a FWM signal as a function of real time t and delay τ, $S(t,\tau)$. (c) After the modification of coordinate, we obtain two parts: a negative delay $S_{\text{neg}}(t,\tau)$ and positive delay $S_{\text{pos}}(t,\tau)$ regimes. The Fourier transformation with respect to times t and τ leads to one-quantum $S_{1\text{Q}}(\epsilon_t,\epsilon_\tau)$ and two-quantum $S_{2\text{Q}}(\epsilon_t,\epsilon_\tau)$ spectra.

Firstly, a conventional delay dependent 1D FWM signal spectrum $S(\epsilon_t,\tau)$ is obtained by performing a Fourier transformation of $S(t,\tau)$ with respect to t. Secondly, we obtain the 2D spectrum through a Fourier transformation with respect to both the τ and t axes. To do this, we modify the coordinate of FWM signal $S(t,\tau)$ as presented in Fig. 5.3 (c). After the modification of the coordinate, the FWM signal is classified into two parts: a negative $S_{\text{neg}}(t,\tau)$ and positive delay regime $S_{\text{pos}}(t,\tau)$. In $S_{\text{neg}}(t,\tau)$ and $S_{\text{pos}}(t,\tau)$, the real time t and delay τ are redefined as presented in Fig. 5.3 (c). Finally, the Fourier transformation of $S_{\text{neg}}(t,\tau)$ and $S_{\text{pos}}(t,\tau)$ with respect to the two time axes respectively leads to “one-quantum" $S_{1\text{Q}}(\epsilon_t,\epsilon_\tau)$ and “two-quantum" $S_{2\text{Q}}(\epsilon_t,\epsilon_\tau)$ 2DFT spectra. Here ϵ_τ and ϵ_t respectively represent the absorption and emission energies.

Experimentally, in the 2DFT spectroscopy, we apply two types of phase correction processes. The first one is applied when obtaining $S(t,\tau)$ at each delay τ. We perform 20 acquisitions for obtaining a single FWM signal $S(t,\tau)$. During these 20 acquisitions, judging from phase fluctuation, we apply a phase correction in order to remove the noisy part of the signal. The second one is concerned with the absolute phase fluctuation between two different delay points [68]. Due to the lack of phase stabilization, the absolute phase varies depending of the delay time τ between two pulses. The second phase correction is performed using the upper-polariton energy as a phase reference. The detailed explanation of these two phase correction processes are given in Appendix A.

5.3 Experimental results and perturbative analysis

We will now study the experimentally obtained 1D and 2D FWM spectra and analyse them based on third-order perturbation theory with the help of the double-sided Feynman diagrams. In this section, the cavity detuning is set at $\delta = -0.38$ meV. Fig. 5.4 (a) shows the amplitude of the 1D FWM spectrum $|S(\epsilon_t,\tau)|$, which results from the Fourier transformation of the real time t of $S(t,\tau)$ in Fig. 5.3 (b). In the 1D FWM spectrum, we find two branches: the lower (LP) and the upper-polariton (UP) branch. The 1D FWM spectrum also shows a delay-dependent oscillation. The delay-dependent oscillation period 1.2 ps corresponds to the Rabi splitting between the lower and upper- polariton. We will find that this oscillation can be interpreted as a quantum beat with the aid of the double-sided Feynman diagrams. Furthermore, fine structures are found in the LP and UP branches. These fine structures are related to the energy-momentum dispersion of polaritons. The detail of the fine structures is addressed in the following through the 2DFT spectra.

Secondly, we perform the Fourier transformation of the 1D FWM spectrum with respect to the delay τ and obtain a one-quantum spectrum $S_{1\mathrm{Q}}(\epsilon_t,\epsilon_\tau)$ in the $\tau < 0$ region and the two-quantum 2DFT spectrum $S_{2\mathrm{Q}}(\epsilon_t,\epsilon_\tau)$ in the $\tau > 0$ region. The amplitude of these 2DFT spectra $|S_{1\mathrm{Q}}(\epsilon_t,\epsilon_\tau)|$ and $|S_{2\mathrm{Q}}(\epsilon_t,\epsilon_\tau)|$are shown in Fig. 5.4 (b) and (c) respectively. Due to the lack of information on the absolute phase of the 2DFT signal, only the amplitudes are presented in the figure. We will also analyse the 2DFT spectra in detail using third-order perturbation theory in the next section.

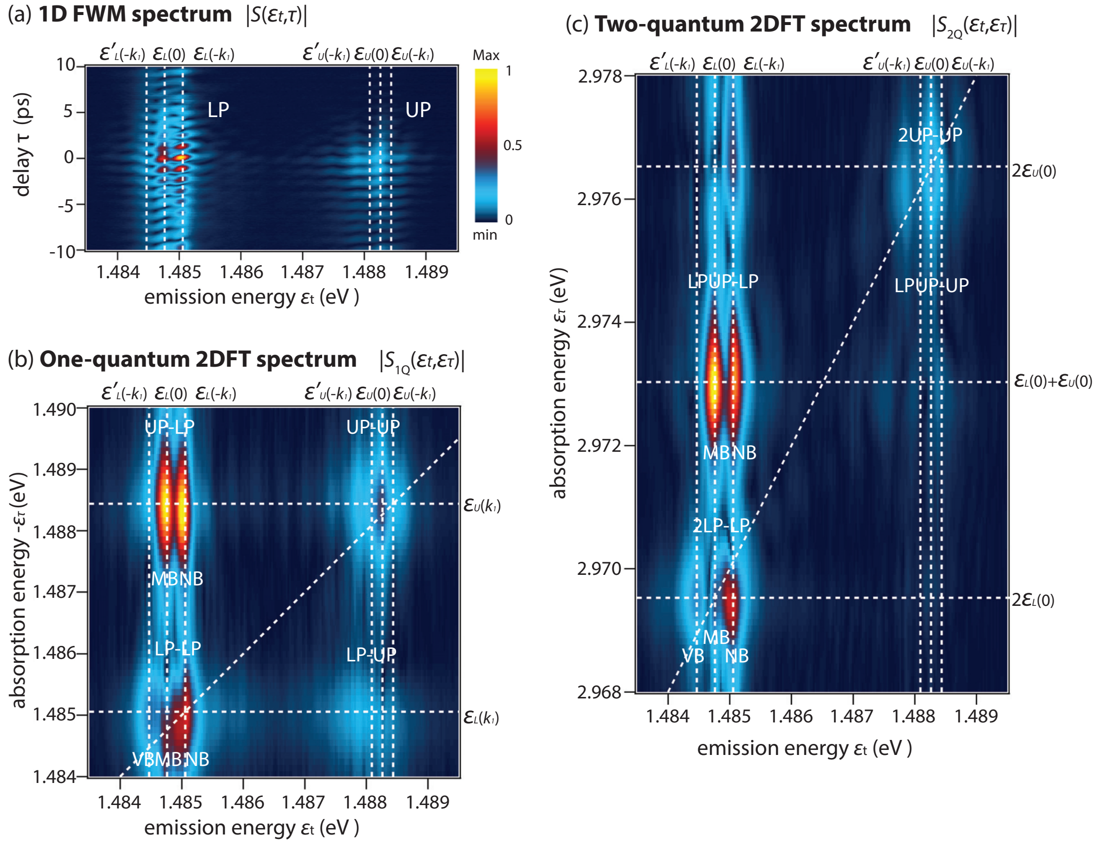

Figure 5.4: (a) Experimental amplitude of FWM spectrum as a function of emission energy and k_2-k_1 pulse delay τ: $|S(\epsilon_t,\tau)|$. (b) Amplitude of 2DFT spectrum for one-quantum $|S_{1Q}(\epsilon_t,\epsilon_\tau)|$ and (c) two-quantum region $|S_{2Q}(\epsilon_t,\epsilon_\tau)|$. Diagonal dashed lines represent $-\epsilon_\tau = \epsilon_t$ for (b) and $\epsilon_\tau = 2\epsilon_t$ for (c). Horizontal and vertical dashed lines respectively represent different absorption and emission energies. $\epsilon_L(k)$ and $\epsilon_U(k)$ are respectively LP and UP energy at a wavevector k. $\epsilon'_{L(U)}(k)$ is a virtual branch (VB). NB and MB refer to normal and middle branch respectively. Colour scales are linear and normalized by the maximum and minimum of the amplitude. The same normalization and colour bar are used in all figures of this section.

5.3.1 2DFT spectrum of one-quantum regime $|S_{1Q}(\epsilon_t,\epsilon_\tau)|$

Firstly, we discuss the 2DFT spectrum in one-quantum regime $|S_{1Q}(\epsilon_t,\epsilon_\tau)|$ (See Fig. 5.4 (b)). In one-quantum regime, the k_1 pulse arrives before the k_2 pulse. In Fig. 5.4 (b), we find two diagonal groups, LP-LP and UP-UP, and two off-diagonal groups, LP-UP and UP-LP. Inside each peak group, fine structures are observed. The fine structures are classified and named as the virtual (VB), middle (MB), and normal (NB) branches going from lower to higher emission energies.

We are going to analyse the origin of these peak groups based on the third-order perturbation theory of four-wave mixing. The main idea of third-order perturbation theory is to calculate the density matrix of polaritons within a third-order of incident electric fields (one k_1 and two k_2 pulses). The detail of the theory and explicit calculation are presented in Appendix B. Here, instead of going into the detailed calculation, we visualize the perturbative evolution of the density matrix of polaritons using the double-sided Feynman diagrams [69, 61, 70]. The double-sided Feynman diagrams for the one-quantum regime are presented in Fig. 5.5. These diagrams represent Liouville-space pathways of the density matrix: each diagram corresponds to the third-order perturbative evolution of the system's density matrix. The FWM signal $S_{\mathrm{neg}}(t,\tau)$ and its Fourier transformation $S_{1\mathrm{Q}}(\epsilon_t,\tau)$ are given as a summation of all pathways.

In each diagram in Fig. 5.5, the vertical line represents the time evolution of the density matrix from bottom to top, with the time ordering of the arrival of k_1, k_2 pulses and the FWM signal emission. In the one-quantum regime, the incident of the first electric field from k_1 pulse creates a coherence between the ground state and a single LP (0-LP) or UP (0-UP) state. In terms of the density matrix representation, these coherences correspond to off-diagonal terms in the density matrices $\rho^{(1)}_{0,L}(\boldsymbol{k}_1)$ and $\rho^{(1)}_{0,U}(\boldsymbol{k}_1)$. Here, the indexes 0, L and U respectively refer to a vacuum $|0\rangle$, single lower $|\mathrm{L}\rangle = \hat{a}^\dagger_L|0\rangle$ and upper-polariton state $|\mathrm{U}\rangle = \hat{a}^\dagger_U|0\rangle$. The index k_1 in the density matrix indicates that the k_1 pulse creates a coherence with momentum k_1 (See Appendix. B).

The second and third electric fields come from the same pulse k_2 after a delay τ. Since the degenerate second and third electric fields arrive simultaneously, the delay between them is fixed as $T = 0$ in the diagrams. For example, in the pathway (A)-(C), as the double-sided Feynamn diagram indicates, the second electric field converts the $\rho^{(1)}_{0,L}(\boldsymbol{k}_1)$ coherence into a diagonal part of the density matrix $\rho^{(2)}_{0,0}(\boldsymbol{k}_2-\boldsymbol{k}_1)$ or $\rho^{(2)}_{L,L}(\boldsymbol{k}_2-\boldsymbol{k}_1)$, which represent respectively the population in the ground and one-lower-polariton state. In the case of path (E),(G) and (L),(N), the second electric field creates a coherence between the lower and upper-polariton: $\rho^{(2)}_{L,U}(\boldsymbol{k}_2-\boldsymbol{k}_1)$ and $\rho^{(2)}_{U,L}(\boldsymbol{k}_2-\boldsymbol{k}_1)$. Finally, the third electric field brings the population and LP-UP coherence back to coherence with momentum $\boldsymbol{k}_{\mathrm{FWM}}$: $\rho^{(3)}_{L(U),0}(\boldsymbol{k}_{\mathrm{FWM}})$ or $\rho^{(3)}_{2L(2U),0}(\boldsymbol{k}_{\mathrm{FWM}})$. Let us recall that the wave vector $\boldsymbol{k}_{\mathrm{FWM}}$ is calculated as $\boldsymbol{k}_{\mathrm{FWM}} = 2\boldsymbol{k}_2 - \boldsymbol{k}_1 = -\boldsymbol{k}_1$. Here, the index $2L(2U)$ represent "two-polaritons" state defined as $|2\mathrm{L}\rangle = \hat{a}^\dagger_L\hat{a}^\dagger_L|0\rangle$ and $|2\mathrm{U}\rangle = \hat{a}^\dagger_U\hat{a}^\dagger_U|0\rangle$. Since the four-wave mixing emission is proportional to the polarization induced by the third-order coherence, the four-wave mixing signal $S_{\mathrm{neg}}(t,\tau)$ is obtained by calculating the $\rho^{(3)}_{L(U),0}(\boldsymbol{k}_{\mathrm{FWM}})$ and $\rho^{(3)}_{2L(2U),0}(\boldsymbol{k}_{\mathrm{FWM}})$.

(a) **One-quantum 2DFT spectrum** $|S_{1Q}(\varepsilon_t,\varepsilon_\tau)|$

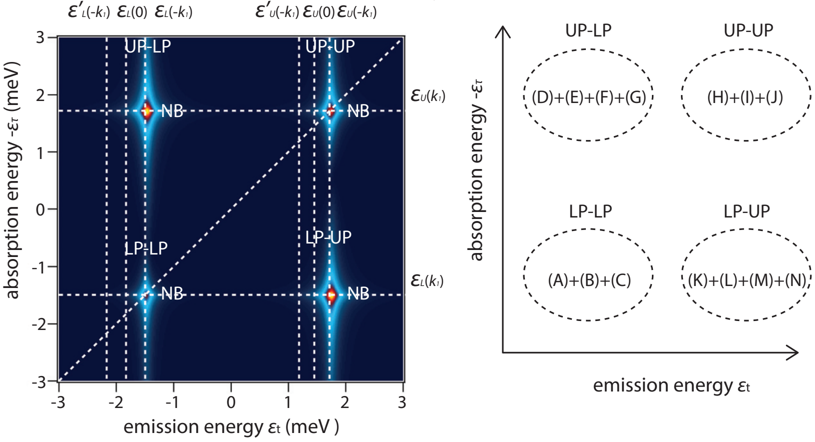

(b) **Double-sided Feynman diagrams for one-quantum regime**

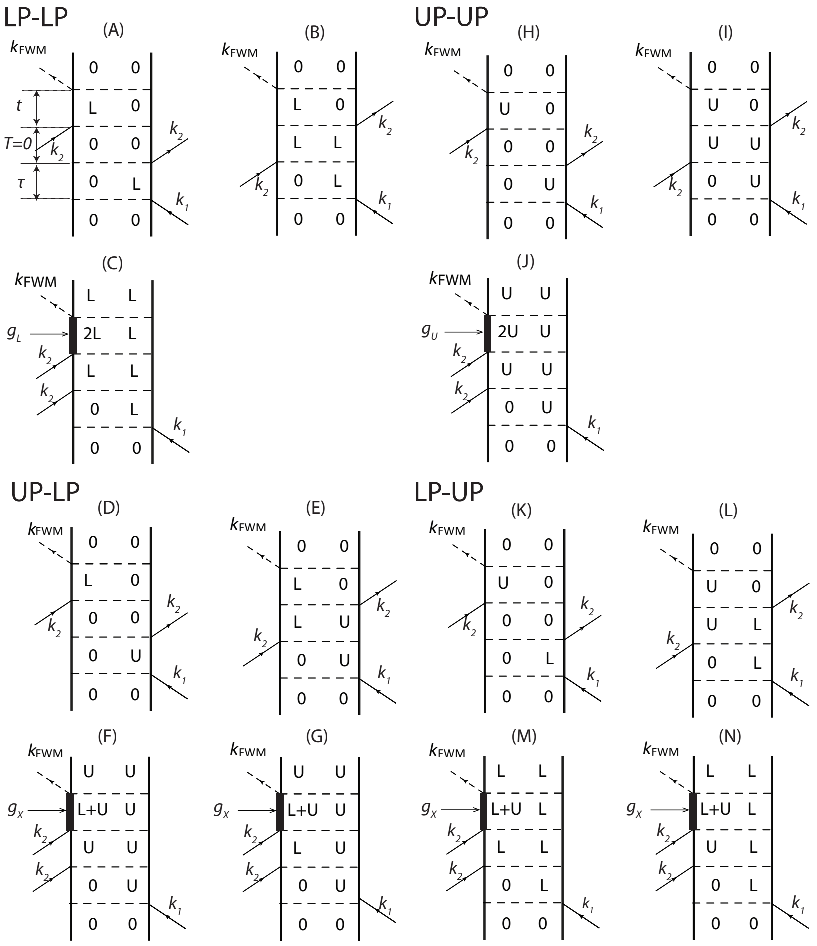
LP-LP
UP-UP
UP-LP
LP-UP
(A)
(B)
(C)
(D)
(E)
(F)
(G)
(H)
(I)
(J)
(K)
(L)
(M)
(N)
kFWM
k1
k2
t
T=0
τ
gL
gU
gX
0
L
U
2L
2U
L+U

Figure 5.5: (a) Computed 2D FT spectrum and (b) double-sided Feynman diagrams (b) in one-quantum regime. Diagrams (A-C) and (H-J) respectively contribute to the diagonal peaks LP-LP and UP-UP, while diagrams (D-G) and (K-N) respectively correspond to the off-diagonal peaks UP-LP and LP-UP. $g_{L(U)}$ and g_X respectively represent self and cross-interaction of polaritons.

Diagonal peak groups: LP-LP and UP-UP

Let us now discuss the diagonal peak groups LP-LP and UP-UP. In the following, $\epsilon_L(k)(\epsilon_U(k))$ is the energy of the lower (upper)-polariton, $\Omega_L(\Omega_U)$ represents the coupling constant between the lower (upper)-polariton and the photon outside the cavity, and $\gamma_L(\gamma_U)$ is the dephasing rate of lower (upper)-polariton. Performing the standard third-order perturbative calculation of nonlinear optics [61, 67] (See the Appendix B), the FWM signal corresponding to the diagram (A) is given by,

$$S^{(A)}(t,\tau) \quad \propto \quad \Omega_L \rho^{(3)}_{L,0}(\boldsymbol{k}_{\mathrm{FWM}}) = |\Omega_L|^4 e^{-(i/\hbar)(\epsilon_L(\boldsymbol{k}_{\mathrm{FWM}})-i\gamma_L)t} e^{(i/\hbar)(\epsilon_L(\boldsymbol{k}_1)+i\gamma_L)|\tau|}.$$

In this pathway, during $|\tau|$ and t, the system evolves keeping coherence between its ground state and a single lower-polariton state (0-LP and LP-0). In the “one-quantum regime", the first order evolution, during time $|\tau|$, is always a coherence between the ground state and single lower or upper-polariton state (0-LP or 0-UP). The Fourier transformation of $S^{(A)}(|\tau|,t)$ reads,

$$S^{(A)}(\epsilon_t,\epsilon_\tau) \quad \propto \quad \frac{|\Omega_L|^4}{[i(\epsilon_t-\epsilon_L(\boldsymbol{k}_{\mathrm{FWM}}))+\gamma_L][i(\epsilon_\tau+\epsilon_L(\boldsymbol{k}_1))+\gamma_L]}.$$

Similarly, the contribution from diagrams (B) leads to

$$S^{(B)}(\epsilon_t,\epsilon_\tau) \quad \propto \quad \frac{|\Omega_L|^4}{[i(\epsilon_t-\epsilon_L(\boldsymbol{k}_{\mathrm{FWM}}))+\gamma_L][i(\epsilon_\tau+\epsilon_L(\boldsymbol{k}_1))+\gamma_L]}.$$

Since the signal corresponds to the path C is given by $S^{(C)}(t,\tau) \propto \sqrt{2}\Omega_L \rho^{(3)}_{2L,L}(\boldsymbol{k}_{\mathrm{FWM}})^1$,

$$S^{(C)}(\epsilon_t,\epsilon_\tau) \quad \propto \quad \frac{-2|\Omega_L|^4}{[i(\epsilon_t-\epsilon_{2L}(\boldsymbol{k}_{\mathrm{FWM}})+\epsilon_L(\boldsymbol{k}_{\mathrm{FWM}}))+\gamma_L][i(\epsilon_\tau+\epsilon_L(\boldsymbol{k}_1))+\gamma_L]}.$$

$S^{(B)}$ is the exactly same as $S^{(A)}$. In these perturbative calculations, the semiconductor microcavity system is treated as two-oscillators (lower and upper-polaritons) weakly coupled to photons outside the cavity with the quasi couplings Ω_L and Ω_U (See Eq. 3.24 in Chapter 3). The detailed background of the polariton basis model will be readdressed in next section on numerical simulations. While path (A) and (B) include only “single-quantum" state (L), the path (C) includes the “two-quantum" state (2L). This two-quantum state (2L) is modified by the polariton-polariton self-interaction, making the energy of 2LP state $\epsilon_{2L}(\boldsymbol{k})$ being slightly blue-shifted from twice that of LP state $2\epsilon_L(\boldsymbol{k})$ (*i.e.*, $\epsilon_{2L}(\boldsymbol{k}) \neq 2\epsilon_L(\boldsymbol{k})$). One of the important consequences is that, if the lower-polariton self-interaction were absent, the relation

---

[1] Let us note that since a non-interactive polariton is assumed to be boson (harmonic oscillator), the dipole strength between the states $|L\rangle$ and $|2L\rangle$ ($\sqrt{2}\Omega_L$) is $\sqrt{2}$ larger than that between the states $|0\rangle$ and $|L\rangle$ (Ω_L) [61].

$\epsilon_{2L}(\boldsymbol{k}) = 2\epsilon_L(\boldsymbol{k})$ would hold and the sum $S^{(A)} + S^{(B)} + S^{(C)}$ would be zero. This is intuitive if we recall that a linear system does not produce a four-wave mixing signal.

We can apply the same description to the UP-UP group resulting from the paths (H)-(J) just replacing the lower-polariton with upper one. The signal from the paths (H)-(J) are given by

$$S^{(H)}(\epsilon_t,\epsilon_\tau) \quad \propto \quad \frac{|\Omega_U|^4}{[i(\epsilon_t-\epsilon_U(\boldsymbol{k}_{\mathrm{FWM}}))+\gamma_U][i(\epsilon_\tau+\epsilon_U(\boldsymbol{k}_1))+\gamma_U]},$$

$$S^{(I)}(\epsilon_t,\epsilon_\tau) \quad \propto \quad \frac{|\Omega_U|^4}{[i(\epsilon_t-\epsilon_U(\boldsymbol{k}_{\mathrm{FWM}}))+\gamma_U][i(\epsilon_\tau+\epsilon_U(\boldsymbol{k}_1))+\gamma_U]},$$

and

$$S^{(J)}(\epsilon_t,\epsilon_\tau) \quad \propto \quad \frac{-2|\Omega_U|^4}{[i(\epsilon_t-\epsilon_{2U}(\boldsymbol{k}_{\mathrm{FWM}})+\epsilon_U(\boldsymbol{k}_{\mathrm{FWM}}))+\gamma_U][i(\epsilon_\tau+\epsilon_U(\boldsymbol{k}_1))+\gamma_U]}.$$

Off-diagonal peak groups: UP-LP and LP-UP

Now, let us discuss the paths (D)-(G), which contribute to the off-diagonal UP-LP peak group. In the same way as for the diagonal peak groups, the signals associated with these diagrams are given by,

$$S^{(D,E)}(\epsilon_t,\epsilon_\tau) \quad \propto \quad \frac{|\Omega_L|^2|\Omega_U|^2}{[i(\epsilon_t-\epsilon_L(\boldsymbol{k}_{\mathrm{FWM}}))+\gamma_L][i(\epsilon_\tau+\epsilon_U(\boldsymbol{k}_1))+\gamma_U]}$$

and

$$S^{(F,G)}(\epsilon_t,\epsilon_\tau) \quad \propto \quad \frac{-|\Omega_L|^2|\Omega_U|^2}{[i(\epsilon_t-\epsilon_{LU}(\boldsymbol{k}_{\mathrm{FWM}})+\epsilon_U(\boldsymbol{k}_{\mathrm{FWM}}))+\gamma_L][i(\epsilon_\tau+\epsilon_U(\boldsymbol{k}_1))+\gamma_U]}.$$

In the pathways (F) and (G) the FWM emission originates from the coherence between the two-quantum state (L+U) and the single-quantum state (U), $\rho^{(3)}_{L+U,U}(\boldsymbol{k}_{\mathrm{FWM}})$. The two-quantum state L+P is defined as $|L+U\rangle = \hat{a}^\dagger_L\hat{a}^\dagger_U|0\rangle$. Similar to the pathways (A)-(C), the energy of UP+LP state is blue-shifted due to the lower and upper-polariton cross-interaction, $\epsilon_{LU}(\boldsymbol{k}) \neq \epsilon_L(\boldsymbol{k})+\epsilon_U(\boldsymbol{k})$. Again, if the lower and upper-polariton cross-interaction does not exist, $\epsilon_{LU}(\boldsymbol{k}) = \epsilon_L(\boldsymbol{k})+\epsilon_U(\boldsymbol{k})$ holds and the summation of the pathways (D)-(G) becomes zero, resulting in the disappearance of the off-diagonal peaks.

We draw similar diagrams (K)-(N) for the LP-UP groups (See Fig. 5.5). The perturbative calculations of the FWM signals resulting from the path (K)-(N) are given by

$$S^{(K),(L)}(\epsilon_t,\epsilon_\tau) \quad \propto \quad \frac{|\Omega_L|^2|\Omega_U|^2}{[i(\epsilon_t-\epsilon_U(\boldsymbol{k}_{\mathrm{FWM}}))+\gamma_U][i(\epsilon_\tau+\epsilon_L(\boldsymbol{k}_1))+\gamma_L]}$$

and

$$S^{(M),(N)}(\epsilon_t,\epsilon_\tau) \quad \propto \quad \frac{-|\Omega_L|^2|\Omega_U|^2}{[i(\epsilon_t-\epsilon_{LU}(\boldsymbol{k}_{\mathrm{FWM}})+\epsilon_L(\boldsymbol{k}_{\mathrm{FWM}}))+\gamma_U][i(\epsilon_\tau+\epsilon_L(\boldsymbol{k}_1))+\gamma_L]}.$$

Discussions on 2DFT spectrum in 1-quantum regime

The plot of the calculated 2DFT spectrum including all pathways in the one-quantum regime is shown Fig. 5.5 (a). As we mentioned above, the diagonal and off-diagonal peaks arise respectively from the polariton self and cross-interactions. Furthermore, the double-sided Feynman diagrams help us to understand intuitively the delay time dependent oscillation in the 1D FWM spectrum $|S(\epsilon_t,\tau)|$ in Fig. 5.4 (a). This oscillation is interpreted as a quantum beat: an interference between the pathways (A)-(C) and (D)-(G) for the lower-polariton branch, while it is an interference between the pathways (H)-(J) and (K)-(N) for the upper-polariton branch. During the delay τ, in the pathways (A)-(C) and (K)-(N) the phase evolves as $e^{(i\epsilon_L/\hbar)\tau}$, while in the pathways (D)-(G) and (H)-(J) it evolves as $e^{(i\epsilon_U/\hbar)\tau}$. Therefore, the amplitude of the 1D FWM spectrum $|S(\epsilon_t,\tau)|$ presents a beat frequency corresponding to the Rabi splitting energy: $\epsilon_U-\epsilon_L \simeq 3.45$ meV.

Let us note that the lower and upper-polariton branches have energy-momentum dispersions: $\epsilon_{\mathrm{L}}(\boldsymbol{k}) \simeq \epsilon_{L,0}+\frac{\hbar^2}{2m_L}\boldsymbol{k}^2$ and $\epsilon_{\mathrm{U}}(\boldsymbol{k}) \simeq \epsilon_{U,0}+\frac{\hbar^2}{2m_U}\boldsymbol{k}^2$ (See Fig. 5.2 (b)). Here, m_L and m_U are the mass of the lower and upper-polaritons respectively defined in Eq. 3.26. For example, due to the relationship: $\epsilon_{L(U)}(\boldsymbol{k}_{\mathrm{FWM}})=\epsilon_{L(U)}(-\boldsymbol{k}_1)=\epsilon_{L(U)}(\boldsymbol{k}_1)$, the LP-LP (UP-UP) peaks are absorbed and emitted at the same energy in the third-order perturbation theory and they are located on the diagonal line. These peaks obtained from the third-order perturbation calculation correspond to the normal branches (NB) of the experimental 2D spectrum in Fig. 5.4 (b). It is important to note that the third-order perturbative model reproduces only the normal branches (NB), which are resonant to the polariton energy-momentum dispersion. Namely, no fine structure is found inside each group. This is because the polariton-polariton interaction is treated only as a level-shift of the eigenstate energy within the third-order perturbation theory. In order to reproduce the fine energy structures, the superposition between different momentum states needs to be created by the polariton-polariton interaction [71]. To do this, in the next Section, we employ non-perturbative numerical simulations based on polariton Gross-Pitaevskii equations.

5.3.2 2DFT spectrum of two-quantum regime $|S_{2\mathrm{Q}}(\epsilon_t,\epsilon_\tau)|$

In this section, we describe the two-quantum regime, where the k_2 pulse arrives before the k_1 pulse. The 2DFT spectrum in two-quantum regime $|S_{2\mathrm{Q}}(\epsilon_t,\epsilon_\tau)|$ (Fig. 5.6 (a)) is obtained from the Fourier transformation of the FWM signal $S_{\mathrm{pos}}(t,\tau)$. Double-sided Feynman diagrams contributing to $|S_{2\mathrm{Q}}(\epsilon_t,\epsilon_\tau)|$ are presented in Fig. 5.6 (b). In all pathways, the two degenerate k_2 pulses create two-quantum coherence $\rho^{(2)}_{0,2L(2U)}(2\boldsymbol{k}_2)$ or $\rho^{(2)}_{0,L+U}(2\boldsymbol{k}_2)$ during time τ. Thus, this regime is called “two-quantum" regime.

Diagonal peak groups: 2LP-LP and 2UP-UP

Firstly, we focus on the 2LP-LP peak groups. With the same calculation as in one-quantum regime, the diagonal FWM signals corresponding to the diagram (O) is given by

$$S^{(O)}(t,\tau) \quad \propto \quad 2|\Omega_L|^4 e^{-(i/\hbar)(\epsilon_L(\boldsymbol{k}_{\mathrm{FWM}})-i\gamma_L)t} e^{-(i/\hbar)(\epsilon_{2L}(\boldsymbol{k}_2)-i\gamma_L)\tau}.$$

The Fourier transformed 2DFT spectrum reads,

$$S^{(O)}(\epsilon_t,\epsilon_\tau) \quad \propto \quad \cdot\frac{2|\Omega_L|^4}{[i(\epsilon_t-\epsilon_L(\boldsymbol{k}_{\mathrm{FWM}}))+\gamma_L][i(\epsilon_\tau-\epsilon_{2L}(\boldsymbol{k}_2))+2\gamma_L]}$$

Similarly,

$$S^{(P)}(\epsilon_t,\epsilon_\tau) \quad \propto \quad \frac{-2|\Omega_L|^4}{[i(\epsilon_t-\epsilon_{2L}(\boldsymbol{k}_{\mathrm{FWM}})+\epsilon_L(\boldsymbol{k}_{\mathrm{FWM}}))+\gamma_L][i(\epsilon_\tau-\epsilon_{2L}(\boldsymbol{k}_2))+2\gamma_L]}.$$

For the 2UP-UP group,

$$S^{(U)}(\epsilon_t,\epsilon_\tau) \quad \propto \quad \cdot\frac{2|\Omega_U|^4}{[i(\epsilon_t-\epsilon_U(\boldsymbol{k}_{\mathrm{FWM}}))+\gamma_U][i(\epsilon_\tau-\epsilon_{2U}(\boldsymbol{k}_2))+2\gamma_U]}$$

and

$$S^{(V)}(\epsilon_t,\epsilon_\tau) \quad \propto \quad \frac{-2|\Omega_U|^4}{[i(\epsilon_t-\epsilon_{2U}(\boldsymbol{k}_{\mathrm{FWM}})+\epsilon_U(\boldsymbol{k}_{\mathrm{FWM}}))+\gamma_U][i(\epsilon_\tau-\epsilon_{2U}(\boldsymbol{k}_2))+2\gamma_U]}.$$

(a) **Two-quantum 2DFT spectrum** $|S_{2Q}(\varepsilon_\tau,\varepsilon_t)|$

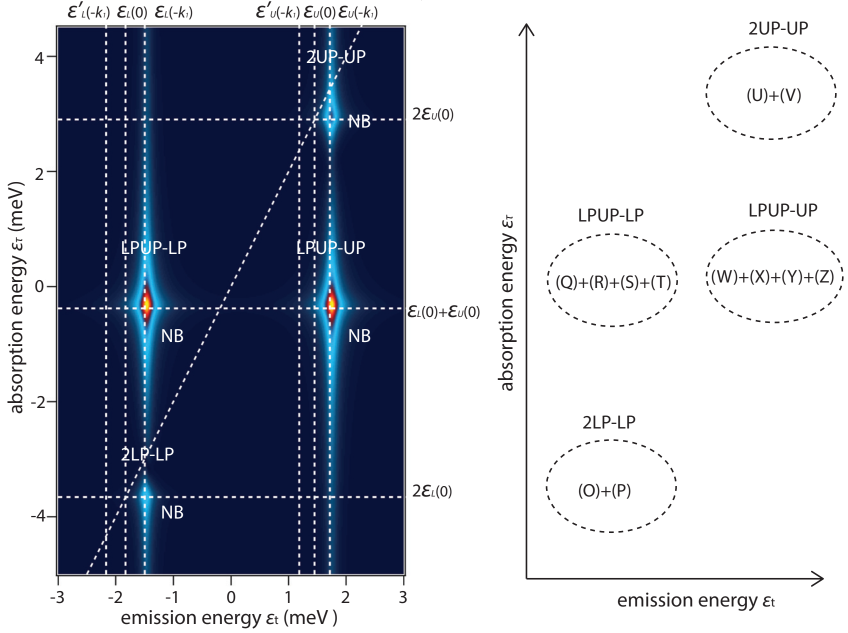

(b) **Double-sided Feynman diagrams for two-quantum regime**

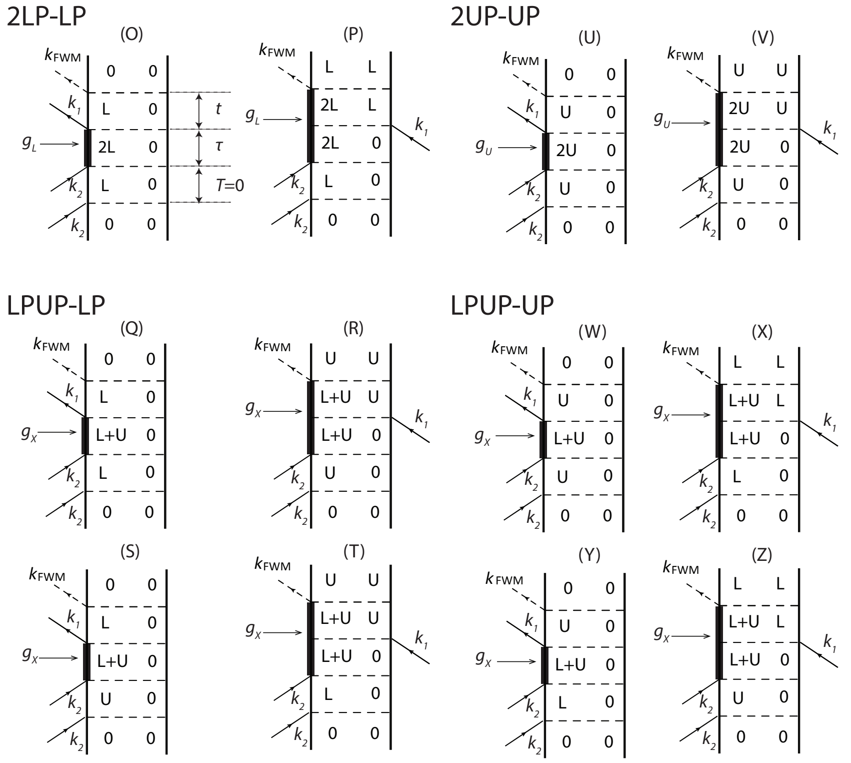
2LP-LP
(O)
(P)
2UP-UP
(U)
(V)
LPUP-LP
(Q)
(R)
(S)
(T)
LPUP-UP
(W)
(X)
(Y)
(Z)
kFWM
k1
k2
gL
gU
gX
t
τ
T=0
0 0
L 0
2L 0
L L
2L L
U 0
2U 0
U U
2U U
L+U 0
L+U U
L+U L

Figure 5.6: (a) Calculated 2DFT spectrum and (b) double-sided Feynman diagrams in two-quantum regime. Diagrams (O-P) and (U-V) respectively contribute to the diagonal peaks 2LP-LP and 2UP-UP, while diagrams (Q-T) and (W-Z) respectively correspond to the off-diagonal peaks LPUP-LP and LPUP-UP. $g_{L(U)}$ and g_X respectively represent self and cross-interactions between polaritons.

Off-diagonal peak groups: LPUP-LP and LPUP-UP

For LPUP-LP groups, the FWM contributions read,

$$S^{(Q),(S)}(\epsilon_t,\epsilon_\tau) \quad \propto \quad \frac{|\Omega_L|^2|\Omega_U|^2}{[i(\epsilon_t-\epsilon_L(\boldsymbol{k}_{\mathrm{FWM}}))+\gamma_L][i(\epsilon_\tau-\epsilon_{LU}(\boldsymbol{k}_2))+\gamma_L+\gamma_U]}$$

and

$$S^{(R),(T)}(\epsilon_t,\epsilon_\tau) \quad \propto \quad \frac{-|\Omega_L|^2|\Omega_U|^2}{[i(\epsilon_t-\epsilon_{LU}(\boldsymbol{k}_{\mathrm{FWM}})+\epsilon_U(\boldsymbol{k}_{\mathrm{FWM}}))+\gamma_L][i(\epsilon_\tau-\epsilon_{LU}(\boldsymbol{k}_2))+\gamma_L+\gamma_U]}$$

In the same way, for the LPUP-UP peak group, the signals are given by

$$S^{(W),(Y)}(\epsilon_t,\epsilon_\tau) \quad \propto \quad \frac{|\Omega_L|^2|\Omega_U|^2}{[i(\epsilon_t-\epsilon_U(\boldsymbol{k}_{\mathrm{FWM}}))+\gamma_U][i(\epsilon_\tau-\epsilon_{LU}(\boldsymbol{k}_2))+\gamma_L+\gamma_U]}$$

and

$$S^{(X),(Z)}(\epsilon_t,\epsilon_\tau) \quad \propto \quad \frac{-|\Omega_L|^2|\Omega_U|^2}{[i(\epsilon_t-\epsilon_{LU}(\boldsymbol{k}_{\mathrm{FWM}})+\epsilon_L(\boldsymbol{k}_{\mathrm{FWM}}))+\gamma_U][i(\epsilon_\tau-\epsilon_{LU}(\boldsymbol{k}_2))+\gamma_L+\gamma_U]}$$

In Fig. 5.6 (a), we plot the calculated 2DFT spectrum of the two-quantum regime. Similarly to the one-quantum regime, the energy shifts induced by self and cross-interactions $\epsilon_{2L}(\boldsymbol{k}) \neq 2\epsilon_L(\boldsymbol{k})$ and $\epsilon_{LU}(\boldsymbol{k}) \neq \epsilon_L(\boldsymbol{k})+\epsilon_U(\boldsymbol{k})$ are necessary for the appearance of the on and off-diagonal peaks respectively. Again, the diagonal and off-diagonal groups are associated with the self and cross-interactions respectively. In the two-quantum regime, the diagonal line is defined as $\epsilon_\tau = 2\epsilon_t$. Namely, the absorption energy is twice larger than the emission energy. This is characteristic of a “two-quantum regime", where the degenerate k_2 pulses create two-quantum state such as 2LP, 2UP and LP-UP. In Fig. 5.6 (a), the dashed diagonal line does not pass through the normal branches (NB) of 2LP-LP and 2UP-UP peaks. This is understood in terms of the polariton energy-momentum dispersion: $\epsilon_{L(U)}(\boldsymbol{k}_{\mathrm{FWM}}) = \epsilon_{L(U)}(\boldsymbol{k}_1) > \epsilon_{L(U)}(\boldsymbol{k}_2) = \epsilon_{L(U)}(0)$ (See Fig. 5.2 (b)). Namely, the FWM emission energy at $\boldsymbol{k}_{\mathrm{FWM}}(=-\boldsymbol{k}_1)$ is higher than the absorption energy at $\boldsymbol{k}_2 = 0$.

5.4 Numerical simulation and detailed study of 2DFT spectra

In this section, we perform non-perturbative numerical simulations based on polariton Gross-Pitaevskii equations. Our starting point of the numerical simulation is polariton basis Hamiltonian explained in Chapter 3.

Firstly, the linear part of the Hamiltonian is given by (Eq. 3.27)

$$\begin{aligned}\hat{H}_{\text{lin}}+\hat{H}_{\text{qm}} \simeq & \int d\mathbf{x}\Big[\hat{\boldsymbol{\psi}}_L^{\dagger}(\epsilon_{L,0}-\frac{\hbar^2\nabla^2}{2m_L})\hat{\boldsymbol{\psi}}_L+\hat{\boldsymbol{\psi}}_U^{\dagger}(\epsilon_{U,0}-\frac{\hbar^2\nabla^2}{2m_U})\hat{\boldsymbol{\psi}}_U \\ & +\Omega_{L,0}^{*}\hat{\boldsymbol{\psi}}_L^{\dagger}\boldsymbol{F}+\Omega_{L,0}\boldsymbol{F}^{*}\hat{\boldsymbol{\psi}}_L+\Omega_{U,0}^{*}\hat{\boldsymbol{\psi}}_U^{\dagger}\boldsymbol{F}+\Omega_{U,0}\boldsymbol{F}^{*}\hat{\boldsymbol{\psi}}_U\Big]. \qquad (5.1)\end{aligned}$$

$\hat{H}_{\text{lin}}+\hat{H}_{\text{qm}}$ is written under a parabolic approximation of polariton energy-momentum dispersion:

$$\epsilon_{\text{L(U)}}(\boldsymbol{k}) \simeq \epsilon_{L(U),0}+\frac{\hbar^2}{2m_{L(U)}}\boldsymbol{k}^2. \qquad (5.2)$$

$\Omega_L = C\Omega_{\text{qm}}$ and $\Omega_U = X\Omega_{\text{qm}}$ are the polariton quasi-mode coupling to the classical electric-field outside the cavity (See Chapter. 3). The polariton mass is given by $1/m_{L(U)} = |X|^2/m_{x(c)} + |C|^2/m_{c(x)}$. For a cavity detuning $\delta = \epsilon_c - \epsilon_x$, the energies $\epsilon_{L,0}$ and $\epsilon_{U,0}$ are respectively defined as

$$\epsilon_{L,0} = \frac{1}{2}\left(2\epsilon_x+\delta-\sqrt{\delta^2+(2\Omega)^2}\right) \qquad (5.3)$$

and

$$\epsilon_{U,0} = \frac{1}{2}\left(2\epsilon_x+\delta+\sqrt{\delta^2+(2\Omega)^2}\right). \qquad (5.4)$$

The above linear Hamiltonian is formally the same as that of two oscillators coupled to classical electric fields with the constant $\Omega_{L(U)}$. Therefore, the third-order perturbation theory and double-sided Feynman diagrams, which are normally used in a weak-coupling system, can be applied to the system in which exciton and photon are strongly coupled inside a microcavity.

Secondly, we introduce polariton-polariton interactions. As is explained in Chapter 3, in the polariton basis, the exciton-exciton interaction term includes nine components (See Eq. (xx a1)-(xx c2) in Chapter 3). For simplicity, we extract only the first three terms in Eq. (xx a1)-(xx a3) of Chapter 3: LP-LP (UP-UP) self and LP-UP cross-interaction terms,

$$\hat{H}_{\text{pint}} = \int d\mathbf{x}\left[\frac{1}{2}g_L\hat{\boldsymbol{\psi}}_L^{\dagger}\hat{\boldsymbol{\psi}}_L^{\dagger}\hat{\boldsymbol{\psi}}_L\hat{\boldsymbol{\psi}}_L+\frac{1}{2}g_U\hat{\boldsymbol{\psi}}_U^{\dagger}\hat{\boldsymbol{\psi}}_U^{\dagger}\hat{\boldsymbol{\psi}}_U\hat{\boldsymbol{\psi}}_U+g_X\hat{\boldsymbol{\psi}}_L^{\dagger}\hat{\boldsymbol{\psi}}_L\hat{\boldsymbol{\psi}}_U^{\dagger}\hat{\boldsymbol{\psi}}_U\right]. \qquad (5.5)$$

Only when the kinetic term (energy-momentum dispersion) in Eq. 5.1 is neglected, we can justify this approximation in the low density regime by using a second-order perturbation theory (For details, please see [59]). With the Hopfield coefficients, we set $g_L = g_0|X|^4$, $g_U = g_0|C|^4$, and $g_X = 2g_0|X|^2|C|^2$. Here, g_0 is the exciton-exciton interaction constant. Since the objective of the numerical simulation is a qualitative understanding of physical phenomena, here we neglect the photon-assisted exchange scattering terms. Using the Heisenberg equations of motion: $i\hbar\frac{d}{dt}\hat{\boldsymbol{\psi}}_{L(U)} = [\hat{\boldsymbol{\psi}}_{L(U)}, \hat{H}_{\text{lin}} + \hat{H}_{\text{int}}]$ and factorizations:

$$\langle\hat{\boldsymbol{\psi}}^\dagger_{L(U)}\hat{\boldsymbol{\psi}}_{L(U)}\hat{\boldsymbol{\psi}}_{L(U)}\rangle = \langle\hat{\boldsymbol{\psi}}^\dagger_{L(U)}\rangle\langle\hat{\boldsymbol{\psi}}_{L(U)}\rangle\langle\hat{\boldsymbol{\psi}}_{L(U)}\rangle$$

and

$$\langle\hat{\boldsymbol{\psi}}^\dagger_{L(U)}\hat{\boldsymbol{\psi}}_{L(U)}\hat{\boldsymbol{\psi}}_{U(L)}\rangle = \langle\hat{\boldsymbol{\psi}}^\dagger_{L(U)}\rangle\langle\hat{\boldsymbol{\psi}}_{L(U)}\rangle\langle\hat{\boldsymbol{\psi}}_{U(L)}\rangle,$$

lower and upper polariton Gross-Pitaevskii equations read,

$$\begin{aligned} i\hbar\dot{\psi}_L &= (\epsilon_{L,0} - \frac{\hbar^2}{2m_L}\nabla^2 + g_L|\psi_L|^2 + g_X|\psi_U|^2 - i\gamma_L)\psi_L + \Omega_L^* f_{\text{ext}} \\ i\hbar\dot{\psi}_U &= (\epsilon_{U,0} - \frac{\hbar^2}{2m_U}\nabla^2 + g_U|\psi_U|^2 + g_X|\psi_L|^2 - i\gamma_U)\psi_U + \Omega_U^* f_{\text{ext}}. \end{aligned} \tag{5.6}$$

$\psi_{L(U)} = \langle\hat{\psi}_{L(U)}\rangle$ is lower (upper) polariton wave function. The polariton decay rate is phenomenologically introduced as $\gamma_{L(U)} = |X|^2\gamma_{x(c)} + |C|^2\gamma_{c(x)}$, where γ_x and γ_c are chosen to be the same (0.33 meV). The k_2 and k_1 pulse excitations are introduced in the external photon field $f_{\text{ext}}(= \boldsymbol{\psi}_b)$ as

$$f_{\text{ext}}(\mathbf{x}, t) = F_{k_1}\exp\left(-\frac{(t-t_{k_1})^2}{\tau_p^2}\right)\exp(-i\omega_{k_1}t + i\boldsymbol{k}_1\cdot\mathbf{x}) + F_{k_2}\exp\left(-\frac{(t-t_{k_2})^2}{\tau_p^2}\right)\exp(-i\omega_{k_2}t + i\boldsymbol{k}_2\cdot\mathbf{x}). \tag{5.7}$$

$\omega_{k_1(k_2)}$ is the center frequency of the $k_1(k_2)$ pulse and always set at the center between the lower and upper-polariton branches. τ_p is the pulse duration. The constant $g_{L(U)}$ represents a self-interaction of lower (upper) polaritons, while g_X is the cross-interaction constant between the lower and upper-polariton. In analogy with non-linear optics, $g_{L(U)}$ and g_X can be called self-phase modulation (SPM) and cross-phase modulation (XPM) terms respectively. Again, similarly to non-linear optics, the XPM term g_X is twice as strong as the SPM term $g_{L(U)}$ [48]. In the simulation, the excitation f_{ext} is a Gaussian pulse with a peak intensity of $|\Omega^*_{qm}F_{k_1}|^2 = |\Omega^*_{qm}F_{k_2}|^2 = 1/g_0$ and a pulse duration of τ_p=250 fs. With this simplified model, we can directly investigate the contribution of self- and cross-polariton interactions through the three non-linear interaction constants: g_L, g_U, and g_X. This is a major advantage of using the polariton basis (normal-mode basis) compared with the exciton-photon basis (local mode basis) Gross-Pitaevskii equations. Since in the local mode basis, the non-linear interaction is represented only by the exciton-exciton interaction constant g_0, we cannot change the self and cross-interaction independently.

We present simulated FWM spectra in Fig. 5.7. All numerical simulations are performed in one-dimensional space. The simulated 2DFT spectra in Fig. 5.7 (b) and (c)) clearly present fine structures (NB and VB) inside the four peak groups. In the following three subsections, we will explain the characteristic physical phenomena behind the experiments and simulations.

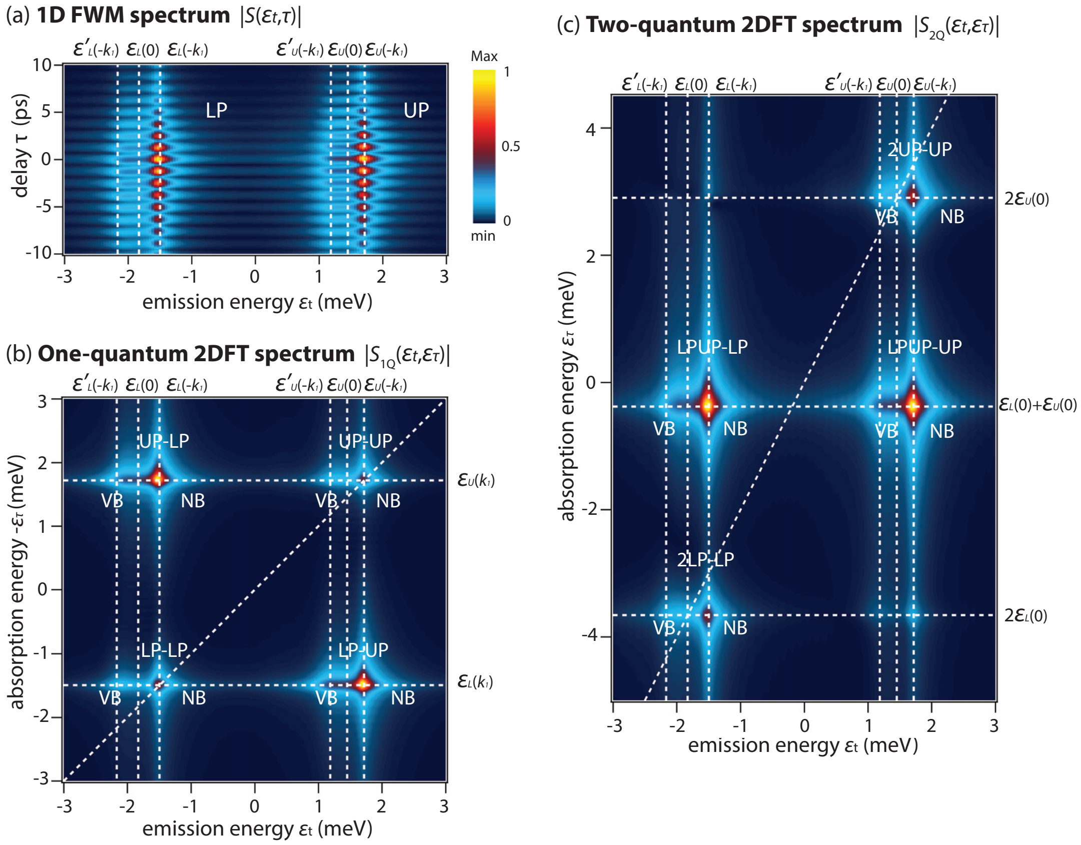

Figure 5.7: (a) Simulated amplitude of FWM spectrum as a function of emission energy and k_2-k_1 pulse delay τ: $|S(\epsilon_t, \tau)|$. (b) Amplitude of 2DFT spectrum for one-quantum $|S_{1Q}(\epsilon_t, \epsilon_\tau)|$ and (c) two-quantum region $|S_{2Q}(\epsilon_t, \epsilon_\tau)|$. Diagonal dashed lines represent $\epsilon_\tau = \epsilon_t$ for (b) and $\epsilon_\tau = 2\epsilon_t$ for (c).

5.4.1 Different interaction contributions

For the purpose of a better insight into the importance of the self and cross-interaction, we show two sets of 2DFT spectra in Fig. 5.8 by turning off either self or cross-interaction.

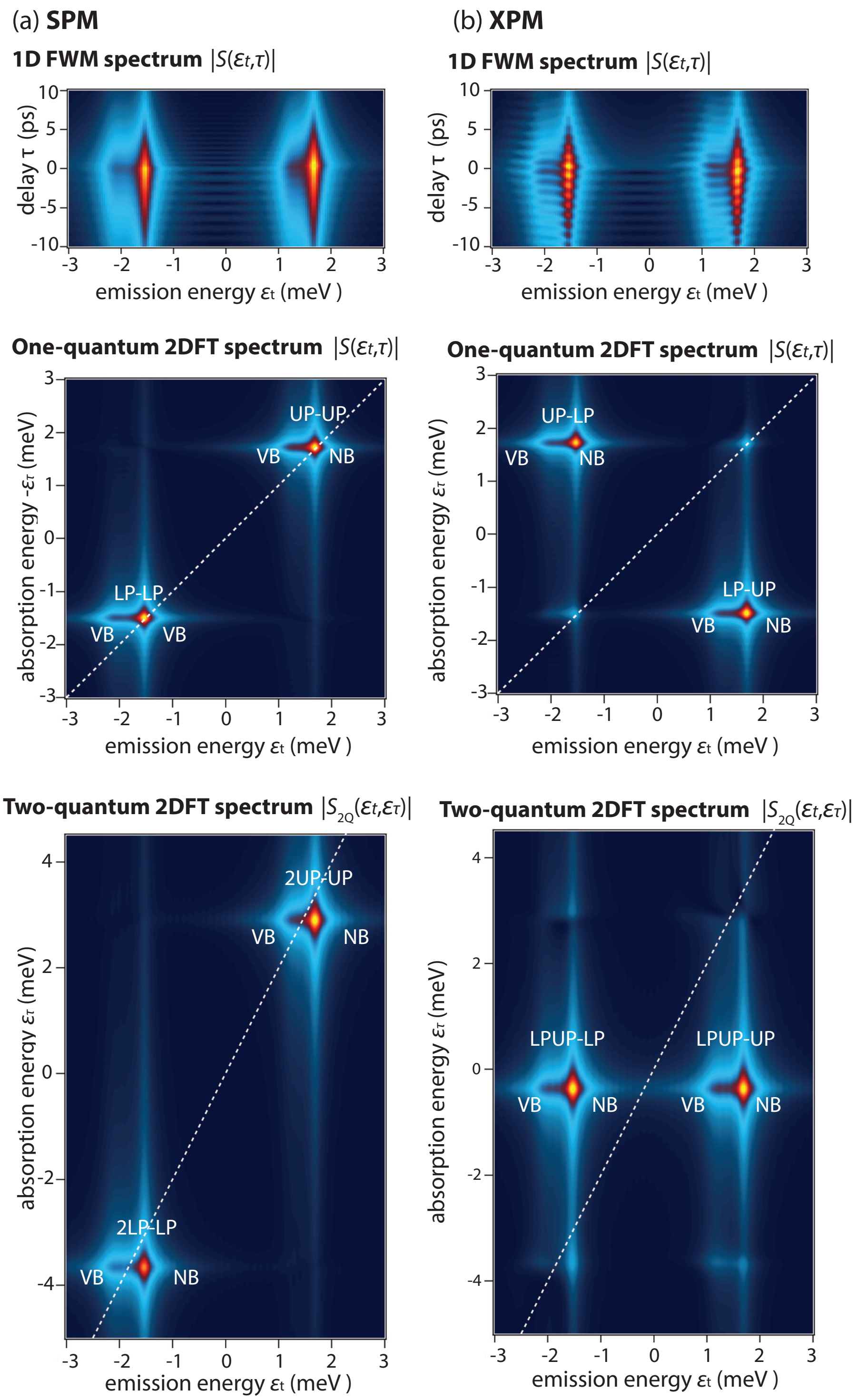

Figure 5.8: Simulated delaymap $|S(\epsilon_t,\tau)|$ and 2DFT spectrum for one-quantum $|S_{1Q}(\epsilon_t,\epsilon_\tau)|$ and two-quantum regime $|S_{2Q}(\epsilon_t,\epsilon_\tau)|$. (a) Simulations are performed including only self-interaction (or self phase modulation: SPM), $g_X = 0$ and (b) for only cross-interaction (or cross phase modulation: XPM), $g_{L(U)} = 0$.

Firstly, Fig. 5.8 (a) is a set of spectra when considering only self-interactions $g_{L(U)}$. The figure presents two main LP-LP (2LP-LP) and UP-UP (2UP-UP) groups along the diagonal line in one (two)-quantum 2DFT spectrum, while we cannot find any peak in the off-diagonal part. This simulation results indicate that the LP-LP (2LP-LP) and UP-UP (2UP-UP) groups originate from the lower-lower and upper-upper self-interactions respectively.

Meanwhile, the 2D spectra which include only the lower-upper cross-interaction g_X (Fig. 5.8 (b)) present only the off-diagonal peak groups UP-LP (LPUP-LP) and LP-UP (LPUP-UP) in one- (two-) quantum 2D spectrum. Only when we include both the self $g_{L(U)}$ and cross g_X interactions, we can reproduce the observed experimental 2D spectra presented in Fig. 5.4. Let us note that, since the cross-interaction constant g_X is twice stronger than the self-interaction constant $g_{L(U)}$, around zero cavity detuning, the off-diagonal peak groups are brighter than the diagonal ones (Fig. 5.4 (b,c)). A similar tendency is observed in the experimental 2DFT spectra (Fig. 5.7 (b,c)).

5.4.2 Fine structures inside peak groups

In this subsection, we discuss the origin of the fine structure in 2DFT spectra. The experimental 2DFT spectra in Fig. 5.4, fine structure (the normal (NB), middle (MB), and virtual branch (VB)) is found inside each peak group. We classify them according to the FWM emission energies. For instance, in the LP-LP group, the emission energies of NB, MB and VB respectively correspond to $\epsilon_{L,0} + \frac{\hbar^2}{2m_L} k_1^2$, $\epsilon_{L,0}$ and $\epsilon_{L,0} - \frac{\hbar^2}{2m_L} k_1^2$. As stated in the previous section, this fine structure is related to the unique polariton energy-momentum dispersion associated with the small polariton mass (Eq. 5.2). The scheme of the four-wave mixing with the polariton energy-momentum dispersion is shown in Fig. 5.9 (one-quantum regime) and 5.10 (two-quantum regime) as energy diagrams. Note that, in the energy diagrams for one-quantum regime (Fig. 5.9), the first arrow representing k_1 pulse is always resonant to the energy-momentum dispersion. The first pulse creates a coherence which evolves with the eigenenergy determined by the polariton energy-momentum dispersion. Meanwhile, the second and third arrows corresponding to k_2 pulse are not always resonant to the energy-momentum dispersion for two reasons. These pulses convert the coherence into a population which does not evolve necessarily with a specific eigenenergy. The k_2 arrows are drawn in such a way as to satisfy the energy conservation.

In the following, for explanations, we focus on the fine structure only in the one-quantum regime, however a similar discussion can be applied to the two-quantum regime. Energy diagrams for the two-quantum regime (Fig. 5.10) are drawn in a similar way to one-quantum ones, but the first two k_2 arrows are always resonant to the energy-momentum dispersion in this regime.

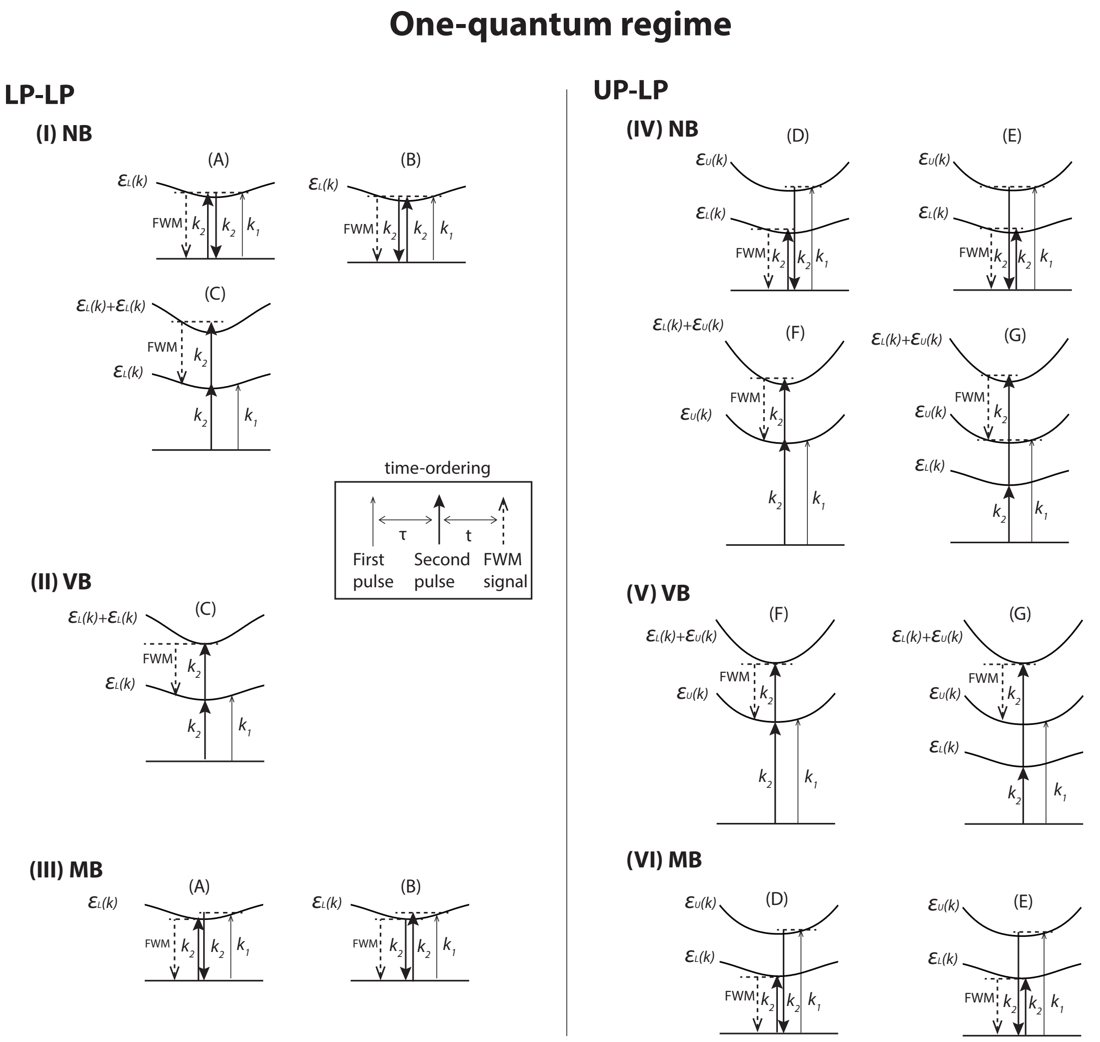
One-quantum regime
LP-LP
(I) NB
(A)
(B)
(C)
εL(k)
εL(k)+εL(k)
FWM
k2
k1
time-ordering
τ
t
First pulse
Second pulse
FWM signal
(II) VB
(III) MB
UP-LP
(IV) NB
(D)
(E)
(F)
(G)
εU(k)
εL(k)+εU(k)
(V) VB
(VI) MB

Figure 5.9: Schematic energy diagrams representing the origin of the fine structures in one-quantum 2D spectrum. Three solid arrows represent two degenerate k_2 pulses and k_1 pulse. The dashed arrows are FWM emissions. For NB schematics, the indices (A)-(G) correspond to those of the double-sided Feynman diagrams in Fig. 5.5

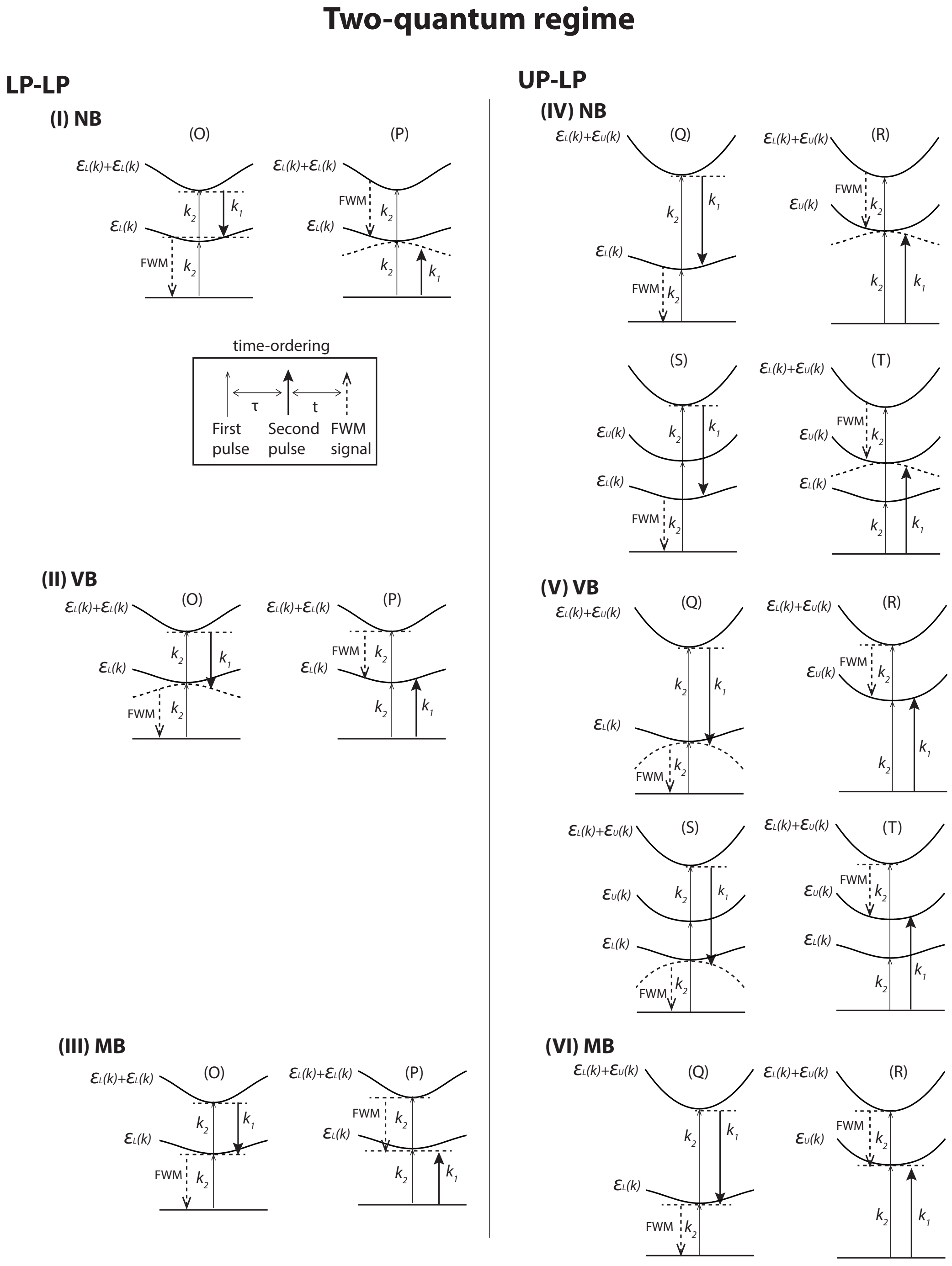
Two-quantum regime
LP-LP
(I) NB
(O)
(P)
$\varepsilon_L(k)+\varepsilon_L(k)$
$\varepsilon_L(k)$
FWM
k_2
k_1
time-ordering
τ
t
First pulse
Second pulse
FWM signal
(II) VB
(III) MB
UP-LP
(IV) NB
(Q)
(R)
(S)
(T)
$\varepsilon_L(k)+\varepsilon_U(k)$
$\varepsilon_U(k)$
(V) VB
(VI) MB

Figure 5.10: Same schematic as Fig. 5.9 for two-quantum 2D spectrum. For normal branch (NB) schematics, the indices (H)-(M) correspond to those of the double-sided Feynman diagrams in Fig. 5.6

Normal branch (NB)

Firstly, let us discuss the normal branches and associated processes. As shown in Fig. 5.9(I) and (IV), NB emission is an on-branch FWM emission. Namely, its FWM emission energy corresponds to $\epsilon_{L(U)}(k_{\mathrm{FWM}}) = \epsilon_{L(U)}(-k_1) = \epsilon_{L(U),0} + \frac{\hbar^2}{2m_{L(U)}}k_1^2$ for both diagonal and off-diagonal peak groups. Third-order perturbative calculations of FWM signal in Fig. 5.5 and 5.6 display only this branch, because, in the perturbative theory, the third-order coherence associated to the FWM signal evolves with the eigenenergy of the polaritons, which corresponds to $\epsilon_{L(U)}(-k_1)$ (See the previous section and Appendix B).

Virtual branch (VB)

We can understand the appearance of the VB in a framework of off-resonant scattering induced by polariton-polariton interactions [71, 59]. The VB results from the processes where the k_1 and k_2 arrows are resonant to the polariton energy-momentum dispersion as consequence of the energy and momentum conservation. As the energy diagrams of the VB, in Fig. 5.9. (II) and (V) show, if the k_1 and k_2 pulses are on-resonant excitation, the energy and momentum conservations demand that the FWM signal emits in an off-resonant way. For example, in the LP-LP group (See Fig. 5.9 (II)), the energy of VB emission is given by $\epsilon'_L(k_{\mathrm{FWM}}) = 2\epsilon_L(\vec{k}_2) - \epsilon_L(\vec{k}_1) = \epsilon_{L,0} - \frac{\hbar^2}{2m_L}k_1^2$. Since NB emission energy is $\epsilon_{L,0} + \frac{\hbar^2}{2m_L}k_1^2$, the separation between NB and VB emission is $2\frac{\hbar^2}{m_L}k_1^2$, which is twice larger than the energy difference between the k_2 and k_1 transmission peak of the lower polariton (See Fig. 5.2 (c)). In the experimental 2DFT spectrum, the energy separation between NB and VB emission is 0.58 meV (See Fig. 5.4 (b) and (c)). This energy separation is twice of the energy separation (0.29 meV) between the k_1 and k_2 transmission peaks of the lower polariton presented in Fig. 5.2 (c). Moreover, this relation holds for both negative and positive cavity detuning (see the next subsection). Thus, we can safely say that the origin of VB peak in LP-LP group can be understood in this framework. We note that although the VB energy-momentum dispersion $\epsilon'_L(k)$ is a mirror image of NB energy-momentum dispersion $\epsilon_L(k)$, in the weak intensity excitation regime, the dispersion is still parabolic. Therefore, we do not consider linearisation of the dispersion due to the Bogoliubov transformation [15]. However, the Bogoliubov theory [45, 15, 71] gives us an insight for understanding the physical origin of the off-resonant scattering in the non-perturbative Gross-Pitaevskii equations. The common feature of the VB and the ghost branch in the Bogoliubov theory is a mixing of different momentum wave-functions, or a creation of a superposition state with different $\boldsymbol{k}$s. In the Bogoliubov theory, this is explicitly described as the creation of a quasi-particle called “bogolon" such as $\hat{a}_{\mathrm{bog}}(\boldsymbol{k}) = u_{\boldsymbol{k}}\hat{a}(\boldsymbol{k}) - v_{\boldsymbol{k}}\hat{a}^{\dagger}(-\boldsymbol{k})$ [45]. In our numerical calculations, the non-linear interaction term $|\psi_{L(U)}|^2\psi_{L(U)}$ gives rise to the mixing of wave-functions with different momenta. This mixing process is possible only in non-perturbative way, thus the numerical simulation in Fig. 5.7 shows VB, while the third-order perturbation in Fig. 5.5 and 5.6 does not.

In the UP-LP group, similar to the LP-LP group, we can draw energy diagrams of VB emission based on the momentum and energy conservation (See Fig. 5.9 (V)). In this case, the VB emission energy corresponds to $\epsilon'_{LU}(k_{\mathrm{FWM}}) = \epsilon_L(\vec{k}_2) + \epsilon_U(\vec{k}_2) - \epsilon_U(\vec{k}_1) = \epsilon_{L,0} - \frac{\hbar^2}{2m_U}k_1^2$. Let us notice that, in Fig. 5.9 (V), the higher energy-momentum dispersion is the sum of two different energy-momentum dispersions $\epsilon_L(\vec{k})$ and $\epsilon_U(k)$. While the VB of the UP-LP group is visible in the simulation, Fig. 5.7, we cannot find the VB in the UP-LP group of the experiment (See Fig. 5.4). The reason for this is not clear yet and further investigation is an issue for the future. We skip the discussion of the LP-UP and the UP-UP groups, which is completely same as that of the UP-LP and LP-LP peak groups. Again, experimentally, we cannot find the VB in the the LP-UP and UP-UP peak groups.

Middle branch (MB)

Finally, we focus on the MB. In the UP-LP group of the experimental 2DFT spectra in Fig. 5.4, a strong peak is found next to NB both in one and two-quantum regime. Since the FWM emission energy of this peak, which corresponds to $\epsilon_L(\vec{k}_2) = \epsilon_{L,0}$, is located in the middle of NB and VB, we name this peak MB. In Fig. 5.4, a weak MB is identified in the LP-LP group. Additionally, the experimental spectra, the peak in UP-UP is also classified as a MB, because the emission energy of the UP-UP peak is $\epsilon_U(\vec{k}_2) = \epsilon_{U,0}$. On the other hand, the numerical simulations in Fig. 5.7 do not display MB at all. This makes the interpretation of MB difficult. Finally, schematically, we associated the origin of MB to the processes depicted in Fig. 5.9(III) and (VI). Again, these processes are drawn in such a way as to satisfy the energy and momentum conservation, but, one of the degenerate fields of the second pulse is not resonant to the energy-momentum dispersion. However, the microscopic explanation of MB is still missing. For a complete understanding of the detailed mechanism of the MB, further investigation and an improved model are required. For instance, taking into account effects such as, excitation induced dephasing (EID) and relaxation from the upper-polariton into exciton reservoirs. The importance of EID in polariton dynamics will be discussed in Chapter 7.

5.4.3 2DFT spectrum at a negative (δ=-2 meV) and positive (δ=2.7 meV) cavity detuning

In order to obtain more insight into the effect of the polariton energy-momentum dispersion on the 2DFT spectra, we perform 2DFT spectroscopy at a negative δ=-2.0 meV and positive δ=2.7 meV cavity detuning. In Fig. 5.11 we display the amplitude of the 2DFT spectra at the two different detunings. Fig. 5.11 (a) and (b) present the same feature as the spectrum obtained at cavity detuning δ=-0.38 meV (Fig. 5.4), however the emission energy separation between the NB and the VB varies with the cavity detuning, which is due to the change of the curvature of the polaritons energy-momentum dispersion.

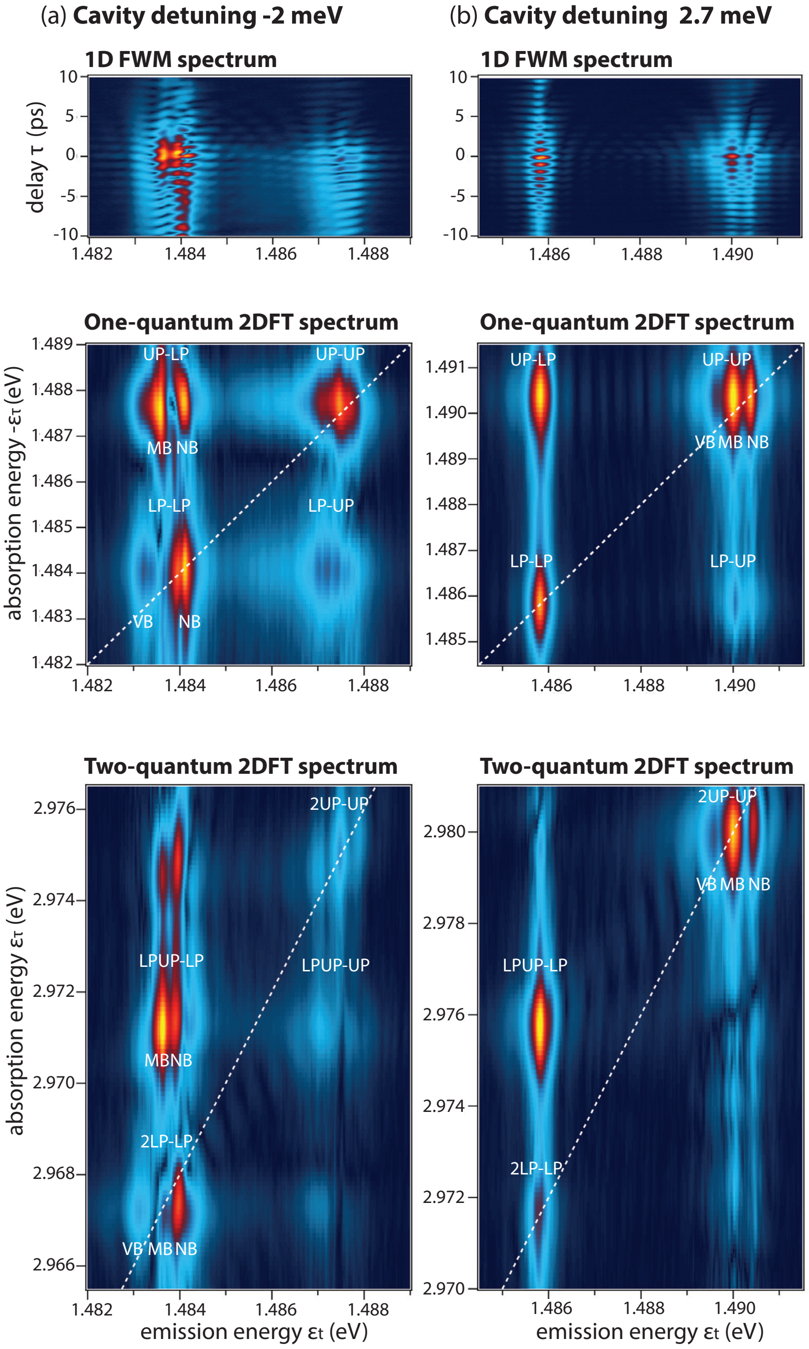

Figure 5.11: Experimental 1D FWM spectrum $|S(\epsilon_t, \tau)|$, one-quantum $|S_{1Q}(\epsilon_t, \epsilon_\tau)|$, and two-quantum 2DFT spectrum $|S_{2Q}(\epsilon_t, \epsilon_\tau)|$ (a) for negative ($\delta = -2$ meV) and (b) for positive ($\delta = 2.7$ meV) cavity detuning.

At negative cavity detuning δ=-2.0 meV, where the cavity photon energy is far below the exciton one, the lower-polariton becomes photon-like and acquires a lighter mass, while the upper-polariton becomes exciton like and becomes heavier. This results in a larger (smaller) curvature of the energy-momentum dispersion for the lower (upper) polariton than the upper (lower) one. Therefore, at the cavity detuning δ=-2.0 meV, the emission energies of NB and VB in the LP-LP group are more separated than at the cavity detuning $\delta = -0.38$ meV. Let us compare the energy separation of the NB and VB in the LP-LP group between Fig. 5.11 (a) and 5.4.

On the contrary, at positive detuning $\delta = 2.7$ meV (Fig 5.11 (b)), the energy-momentum dispersion for the lower-polariton acquires a heavier mass than the upper one. Since the heavier mass results in a smaller curvature of the lower-polariton dispersion, the fine structures in the LP-LP group are almost degenerate and impossible to resolve. In Fig 5.11 (b), we also find three fine structure peaks in UP-UP (2UP-UP) group. This can be associated to the lighter mass and a large curvature of the upper-polariton dispersion. However, the MB peak cannot be described within our simple model. This might be linked to the dynamic red-shift of the upper-polariton's mean field energy [15, 16]. Again, the confirmation of their origin is the subject of further investigations .

We present the numerical simulations for negative ($\delta = -2$ meV) and positive ($\delta = 2.7$ meV) cavity detuning in Fig. 5.12. As expected, for negative detuning (Fig. 5.12 (a)), the energy separation of fine structures (NB and VB) in the LP-LP group increases due to the large curvature of the lower-polariton energy-momentum dispersion. Conversely, for positive detuning (Fig. 5.12 (b)), we cannot resolve the fine structure in the LP-LP group because the energy-momentum dispersion of the lower-polariton has a small curvature. The fine structure of UP-UP group displays the inverse detuning dependence compared to the LP-LP group. Namely, for the UP-UP group, a small energy separation for $\delta = -2$ meV and a large separation for $\delta = 2.7$ meV. Now, it is worth mentioning that the energy separations between NB and VB in UP-LP (LPUP-LP) and LP-UP (LPUP-UP) groups are the average of those of LP-LP (2LP-LP) and UP-UP (2LP-LP) groups. This can be understood by recalling the energy diagrams for NB and VB in the LP-UP (LPUP-UP) group in Fig. 5.9 and 5.10.

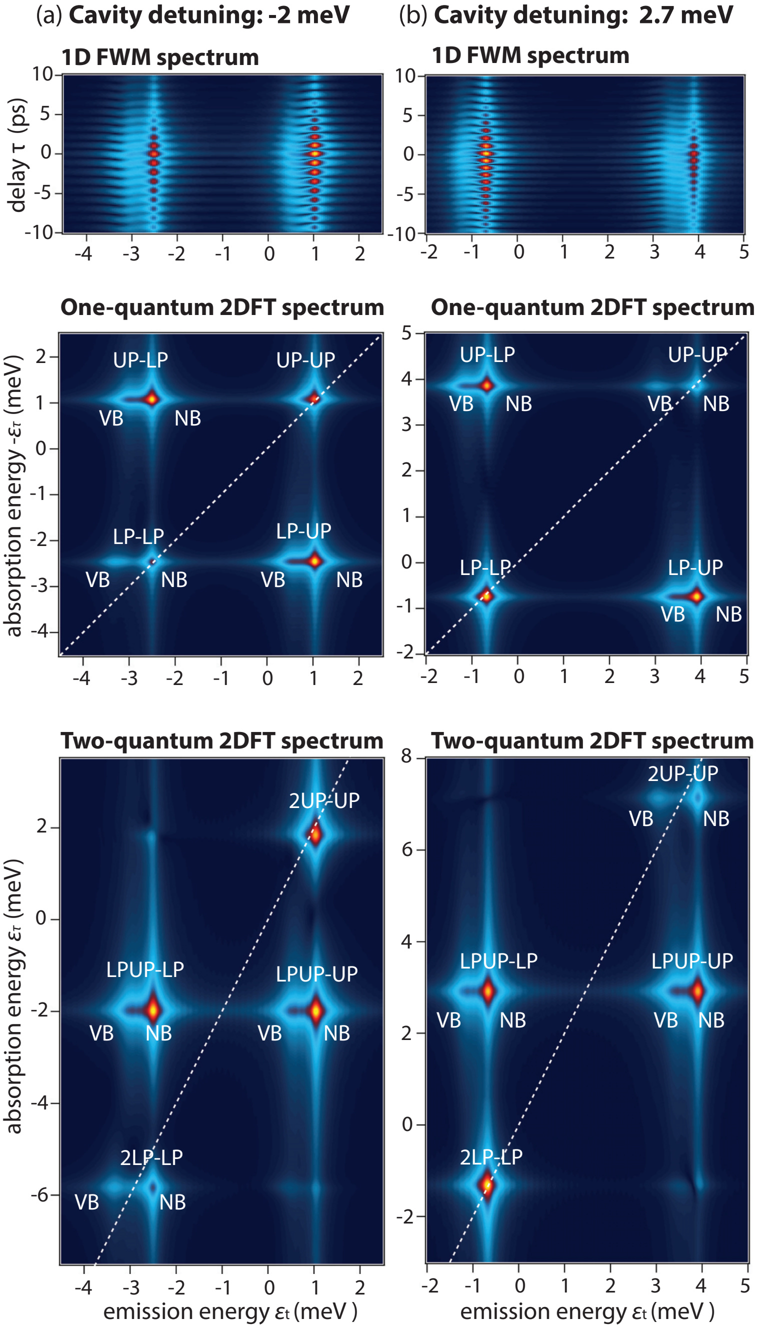

Figure 5.12: Simulated 1D FWM spectrum $|S(\epsilon_t,\tau)|$ and one-quantum $|S_{1Q}(\epsilon_t,\epsilon_\tau)|$ and two-quantum 2DFT spectrum $|S_{2Q}(\epsilon_t,\epsilon_\tau)|$ (a) for negative ($\delta = -2$ meV) and (b) for positive ($\delta = 2.7$ meV) cavity detuning.

5.4.4 Comparison with experiments

When we compare the experiment (Fig. 5.4) with the numerical simulation (Fig. 5.7), we can easily notice that a striking asymmetry exist between UP-LP (LPUP-LP) and LP-UP (LPUP-UP) groups in the experiment. On the other hand, the numerical simulation does not display such an asymmetry. In particular, while in the simulation the fine structure inside the LP-UP (2LP-UP) group is present in the same way as inside UP-LP (LPUP-LP) group, experimentally the LP-UP (LPUP-UP) group is too weak to resolve the fine structure. This type of asymmetry along the off-diagonal axis has already been reported in a semiconductor microcavity system [66] and in bare quantum wells [70, 65].

Although a microscopic model completely describing these observations is still missing, we can attempt to phenomenologically fit the asymmetric amplitude of the experimental 2DFT spectra at the cavity detuning $\delta = -0.38$ meV (Fig. 5.4) with the following polariton Gross-Pitaevskii equations:

$$i\hbar\dot{\psi}_L = (\epsilon_{L,0} - \frac{\hbar^2}{2m_L}\nabla^2 + g'_L|\psi_L|^2 + g'_{UL}|\psi_U|^2 - i\gamma_L)\psi_L + \Omega_L^* f_{\text{ext}} \tag{5.8}$$

$$i\hbar\dot{\psi}_U = (\epsilon_{U,0} - \frac{\hbar^2}{2m_U}\nabla^2 + g'_U|\psi_U|^2 + g'_{LU}|\psi_L|^2 - i\gamma_U)\psi_U + \Omega_U^* f_{\text{ext}}. \tag{5.9}$$

The above equations are the same as Eq. 5.6, but the interaction constants: g'_L, g'_U, g'_{LU}, and g'_{UL} are no more linked to the exciton-exciton interaction Hamiltonian $\hat{H}_{int}$. Instead, we deal with these interaction constants as fitting parameters. Therefore, in Eq. 5.9, g'_{LU} needs not to be equal to g'_{UL}. Actually, this shows the advantage of the polariton basis Gross-Pitaevskii equations compared to the conventional exciton-photon Gross-Pitaevskii equations (Eq. 3.10 and 3.11), in which the non-linearity is mediated by the single exciton-exciton interaction constant g_0 and the amplitude of LP-UP group is always equal to that of UP-LP groups. In Fig. 5.13, we show simulated 2DFT spectra with interaction constants as $g'_L : g'_U : g'_{LU} : g'_{UL} = 1 : 0.6 : 0.3 : 1.6$ (meV/n_0), which correspond to the ratio of the integrated amplitudes of peaks groups LP-LP, UP-UP, LP-UP and UP-LP in Fig. 5.4(b). The other parameters are the same as those in Fig. 5.7. It is clear that the phenomenological model displays a better reproduction of the asymmetric peak intensities along the diagonal axis.

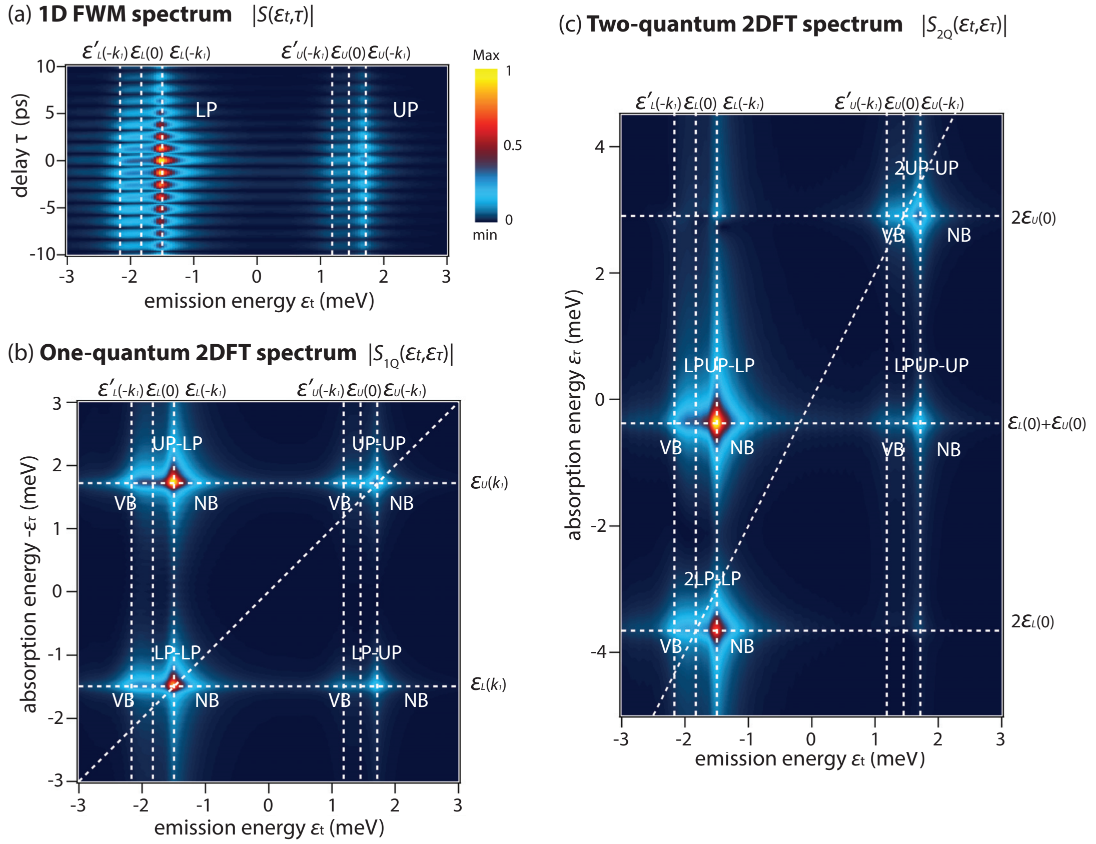

Figure 5.13: Simulation based on interaction constants as free parameters. The cavity detuning is $\delta = -0.38$ meV. The interaction constants set as $g'_L : g'_U : g'_{LU} : g'_{UL} = 1:0.6:0.3:1.6$ (meV/n_0). Simulated amplitude of FWM spectrum as a function of emission energy and k_2-k_1 pulse delay τ: $|S(\epsilon_t,\tau)|$ (a). Amplitude of 2DFT spectrum for one-quantum $|S_{1Q}(\epsilon_t,\epsilon_\tau)|$ (b) and two-quantum region $|S_{2Q}(\epsilon_t,\epsilon_\tau)|$ (c). Diagonal dashed lines represent $\epsilon_\tau = \epsilon_t$ for (b) and $\epsilon_\tau = 2\epsilon_t$ for (c).

5.5 Conclusion

In conclusion, 2D Fourier transformation (2DFT) spectroscopy has been performed to investigate polariton-polariton interactions in a semiconductor microcavity. The measured 2DFT spectra display two important aspects. Firstly, the four peak groups of 2DFT spectra both in one and two-quantum regime can be associated with lower-lower (upper-upper) polariton self-interaction and lower-upper polaritons cross-interaction. In particular, the lower-upper cross interaction is the consequence of the non-linearity between two normal modes (lower and upper-polariton) mediated from a local mode non-linearity (exciton interaction). Additionally, the energy-momentum dispersion associated with the light effective mass of polaritons gives rise to complex fine structure inside the peak groups. Both features are analysed and captured through third-order perturbation theory and non-perturbative simulation with polariton Gross-Pitaevskii equations. However, the deviations between the experiments and simulations leave issues for future investigation. The observed strong asymmetry of the 2DFT spectra along the diagonal axis and the middle branch of the fine structure indicate complex many-body effects such as exciton-exciton correlation [33, 72, 66], photon-assisted exchange scattering (PAE) [73] and population relaxation of the upper-polariton to reservoir due to excitation induced dephasing (EID).

6 Spinor polariton interaction

In this chapter, we investigate spin-dependent interaction of polaritons called “spinor polariton interaction". As we have explained in Chapter 2, a quantum well exciton has two spin projections, spin-up and spin-down. Therefore, we can consider two configurations for polariton-polariton (exciton-exciton) collision: collision with parallel and anti-parallel spins. Moreover, due to the one to one correspondence between an exciton and a photon, we can investigate the spin-dependent interaction of polaritons via the polarization of light.

Actually, the spinor polariton interaction plays important roles in fundamental physical processes of polaritons. For example, spin anisotropic nonlinearities result in unique spin dynamics of polaritons [17, 18], the transport of spin polarized polaritons [19], the optical spin Hall effect [20, 21, 22], multistability [27, 28, 29] and polariton switching [8, 9]. Additionally, the polariton spinor interaction is important also in the context of non-resonant polariton condensates, for instance, the generation of polarization vortices [23, 24], half quantum vortices [25], spontaneous polarization buildup in polariton Bose-Einstein condensation [26].

Despite the importance of the polariton spinor interactions, they only have been investigated through indirect ways. Several previous measurements indicates that polariton-polariton interaction with parallel spins is repulsive, while the interaction with anti-parallel spins is attractive due to the effect of exciton molecule called “biexciton" [34, 74, 75]. On the other hand, other experiments suggest that polariton-polariton interaction with anti-parallel spins can be repulsive [28, 29, 8, 76]. Therefore, it is very important to study the polariton spinor interaction in a simple and direct way, namely with polarization dependent pump-probe spectroscopy.

Firstly, we describe the experimental configuration of the polarization dependent pump-probe spectroscopy. Secondly, we present the experimental results and analysis based on spin-dependent Gross-Pitaevskii equation including a biexciton effect. Finally, we focus on the polariton-polariton interaction with anti-parallel spins, where the biexciton plays a very important role in the polariton interaction through resonance scattering named “polaritonic Feshbach resonance". The results of this section are based on our articles [55, 56].

6.1 Experimental setup for pump-probe experiment

We display the experimental configuration of the pump-probe spectroscopy in Fig. 6.1. This configuration has a similarity to that of the four-wave mixing (FWM) spectroscopy in Chapter 5, however, in the pump-probe spectroscopy the signal we measure is in the k_1 direction instead of the FWM direction. Moreover, in the excitation, the two pulses are almost degenerate and we consider $k_1 \simeq k_2 = 0\ \mu\text{m}^{-1}$. This degenerate configuration is employed in order to avoid the effect of the polariton energy-momentum dispersion. The delay between the two pulses is zero. In the pump-probe spectroscopy, we label k_2 and k_1 beams respectively as “pump" and “probe".

Since our objective is to investigate the spin dependence of the polariton interaction, the pump pulse is either σ^+ or σ^- circularly polarized, while the polarization of the probe pulse is fixed as σ^+. When the polarization is the same (opposite) between the pump and the probe, we call it co- (counter-) circular polarization.

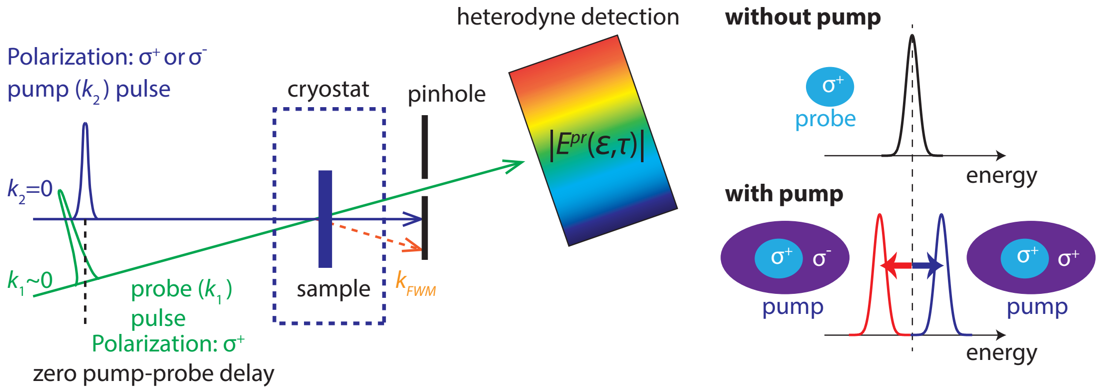
heterodyne detection
without pump
Polarization: σ^+ or σ^-
pump (k_2) pulse
cryostat
pinhole
$|E^{pr}(\varepsilon,\tau)|$
σ^+
probe
energy
k_2=0
with pump
k_1~0
probe (k_1) pulse
sample
k_{FWM}
Polarization: σ^+
zero pump-probe delay
σ^+ σ^-
pump
σ^+ σ^+
pump
energy

Figure 6.1: Scheme of excitation and detection configuration for the polarization dependent pump-probe spectroscopy. The semiconductor microcavity sample is excited by two pulses: pump (k_2) and probe (k_1) pulse. Since the angle between the two beams is small, the wave vectors of the two beams are considered degenerate. The delay between pump and probe pulses is zero. By changing the polarization of the pump pulse, we excite the sample with a co- and counter-circular polarization configuration. Using a pinhole, we spatially select the probe beam and transfer it to the heterodyne detection path (See Fig. 4.3 in Chapter 4). Depending on the polarization of the pump, blue or redshift of the probe spectrum is observed.

As shown in Fig. 6.1, the transmitted probe beam is spatially selected and transferred to the heterodyne detection path explained in Chapter 4. Using the heterodyne detection, we obtain the amplitude of the transmitted probe spectrum $|E^{pr}(\epsilon, \tau = 0)|$ at zero pump-probe delay. Finally, with the aid of a numerical low-pass filter, we remove the noise in the probe spectrum coming from the spectrum envelope of the laser source.

6.2 Pump-probe spectrum and polariton interaction

In this section, we describe the principle of the polariton interaction measurement based on the pump-probe spectroscopy. The main idea is to measure the energy renormalization induced by the polariton interactions through the energy shift of the probe spectrum (See Fig. 6.1). The circularly polarized strong pump pulse generates spin polarized polaritons, then they are spectrally probed with the circularly polarized probe pulse. When the pump and probe pulse are co-circularly polarized the energy shift of the probe pulse reflects the interaction of polaritons with parallel spins, while the energy shift of the probe for the counter-circular polarization pump-probe configuration is associated with the polariton interactions with anti-parallel spins. Since the probe pulse is weak (ten times smaller than the pump) $\sim 10^{12}$ photons pulse^{-1}cm^{-2}, we neglect the energy shift induced by the probe population itself.

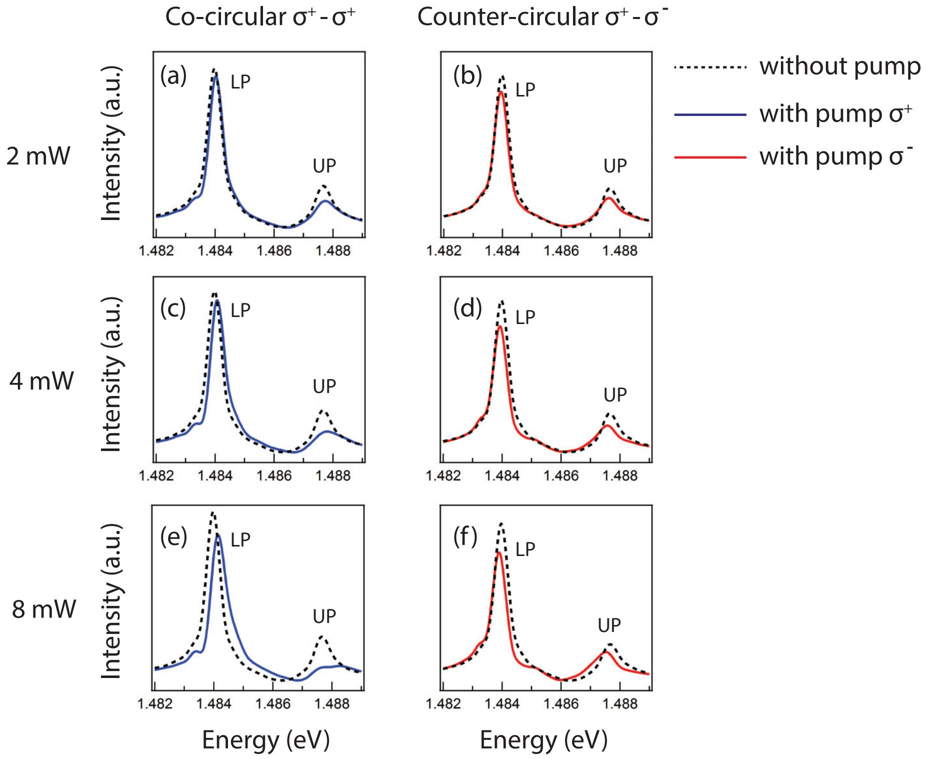

Figure 6.2: Co- (blue) and counter- (red) circularly polarized pump-probe spectra at the cavity detuning of $\delta = -1.5$ meV. Spectra are for three different pump intensities: 3.0×10^{13} (a,b), 5.9×10^{13} (c,d) and 1.2×10^{14} (e,f) photons pulse^{-1} cm^{-2}. Transmitted probe spectra without pump and with pump pulse are respectively presented with dashed and solid lines. LP and UP respectively represent the lower and upper polariton resonances.

We display the pump-probe spectra for co- and counter-circular polarization configuration for three different pump intensities in Fig. 6.2. The cavity detuning is $\delta = -1.5$ meV. Let us compare the pump-probe spectrum with and without the pump. As we can see from Fig. 6.2, both lower (LP) and upper (UP) polariton present blue-shifts for the co-circular polarization configuration ($\sigma^+ - \sigma^+$), which is the signature of repulsive interaction between polaritons with parallel spins. Additionally, as the pump intensity increases the blue-shift increases because the energy renormalization is proportional to the population of the pump polaritons. At negative cavity detuning the lower polariton is photon-like, while the upper-polariton is exciton-like. Since the polariton interaction originates from the excitonic part of the polariton, the blue-shift is larger for the upper-polariton than for the lower one. In counter-circular polarization ($\sigma^+ - \sigma^-$), both lower and upper polariton present red-shifts and the energy shift increases following the increase of the pump intensity, which indicates the attractive interaction of polaritons with anti-parallel spins. However, in the following sections we will find that the behaviour of the energy shift in counter-circular polarization configuration is more complex than that in co-circular one, because of the presence of a biexciton resonance when using polaritons with anti-parallel spins [77, 78]. The pump-probe spectra are obtained at different cavity detunings in order to investigate the role of the excitonic content and the biexciton effect on the polariton-polariton interactions.

6.3 Experimental results: energy shifts vs cavity detuning

The energy shift is defined as a difference in peak energy position between the probe transmitted spectrum with and without the presence of the pump pulse. In order to quantitatively extract the peak energy of the polariton resonance, we fit the pump-probe spectra using a Lorentzian function. We mutually analyse the energy shift of the lower and upper-polariton and plot them as a function of the cavity detuning in Fig. 6.3 and 6.4.

6.3.1 Polariton interaction with parallel spins

Fig. 6.3 presents the energy shifts of the lower and upper polaritons for the co-circularly polarization configuration. We can find in that both lower and upper polaritons show blue-shifts. Additionally, the two branches form a mirror image as a function of the cavity detuning: the blue-shift of the lower-polariton increases with the cavity detuning, while the upper-polariton blue-shift behaves in the opposite way. This behaviour results from the excitonic fraction of the lower and upper polaritons. Namely, from negative to positive cavity detuning, the lower-polariton becomes more exciton-like, while the upper polariton becomes more photon-like.

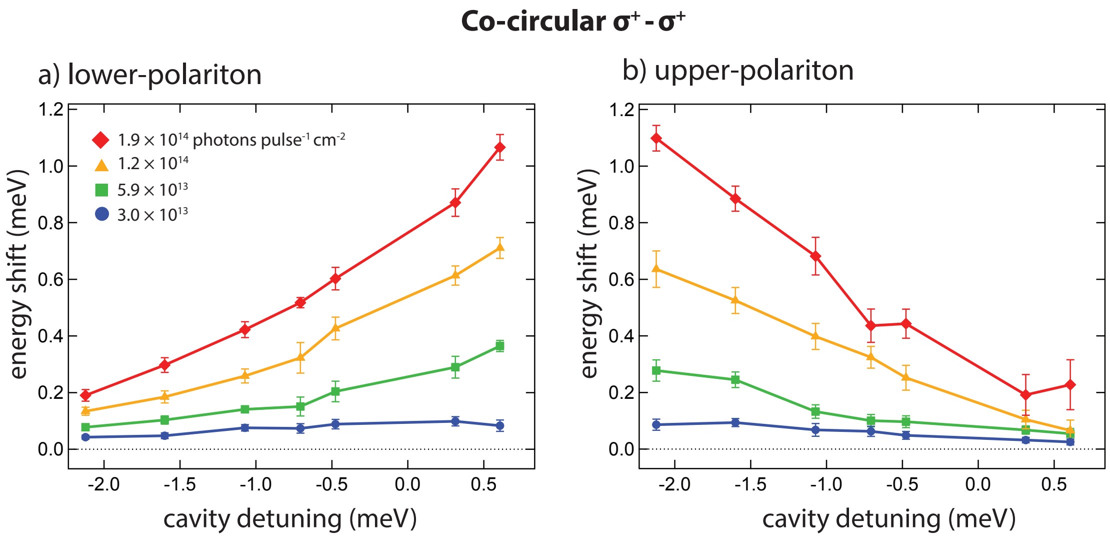

Figure 6.3: Energy shifts of lower (a) and upper (b) polariton resonances in co-circularly polarization configuration as a function of the cavity detuning. Four different symbols represent different pump intensities.

In Fig. 6.3, we notice that the mirror symmetry axis is not at zero detuning but slightly at a negative detuning (~ -0.7 meV). For the origin of this, we can consider two possibilities: the photon-assisted exchange interaction (PAE) and a relaxation from the upper-polariton into an exciton reservoir. The former one is related to the fact that PAE contributes to the attractive interaction between upper-polaritons as shown in Eq. (pae a3) in Chapter 3. Meanwhile, the latter one is associated with the conversion of the upper-polariton into incoherent excitons induced by a dephasing effect. In order to deal with both effect properly, the excitonic Bloch equation approach is required, which will be discussed in Chapter 7. In this chapter, since we analyse the experimental results in the framework of coherent limit approximation, we neglect the reservoir effect. Therefore, in the next section, we analyse the energy shifts based only on the exciton-photon Gross-Pitaevskii equations. We should note that this is a first discussion because we are neglecting the cross interaction between the lower and upper polaritons discussed in Chapter 5.

6.3.2 Polariton interaction with anti-parallel spins

Fig 6.4 shows the energy shifts of the lower and upper polaritons for the counter-circular polarization configuration. Contrary to the co-circular polarization configuration, the lower polariton energy red-shifts more with the increase of the pump intensity. This provides the evidence for the attractive interaction of the lower-polaritons with anti-parallel spins. Interestingly, we notice that the red-shift decreases with the positive detuning. We will find that this behaviour can be explained as a resonant scattering of the lower-polariton through a biexciton (Feshbach resonance) using the exciton-photon Gross-Pitaevskii equations including a biexciton coupling. On the other hand, the upper polariton presents a very complex behaviour: at the low pump intensities ($\sim 3.0 \times 10^{13}$ photons pulse^{-1}cm^{-2}), the red-shift is small for all cavity detunings, while at the high pump intensity a very large red-shifts are present in the negative cavity detunings.

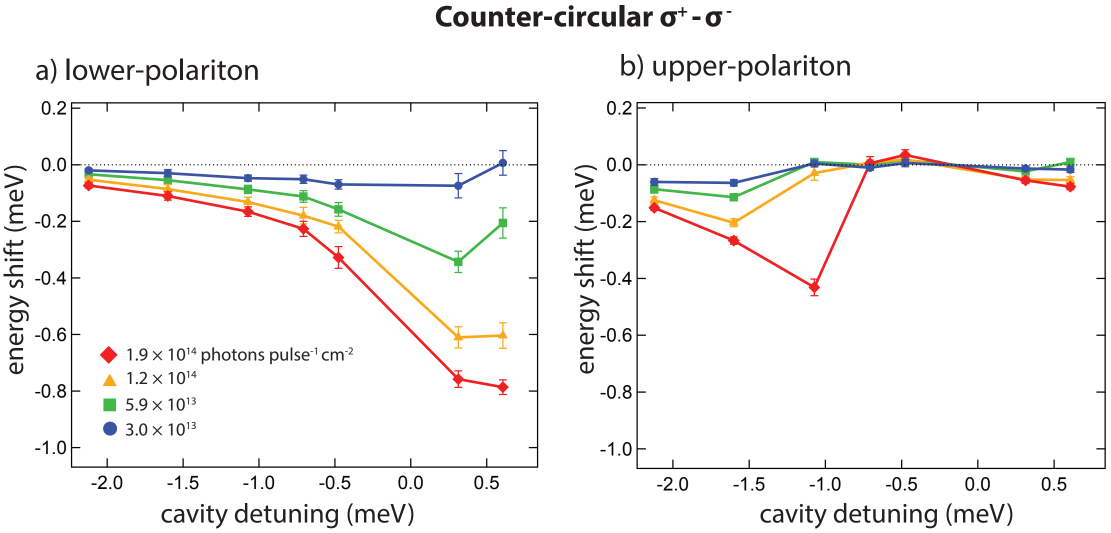

Figure 6.4: Energy shifts of lower (a) and upper (b) polaritons for counter-circularly polarization configuration as a function of the cavity detuning. Four different symbols represent different pump intensities.

Firstly, it is worth mentioning that the results at higher pump intensities (1.2×10^{14} and 1.9×10^{14} photons pulse^{-1}cm^{-2}), the system can reach the transition from strong-to-weak coupling regime. As we will find in Chapter 7, in this regime, the coherent limit description based on the Gross-Pitaevskii does not explain the real experimental results at all. Instead, the excitonic Bloch equations (EBEs) approach including incoherent exciton (or reservoir effect) is indispensable. Since the EBE approach including the biexciton effects has not been established yet, we are going to fit only the results in low pump intensity within the coherent limit approximation in this chapter.

6.4 Theoretical model

We introduce the exciton-photon basis Hamiltonian which includes the exciton-biexciton coupling (see Chapter 3) [50, 79, 80, 81],

$$\hat{H} = \hat{H}_{\text{lin}} + \hat{H}_{\text{int}} + \hat{H}_{\text{qm}}. \tag{6.1}$$

The $\hat{H}_{\text{lin}}$, $\hat{H}_{\text{int}}$, and $\hat{H}_{\text{qm}}$ are respectively given by

$$\begin{aligned} \hat{H}_{\text{lin}} &= \sum_{\sigma=\{\uparrow\downarrow\}} \int d\mathbf{x} \Big[\hat{\boldsymbol{\psi}}^{\dagger}_{x,\sigma}(\epsilon_x - \frac{\hbar^2\nabla^2}{2m_x})\hat{\boldsymbol{\psi}}_{x,\sigma} + \hat{\boldsymbol{\psi}}^{\dagger}_{c,\sigma}(\epsilon_c - \frac{\hbar^2\nabla^2}{2m_c})\hat{\boldsymbol{\psi}}_{c,\sigma} + \epsilon_B \hat{\boldsymbol{\psi}}^{\dagger}_{B}\hat{\boldsymbol{\psi}}_{B} \\ & \quad + \Omega(\hat{\boldsymbol{\psi}}^{\dagger}_{c,\sigma}\hat{\boldsymbol{\psi}}_{x,\sigma} + \hat{\boldsymbol{\psi}}^{\dagger}_{x,\sigma}\hat{\boldsymbol{\psi}}_{c,\sigma}) \Big], \end{aligned} \tag{6.2}$$

$$\begin{aligned} \hat{H}_{\text{int}} &= \sum_{\sigma=\{\uparrow\downarrow\}} \int d\mathbf{x} [\, \frac{1}{2} g \hat{\boldsymbol{\psi}}^{\dagger}_{x,\sigma}\hat{\boldsymbol{\psi}}^{\dagger}_{x,\sigma}\hat{\boldsymbol{\psi}}_{x,\sigma}\hat{\boldsymbol{\psi}}_{x,\sigma} + \frac{1}{2} g_{+-} \hat{\boldsymbol{\psi}}^{\dagger}_{x,\sigma}\hat{\boldsymbol{\psi}}^{\dagger}_{x,-\sigma}\hat{\boldsymbol{\psi}}_{x,-\sigma}\hat{\boldsymbol{\psi}}_{x,\sigma} \\ & \quad + \frac{1}{2} g_{bx}(\hat{\boldsymbol{\psi}}_{B}\hat{\boldsymbol{\psi}}^{\dagger}_{x,\sigma}\hat{\boldsymbol{\psi}}^{\dagger}_{x,-\sigma} + \hat{\boldsymbol{\psi}}_{x,\sigma}\hat{\boldsymbol{\psi}}_{x,-\sigma}\hat{\boldsymbol{\psi}}^{\dagger}_{B}) \\ & \quad - g_{\text{pae}}(\hat{\boldsymbol{\psi}}^{\dagger}_{c,\sigma}\hat{\boldsymbol{\psi}}^{\dagger}_{x,\sigma}\hat{\boldsymbol{\psi}}_{x,\sigma}\hat{\boldsymbol{\psi}}_{x,\sigma} + \hat{\boldsymbol{\psi}}^{\dagger}_{x,\sigma}\hat{\boldsymbol{\psi}}^{\dagger}_{x,\sigma}\hat{\boldsymbol{\psi}}_{x,\sigma}\hat{\boldsymbol{\psi}}_{c,\sigma})\,], \end{aligned} \tag{6.3}$$

and

$$\hat{H}_{\text{qm}} = \sum_{\sigma=\{\uparrow\downarrow\}} \int d\mathbf{x}\, \Omega_{qm}(\hat{\boldsymbol{\psi}}^{\dagger}_{c,\sigma}\boldsymbol{F}_{\sigma} + \boldsymbol{F}^{*}_{\sigma}\hat{\boldsymbol{\psi}}_{c,\sigma}). \tag{6.4}$$

Here, $\hat{\boldsymbol{\psi}}_{x,\uparrow(\downarrow)}$ represents an exciton with a spin-up (-down). Similarly, $\hat{\boldsymbol{\psi}}_{c,\uparrow(\downarrow)}$ is the cavity photon operator with σ^+ (σ^-) polarization. The important property of the above Hamiltonian is that the coupling constant g_{bx} couples two excitons with opposite spins (spin-up and -down) to a bosonic exciton molecular state called “biexciton" $\hat{\boldsymbol{\psi}}_B$. g and g_{pae} are respectively the strength of the exciton-exciton interaction and photon-assisted exchange scattering. ϵ_x, ϵ_c, and ϵ_B are the eigen-energies of the exciton, photon, and biexciton respectively. The commutation relations of these operators are written in Chapter 3. Another coupling constant

g_{+-} represents a “background" exciton-exciton interaction with anti-parallel spins.

Our biexciton formation model is called “bipolariton model" [80, 81], where the biexciton is created from two excitons with opposite spins through the exciton-exciton interaction [1]. The idea lying in the Hamiltonian H_{bx} and the background interaction is to phenomenologically approximate an interaction potential of excitons with anti-parallel spins [82] as a combination of the bound state $\hat{\boldsymbol{\psi}}_B$ and residual delta-function like scattering potential represented by the term g_{+-}. This background scattering term g_{+-} does not appear in the simplest calculation of exciton-exciton scattering matrix based on the Born approximation [41]. However, several state of the art theories beyond the Born approximation imply that the inclusion of the higher-order scattering matrices gives rise to the background interaction g_{+-}, which is referred to as "continuum correlations" [51, 52, 53, 33]). In our study, the background interaction is important because we cannot fit our data without the term g_{+-}. Finally, let us note that the Hamiltonian $\hat{\boldsymbol{\psi}}_B$ is formally the same as that of the two-channel model of the Feshbach resonance in cold atoms, which results in a resonance scattering of atoms via a molecular bound state [83, 84].

In the same way as in Chapter 5, with the aid of the Heisenberg equations of motion and coherent state approximation, we obtain three coupled equations of motion for the exciton, photon, and biexciton wave functions as

$$\begin{aligned}
i\hbar\dot{\psi}_{x,\uparrow} &= (\epsilon_x + g|\psi_{x,\uparrow}|^2 + g_{+-}|\psi_{x,\downarrow}|^2 - i\gamma_x)\psi_{x,\uparrow} \\
&\quad + g_{bx}\psi_B\psi^*_{x,\downarrow} + (\Omega - 2g_{\mathrm{pae}}|\psi_{x,\uparrow}|^2)\psi_{c,\uparrow} \qquad (6.5) \\
i\hbar\dot{\psi}_{c,\uparrow} &= (\epsilon_c - \frac{\hbar^2}{2m_c}\nabla^2 - i\gamma_c)\psi_{c,\uparrow} + (\Omega - g_{\mathrm{pae}}|\psi_{x,\uparrow}|^2)\psi_{x,\uparrow} - f_{\mathrm{ext},\uparrow} \qquad (6.6) \\
i\hbar\dot{\psi}_B &= (\epsilon_B - i\gamma_B)\psi_B + g_{bx}\psi_{x,\uparrow}\psi_{x,\downarrow}, \qquad (6.7)
\end{aligned}$$

where γ_x, γ_c, and γ_B are respectively decay rates of exciton, photon, and biexciton.

The ratio between the constants g_{pae} and g is estimated as $g_{\mathrm{pae}}/g \simeq \hbar\Omega/6n_sE_ba_0^2$ [85]. Considering a Bohr radius a_{B}=12 nm, a dielectric constant $\epsilon_m = 13.9\epsilon_0$ (ϵ_0 is the vacuum permittivity) [86], the ratio reads, $g_{\mathrm{pae}}/g_0 \simeq 0.22$. Since the exciton-exciton interaction term is dominant compared to PAE, in the following fitting, the photon-assisted exchange scattering (PAE) is omitted, $g_{\mathrm{pae}} = 0$. Even if we include the PAE, it is impossible to obtain a better fitting. This is probably because of the limitation of the coherent limit approximation of the Gross-Pitaevskii equations.

---

[1] There exists another type of biexciton formation model called “giant oscillator strength model", where a biexciton is formed from one exciton with spin-up (spin-down) and one photon with σ^- (σ^+) polarization. The data analysis based on the giant oscillator strength model is discussed in [56] and in Appendix C.

6.4.1 A. Parallel spin polariton interaction

For the co-circularly polarization configuration, only the exciton-exciton interaction term g is involved. Therefore, we will omit the index of spin. Now, we assume that the exciton and photon wave function can be written as combinations of finite modes: pump ($\boldsymbol{k}_2 = 0$), probe ($\boldsymbol{k}_1$), and idler modes ($\boldsymbol{k}_{\text{FWM}} = 2\boldsymbol{k}_2 - \boldsymbol{k}_1 = -\boldsymbol{k}_1$). Within this assumption, the wave functions are written as

$$\psi_{x(c)}(\mathbf{x}, t) = \psi^{pu}_{x(c)}(t) + \psi^{pr}_{x(c)}(t) \cdot e^{i\boldsymbol{k}_1 \cdot \mathbf{x}} + \psi^{id}_{x(c)}(t) \cdot e^{-i\boldsymbol{k}_1 \cdot \mathbf{x}} \tag{6.8}$$

Here, “idler" or “id" has the same meaning as the four-wave mixing signal. Recalling $|\psi^{pu}_{x(c)}| >> |\psi^{pr,id}_{x(c)}|$, the feedback of the signal and idler wave functions to the pump can be neglected (same as the Bogoliubov approximation [45, 87]). Under this approximation, the dynamics of the set of wave functions

$$\vec{u}(t) = \left(\psi^{pr}_x(t), \psi^{pr}_c(t), \psi^{id*}_x(t), \psi^{id*}_c(t)\right) \tag{6.9}$$

can be summarized as a simple equation given by [87]

$$i\hbar \frac{d}{dt}\vec{u} = M^{++}\vec{u} - \vec{F}^{pr}. \tag{6.10}$$

The vector $\vec{F}^{pr}$ represents the probe pulse excitation approximated as an instantaneous pulse incident at a time $t = 0$.

$$\vec{f}^{pr} = (0\,, F^{pr}\delta(t)\exp(-i\omega_{pr}t), 0\,, 0\,) \tag{6.11}$$

The matrix M^{++} reads,

$$M^{++} = \begin{pmatrix} \epsilon_x + 2g|\psi^{pu}_x|^2 - i\gamma_x & \Omega & g\psi^{pu2}_x & 0 \\ \Omega & \epsilon_c - i\gamma_c & 0 & 0 \\ -g\psi^{pu*2}_x & 0 & -(\epsilon_x + 2g|\psi^{pu}_x|^2) - i\gamma_x & -\Omega \\ 0 & 0 & -\Omega & -\epsilon_c - i\gamma_c \end{pmatrix}. \tag{6.12}$$

Here we neglected the parabolic energy-momentum dispersion of the photon because $\boldsymbol{k}_1 \sim 0$ is sufficiently small. Independently from the above probe dynamics, the dynamics of the pump wave functions are calculated as

$$i\hbar\dot{\psi}^{pu}_x = (\epsilon_x + g|\psi^{pu}_x|^2 - i\gamma_x)\psi^{pu}_x + \Omega\psi^{pu}_c \tag{6.13}$$

$$i\hbar\dot{\psi}^{pu}_c = (\epsilon_c - i\gamma_c)\psi^{pu}_c + \Omega\psi^{pu}_x - f^{pu}. \tag{6.14}$$

Since the pump is much stronger than the probe and idler, the pump wave functions can be calculated self-consistently. The pump excitation f^{pu} is given by

$$f^{pu} = F^{pu}\delta(t)\exp(-i\omega_{pu}t) \tag{6.15}$$

The numerical simulation is performed firstly for the pump wave function (Eq. 6.13). Secondly, we calculate the probe and the idler wave function (Eq. 6.10) using the recorded time evolution of the pump wave function dynamics. We set $\omega_{pu(pr)}$ as $\omega_{pu(pr)} = \epsilon_x/\hbar$. The lower and upper polaritons are excited with spectrally broad pump and probe pulses. We obtain the pump-probe spectra through Fourier transformation of the temporal photon probe wave function. Finally, we calculate the energy shifts of the peak energies from pump-probe spectra with and without pump. Figure 6.5 displays the plots of the measured and simulated energy shifts as a function of the cavity detuning in co-circularly polarization configuration. The comparison is performed for the two lower pump intensities, 3.0×10^{13} and 5.9×10^{13} photons pulse^{-1} cm^{-2}.

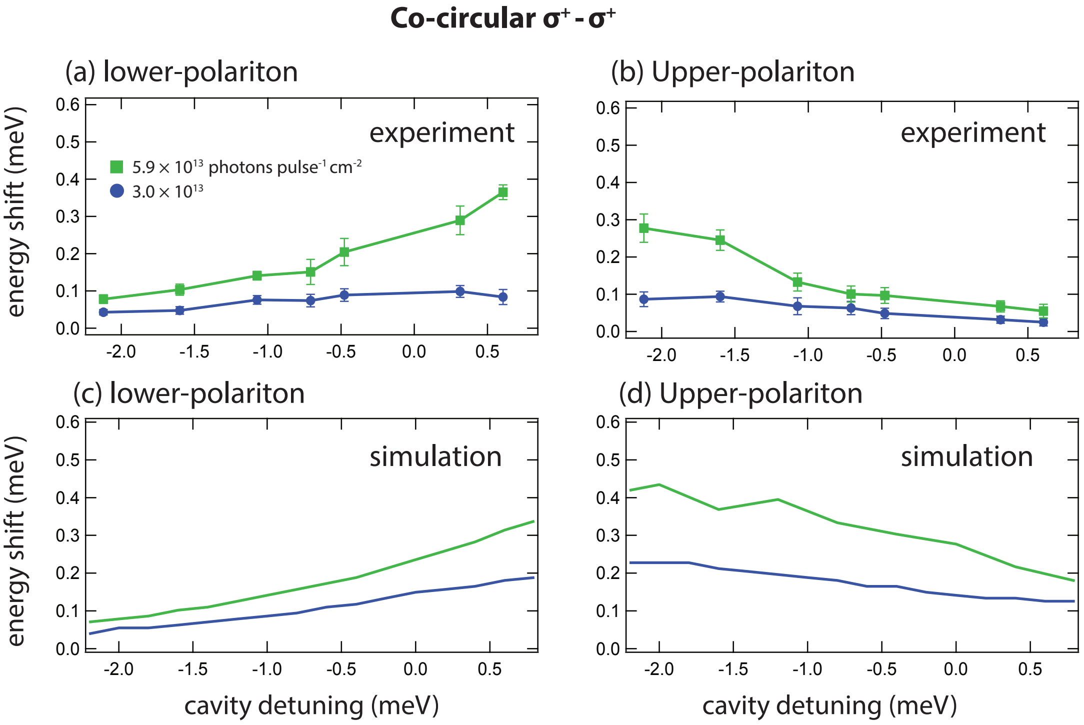

Figure 6.5: Experimental and simulated energy shift for co-circular polarization configuration. Measured energy shifts of the lower (a) and upper (b) polaritons as a function of the cavity detuning. Simulation of the energy shift as a function of the cavity detuning for the lower (c) and upper (d) polariton. The blue and green line respectively represents the experimental (simulated) pump photon density: 3.0×10^{13} ($|F^{pu}|^2 = 1$) and 5.9×10^{13} ($|F^{pu}|^2 = 2$) photons pulse^{-1} cm^{-2}. $|F^{pu}|^2$ is a normalized excitation pump photon density. The parameters for the simulations are g=2 meV/n_0 and $\gamma_x = \gamma_c = 0.265$ meV.

For the fitting, the parameters $\gamma_x = \gamma_c = 0.265$ meV and $\Omega = 1.63$ meV are used [56]. We obtain the interaction constant $g_{++} = 2$ meV$/n_0$ by simulating the lower and upper polariton energy shifts for the two pump powers (Figure 4(c) and (d)). Here, n_0 is a normalization particle density for the excitation pump photon density $|F^{pu}|^2 = 1$. The simulation reproduces the basic features of the experiments: from negative to positive cavity detuning, the blue-shift of the lower polariton increases, while the upper polariton's blue-shift decreases. This highlights the role of the exciton fraction in polariton interactions with parallel spins.

6.4.2 B. Anti-parallel spin polariton interaction

In the counter-circular polarization configuration, we need to consider the exciton-biexciton coupling. Meanwhile, the idler beam (four-wave mixing signal) does not appear in this spin configuration, because the spin momentum conservation is not satisfied [88]. Thus, the dynamics of the probe is described as a set of coupled equations of probe exciton, probe photon, and biexciton wave functions. Firstly, we approximate the form of the wave functions as

$$\psi_{x(c)\uparrow}(\mathbf{x}, t) = \psi^{pu}_{x(c)\downarrow}(t) + \psi^{pr}_{x(c)\uparrow}(t) \cdot e^{i\boldsymbol{k}_1 \cdot \mathbf{x}} \tag{6.16}$$

and

$$\psi_B(\mathbf{x}, t) = \psi_B(t) \cdot e^{i\boldsymbol{k}_1 \cdot \mathbf{x}}. \tag{6.17}$$

We define that the polarization of the pump and probe pulse are respectively σ^- and σ^+. Defining a vector $\vec{u}$ as

$$\vec{u}(t) = \left(\psi^{pr}_{x,\uparrow}(t), \psi^{pr}_{c\uparrow}(t), \psi_B(t)\right) \tag{6.18}$$

The dynamics of the vector $\vec{u}$ follows an equation of motion:

$$i\hbar \frac{d}{dt}\vec{u} = M^{+-}\vec{u} - \vec{F}^{pr}_{\uparrow}. \tag{6.19}$$

The vector $\vec{F}^{pr}_{\uparrow}$ representing the incident probe pulse is defined as

$$\vec{f}^{pr} = (0\,, F^{pr}_{\uparrow}\delta(t)\exp(-i\omega_{pr}t), 0\,, 0\,) \tag{6.20}$$

The matrix M^{+-} is given by

$$M^{+-} = \begin{pmatrix} \epsilon_x + g_{+-}|\psi^{pu}_{x,\downarrow}|^2 - i\gamma_x & \Omega & g_{bx}\psi^{pu*}_{x,\downarrow} \\ \Omega & \epsilon_c - i\gamma_c & 0 \\ g_{bx}\psi^{pu}_{x,\downarrow} & 0 & \epsilon_B - i\gamma_B \end{pmatrix}. \tag{6.21}$$

On the other hand, the pump wave functions independently obey the following equations:

$$i\hbar\dot{\psi}^{pu}_{x,\downarrow} = (\epsilon_x + g|\psi^{pu}_{x,\downarrow}|^2 - i\gamma_x)\psi^{pu}_{x,\downarrow} + \Omega\psi^{pu}_{c,\downarrow} \tag{6.22}$$

$$i\hbar\dot{\psi}^{pu}_{c,\downarrow} = (\epsilon_c - i\gamma_c)\psi^{pu}_{c,\downarrow} + \Omega\psi^{pu}_{x,\downarrow} - f^{pu}_{\downarrow}. \tag{6.23}$$

The pump excitation pulse f^{pu} is defined as

$$f^{pu} = F^{pu}_{\downarrow}\delta(t)\exp(-i\omega_{pu}t) \tag{6.24}$$

$\omega_{pu(pr)}$ is set as $\omega_{pu(pr)} = \epsilon_x/\hbar$. These Equations 6.22-6.24 are same as Eq. 6.13-6.15 for the co-circular polarization configuration.

Counter-circular σ+ - σ-

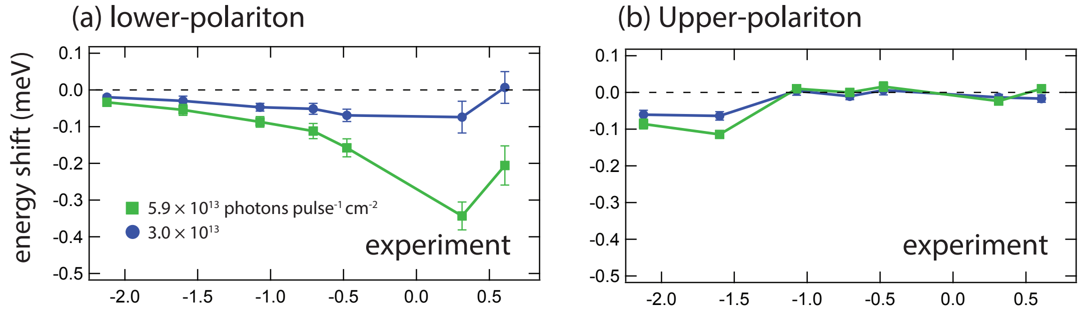

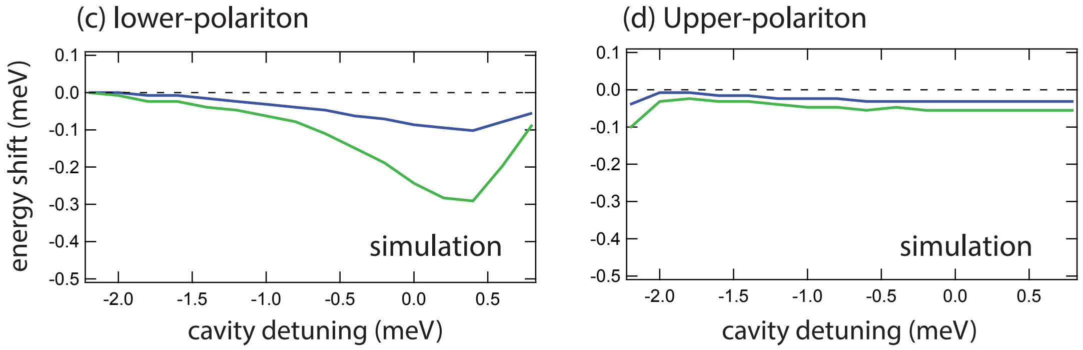

Figure 6.6: Experimental and simulated polariton energy shifts as a function of the cavity detuning for the counter-circularly polarization configuration. Measured energy shifts of the lower (a) and upper (b) polaritons. Simulation of the energy shift for the lower (c) and upper (d) polariton. The blue and green line respectively represents the experimental (simulated) pump photon density: 3.0×10^{13} ($|F^{pu}|^2 = 1$) and 5.9×10^{13} ($|F^{pu}|^2 = 2$) photons pulse^{-1} cm^{-2}. The parameters for the simulations are $g_{++} = 2/n_0$, $g_{+-} = -1.2/n_0$, $g_{bx} = 1.2/\sqrt{n_0}$ meV and $\gamma_x = \gamma_c = 1.06$ meV.

Figure 6.6 presents measured and simulated energy shifts for the counter-circular polarization configuration as a function of the cavity detuning. The plots are presented for the two lower pump intensities, 3.0×10^{13} and 5.9×10^{13} photons pulse^{-1} cm^{-2}. In the numerical simulation, we set $\epsilon_B = 2\epsilon_x - 2.5$ meV and $\gamma_B = 2.2$ meV. The interaction constants are $g_{bx} = 1.2\ \text{meV}/\sqrt{n_0}$ and $g_{+-} = -1.2\ \text{meV}/n_0$. The simulation displays the enhancement of the lower polariton redshift energy with the decrease of the cavity detuning (see Fig. 6.6 (c)). The enhancement of the red-shift of the lower-polariton can be understood as a scattering resonance of the lower-polariton (LP) to the biexciton (BX) state (LP-LP → BX). Actually, the biexciton plays a crucial role in the interaction of polariton with anti-parallel spins. The effect of the biexciton scattering resonance is not only the renormalization of the lower-polariton energy but also contributes to a strong non-linear loss of the lower-polariton (not shown in Fig. 6.6). Since this is an analogue of the Feshbach resonance in cold atoms [83, 84] , we call this effect "polaritonic Feshbach resonance" [55]. We will investigate the polaritonic Feshbach resonance more deeply in the following sections. For the upper polariton mode, the very small energy redshift observed in the experiment is reproduced by the simulation (Fig. 6.6 (d)). This behavior might be related to the presence of biexcitons. However, further investigations are required for its deep understanding. One of the important consequence of the measurement in the counter-circularly polarization configuration is that the polariton interaction with anti-parallel spins cannot be considered to be very small. In particular, when the two lower-polaritons' energy comes close to that of the biexciton, the anti-parallel spin lower-polariton interaction is enhanced and becomes comparable to that of parallel spins.

In order to understand the role of the biexciton in the lower-polariton, it is useful to move to the lower-polariton basis. In the next section we discuss the polariton interactions in the lower-polariton basis.

6.5 Lower-polariton interaction constants

Firstly we rewrite the exciton-photon Hamiltonian with a biexciton Eq. 6.1 in terms of a polariton basis. As shown in Chapter 3, the lower polariton basis Hamiltonian coupled to the biexciton state is given by $\hat{H}_{\text{LP}} = \hat{H}_{\text{lin,LP}} + \hat{H}_{\text{int,LP}} + \hat{H}_{\text{qm,LP}}$. The linear, interaction and quasi-mode couling terms of the Hamiltonian are respectively given by

$$\hat{H}_{\text{lin,LP}} = \sum_{\sigma=\{\uparrow\downarrow\}} \int d\mathbf{x} \left[\hat{\boldsymbol{\psi}}^{\dagger}_{L,\sigma} (\epsilon_{L,0} - \frac{\hbar^2 \nabla^2}{2m_L}) \hat{\boldsymbol{\psi}}_{L,\sigma} \right], \tag{6.25}$$

$$\begin{aligned} \hat{H}_{\text{int,LP}} \quad = \quad & \sum_{\sigma=\{\uparrow\downarrow\}} \int d\mathbf{x} [\, (\frac{1}{2} g X_{\mathbf{0}}^4 + 2 g_{\text{pae}} X_{\mathbf{0}}^3 |C_{\mathbf{0}}|) \hat{\boldsymbol{\psi}}^{\dagger}_{L,\sigma} \hat{\boldsymbol{\psi}}^{\dagger}_{L,\sigma} \hat{\boldsymbol{\psi}}_{L,\sigma} \hat{\boldsymbol{\psi}}_{x,\sigma} \\ & + \frac{1}{2} g_{+-} X_{\mathbf{0}}^4 \hat{\boldsymbol{\psi}}^{\dagger}_{L,\sigma} \hat{\boldsymbol{\psi}}^{\dagger}_{L,-\sigma} \hat{\boldsymbol{\psi}}_{L,-\sigma} \hat{\boldsymbol{\psi}}_{L,\sigma} \\ & + \frac{1}{2} g_{bx} X_{\mathbf{0}}^2 (\hat{\boldsymbol{\psi}}_B \hat{\boldsymbol{\psi}}^{\dagger}_{L,\sigma} \hat{\boldsymbol{\psi}}^{\dagger}_{L,-\sigma} + \hat{\boldsymbol{\psi}}_{L,\sigma} \hat{\boldsymbol{\psi}}_{L,-\sigma} \hat{\boldsymbol{\psi}}^{\dagger}_B)\,], \end{aligned} \tag{6.26}$$

and

$$\hat{H}_{\mathrm{qm,LP}} = \sum_{\sigma=\{\uparrow\downarrow\}} \int d\mathbf{x} \left[\Omega^*_{L,0}\hat{\boldsymbol{\psi}}^\dagger_L \boldsymbol{F} + \Omega_{L,0}\boldsymbol{F}^*\hat{\boldsymbol{\psi}}_L\right]. \tag{6.27}$$

Assuming coherent states for the lower-polariton and biexciton states, from the Heisenberg equations of motion, the equations of motion read,

$$\begin{aligned} i\hbar\dot{\psi}_{L,\uparrow} &= \left[\epsilon_{L,0} - \frac{\hbar^2}{2m_L}\nabla^2 + \left(gX_{\mathbf{0}}^4 + 4g_{\mathrm{pae}}X_{\mathbf{0}}^3|C_{\mathbf{0}}|\right)|\psi_{L,\uparrow}|^2 + g_{L,+-}X_{\mathbf{0}}^4|\psi_{L,\downarrow}|^2 - i\gamma_L\right]\psi_{L,\uparrow} \\ &\quad + g_{bx}X_{\mathbf{0}}^2\psi_B\psi^*_{L,\downarrow} - f_{\mathrm{ext},\uparrow} \qquad (6.28) \\ i\hbar\dot{\psi}_B &= (\epsilon_B - i\gamma_B)\psi_B + g_{bx}X_{\mathbf{0}}^2\psi_{L,\uparrow}\psi_{L,\downarrow}. \qquad (6.29) \end{aligned}$$

The eigenenergy of the lower-polariton at $\boldsymbol{k} = 0$ as a function of the cavity detuning δ is given by

$$\epsilon_{L,0} = \frac{1}{2}\left(2\epsilon_x + \delta - \sqrt{\delta^2 + (2\Omega)^2}\right) \tag{6.30}$$

6.5.1 Lower-polariton interaction constants α_1 and α_2

Now, we introduce the widely used lower-polariton interaction constants α_1 and α_2. The constants α_1 and α_2 respectively represent the strengths of the lower-polariton interaction with parallel and anti-parallel spins. We define them in terms of mean-field energy shifts. In the case of the parallel spin configuration, the mean-field energy shift ΔE_{++}, straightforwardly written as $\Delta E_{++} = \alpha_1|\psi_{L,\sigma}|^2$, is

$$\Delta E_{++} = \left(gX_{\mathbf{0}}^4 + 4g_{\mathrm{pae}}X_{\mathbf{0}}^3|C_{\mathbf{0}}|\right)|\psi_{L,\sigma}|^2, \tag{6.31}$$

where $|\psi_{L,\downarrow}|^2$ is the lower polariton density. Thus, the lower polariton interaction constant with parallel spins α_1 is defined as

$$\alpha_1 = gX_{\mathbf{0}}^4 + 4g_{\mathrm{pae}}X_{\mathbf{0}}^3|C_{\mathbf{0}}|. \tag{6.32}$$

Note that the energy shift ΔE_{++} defined above is different from the energy shift of the probe in pump-probe measurement, which is described in a similar way to Eq. 6.10 and 6.12.

On the other hand, obtaining the constant α_2 of the lower-polariton interaction with anti-parallel spins is more complicated than for α_1. Here, we try to obtain α_2 from the energy shift of the lower-polariton in continuous-wave (CW) pump-probe spectroscopy in the counter-circularly polarization configuration. Similarly to the previous section, we assume the wave functions as $\psi_{L,\uparrow}(\mathbf{x},t) = \psi^{pr}_{L,\uparrow}(t)\cdot e^{i\boldsymbol{k}_1\cdot\mathbf{x}}$, $\psi_{L,\downarrow}(\mathbf{x},t) = \psi^{pu}_{L,\downarrow}(t)$, and $\psi_B(\mathbf{x},t) = \psi_B(t)\cdot e^{i\boldsymbol{k}_1\cdot\mathbf{x}}$ and define the probe and biexciton wave functions $\vec{u}$:

$$\vec{u}(t) = \left(\psi^{pr}_{L,\uparrow}(t), \psi_B(t)\right). \tag{6.33}$$

Using a matrix M_L^{+-} defined as

$$M_L^{+-} = \begin{pmatrix} \epsilon_{L,0} + g_{+-}X_{\mathbf{0}}^4|\psi^{pu}_{L,\downarrow}|^2 - i\gamma_L & g_{bx}X_{\mathbf{0}}^{*2}\psi^{pu*}_{L,\downarrow} \\ g_{bx}X_{\mathbf{0}}^2\psi^{pu}_{L,\downarrow} & \epsilon_B - i\gamma_B \end{pmatrix}, \tag{6.34}$$

the equation of motion for the vector $\vec{u}$ is given by

$$i\hbar\frac{d}{dt}\vec{u} = M_L^{+-}\vec{u} - \vec{F}^{pr}_{\uparrow}. \tag{6.35}$$

Differently from the pulse excitation in the previous section, here we consider the continuous-wave (CW) pump excitation resonant to the lower-polariton branch. Therefore, the pump excitations is expressed as

$$\psi^{pu}_{L,\downarrow} = |\psi^{pu}_{L,\downarrow}|e^{-i\epsilon_{L,0}\cdot t/\hbar}. \tag{6.36}$$

We assume that the system is probed with a CW probe beam with energy ϵ, which reads,

$$\vec{F}^{pr} = (1,0)\cdot e^{-i\epsilon\cdot t/\hbar}. \tag{6.37}$$

The steady state solutions is obtained analytically assuming the biexciton wave function as

$$\psi_B(t) = \psi_B(\epsilon)e^{-i(\epsilon+\epsilon_{L,0})t/\hbar}. \tag{6.38}$$

Substituting Eq. 6.36 and 6.37 in the equation of motion Eq. 6.34, thus replacing $\psi^{pu}_{L,\downarrow}$ and $\psi^{pu*}_{L,\downarrow}$ with $|\psi^{pu}_{L,\downarrow}|$ in the matrix M^{+-}, the steady-state solution of the probe lower-polariton is obtained as

$$\psi^{pr}_{L,\uparrow}(\epsilon) = \begin{pmatrix} 1 & 0 \end{pmatrix}\left[M_L^{+-} - \begin{pmatrix} \epsilon & 0 \\ 0 & \epsilon_{L,0}+\epsilon \end{pmatrix}\right]^{-1}\begin{pmatrix} 1 \\ 0 \end{pmatrix}. \tag{6.39}$$

Finally, the analytic solution of $\psi^{pr}_{lp\uparrow}(\epsilon)$ reads[2],

$$\psi^{pr}_{L,\uparrow}(\epsilon) = \left[\epsilon_{L,0} - \epsilon \; + \; g_{+-}X_{\mathbf{0}}^4|\psi^{pu}_{L,\downarrow}|^2 - i\gamma_L - \frac{g_{bx}^2X_{\mathbf{0}}^4|\psi^{pu}_{L,\downarrow}|^2}{\epsilon_B - \epsilon_{L,0} - \epsilon - i\gamma_B}\right]^{-1}. \tag{6.40}$$

This spectrum shows two-mode solution in the high density polariton regime. Assuming a weak exciton-biexciton coupling and a low pump excitation density: $g_{bx}|\psi^{pu}_{L,\downarrow}| < \gamma_B$, the two-mode solutions of $\psi^{pr}_{L,\uparrow}(\epsilon)$ might be approximated by a single solution. Indeed, substituting

---

[2] A similar formula has been obtained with Green functions approach in [81]

$\epsilon = \epsilon_{L,0}$ and taking the real-part of Eq. (6.40), the pump induced energy shift ΔE_{+-} can be approximated as

$$\Delta E_{+-} \simeq g_{+-} X_{\mathbf{0}}^4 |\psi_{L,\downarrow}^{pu}|^2 - \frac{g_{bx}^2 X_{\mathbf{0}}^4 |\psi_{L,\downarrow}^{pu}|^2 (\epsilon_B - 2\epsilon_{L,0})}{(\epsilon_B - 2\epsilon_{L,0})^2 + \gamma_B^2}. \tag{6.41}$$

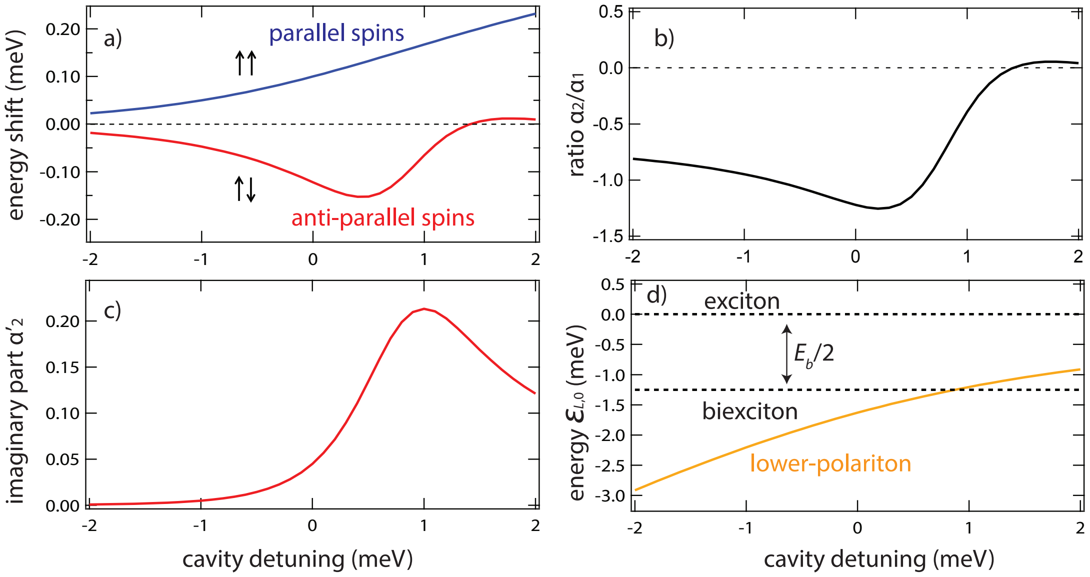

Figure 6.7: The energy shift ΔE_{++} (blue) and ΔE_{+-} (red) respectively obtained in Eqs. (6.31) and (6.41) as a function of the cavity detuning for the pump polariton density $|\psi_{lp,\downarrow}|^2 = 0.2$ (a). The ratio α_2/α_1 as a function of the cavity detuning (b). The imaginary part of the interaction constant with anti-parallel spins is shown as $\alpha_2'|\psi_{lp}|^2$ (c). The lower polariton energy $\epsilon_{L,0}$ as a function of the cavity detuning and the biexciton energy (d).

Since the lower-polariton interaction constant with anti-parallel spins α_2 is defined as $\Delta E_{+-} = \alpha_2|\psi_{L,\downarrow}|^2$, removing the pump polariton density $|\psi_{L,\downarrow}^{pu}|^2$, the lower polariton interaction with anti-parallel spins is defined as,

$$\alpha_2 \simeq g_{+-} X_{\mathbf{0}}^4 - \frac{g_{bx}^2 X_{\mathbf{0}}^4 (\epsilon_B - 2\epsilon_{L,0})}{(\epsilon_B - 2\epsilon_{L,0})^2 + \gamma_B^2}. \tag{6.42}$$

There are two terms that contribute to the energy shift in Eq. 6.42. The first term is a contribution from the background interaction g_{+-}, which is a non resonant scattering term. The constant g_{+-} is negative as we shall see in the next section. The second term represents the scattering resonance via the biexciton state. This term can be both negative and positive depending on the energy of the lower-polariton with respect to that of biexciton.

Now it is interesting to obtain the imaginary part of Eq. 6.40 and to define the imaginary interaction constant α'_2 as

$$\alpha'_2 \simeq \frac{g_{bx}^2 X_{\mathbf{0}}^4 \gamma_B^2}{(\epsilon_B - 2\epsilon_{L,0})^2 + \gamma_B^2}. \tag{6.43}$$

While the real part α_2 contributes to the energy shift, the imaginary part α'_2 is associated with the decay of the lower polariton due to the biexciton creation. Since the α'_2 has a Lorentzian profile, the biexciton decay rate represents the width of the resonant scattering. The interaction constants Eq. 6.42 and 6.43 has a strong similarity to the expressions for optical Feshbach resonance in cold atoms [89].

Substituting the parameters extracted experimentally in the previous section, Fig. 6.7 (a) presents the energy shift of the lower-polariton for co- (Eq. 6.31) and counter-circularly polarization (Eq. 6.41) configuration and for the pump polariton density $|\psi_{lp}|^2 = 0.2$. The ratio α_2/α_1 is displayed in Fig. 6.7 (b). The imaginary part of the interaction constant with anti-parallel spins is shown in Fig. 6.7 (c) as $\alpha'_2|\psi_{lp}|^2$. For the co-circularly polarization configuration, the energy shift ΔE_{++} increases monotonously following $X_{\mathbf{0}}^4$. For the counter-circular polarization configuration, the energy shift ΔE_{+-} displays a change of sign and amplitude when the energy of two lower-polaritons crosses the biexciton energy, while the damping represented by α'_2 shows a maximum at the crossing point[55] (See Fig. 6.7 (c) and (d)). Both are the signature of the scattering resonance. The plot of the ratio α_2/α_1 shows that α_2/α_1 progressively increases until the resonance and $|\alpha_2|$ becomes comparable to α_1 as reported by [75]. After the resonance, the ratio decreases suddenly and reaches a slightly positive value. All these features are detailed in the next section when we demonstrate the polaritonic Feshbach resonance.

6.6 Polariton Feshbach resonance

6.6.1 Concept of Feshbach resonance

In this section, focusing on the counter-circular polarization configuration, we experimentally investigate the resonance in the polariton scattering via the biexciton (polaritonic Feshbach resonance) in detail. A Feshbach resonance is a scattering resoance which occurs when the energy of two free particles reaches that of a molecular bound state [83]. In the vicinity of the resonance, the interaction strength of the two interacting particles dramatically changes. In cold atoms the Feshbach resonance is an essential tool to control the atom-atom interactions. It is even possible to switch the sign of atomic interactions from repulsive to attractive. For example, the instability and explosion of Bose-Einstein condensates have been realized with an attractively interacting Bose gas [90]. Moreover, in degenerate fermionic cold atomic gases, the BEC-BCS crossover has been observed by tuning the atomic interaction from repulsive to attractive [91]. Here we demonstrate the existence of the Feshbach resonance in polariton spinor interactions. It is characterized by the enhanced decay and the change of polariton interaction: the enhancement of attractive interactions and the change to repulsive interaction [55][3]. As shown schematically in Fig. 6.8, the resonance is induced by tuning the energy of two polaritons with opposite spins across the biexciton bound state energy. For the analysis, we employ a mean field two-channel model. The polaritonic Feshbach resonance can be used as a new tool to tune the spin anisotropic polariton interactions.

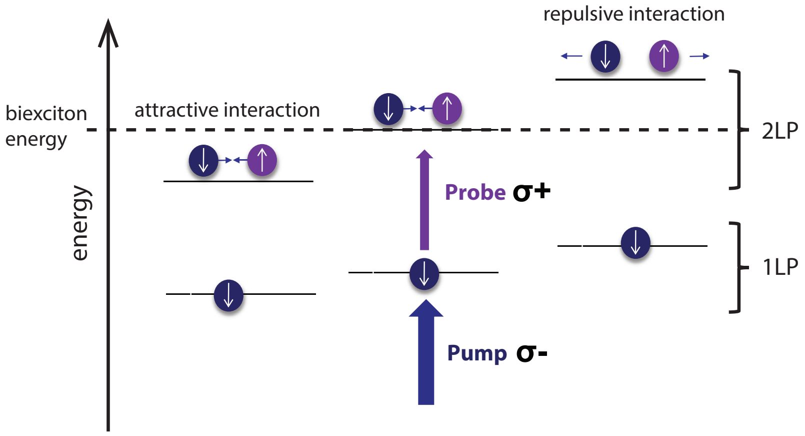

Figure 6.8: Schematics of the pump-probe experiment inducing the polaritonic Feshbach resonance. A large portion of polaritons with spin-down (blue) is created by the pump pulse, then the probe introduces small portion of spin-up polaritons (violet) which interact with the spin-down polaritons. The relative energy position with respect to the biexciton state determines the sign of interactions: attractive (below the biexciton energy) or repulsive (above the biexciton energy).

---

[3] Recently, the signature of the polaritonic Feshbach resonance is reported with two-dimensional Fourier transform spectroscopy [92]

Firstly, let us recall the Hamiltonian representing the coupling between the lower-polariton and biexciton used in the previous section (Eq. 6.26):

$$\sum_{\sigma=\{\uparrow\downarrow\}} \int d\mathbf{x} \left[\frac{1}{2} g_{bx} X_{\mathbf{0}}^{2} (\hat{\boldsymbol{\psi}}_{B} \hat{\boldsymbol{\psi}}^{\dagger}_{L,\sigma} \hat{\boldsymbol{\psi}}^{\dagger}_{L,-\sigma} + \hat{\boldsymbol{\psi}}_{L,\sigma} \hat{\boldsymbol{\psi}}_{L,-\sigma} \hat{\boldsymbol{\psi}}^{\dagger}_{B})\right], \tag{6.44}$$

This term is schematically represented in Fig 6.9 (a). Differently from the exciton-biexciton coupling, the energy difference between the lower-polariton and biexciton can be tuned by the cavity detuning (See Fig. 6.7 (d) and 6.8). When the energy of two lower-polaritons reaches the biexciton energy, the probability to form the biexciton increases.

(a) **Coupling between lower-polariton and biexciton: g_{bx}**

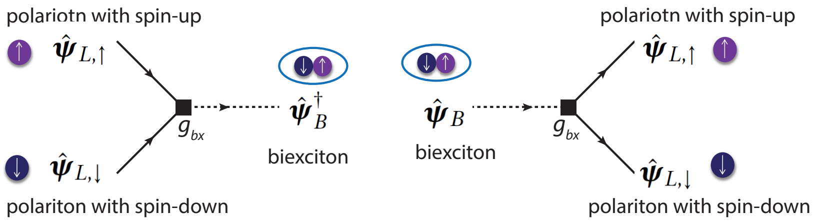
polariotn with spin-up
↑
$\hat{\psi}_{L,\uparrow}$
↓
$\hat{\psi}_{L,\downarrow}$
polariton with spin-down
g_{bx}
↓↑
$\hat{\psi}^{\dagger}_{B}$
biexciton
↓↑
$\hat{\psi}_{B}$
biexciton
g_{bx}
polariotn with spin-up
$\hat{\psi}_{L,\uparrow}$
↑
$\hat{\psi}_{L,\downarrow}$
↓
polariton with spin-down

(b) **Polaritonic Feshbach resonance**

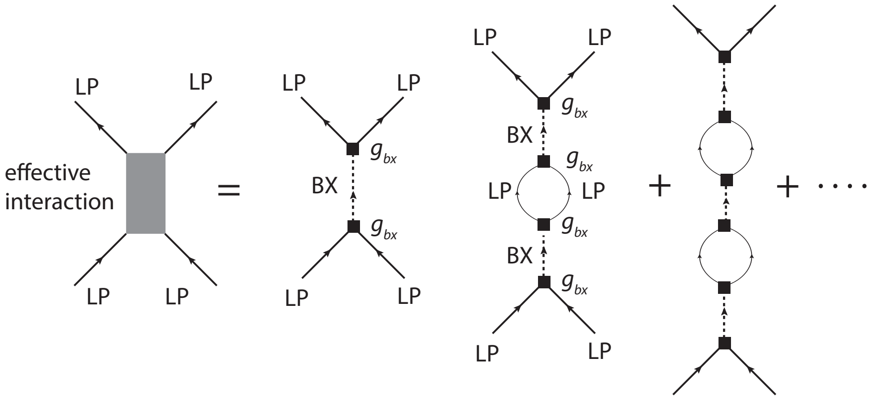
LP
LP
effective
interaction
LP
LP
=
LP
LP
g_{bx}
BX
g_{bx}
LP
LP
LP
LP
g_{bx}
BX
g_{bx}
LP
LP
g_{bx}
BX
g_{bx}
LP
LP
+
+ · · · ·

Figure 6.9: Schematic representation of the coupling between lower-polariton and biexciton (Eq. 6.44) (a) and the polaritonic Feshbach resonance. The term $g_{bx}X_{\mathbf{0}}^{2}$ in Eq. 6.44 couples two lower-polariton with anti-parallel spins to biexciton. When the energy of the lower-polariton is tuned to that of the biexciton, the resonance occurs. The effective scattering of the lower-polaritons is represented as a sum of all orders of processes, which include a biexciton creation, dissociations, and recombination [93].

In this vicinity, as shown in the schematic in Fig. 6.9 (b), two lower-polaritons combine into a biexciton, then the biexciton may dissociate into two lower-polaritons [93]. The scheme in Fig. 6.9 (b) includes higher order processes which include the recombinations and dissociations, which is the signature of a resonance. Finally, the processes depicted in Fig. 6.9 (b) contribute to the effective interaction of the lower polaritons. This effective interaction is represented by α_2 in Eq. 6.42. Additionally, since the biexciton has a finite lifetime and behaves as an additional decay channel, in the vicinity of the resonance the decay rate of the lower-polariton increases. This is described as α_2' in Eq. 6.43.

6.6.2 Measurements and model

We investigate both effects of the polaritonic Feshbach resonance with the same pump-probe spectroscopy method as in the previous sections. However, here we measure at zero pump-probe delay, both energy shift and change of the amplitude of the lower-polariton resonance as a function of the cavity detuning. In the following experiments, the spot of the pump beam is much larger than that of the probe, which allows for a homogeneous excitation of the probe region. The examples of pump-probe spectra are presented in Fig. 6.10. The spectra are obtained for low and high pump intensities in the vicinity of the biexciton resonance at the cavity detuning of δ=0.25 meV (See Fig. 6.7 (d)). We observe a red-shift of the lower-polariton resonance peak and a strong decrease of its amplitude in the transmitted probe spectra in the presence of the pump beam. The energy shift and the absorption of the probe spectrum are the signatures predicted respectively through the real and imaginary parts of the polariton interaction with opposite spins (Eq. 6.42 and 6.43). Additionally, a new small peak can be observed in the spectrum for the highest pump intensity (See Fig. 6.10 (b)). We associate this feature with the effect of strong polariton-biexciton coupling induced by the strong pump pulse.

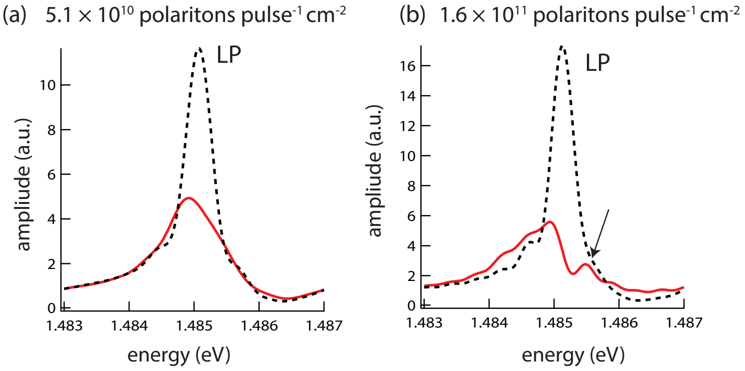

Figure 6.10: Probe spectrum with (red solid line) and without (black dashed line) the presence of pump beam for low pump (a) and high pump intensities (b). The low and high pump intensities are respectively 5.1×10^{10} and 1.6×10^{11} polariton pulse^{-1} cm^{-2}. The arrow in (b) indicates the appearance of a new resonance due to the strong coupling between lower-polariton and biexciton. The cavity detuning is δ=0.25 meV.

In Fig. 6.11, we show the energy shift and absorption changes of the main peaks of the probe spectra as a function of the cavity detuning. The pump polariton intensities are 5.1 × 10^{10} (a,b) and 1.6 × 10^{11} polariton pulse^{-1} cm^{-2} (c,d). The green region is an expected range where the energies of two-lower polaritons and biexciton overlap. We set the energy of biexciton 1.5 meV below the exciton energy [35]. Firstly in the low polariton density (Fig. 6.11 (a)), the energy shift clearly displays a dispersive shape, which is characteristic of the resonant scattering. Additionally, the result directly shows that the energy shift switches from redshift to blueshift at the resonance, which results from the modification of the interaction. Namely the sign of the polariton interaction switches from attractive to repulsive.

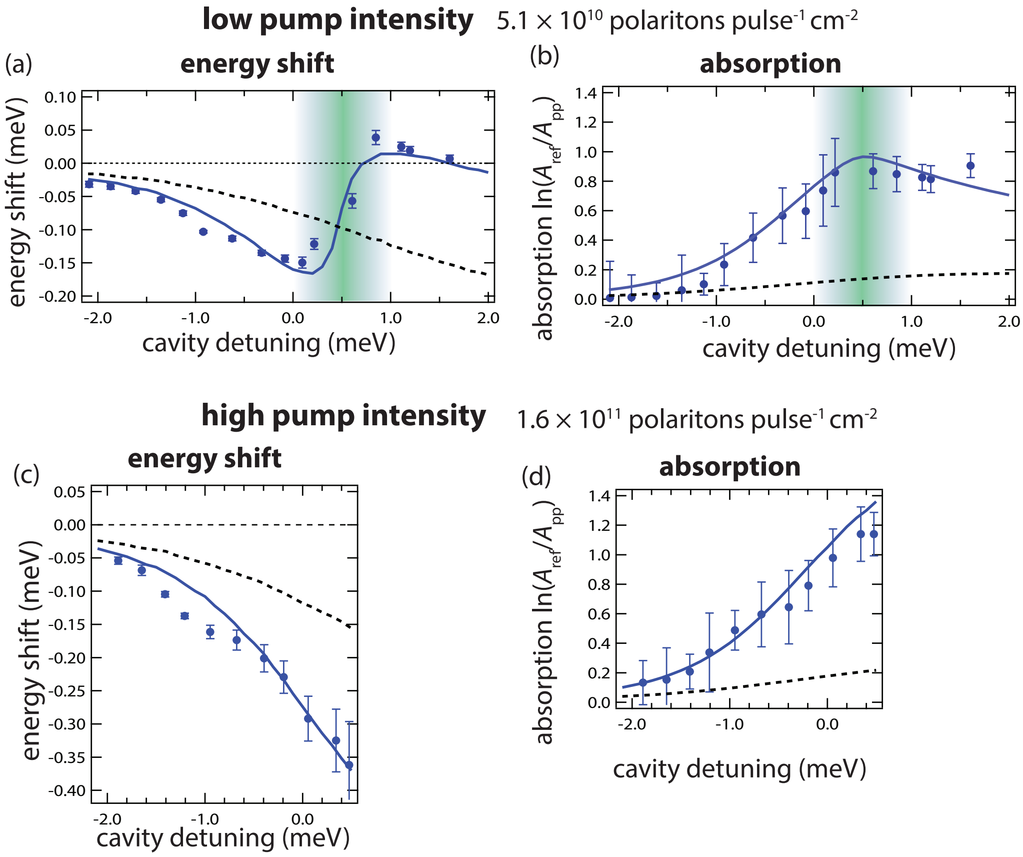

Figure 6.11: Energy shifts (a,c) and (b,d) absorption of the pump spectrum as a function of cavity detuning. The intensities of pump polaritons are 5.1 × 10^{10} (a,b) and 1.6 × 10^{11} polariton pulse^{-1} cm^{-2} (c,d). The blue circles are experimental results, solid lines and dashed lines are numerical simulations respectively with and without the biexciton effect. The green shaded areas represent the biexciton resonance vicinity (LP+LP→BX). For the numerical calculation, we use the following parameters. The biexciton energy is defined as $\epsilon_B = \epsilon_x - E_{\mathrm{bin}}/2$ and $E_{\mathrm{bin}} = 1.5$ meV. The biexciton linewidth is $\gamma_B = 1.1$ meV. The coupling between exciton and biexciton is set to $g_{bx} = 0.36\ \mathrm{meV}/\sqrt{n_0}$. The background interaction is $g_{+-} = -0.18\ \mathrm{meV}/\sqrt{n_0}$, where n_0 is the normalized density of spin-up polaritons. The other parameters are the photon linewidth $\gamma_c = 0.3$ meV, exciton linewidth $\gamma_x = 0.6$ meV. For the pump density, $n_p = n_0$ is used. n_0 is a normalization density.

Secondly, we present the absorption in Fig.6.11 (b). Here the absorption is defined as

$$\ln\left(\frac{A_{\mathrm{ref}}}{A_{\mathrm{pp}}}\right), \tag{6.45}$$

where A_{pp} and A_{ref} represent the amplitude of the lower-polariton resonance respectively with and without the pump pulse. With this definition, we can extract the absorption induced by the presence of the pump. Figure 6.11 (b) shows that the absorption increases and reaches a maximum at resonance. This is because at resonance, the biexciton formation from two polaritons with anti-parallel spins is enhanced. Since the biexciton has a short lifetime, the biexciton state works as an additonal decay channel and the increase of the biexciton formation is accompanied by the enhancement of the absorption. In the higher polariton density regime, as expected the redshift and the absorption are enhanced. This is displayed in Fig. 6.11 (c) and (d).

In order to analyse the observations, we calculate energy shift and absorption based on a mean-field two-channel model. For the simulation, we use the same Hamiltonian as the one used in the previous section, but here we employ the simplest non-dynamical approach. The effective Hamiltonian for the spin-up probe operators and the biexciton amplitude is given by:

$$\hat{H}_{\mathrm{eff}} = \begin{bmatrix} \hat{\psi}_{x,\uparrow} & \hat{\psi}_{c,\uparrow} & \hat{\psi}_{B} \end{bmatrix}^{\dagger} \begin{bmatrix} \epsilon_x + g_{+-} n_{x,\downarrow} - i\gamma_x & \Omega & g_{bx}\sqrt{n_{x,\downarrow}} \\ \Omega & \epsilon_c - i\gamma_c & 0 \\ g_{bx}\sqrt{n_{x,\downarrow}} & 0 & \epsilon_B - i\gamma_B \end{bmatrix} \begin{bmatrix} \hat{\psi}_{x,\uparrow} \\ \hat{\psi}_{c,\uparrow} \\ \hat{\psi}_{B} \end{bmatrix}, \tag{6.46}$$

where $n_{x,\uparrow}$ represents the density of the pump exciton assumed to be

$$n_{x,\uparrow} = \frac{n_p}{2}\left(1 + \frac{\delta}{\sqrt{\delta^2 + \Omega^2}}\right). \tag{6.47}$$

Finally, the probe spectrum $\psi_{c,\uparrow}^{\mathrm{probe}}(\epsilon)$ is calculated as

$$\psi_{c,\uparrow}^{\mathrm{probe}}(\epsilon) = \begin{pmatrix} 0 & 1 & 0 \end{pmatrix} \left[\frac{1}{H_{\mathrm{MF}} - \epsilon \cdot \mathbb{1}}\right] \begin{pmatrix} 0 \\ 1 \\ 0 \end{pmatrix}. \tag{6.48}$$

The matrix H_{MF} represents the 3×3 matrix in Eq. 6.46. The simulated energy shift and absorption changes are displayed in Fig. 6.11 as solid lines. On the other hand, the dashed lines are simulations with $g_{bx} = 0$, namely calculations considering only the background anti-parallel spins interaction. From the fit, this background interaction is found to be attractive $g_{+-} = -0.18$ meV$/\sqrt{n_0}$. Note that either with $g_{+-} = 0$ or $g_{+-} > 0$, we cannot fit the results [55]. The attractive background interaction with anti-parallel spins is used also in the dynamical simulation in the previous section. As we expect, we cannot reproduce the dispersive shape of the energy shift just with the background interaction. In order to fit the resonance, the exciton-biexciton coupling constant $g_{bx} = 0.36$ meV$/\sqrt{n_0}$ has to be introduced. Here, we comment that the small absorption exists only with the background interaction and it depends on the cavity detuning (See the dashed line in Fig. 6.11 (b) and (d)). This is due to the reduction of the photonic component of the polariton accompanied by the red-shift (in the other words, an effective increase of the cavity detuning), which is reported in [94]. However, the background interaction alone cannot reproduce the observed dispersive shape and the strong absorption.

In order to highlight the resonance due to the exciton-biexciton coupling, we plot energy shift and absorption ratios in Fig. 6.12. These ratios are calculated from the numerical plots in Fig. 6.11 (a) and (b). The interaction and absorption ratios are obtained dividing the total contribution (solid curve) by the background contribution (dashed curves). The two ratios show a familiar behavior of a scattering resonance. The interaction ratio (orange curve) has a dispersive shape and a large variation both in sign and in amplitude with respect to the resonance point. The profile of the absorption ratio (blue curve) also displays a typical enhancement of the absorption at the resonance associated with the two-body loss process of lower polaritons. A similar behaviour is reported for optical Feshbach resonance in ^{87}Rb condensate [89].

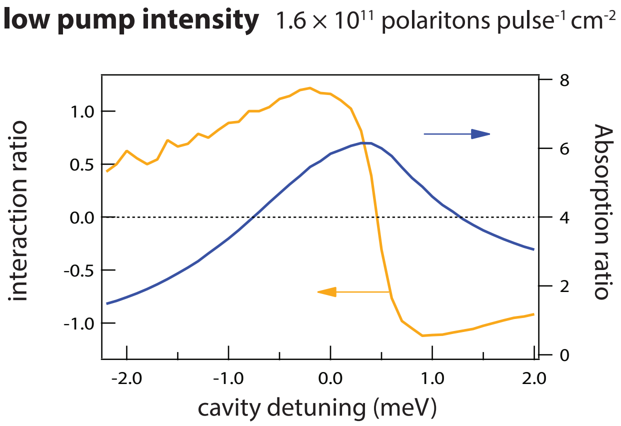

Figure 6.12: Interaction (orange line) and absorption (blue line) ratios as a function of the cavity detuning. The interaction and absorption ratios are the ratio between the solid (with $g_{bx} \neq 0$) and dashed ($g_{bx} = 0$) lines extracted respectively from Fig. 6.11 (a) and (b).

Secondly, let us focus on the coupling between polaritons and biexcitons in the matrix of the effective Hamiltonian (Eq. 6.46). The coupling term $g_{bx}\sqrt{n_x,\downarrow}$ depends not only on the constant g_{bx} but also on the excitonic population of polariton $\sqrt{n_x,\downarrow}$. At low pump power, the coupling term $g_{bx}\sqrt{n_x,\downarrow}$ is much smaller than the decay rate of the biexciton: $g_{bx}\sqrt{n_{x,\downarrow}} < \gamma_B$. Therefore, in this low density regime, the energy shift displays the smooth dispersive shape (See Fig. 6.11 (a)). Now, we are going to investigate the high pump density region. In Fig. 6.13, we plot as a function of the cavity detuning the two peaks (see Fig. 6.10 (b)) for the density of 1.6×10^{11} polariton pulse^{-1} cm^{-2} polaritons density. For the simulation, we extracted the second peak by setting $\gamma_B = 0$. Comparing the simulation and experiment, we associate the appearance of the two resonances as a “strong-coupling" between exciton and biexciton [35]. Since the biexciton coupling term depends on the pump polariton population as $g_{bx}\sqrt{n_{x,\downarrow}}$, in the high polariton density, the polariton-biexciton coupling becomes comparable to the linewidths of the involved states ($g_{bx}\sqrt{n_{x,\downarrow}} \sim \gamma_B$). Figure 6.13 might be interpreted as an “anti-crossing" between the lower-polariton and the biexciton resonance.

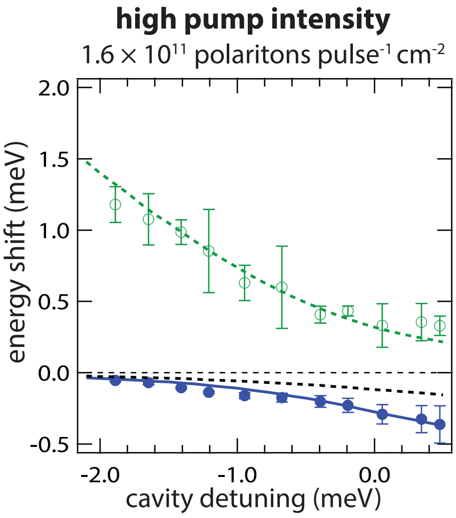

Figure 6.13: Energy shifts of the two peaks of the pump spectrum as a function of cavity detuning. The intensities of pump polaritons is 1.6×10^{11} polariton pulse^{-1} cm^{-2}. The filled and unfilled circles are experimental results of the double resonance (Shown in Fig. 6.10). Solid lines and dashed lines are numerical simulations respectively with and without the biexciton effect. For the pump density, $n_p = 2.44 n_0$ is used. n_0 is a normalization density.

Finally, we comment on the relation between the polaritonic Feshbach resoance and atomic Feshbach resonance. The Hamiltonian Eq. 6.44 is same as a two-channel model that describes atomic Feshbach resonances. The scheme and characteristic signature of Feshnach resonance in cold atoms is presented in Fig. 6.14. In the case of cold atoms, unbound atomic states and bound molecular state belong to different channels (spin states), thus the relative energy of the two states can be controlled by tuning the magnetic field (See Fig. 6.14 (a)). When the energy of the unbound atomic state coincides with that of the molecular bound state at the magnetic field B_0, the enhancement of the interaction (scattering length) and atomic loss are observed as signatures of the Feshbach resonance [83] (See Fig. 6.14 (b)). It is worth noting that the origin of the atomic loss is not the decay of molecule but a three-body loss associated with the increase of the scattering length, because the molecular state in cold atom has a very long lifetime. Additionally, the long lifetime of the molecular state leads to the sharp divergence of the atom-atom interaction (scattering length). This is a striking contrast with the polaritonic Feshbach resonance, where the short lifetime of the biexciton is the origin of the polariton decay at the resonance, thus the divergence of the interaction does not occur at resonance. Actually, this is more similar to the case of optical Feshbach resonance, where the optically excited molecular state has a finite life-time, thus the dominant mechanism of the atomic loss at the resonance point is the radiative decay of the molecular state [89] (Fig. 6.14 (c)).

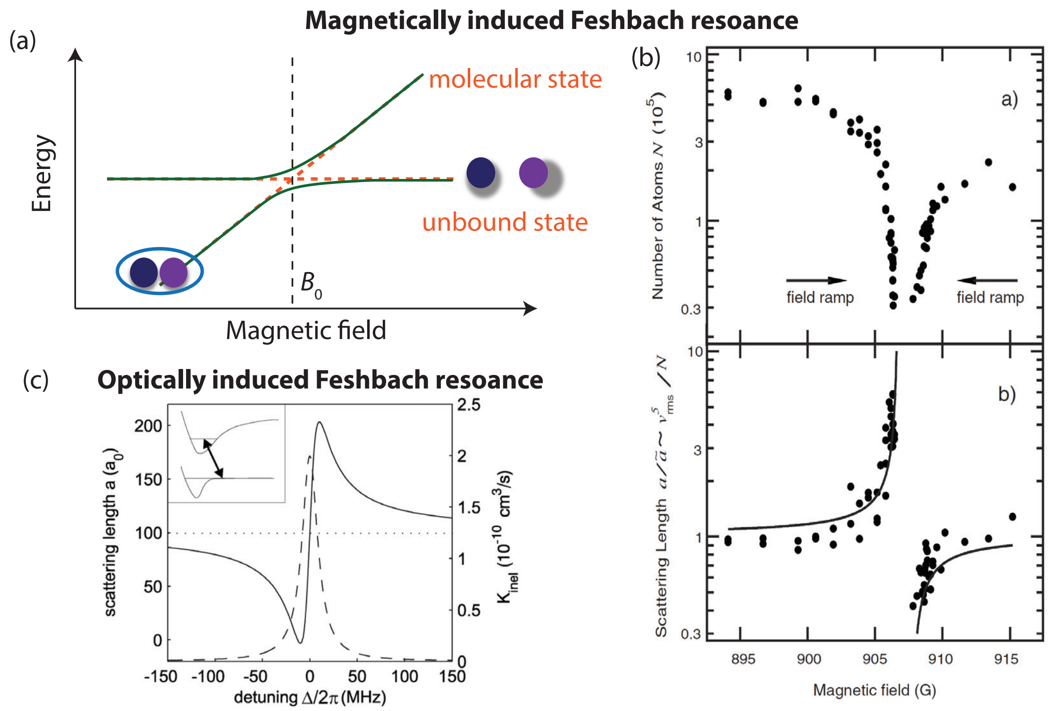

Figure 6.14: Scheme and experimental signature of a magnetically tuned Feshbach resonance (a) and (b) from [83]. The scattering length (solid line) and inelastic scattering rate (dashed line) of optically induced Feshbach resonance from [89] (c). The relative energy of the unbound atomic state and bound molecular state can be tuned by the Zeeman shift indyuced by the magnetic field (a). At the resonance, the enhanced three-body loss rate leads to the atomic loss. In the magnetically induced Feshbach resonance, the atom-atom interaction (scattering length) displays a divergence at the resonance. On the other hand, in the optical Feshbach resonance, the scattering length shows a smooth dispersive shape in the same way as in the polaritonic Feshbach resonance

6.6.3 delay dependence

Finally, in Fig. 6.15, we present the low pump intensity results with delays different from $\tau = 0$. Figure. 6.15 is the energy shift (left) and absorption (right) of the lower polariton resonance as a function of cavity detuning for different delays. The results are obtained at negative, zero, and positive delays: -3, -1.5, 0, 1.5, and 3 ps. The delay dependence of the energy shift and absorption strongly reflect the coherent and incoherent natures of the system (See also Chapter. 7). In the negative delay configuration (See Fig. 6.15 (a,b)), the pump pulse affects the probe signal only within the polariton coherence. Therefore, the delay dependence of the pump-probe signal in the negative delay configuration is proving the coherent aspect of the polaritonic Feshbach resonance. Actually, the shifts and absorption decreases with the increase of the negative delay, however the resonance feature is always present. In the negative delays, the polaritonic Feshbach resonance persists during the coherence time of the polariton system.

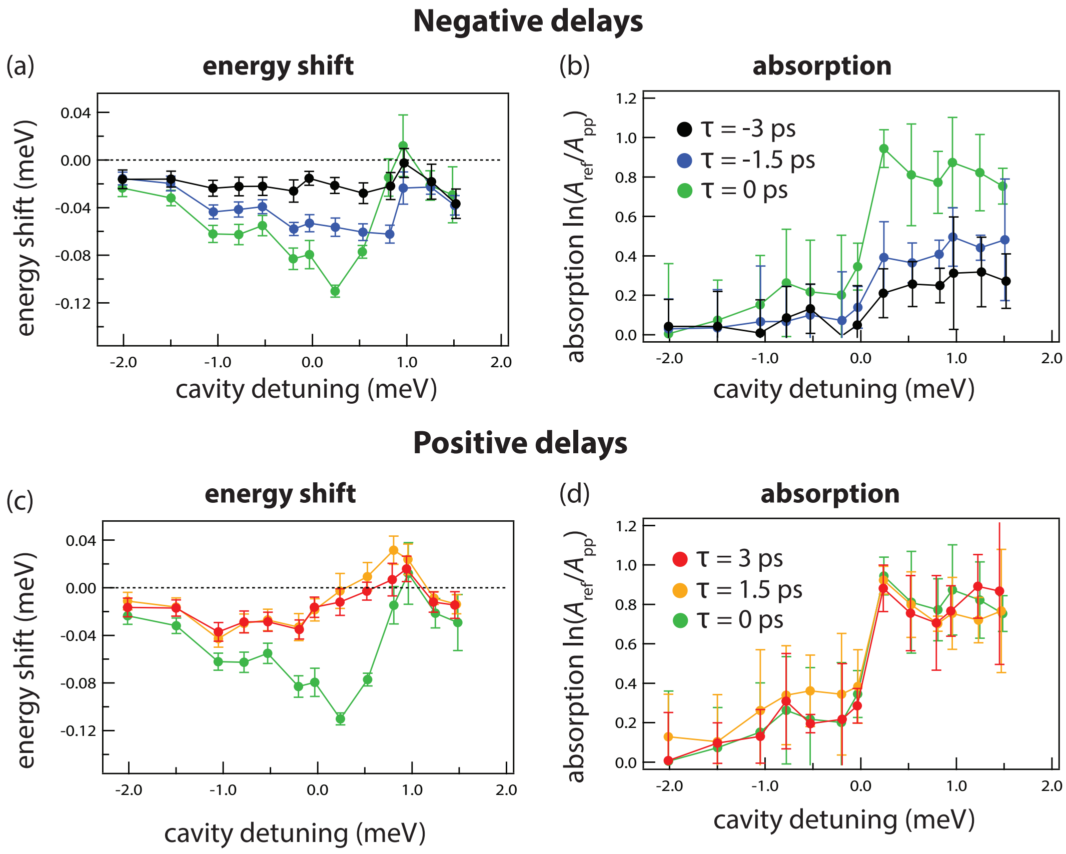

Figure 6.15: Energy shifts and absorption of the lower polariton resonance as a function of the cavity detuning for different pump-probe delays τ: $\tau = -3, -1.5, 0, 1.5$, and 3 ps. In the negative delay configuration (a,b), the energy shift and absorption gradually decreases as the increase of the delay, while in the positive delay configuration (c,d), only the absorption persists even at τ=3 ps due to a long living incoherent exciton population.

On the other hand, in the positive delay configuration (See Fig. 6.15 (c,d)), the pump pulse arrives first. The pump pulse creates not only the coherent exciton (exciton polarization) but also incoherent exciton population. Since the incoherent exciton population is decoupled from the light field, it has a long lifetime (>50 ps). The pump-probe signal, therefore, exists even if the system loses its coherence. Thus, at positive delays, the pump-probe signal exhibit features related to both coherent and incoherent effects [35]. Namely, with the increase of the positive pump-probe delay, the resonance feature of the energy shift disappears due to the loss of the exciton coherence, while the absorption persists due to the presence of incoherent exciton population.

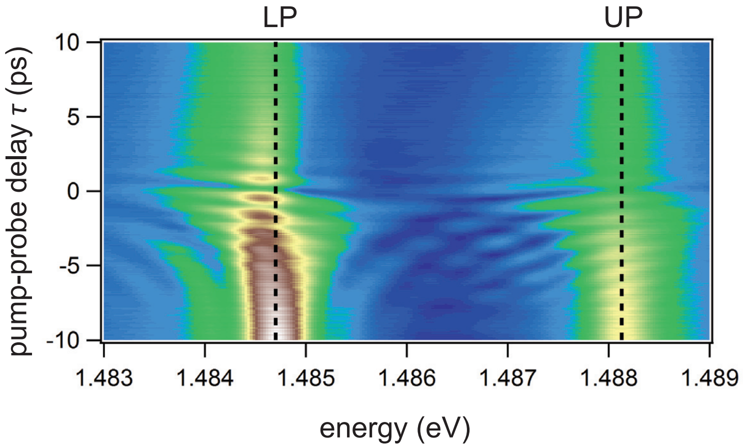

Figure 6.16: Experimental probe transmission spectrum as a function of energy and time delay between pump and probe pulse. The cavity detuning is set at $\delta = -0.5$ meV. The pump pulse intensity is 5.9×10^{13} photons pulse^{-1} cm^{-2}. The black dashed lines are the lower and upper-polariton peak energies without pump pulse. The experimental configuration is same as that in Fig. 6.4.

Finally, we display in Fig. 6.16 the amplitude of the probe spectrum as a function of the pump-probe delay τ at the cavity detuning $\delta = -0.5$ meV. Figure 6.16 clearly presents that the redshift and absorption remains for long delay time in the positive pump-probe delays. On the other hand, at negative delays, the redshift and absorption decrease with the increase of the delay, which is the expected behaviour in the coherent limit model. In order to simulate the probe behaviour in the positive delay, we need to include the incoherent population effect of excitons. Actually, by neglecting the coherent exciton, a sophisticated theory presented in [35] succeeded in modelling the transition between incoherent exciton population and biexciton in a long positive pump-probe delay. However, unfortunately, the theory that models both coherent and incoherent exciton effects on biexcitons is not yet known. In Chapter 8, we will discuss the possibility of the general theory which can include the two effects.

6.7 Conclusion

In conclusion, we have performed pump-probe spectroscopy with co and counter-circular polarization configuration in order to investigate the spinor polariton interactions. From the energy shifts of the probe spectra induced by the pump, we clearly find the polarization dependence of the polariotn interactions: the interactions are repulsive or attractive respectively for parallel or anti-parallel spins. Additionally, we have investigated the important role of the molecular bound state of excitons (biexciton) on the lower-polariton interaction with the opposite spins. We found a dispersive shape of the energy-shift and an enhancement of the absorption of the probe spectra with the counter-circular polarization configuration. These behaviour can be associated with a scattering resonance of the lower-polaritons via the biexciton (polaritonic Feshbach resonance). For the analysis, a spin-dependent Hamiltonian including the coupling between excitons and biexciton has been employed. Finally, we briefly discussed the effect of incoherent exciton on the spinor polariton interactions. In the next chapter, we will investigate more deeply the incoherent exciton in the co-circular polarization configuration. In this chapter, both pump and probe pulse are exciting the lower and upper polariton branches and the coherent limit approximation is assumed in the modelling. In the last chapter, we will discuss the new experiments with a narrow band pump pulse and possibility of constructing a theoretical model including the incoherent exciton population effect.

7 Effect of dephasing in pump-probe spectroscopy

Until this chapter, we described the coherent dynamics of exciton-polaritons with Gross-Pitaevskii equations. In this chapter, we will now discuss the possible changes brought by an incoherent exciton population. To this aim, we perform pump-probe spectroscopy and analyse it in a theoretical framework called Excitonic Bloch equations (EBEs) [32, 95]. Actually, one of the important properties of a semiconductor system is the dephasing [96, 97, 98]. The study of dephasing, accompanied by decoherence, is important both for understanding the physics of exciton-polaritons and for designing semiconductor microcavity devices such as nonlinear optical devices and polariton-based qubits [99, 100]. Additionally, the effects of dephasing are interesting in terms of the microscopic understanding of the “excitonic reservoir" in polariton Bose-Einstein condensation. In order to model the polariton condensates under non-resonant excitation, Gross-Pitaevskii equation coupled to two excitonic reservoirs (active and inactive reservoir) are phenomenologically employed [101, 102]. Our findings are that, even when we excite the lower and upper polariton branch resonantly with a coherent laser source, the exciton-exciton interaction (more precisely excitation induced dephasing (EID)) convert the coherent exciton into an incoherent exciton population, which does not couple to light. Our experiment and analysis cast light on the link between the “inactive reservoir" and incoherent exciton population.

7.1 Experimental setup for pump-probe experiment

The experimental configuration is same as that of the pump-probe experiment presented in Chapter 6. As the scheme of Fig. 7.1 shows, the semiconductor microcavity is excited by two pulses k_2 and k_1. The broadband pump and probe pulses excite both lower and upper polariton branches. The center frequency of the pump and probe pulse is set at the middle of the two branches. Since the angle between k_2 and k_1 pulses is small, we consider $k_1 \simeq k_2 = 0$ μm^{-1} and neglect the effect of the polariton energy-momentum dispersion. In the same way as in Chapter 6, the k_2 and k_1 pulses are respectively referred to as “pump" and “probe" pulse. We select only the transmitted probe beam with a pinhole having a diameter of 3 μm and transfer this probe beam to the heterodyne detection part. Finally, with the heterodyne measurement system, we obtain the amplitude of the electric field as a function of the pump-probe delay $|E^{pr}(\epsilon,\tau)|$. Additionally, with the aid of a numerical low-pass filter, we remove the noise coming from the laser spectrum envelope. The important difference from Chapter 6 is that here we obtain the probe spectrum as a function of the pump-probe ($\tau = t_{k_2} - t_{k_1}$) pulse delay. In particular, the probe spectrum at positive delay, where the pump pulse arrives before the probe, provides us information on long-lived incoherent exciton population.

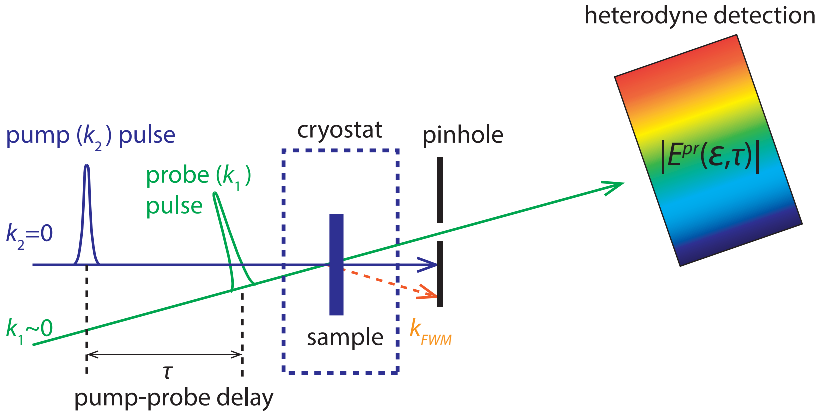
heterodyne detection
pump (k_2) pulse
cryostat
pinhole
probe (k_1) pulse
$|E^{pr}(\varepsilon,\tau)|$
k_2=0
k_1~0
sample
k_{FWM}
τ
pump-probe delay

Figure 7.1: Scheme of excitation configuration and pulse sequence for pump-probe experiments. The semiconductor microcavity sample is excited by two pulses: pump (k_2) and probe (k_1) pulse. Since the angle between the two beams is small, the wave vectors of the two beams are considered degenerate. With a pinhole, we spatially select the probe beam and analyse it with a heterodyne detection technique.

7.2 Excitonic Bloch equations (EBE)

In this section, we repeat the discussion on excitonic Bloch equations (EBEs) mentioned in Chapter 3 and explain it in detail. For the derivation of EBEs, we start from a Hamiltonian that fully includes the exciton-exciton interaction and photon-assisted exchange scattering (PAE) in the exciton-photon (local mode) basis (See Chapter. 3):

$$\hat{H} = \hat{H}_{\text{lin}} + \hat{H}_{\text{int}} + \hat{H}_{\text{qm}}. \tag{7.1}$$

Firstly, the linear part $\hat{H}_{\text{lin}}$ representing the exciton-photon eigenmodes and the linear coupling is given by (Eq. 3.1)

$$\hat{H}_{\text{lin}} \;=\; \int d\mathbf{x}\left[\epsilon_x \hat{\boldsymbol{\psi}}_x^\dagger \hat{\boldsymbol{\psi}}_x + \hat{\boldsymbol{\psi}}_c^\dagger(\epsilon_c - \frac{\hbar^2\nabla^2}{2m_c})\hat{\boldsymbol{\psi}}_c + \Omega(\hat{\boldsymbol{\psi}}_c^\dagger \hat{\boldsymbol{\psi}}_x + \hat{\boldsymbol{\psi}}_x^\dagger \hat{\boldsymbol{\psi}}_c)\right]. \tag{7.2}$$

The energy-momentum dispersion of the exciton is neglected because of its large mass compared the polariton mass.

Secondly the interaction part $\hat{H}_{\text{int}}$ (Eq. 3.2) is

$$\hat{H}_{\text{int}} \;=\; \int d\mathbf{x}\left[\frac{1}{2} g \hat{\boldsymbol{\psi}}_x^\dagger \hat{\boldsymbol{\psi}}_x^\dagger \hat{\boldsymbol{\psi}}_x \hat{\boldsymbol{\psi}}_x - g_{\text{pae}}(\hat{\boldsymbol{\psi}}_c^\dagger \hat{\boldsymbol{\psi}}_x^\dagger \hat{\boldsymbol{\psi}}_x \hat{\boldsymbol{\psi}}_x + \hat{\boldsymbol{\psi}}_x^\dagger \hat{\boldsymbol{\psi}}_x^\dagger \hat{\boldsymbol{\psi}}_x \hat{\boldsymbol{\psi}}_c)\right] \tag{7.3}$$

The interaction constants g and g_{pae} respectively represent the exciton-exciton interaction and photon-assisted exchange interaction. Finally, the quasi-mode coupling between the cavity photon and classical electric field outside the cavity is written as (Eq. 3.3)

$$\hat{H}_{\text{qm}} = \int d\mathbf{x}\, \Omega_{qm}(\hat{\boldsymbol{\psi}}_c^\dagger \boldsymbol{F} + \boldsymbol{F}^* \hat{\boldsymbol{\psi}}_c). \tag{7.4}$$

Using the Heisenberg equations of motion formalism $i\hbar\frac{d}{dt}\hat{\boldsymbol{\psi}} = [\hat{\boldsymbol{\psi}}, \hat{H}]$, we obtain the equations of motion for the operators $\hat{\boldsymbol{\psi}}_x$, $\hat{\boldsymbol{\psi}}_x^\dagger \hat{\boldsymbol{\psi}}_x$, and $\hat{\boldsymbol{\psi}}_c$. We can easily find that the non-linear term $\hat{H}_{\text{int}}$ causes a “hierarchy" problem. For example, the time evolution of operator $\hat{\boldsymbol{\psi}}_x$ is determined by the terms such as $\hat{\boldsymbol{\psi}}_x^{\dagger\prime}\hat{\boldsymbol{\psi}}'_x\hat{\boldsymbol{\psi}}_x$, then the time evolution of $\langle\hat{\boldsymbol{\psi}}_x^{\dagger\prime}\hat{\boldsymbol{\psi}}'_x\hat{\boldsymbol{\psi}}_x\rangle$ is determined by the next order term, and this goes on to an infinite order. Therefore, we need to truncate the hierarchy by assuming some sort of factorization. The simplest one is to use a coherent state (coherent limit), where the expectation value $\langle\hat{\boldsymbol{\psi}}_x^{\dagger\prime}\hat{\boldsymbol{\psi}}'_x\hat{\boldsymbol{\psi}}_x\rangle$ is simply factorized as $\langle\hat{\boldsymbol{\psi}}_x^{\dagger\prime}\hat{\boldsymbol{\psi}}'_x\hat{\boldsymbol{\psi}}_x\rangle = \langle\hat{\boldsymbol{\psi}}_x^{\dagger\prime}\rangle\langle\hat{\boldsymbol{\psi}}'_x\rangle\langle\hat{\boldsymbol{\psi}}_x\rangle$. As we have seen in previous chapters, this factorization is assumed in the derivation of the Gross-Pitaevskii equations. In this section, in order to describe the incoherent population of excitons, we have to write the expectation value of the exciton population as $\langle\hat{\boldsymbol{\psi}}_x^\dagger\hat{\boldsymbol{\psi}}_x\hat{\boldsymbol{\psi}}_x\rangle \simeq \langle\hat{\boldsymbol{\psi}}_x^\dagger\hat{\boldsymbol{\psi}}_x\rangle\langle\hat{\boldsymbol{\psi}}_x\rangle$, $\langle\hat{\boldsymbol{\psi}}_x^{\dagger\prime}\hat{\boldsymbol{\psi}}'_x\hat{\boldsymbol{\psi}}_x\rangle \simeq \langle\hat{\boldsymbol{\psi}}_x^{\dagger\prime}\hat{\boldsymbol{\psi}}'_x\rangle\langle\hat{\boldsymbol{\psi}}_x\rangle$, $\langle\hat{\boldsymbol{\psi}}_x\hat{\boldsymbol{\psi}}_x\rangle = 0$, and $\langle\hat{\boldsymbol{\psi}}_x^\dagger\hat{\boldsymbol{\psi}}'_x\hat{\boldsymbol{\psi}}'_x\rangle \simeq \langle\hat{\boldsymbol{\psi}}_x^\dagger\rangle\langle\hat{\boldsymbol{\psi}}'_x\hat{\boldsymbol{\psi}}'_x\rangle = 0$[1]. The last two parts are the assumption that “two-exciton state" does not exist. Finally, we obtain equations of motion for exciton polarization $P(\mathbf{x},t) = \langle \hat{\boldsymbol{\psi}}_x \rangle$, exciton population $N(\mathbf{x},t) = \langle \hat{\boldsymbol{\psi}}_x^\dagger \hat{\boldsymbol{\psi}}_x \rangle$ and cavity photon field $E(\mathbf{x},t) = \langle \hat{\boldsymbol{\psi}}_c \rangle$ [32]. This leads to the excitonic Bloch equations (BE):

---

[1] When deriving the equation of motion for $N(\mathbf{x}, t)$, we apply the factorizations $\langle\hat{\boldsymbol{\psi}}_x^{\dagger\prime}\hat{\boldsymbol{\psi}}'_x\hat{\boldsymbol{\psi}}_x\rangle \simeq \langle\hat{\boldsymbol{\psi}}_x^{\dagger\prime}\hat{\boldsymbol{\psi}}'_x\rangle\langle\hat{\boldsymbol{\psi}}_x\rangle$

$$
\begin{aligned}
i\hbar\dot{N} &= -i\Gamma_x N - 2i(\Omega - 2g_{\text{pae}}N)\text{Im}[PE^*] && (7.5)\\
i\hbar\dot{P} &= (\epsilon_x + g_0 N - i\gamma_x(N))P + (\Omega - 2g_{\text{pae}}N)E && (7.6)\\
i\hbar\dot{E} &= (\epsilon_c - \frac{\hbar^2}{2m_c}\nabla^2 - i\gamma_c)E + (\Omega - g_{\text{pae}}N)P - f_{\text{ext}}. && (7.7)
\end{aligned}
$$

The term $f_{ext}(= -\Omega_{qm}\boldsymbol{F})$ corresponds to the excitation by the external electric field. In EBEs, the exciton-exciton interaction constant g in Eq. 7.3 is phenomenologically divided into a real and imaginary part,

$$
g = g_0 + ig'. \qquad (7.8)
$$

The real part g_0 contributes to a population dependent energy shift, while the imaginary part g' is a population dependent damping of the polarization, which represents the strength of excitation induced dephasing (EID). Actually, the imaginary part g' exists in the decay term of the polarization $\gamma_x(N)$ as

$$
\gamma_x(N) = \Gamma_x/2 + \gamma_x^* + g'N. \qquad (7.9)
$$

Here, Γ_x is the decay rate of the exciton population (See Eq. 7.5), which could be called “life-time" Γ_x^{-1} of the exciton. γ_x^* represents a pure dephasing rate of exciton. The pure dephasing does not depend on the exciton population. If the pure dephasing would not exist ($\gamma_x^* = 0$) and the strength of EID would be zero ($g' = 0$), then the system would be in the coherent limit: $\gamma_x = \Gamma_x/2$. In this limit, the factorization $\langle \hat{\boldsymbol{\psi}}_x^\dagger \hat{\boldsymbol{\psi}}_x \rangle = \langle \hat{\boldsymbol{\psi}}_x^\dagger \rangle \langle \hat{\boldsymbol{\psi}}_x \rangle$ is satisfied and the EBEs are reduced to the conventional exciton-photon Gross-Pitaevskii equations:

$$
\begin{aligned}
i\hbar\dot{P} &= (\epsilon_x + g_0|P|^2 - i\Gamma_x/2)P + (\Omega - 2g_{\text{pae}}|P|^2)E && (7.10)\\
i\hbar\dot{E} &= (\epsilon_c - \frac{\hbar^2}{2m_c}\nabla^2 - i\gamma_c)E + (\Omega - g_{\text{pae}}|P|^2)P - f_{\text{ext}}. && (7.11)
\end{aligned}
$$

We can easily verify this factorization from the fact that $i\hbar\frac{d}{dt}|P|^2 = i\hbar(\dot{P}*P + P*\dot{P})$ has the same form as the equation of motion for the population Eq. 7.5 in the coherent limit $\gamma_x = \Gamma_x/2$. Consequently, it follows that, in the coherent limit, the dynamics of the population is uniquely determined by $N(\mathbf{x},t) = |P(\mathbf{x},t)|^2$. On the other hand, if there is pure dephasing or EID, the dynamics of the exciton population and polarization evolve independently, thus we need to follow the time evolution of both population and polarization with EBEs. It is worth noticing the similarity between the EBEs and modified optical Bloch equations (OBE).

---

and $\langle \hat{\boldsymbol{\psi}}_x^\dagger \hat{\boldsymbol{\psi}}'_x \hat{\boldsymbol{\psi}}'_x \rangle \simeq \langle \hat{\boldsymbol{\psi}}_x^\dagger \rangle \langle \hat{\boldsymbol{\psi}}'_x \hat{\boldsymbol{\psi}}'_x \rangle = 0$ before the spatial integral of the Hamiltonian $\hat{H}_{\text{int}}$.

The OBEs are used to describe the dynamics of a two-level system coupled to an electric field. The conventional OBEs include only saturation effect as a non-linearity, while several articles [62, 98] developed modified OBEs in order to describe interacting exciton system. The modified OBEs are given by

$$
\begin{aligned}
i\hbar\dot{N} &= -i\Gamma_x N - 2i\Omega \mathrm{Im}[PE^*] && (7.12)\\
i\hbar\dot{P} &= (\epsilon_x + g_0 N - i\gamma_x(N))P + \Omega(1-2N)E && (7.13)\\
i\hbar\dot{E} &= (\epsilon_c - \frac{\hbar^2}{2m_c}\nabla^2 - i\gamma_c)E + \Omega P - f_{\mathrm{ext}}. && (7.14)
\end{aligned}
$$

Like EBEs, the OBEs can calculate the incoherent and coherent part of two-level systems. This analogy indicates that Γ_x and γ_x respectively correspond to the inverse of the lifetime T_1 and the coherence time T_2 times. The difference between EBEs and OBEs is that OBEs are based on a two-level system, while EBEs are based on a bosonic exciton basis [32] with a fermionic correction through the term g_{pae}. Therefore, the saturation effect always exists in the OBEs, while in the EBEs we can turn it off by setting $g_{\mathrm{pae}} = 0$.

7.3 Experimental results and analysis based on EBE

7.3.1 Experimental results

In Fig. 7.2, we present the experimental probe spectra $|E^{pr}(\epsilon,\tau)|$ as a function of pump-probe time delay τ. The results are obtained at a cavity detuning of $\delta = \epsilon_c - \epsilon_x = 0.8$ meV. Firstly, let us discuss the low pump intensity result (Fig. 7.2 (a)). If we focus on the energy shift of the lower polariton branch, a maximum blueshift occurs at zero delay ($\tau = 0$ ps). The remarkable thing is that the delay dependence of the lower-polariton blue shift is asymmetric with respect to zero delay. The blueshift gradually decreases toward negative delays, while it stays almost constant at positive delays for long delay times. For high pump intensity, the spectra (Fig. 7.2 (c)) displays a triple peak structure at negative delays, while a single peak is found at positive delays. For the upper-polariton, we cannot find a clear energy shift for all delays for both low and high pump intensity regimes. The origin of this peak structure is addressed in the following sections. Secondly, the bleaching and broadening of both lower and upper polariton resonances are clearly visible (stronger effect on the upper polariton branch). Additionally, the bleaching becomes strong with the increase of the pump intensity. This polariton density dependent bleaching is a clear signature of the EID effect (See Eq. 7.9). Finally, we find that the delay dependent oscillation of the pump-probe spectra corresponds to quantum beats, which has the same origin as the delay dependent beat observed in four-wave mixing signals (See Chapter 5).

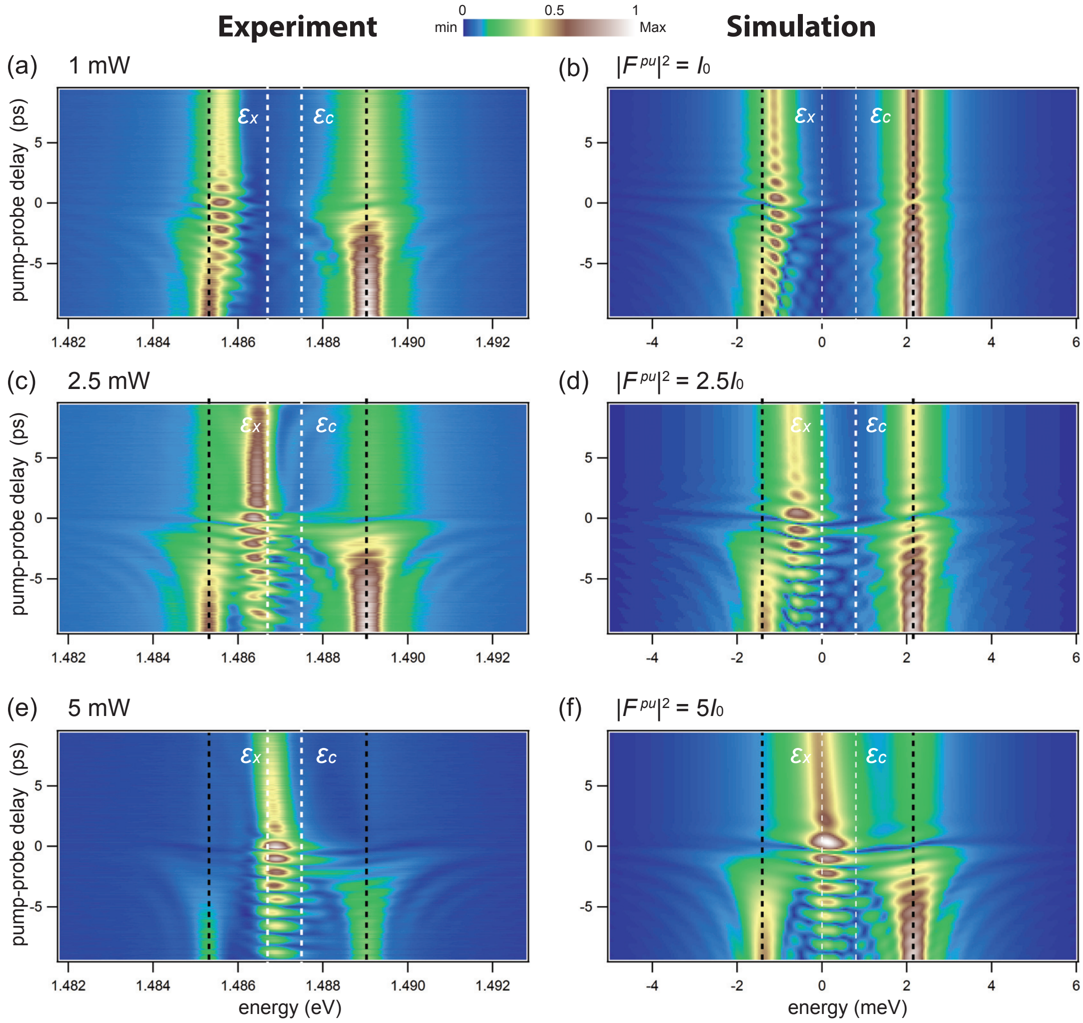

Figure 7.2: Experimental and simulated probe transmission spectra as a function of the time delay between pump and probe pulses. The experimental spectra are obtained for three different pump pulse intensities: 1.48×10^{13} (1 mW) (a), 3.7×10^{13} (2.5 mW) (b), and 7.4×10^{13} (5 mW) (c) photons pulse^{-1} cm^{-2}. Corresponding simulated spectra are attached next to the experiments: (b), (d), and (f). The black dashed lines are the lower and upper-polariton energies without pump pulse. In the simulation, the parameters are $g' = 0.4g_0$, $g_{\text{pae}} = 0.3g_0$, $\gamma_c = 0.1$ meV, $\gamma_x^* = 0.1$ meV and $\Gamma_x = 0.01$ meV. The white dashed lines represent the cavity photon (ϵ_c) and exciton (ϵ_x) energies. In the simulation, the intensity I_0 is defined as $I_0 = 0.8/g_0$.

7.3.2 Details of simulations

In Fig. 7.2, the numerical simulation of pump-probe spectra based on EBEs are need to be shown. Before, going into the comparison between experiments and simulation, we explain the detailed method of numerical simulation with EBEs. In order to calculate pump-probe spectra, we apply coupled-mode theory to EBEs. The coupled-mode theory is a standard approximation in the calculation of four-wave mixing [103, 104]. The main idea of the coupled-mode theory is to approximate the population, polarization and photon field as a combination of finite modes: pump ($\boldsymbol{k}_2 = 0$), probe ($\boldsymbol{k}_1$), and idler modes ($\boldsymbol{k}_{\mathrm{FWM}} = 2\boldsymbol{k}_2 - \boldsymbol{k}_1 = -\boldsymbol{k}_1$). Here, the "idler" is another name of the four-wave mixing signal. More specifically, we approximate the three components of EBEs as

$$\begin{aligned}
N(\mathbf{x},t) &= N^{pu}(t) + N^{pr}(t)\cdot e^{i\boldsymbol{k}_1\cdot\mathbf{x}} + N^{pr*}(t)\cdot e^{-i\boldsymbol{k}_1\cdot\mathbf{x}} \\
P(\mathbf{x},t) &= P^{pu}(t) + P^{pr}(t)\cdot e^{i\boldsymbol{k}_1\cdot\mathbf{x}} + P^{id}(t)\cdot e^{-i\boldsymbol{k}_1\cdot\mathbf{x}} \qquad (7.15)\\
E(\mathbf{x},t) &= E^{pu}(t) + E^{pr}(t)\cdot e^{i\boldsymbol{k}_1\cdot\mathbf{x}} + E^{id}(t)\cdot e^{-i\boldsymbol{k}_1\cdot\mathbf{x}}.
\end{aligned}$$

The indices pu, pr, and id respectively represent pump, probe, and idler (FWM) modes. For, the population, $N^{id} = N^{pr*}$ because the population $N(\mathbf{x},t) = \langle \hat{\boldsymbol{\psi}}_x^\dagger \hat{\boldsymbol{\psi}}_x \rangle$ must be a real value. Substituting Eq. 7.15 into EBEs in (Eq. 7.5, 7.6, and 7.7), we obtain eight coupled equations,

$$\begin{aligned}
i\hbar\dot{N}^{pu} &= -i\Gamma_x N^{pu} - \Omega a_{pu} + 2g_{\mathrm{pae}}(a_{pu}N^{pu} + b_{id}N^{pr} + b_{pr}N^{pr*}) \\
i\hbar\dot{N}^{pr} &= -i\Gamma_x N^{pr} - \Omega b_{pr} + 2g_{\mathrm{pae}}(b_{pr}N^{pu} + a_{pu}N^{pr} + cN^{pr*}) \\
\\
i\hbar\dot{P}^{pu} &= (\epsilon_x - i\gamma_x)P^{pu} + g(N^{pu}P^{pu} + N^{pr*}P^{pr} + N^{pr}P^{id}) \\
&\quad +\Omega E^{pu} - 2g_{\mathrm{pae}}(N^{pu}E^{pu} + N^{pr*}E^{pr} + N^{pr}E^{id}) \\
i\hbar\dot{P}^{pr} &= (\epsilon_x - i\gamma_x)P^{pr} + g(N^{pu}P^{pr} + N^{pr}P^{pu}) \\
&\quad +\Omega E^{pr} - 2g_{\mathrm{pae}}(N^{pu}E^{pr} + N^{pr}E^{pu}) \qquad (7.16)\\
i\hbar\dot{P}^{id} &= (\epsilon_x - i\gamma_x)P^{id} + g(N^{pu}P^{id} + N^{pr*}P^{pu}) \\
&\quad +\Omega E^{id} - 2g_{\mathrm{pae}}(N^{pu}E^{id} + N^{pr*}E^{pu}) \\
\\
i\hbar\dot{E}^{pu} &= (\epsilon_c - i\gamma_c)E^{pu} + \Omega P^{pu} - g_{\mathrm{pae}}(N^{pu}P^{pu} + N^{pr}P^{id} + N^{pr*}P^{pr}) - f_{\mathrm{ext}}^{pu} \\
i\hbar\dot{E}^{pr} &= (\epsilon_c - i\gamma_c)E^{pr} + \Omega P^{pr} - g_{\mathrm{pae}}(N^{pu}P^{pr} + N^{pr}P^{pu}) - f_{\mathrm{ext}}^{pr} \\
i\hbar\dot{E}^{id} &= (\epsilon_c - i\gamma_c)E^{id} + \Omega P^{id} - g_{\mathrm{pae}}(N^{pu}P^{id} + N^{pr*}P^{pu}).
\end{aligned}$$

Now the quantities a_{pu}, b_{pr}, b_{id} and c are given by

$$\begin{aligned}
a_{pu} &= 2i\mathrm{Im}(P^{pu}E^{pu*} + P^{pr}E^{pr*} + P^{id}E^{id*}) \\
b_{pr} &= P^{pu}E^{id*} - P^{id*}E^{pu} + P^{pr}E^{pu*} - P^{pu*}E^{pr} \\
b_{id} &= P^{pu}E^{pr*} - P^{pr*}E^{pu} + P^{id}E^{pu*} - P^{pu*}E^{id} \qquad (7.17)\\
c &= P^{pr}E^{id*} - P^{id*}E^{pr}.
\end{aligned}$$

In order to obtain the above equations, we neglected terms which have wave-vectors such as $e^{\pm i2\boldsymbol{k}_1\cdot\mathbf{x}}$ and $e^{\pm i3\boldsymbol{k}_1\cdot\mathbf{x}}$. Since the wave-vector $\boldsymbol{k}_1$ is sufficiently small, we also neglect the energy-momentum dispersion of the cavity photon energy ϵ_c. The pump and probe pulses are introduced from f^{pu} and f^{pr} as

$$f^{pu}(t) = F^{pu}\exp\left(-\frac{(t-t_{pu})^2}{\tau_{pu}^2}\right)\exp(-i\omega_{pu}t) \tag{7.18}$$

$$f^{pr}(t) = F^{pr}\exp\left(-\frac{(t-t_{pr})^2}{\tau_{pr}^2}\right)\exp(-i\omega_{pr}t). \tag{7.19}$$

In the numerical simulations a pulse width $\tau_{pu(pr)}$=0.5 ps is used. The center frequency of the laser is in the middle of the lower and upper polariton branches: $\omega_{pu(pr)} = (\epsilon_c + \epsilon_x)/2$. The probe spectrum $E^{\mathrm{pr}}(\epsilon)$ is obtained through the Fourier transformation of $E^{\mathrm{pr}}(t)$ with respect to t. For the numerical simulation, Γ_x and γ_c are respectively set as 0.01 meV and 0.1 meV. Note that the decay rate of the exciton population is much smaller than that of the cavity photon. The pure dephasing is set to $\gamma_x^* = 0.1$ meV [105]. The strength of EID and of the photon-assisted exchange scattering are respectively $g' = 0.4g_0$ and $g_{\mathrm{pae}} = 0.3g_0$.

7.3.3 Comparison between experiments and simulation

Let us now compare the experiments and simulations presented in Fig. 7.2. We find that there are striking similarity between the measured and simulated spectra.

low pump intensity

In the low pump intensity case (Fig. 7.2 (a) and (b)), both experiment and simulation displays a long lasting blue-shift of the lower-polariton at positive delay, on the other hand, the blue-shift builds up on a shorter time scale at negative delays. The decay rates used in the simulation suggest that the long lasting decay rate at positive delays is determined by $\sim \hbar/\Gamma_x$, while the short build time at negative delays is determined by $\sim 2\hbar/(\gamma_c + \gamma_x^*)$. As far as the energy shift of the upper-polariton is concerned, no shift is perceptible both in the experiment and simulation, this due to the cancellation of the blue and red-shift contributions induced by g_0 and g_{pae} respectively.

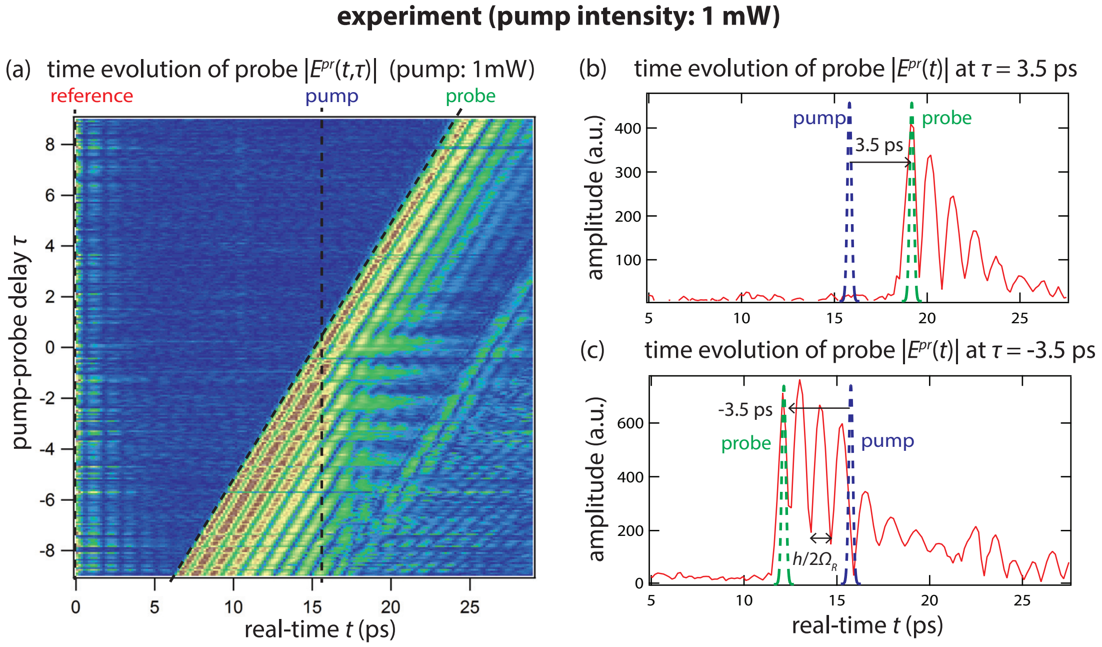

Figure 7.3: (a) The amplitude of the real-time evolution of the probe signal as a function of the pump-probe delay τ: $|E^{\text{pr}}(t,\tau)|$. The experiment is same as Fig. 7.2 (a). The time evolution of the probe at the positive pump-probe delay τ=3.5 ps (b) and negative pump-probe delay τ=-3.5 ps (c) are presented. The arrival times of pump, probe, and reference pulses are schematically represented by dashed lines. The revival of the signal 10 ps after the probe in (a) is due to the reflection of the pulse by the substrate of the sample. Similarly, in (c), the revival of the probe pulse at 22 ps is the reflected probe pulse. The real time evolution is obtained with the heterodyne measurement technique explained in Chapter 4.

Additionally, in Fig. 7.3 (a), we present the amplitude of the real-time evolution of the probe signal for a pump intensity of 1 mW. Figure 7.3 (b) and (c) are the real-time evolutions of the probe signal respectively at 3.5 ps and -3.5 ps delays. This real-time evolution is obtained through the heterodyne technique explained in Chapter 4. Notice that the period of the real-time oscillation of the probe signal before the arrival of the pump pule is $h/2\Omega_R$ (See Fig. 7.3 (c)). Since Ω_R is the Rabi coupling, this oscillation is a direct manifestation of the Rabi oscillation between an exciton and a photon. Even at 3.5 ps delay (See Fig. 7.3 (b)) we can find the real-time oscillation of the probe signal. This means that the incident of the weak intensity pump pulse creates a small polariton population and it modulates the oscillation period of the system, which is the origin of the blueshift, but the coherence is still surviving.

high pump intensity

When the pump intensity is increased, a new peak develops in the pump-probe spectra (Fig. 7.2 (c)-(f)). By increasing the pump power, the middle peak energy blue shifts (Fig. 7.2 (c,d)) and for the highest pump intensity (Fig. 7.2 (e,f)) both measurement and simulation present three peaks at negative delays and a single peak at positive delays.

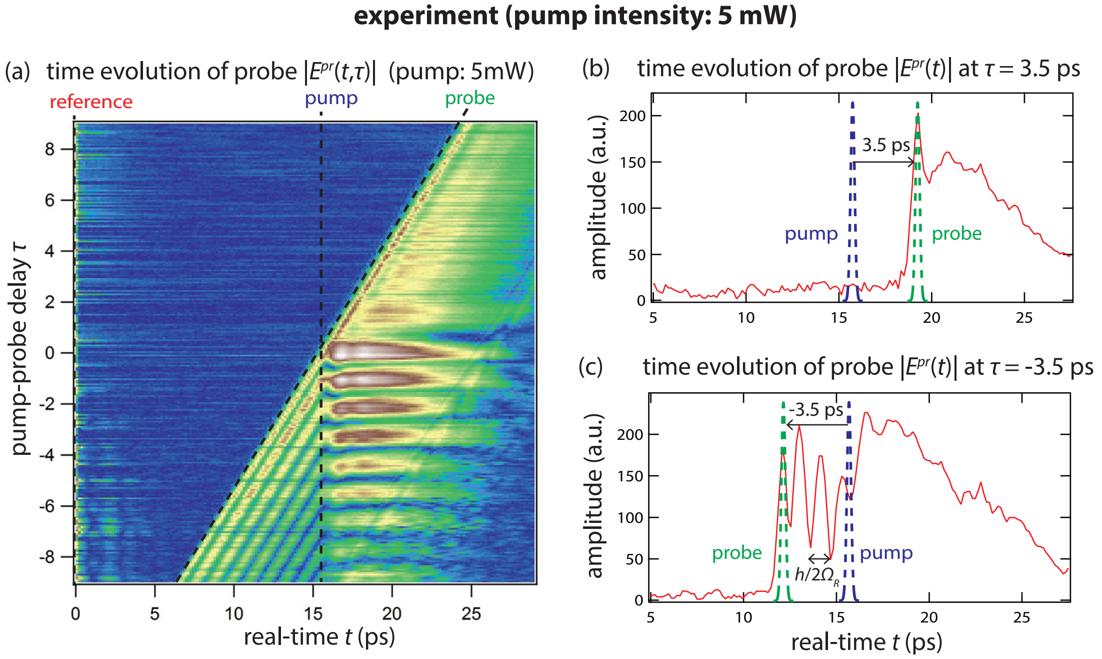

Figure 7.4: (a) The amplitude of the real-time evolution of the probe signal as a function of the pump-probe delay τ: $|E^{\mathrm{pr}}(t,\tau)|$. The experiment is same as Fig. 7.2 (e). The time evolution of the probe at the positive pump-probe delay τ=3.5 ps (b) and negative pump-probe delay τ=-3.5 ps (c) are presented. The arrival times of pump, probe, and reference pulses are schematically represented by dashed lines. The real-time evolution is obtained with the heterodyne measurement technique explained in Chapter 4.

In order to explain the complex behaviour of the probe signal in Fig. 7.2 (e-f), in Fig. 7.4 (a), we display the amplitude of the real-time evolution of the probe signal for the pump intensity of 5 mW. Figure 7.4 (b) and (c) display the real-time evolutions of the probe signal respectively at 3.5 ps and -3.5 ps delays. The three peaks at negative delays result from the temporal convolution of modulated and non modulated parts of the probe pulse (See Fig. 7.4 (c)). More precisely, the side peaks occur from the portion of the probe transmitted before the arrival of the pump pulse, while the middle peak is originated from the arrival of the pump pulse during the short lifetime of the probe polarization given by $\sim 2\hbar/(\gamma_c+\gamma_x^*)$. On the other hand, at positive delays the probe pulse is always modified by the strong pump pulse (See Fig. 7.4 (b)). Therefore, the blue-shift of the single middle peak stays for a long time, which is determined by the long lasting exciton population $\sim \hbar/\Gamma_x$.

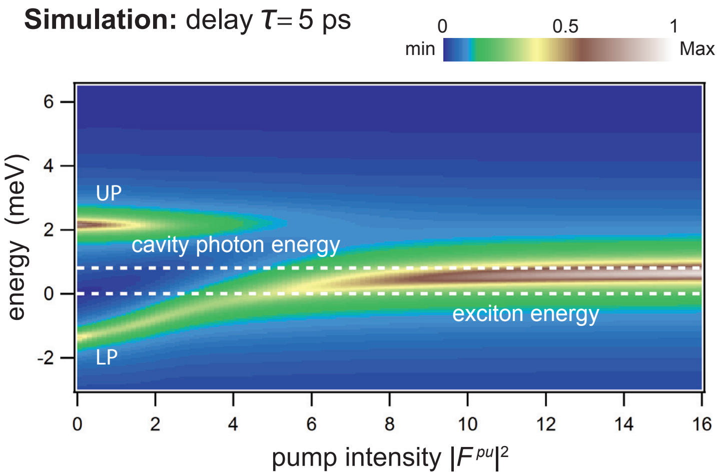

Figure 7.5: Simulated probe transmission at the pump-probe time delay τ=5 ps as a function of the pump intensity. The cavity detuning is $\delta = 0.8$ meV. The other parameters are the same as those employed in Fig. 7.2. The white dashed lines represent the cavity photon and exciton energies. As the pump intensity $|F^{pu}|^2$ increases, the lower polariton (LP) asymptotically reaches the cavity photon energy, while the upper polariton (UP) branch energy almost stays at the same position and gradually disappears due to the EID effect.

If the intensity of the pump increases further, since $\gamma_x(N)$ becomes comparable to the effective Rabi coupling $\Omega - 2g_{\text{gpae}}N$, the lower-polariton peak reaches the cavity mode, which is the signature of the strong to weak coupling transition [106]. To illustrate this transition, we present in Fig. 7.5 a simulated probe transmission spectrum at 5 ps pump-probe delay as a function of pump intensity. As the pump intensity increases, the lower polariton resonance shifts up in energy while the upper polariton resonance remains steady in energy and its intensity gradually vanishes due to the EID. In this simulation, not only g_{pae} and g', but also the exciton-exciton interaction g_0 assists the lower-polariton branch to reach the cavity mode.

Here, we would like to comment on the observation of the strong-to-weak coupling transition performed by F. Quochi *et al.* [106, 107]. In the pump-probe spectrum of a semiconductor microcavity, they observed that the polariton doublet collapses into a single branch, then it evolves into the AC stark triplet (also referred to as Mollow triplet) by increasing the pump intensity more than 40 times above the exciton saturation density. Actually, neither experimental spectrum nor theoretical prediction in Fig. 7.5 evidence the AC stark triplet. Why is the AC stark triplet not visible in our sample? Firstly, it is important to note that the semiconductor microcavity used in [106, 107] has parameters completely different from our sample. The semiconductor microcavity in [106, 107] has a larger Rabi splitting $2\Omega_R$=8 meV (six quantum wells) and a huge inhomogeneous broadening of 5.5 meV. In these parameters range, the system would behave more like bare quantum wells in the weak coupling regime [108]. Theoretically speaking, the striking difference between EBEs and OBEs might exist here. The AC stark triplet is a consequence of the Rabi flopping, which is a rotation of the Bloch vector between the north and south poles of the Bloch sphere [36]. Therefore, in order to reproduce the AC stark splitting, two-level system description would be necessary. Since EBEs are not based on two-level state model, EBEs cannot reproduce the AC stark triplet. Probably, in [106, 108], where the measurement are performed at very high pump intensity (more than 40 times above the exciton saturation density), an electron and a hole picture with two levels (valence band and conduction band) would be more suitable than the bosonic exciton model. Actually, the experimental observation of [106, 107, 108] are well reproduced with two-level like theoretical models, OBEs and semiconductor Bloch equations (SBEs).

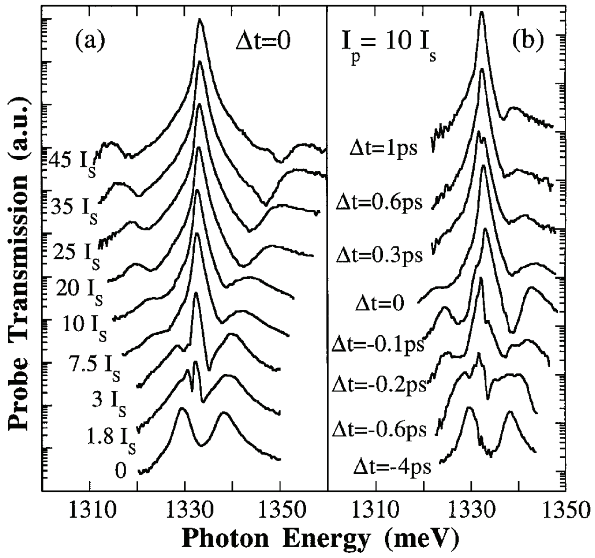

Figure 7.6: Probe transmission spectra for different pump intensities in semiconductor microcavity with six quantum wells from [106]. The lower and upper polariton doublet evolves into a single peak (the strong-to-weak coupling transition). When we make the pump intensity higher, two side peaks appear, which is the AC stark triplet (Mollow triplet)

7.4 The effect of dephasing

7.4.1 Pump-probe spectra in coherent limit

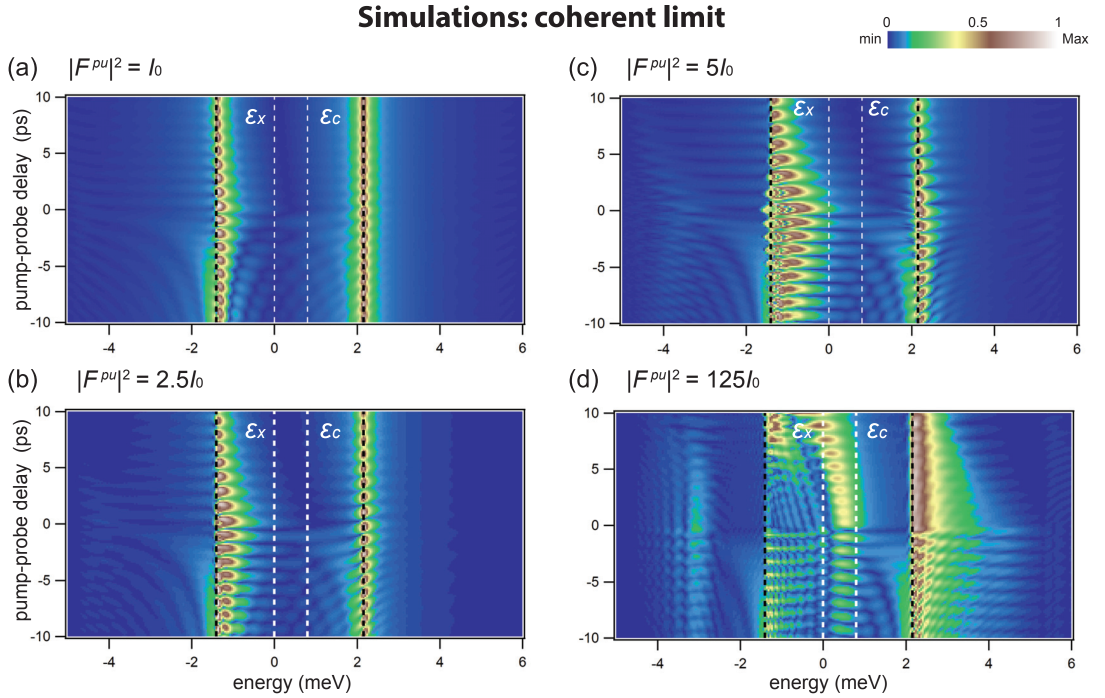

Figure 7.7: Simulated probe transmission as a function of energy and pump-probe time delay without EID and pure dephasing ($g' = \gamma_x^* = 0$ meV) for four different pump intensities: I_0 (a), $2.5I_0$ (b), $5I_0$ (c), and $125I_0$ (d). The first three intensities correspond to Fig. 7.2 (b), (d), and (f). The other parameters are the same as those used in the simulation of Fig. 7.2. (d) is a simulation with a very high pump power. This region is considered as a weak coupling regime, thus the lower polariton branch almost reaches the cavity mode. The signal around -3 meV might be the result of higher-order four-wave mixing processes.

In order to understand more deeply the effect of the incoherent exciton population and of EID on the two polariton resonances, we show simulations based on EBEs but without EID and pure dephasing ($g' = \gamma_x^* = 0$ meV) in Fig. 7.7. The other parameters are same as in Fig. 7.2. This configuration can be called coherent limit, thus the simulation in Fig. 7.7 is qualitatively same as that of GPEs. Namely, the decay of the population is twice faster than that of the polarization ($\gamma_x(N) = \Gamma_x/2 = 0.005$ meV). Roughly speaking, in pump-probe spectroscopy as a function of pump-probe delay, the energy-shit at positive and negative delays are respectively sensitive to the population (Γ_x) and polarization decay rate (γ_x). Therefore, in the coherent limit, the blue-shift decays twice faster at positive delays than negative delays (See Fig. 7.7). Additionally, we find that the polariton branch is broadened towards the high energy side. This is understood as a “dynamical energy-shift". Namely, the time integration of the temporal decrease of the energy-shift induces a broadening of the polariton branches. When comparing the simulations in Fig. 7.7 with experiments in Fig. 7.2, we clearly find that the experiments cannot be reproduced under the condition of coherent limit (GPE). Especially, in the high pump intensity simulation (Fig. 7.7 (b) and (c)), neither the three peaks structure nor the disappearance of the quantum beat at positive delays are reproduced because of the lack of EID. At very high pump intensity, the transition to weak coupling regime is also observed with the GPEs. However as the figure shows, a very strong dynamical blue-shift also exists, which is different from the observed experimental behaviour.

7.4.2 Dynamics of population and polarization

For the purpose of understanding the effects of dephasing, it is useful to present simulations of the real-time evolutions of the exciton population and polarization. Figure. 7.8 is the time evolutions of the polarization $|P(t)|^2$ and population $N(t)$ at $\boldsymbol{k} = 0$ μm^{-1} after the arrival of a single pump pulse. Simulation are performed with dephasing and without dephasing.

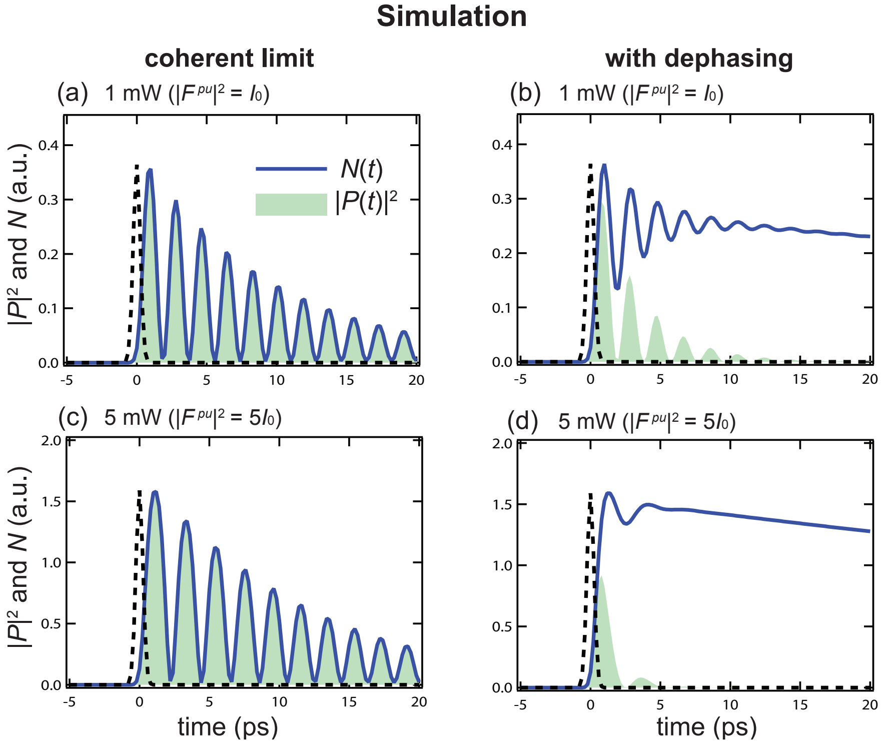

Figure 7.8: Simulated time evolution of the polarization $|P(t)|^2$ and population $N(t)$ at $\boldsymbol{k} = 0$ μm^{-1} as a function of time after an arrival of a single pulse. Simulations in a coherent limit ($g' = \gamma^* = 0$ meV) (a,c) and with dephasing (EID and pure dephasing) (b,d) are presented for two different laser pulse intensities 1 mW (a,b) and 5 mW (c,d). The parameters are the same as the simulation of Fig. 7.2. The dashed lines represent scaled laser pulses.

Firstly in the coherent limit (Fig. 7.8 (a) an (c)), the time evolution of the exciton population $N(t)$ coincides with that of $|P(t)|^2$. This is because the dynamics of the exciton population is uniquely determined as $N(\mathbf{x},t) = |P(\mathbf{x},t)|^2$ and the factorization $\langle\hat{\boldsymbol{\psi}}_x^\dagger\hat{\boldsymbol{\psi}}_x\rangle = \langle\hat{\boldsymbol{\psi}}_x^\dagger\rangle\langle\hat{\boldsymbol{\psi}}_x\rangle$ takes place. Therefore, in the coherent limit, the lifetime of the system is determined mainly by the cavity photon lifetime $\hbar/(\gamma_c+\gamma_x) \sim \hbar/\gamma_c$, because γ_c(=0.1 meV) is much larger than γ_x(=0.005 meV).

On the other hand, when pure dephasing and EID are introduced (See Fig. 7.8 (b) an (d))), temporal separation of time evolution of the population and polarization takes place. In particular, at high pump intensity (Fig. 7.8 (d)), the polarization decays fast due to EID ($\sim \hbar/(\gamma_c+\gamma_x(N)$), while the population lives for a long time ($\sim \hbar/\Gamma_x$). These results indicate that, with the existence of dephasing, the population can have a long lifetime because it is decoupled from the light field after the disappearance of the polarization.

7.5 Discussion

7.5.1 Dephasing mechanism

In this section, we discuss the origin of dephasing and comment about a link between the EBE model and exciton reservoir. Until now, we dealt with the dephasing as a phenomenological damping of the exciton polarization. Using the idea of Kubo's Brownian oscillator model [109, 61, 110], the dephasing mechanism might be explained more microscopically. As the name “dephase" indicates, the dephasing can be understood in terms of a phase fluctuation of the polarization. Let us consider that the polarization as a classical ensemble of single exciton wave-functions: $P(\mathbf{x},t) = \langle\psi_x(\mathbf{x},t)\rangle$. The wave-function may obey the following stochastic Gross-Pitaevskii equations (sGPE) [109].

$$\begin{aligned} i\hbar\dot{\psi}_x &= (\epsilon_x + \delta\epsilon(t) + g_0|\psi_x|^2 - i\Gamma_x/2)\psi_x + (\Omega - 2g_{\text{pae}}|\psi_x|^2)E && (7.20)\\ i\hbar\dot{E} &= (\epsilon_c - \frac{\hbar^2}{2m_c}\nabla^2 - i\gamma_c)E + (\Omega - g_{\text{pae}}|\psi_x|^2)\langle\psi_x\rangle - f_{\text{ext}}. && (7.21)\end{aligned}$$

Here, $\delta\epsilon(t)$ represents the energy fluctuations, which induce phase fluctuations. The energy fluctuations satisfy the following properties.

$$\begin{aligned} \langle\delta\epsilon(t)\rangle &= 0 && (7.22)\\ \langle\delta\epsilon(\tau)\delta\epsilon(0)\rangle &= M(\tau). && (7.23)\end{aligned}$$

$M(\tau)$ is a correlation function, which can depend on $|\psi_x|^2$. Let us note that the electric field is coupled to the polarization $P(\mathbf{x},t) = \langle\psi_x(\mathbf{x},t)\rangle$, which is an expectation value of the ensemble of the exciton wave function. Numerically solving the above equation is not easy and it is a future issue. Here, we use the stochastic equation for a qualitative explanation of the dephasing mechanism. In this stochastic theory, the most important thing is that the energy fluctuation $\delta\epsilon(t)$ introduces a random phase fluctuation to the wave-function such as $\psi_x(\mathbf{x},0)e^{-i(\epsilon_x+\delta\epsilon(t))t/\hbar}$, thus the polarization as an ensemble $P(\mathbf{x},t) = \langle\psi_x(\mathbf{x},t)\rangle$ decays. On the other hand, the population of the ensemble $N(\mathbf{x},t) = \langle\psi_x^*(\mathbf{x},t)\psi_x(\mathbf{x},t)\rangle$ does not suffer from the phase fluctuations, because the phase terms of $\psi_x(\mathbf{x},t)$ and $\psi_x^*(\mathbf{x},t)$ cancel with each other such that $e^{-i(\epsilon_x+\delta\epsilon(t))t/\hbar}\cdot e^{i(\epsilon_x+\delta\epsilon(t))t/\hbar} = 1$. Therefore, the ensemble population $N(\mathbf{x},t)$ is simply given by $N(\mathbf{x},t) = |\psi_x(\mathbf{x},t)|^2$. Two different origins can be considered for the energy fluctuation: the intrinsic one due to the environment and the exciton-exciton collision. The former one is associated with pure dephasing γ_x^*, while the latter one is associated with EID g'. This is why EID is also referred to as “collisional broadening". For the intrinsic energy fluctuation, various origins such as phonons, and impurities are possible [105].

7.5.2 Relation between EBE and two reservoirs model

Secondly, let us comment that the EBE model will cast a light to an understanding of excitonic reservoir in non-resonantly excited polariton condensates [101, 102]. Polariton condensates are well modelled by a Gross-Pitaevskii equation coupled with two reservoirs [111, 101, 112]:

$$\dot{n}_I = -\gamma_I n_I - \frac{1}{\tau_R} n_I + P \tag{7.24}$$

$$\dot{n}_A = -(\gamma_A + R_R|\psi_L|^2)n_A + \frac{1}{\tau_R} n_I \tag{7.25}$$

$$i\hbar\dot{\psi}_L = \left\{-\frac{\hbar^2}{2m}\nabla^2 + g_L|\psi_L|^2 + g_R n_A + g_R n_I - \frac{i}{2}[\gamma_L - R_R n_A]\right\}\psi_L, \tag{7.26}$$

where n_I and n_A are respectively the “inactive" and “active" excitonic reservoirs. ψ_L is the condensate wavefunction of lower-polaritons. P represents the creation of population in the inactive reservoir by an external non-resonant pump. The interaction constants contributing from the condensates and the reservoirs are respectively represented by g_L are g_R. The decay rates γ_I, γ_A, and γ_L are those of the inactive reservoir, active reservoir, and condensate. $1/\tau_R$ represents a stimulation scattering rate of the active reservoir into the condensate. The external non-resonant pump P firstly creates the long-lived inactive excitonic reservoir (typically $\gamma_I \sim 1$ ns^{-1} [112]), which supplies the active excitonic reservoir with a short lifetime (typically $\gamma_A \sim 15$ ps^{-1} [112]). Finally, the population in the active reservoir scatters into the coherent ground state of lower-polaritons under stimulated scattering. This process is schematically drawn in Fig. 7.9. Our study suggests that the inactive reservoir can be interpreted as the incoherent exciton population N in EBEs. Actually, both incoherent exciton population and inactive excitonic reservoir have a long lifetime and contribute to the energy shift of the polariton resonances [76]. Additionally, similarly to the incoherent exciton population of EBEs, the inactive reservoir n_I contributes to the mean field blueshift of the lower-polariton condensates through the interaction constant g_R even though it is not coupled to the cavity photons.

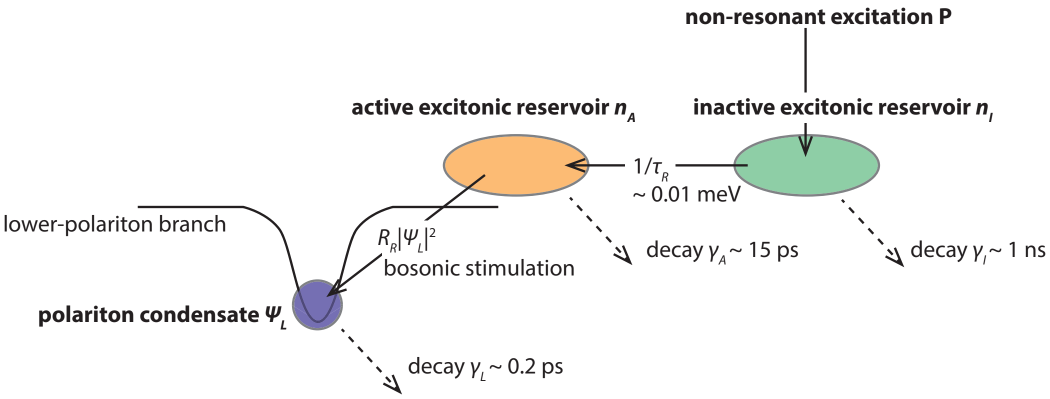
non-resonant excitation P
active excitonic reservoir n_A
inactive excitonic reservoir n_I
$1/\tau_R$
~ 0.01 meV
lower-polariton branch
$R_R|\Psi_L|^2$
bosonic stimulation
decay γ_A ~ 15 ps
decay γ_I ~ 1 ns
polariton condensate Ψ_L
decay γ_L ~ 0.2 ps

Figure 7.9: Scheme of two reservoirs model for non-resonant polariton condensates. The external non-resonant pump P creates the inactive excitonic reservoir n_I, then the inactive reservoir n_I supplies the exciton population into the active excitonic reservoir n_A. Finally, the condensates of lower-polaritons ψ_L grow through the stimulation scattering from the active excitonic reservoir.

7.6 Conclusion

In conclusion, we studied the importance of decoherence associated with excitation induced dephasing (EID) in a semiconductor microcavity both experimentally and theoretically. Time-resolved femtosecond pump-probe spectroscopy was carried out and for the theoretical description of our results we used excitonic Bloch equations (EBEs), which can explicitly take into account the coherent polarization and the incoherent population of excitons. While numerical simulations with EBEs reproduced the experimental results with a great fidelity, commonly used Gross-Pitaevskii equations (GPE) fail to simulate them. This is because GPE has an implicit assumption that the exciton is described as a coherent polarization (coherent limit). An important future perspective is to investigate pump-probe spectroscopy with selective excitation of a single branch (either lower or upper polariton branch) with a narrow spectral band pulse. In addition to this, the effect of incoherence associated with a biexciton in counter-circular polarization configuration is a very interesting issue. Actually, preliminary results have been obtained by installing a pulse shaper for the optics of the pump beam. We will discuss these in the next chapter.

8 Future perspective

We discuss now the future directions of the experiment and the theoretical model in this chapter. Experimentally, one of the important new experimental implementations is a pulse shaper (See Fig. 4.3 in Chapter 4). In the experiments of previous sections, the broadband pump pulse excites both lower and upper-polariton branch. By installing a pulse shaper in the optical pathway of the pump beam, the spectral width of the pump pulse can be squeezed to the linewidth of a single polariton branch (< 1 meV). The principle of pulse shaping is a spectral filtering. After the pulse is spectrally decomposed by a grating, we pick up only a narrowband part of the spectrum, then the spectrally decomposed pulse is recombined again into the time domain by the grating. With this technique, we are able to excite only a single branch of polariton (lower or upper polariton). In order to go further in the investigation of the lower-upper cross interaction and the strength of dephasing of each branch, it is important to excite a single polariton branch. This will give supplemental information to the broadband pump-probe experiment described in previous sections.

In Fig. 8.1 we present preliminary results of pump-probe spectroscopy with a narrowband pump pulse and a broadband probe pulse in the co-circular polarization configuration. In the experiment (a) and simulation (c) only lower-polariton branch is excited by the pump. On the other hand, in the experiment (b) and simulation (d), the pump pulse excites only upper-polariton branch. Focusing on positive delays of the experiments, we find that the center energy of the lower-polariton resonance returns to the reference black line in (a). Meanwhile, in (b) the blueshift of the lower-polariton branch stays for long time (more than 10 ps) similarly to the results presented in Chapter 7, which indicates the existence of the long-living incoherent exciton population. This result shows the importance to go further in this kind of investigation by the excitation of a single polariton branch.

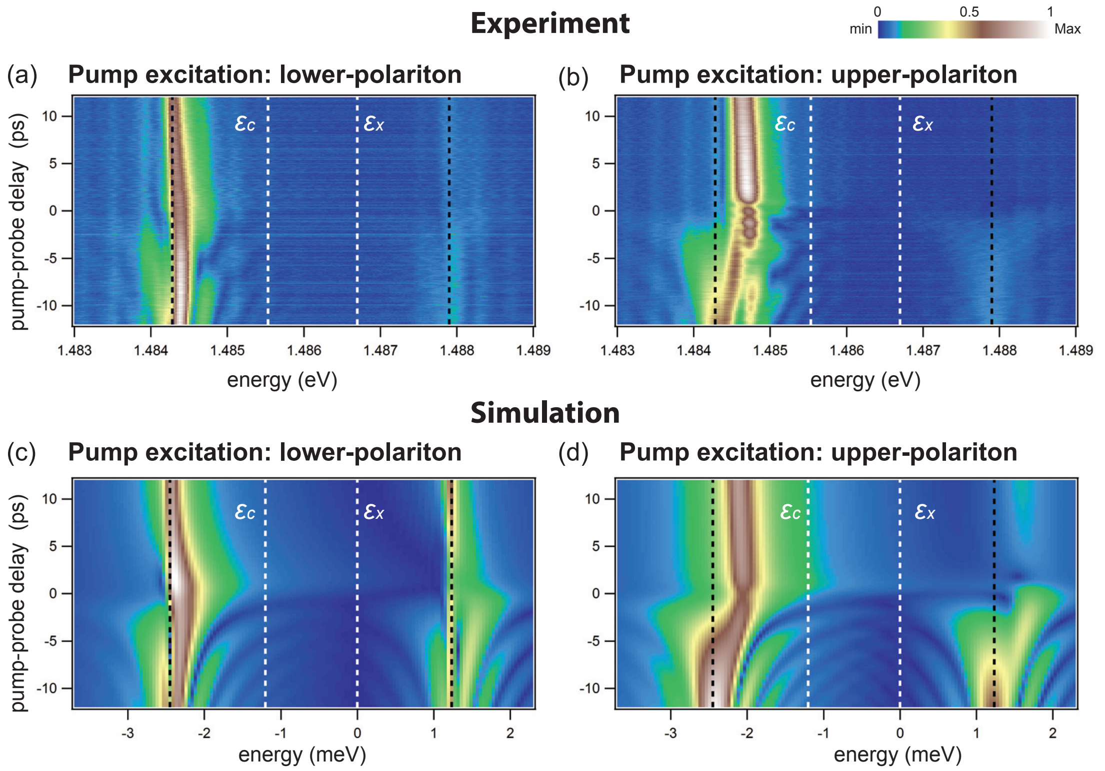

Figure 8.1: Experimental and simulated probe transmission spectra as a function of pump-probe delay with narrowband pump pulses. The measurements are done in the co-circular polarization configuration. Only lower and upper polariton branch are excited by the pump respectively in (a,c) and (b,d). The cavity detuning set at δ=-1.2 meV. The experimental pump pulse intensity is 1.48×10^{13} (1 mW) photons pulse^{-1} cm^{-2}. In the simulation, for (c) the parameters are g_0 and $g' = 0$ (coherent limit), while for (d) g_0 and $g' = 0.4g_0$ (with EID). The other parameters are set as $g_{\text{pae}} = 0.3g_0$, $\gamma_c = 0.1$ meV, $\gamma_x^* = 0$ meV and $\Gamma_x = 0.01$ meV. The white dashed lines represent the cavity photon (ϵ_c) and exciton (ϵ_x) energies. The black dashed lines are the lower and upper polariton resonance energies without a pump pulse. In the simulation, the pump intensity is $|F^{pu}|^2 = 0.15/g_0$. The pulse durations of the pump and probe are respectively set to 1.5 ps and 2.1 ps. Here g_0 has the same value as in Chapter 7.

The numerical simulations displayed in Fig. 8.1 are based on the excitonic Bloch equations (EBE):

$$\begin{aligned} i\hbar\dot{N} &= -i\Gamma_x N - 2i(\Omega - 2g_{\text{pae}}N)\text{Im}[PE^*] \qquad (8.1)\\ i\hbar\dot{P} &= (\epsilon_x + g_0 N - i\gamma_x(N))P + (\Omega - 2g_{\text{pae}}N)E \qquad (8.2)\\ i\hbar\dot{E} &= (\epsilon_c - \frac{\hbar^2}{2m_c}\nabla^2 - i\gamma_c)E + (\Omega - g_{\text{pae}}N)P - f_{\text{ext}}. \qquad (8.3) \end{aligned}$$

The constants g_0 and g' are respectively the real and imaginary parts of the exciton-exciton interaction g,

$$g = g_0 + i g'. \tag{8.4}$$

These are the same equations as Eq. 7.5-7.7 in Chapter 7. In order to qualitatively reproduce the experiments, we need to assume coherent limit ($g' = 0$) in Fig. 8.1 (c), while the excitation induced dephasing (EID) is necessary ($g' = 0.4g_0$) in 8.1 (d). Let us note that the pump intensity is same for both configurations.

These findings indicate that the formation of exciton reservoir is favoured when exciting the upper-polariton branch. This leads to a surprising consequence: the frequency dependence of the EID strength.

Even though these are preliminary results and it is too early to conclude, sophisticated theoretical ideas could be a hint for their explanations. Firstly, under the coherent limit, since $N(t) = |P(t)|^2$ is satisfied, the interacting part of the polarization in Eq. 8.2 is reduced to be $Q_{xx}(t) = g|P(t)|^2 P(t)$. This interacting term can be generalized as [33, 51, 53, 52, 72]

$$Q_{xx}(t) = P^*(t) \int G(t' - t) P(t') P(t') dt'. \tag{8.5}$$

Here $G(\tau) = G(t' - t)$ is a correlation function of the exciton-exciton interaction. In the derivation of the simple equations such as GP and EBE, we are implicitly assuming “Markovian" approximation, $G(t' - t) = (g_0 + i g')\delta(t' - t)$. In this approximation, the interacting term $Q_{xx}(t)$ is reduced back to the conventional form $Q_{xx}(t) = (g_0 + i g')|P(t)|^2 P(t)$. The physical meaning of this is to approximate the exciton-exciton as an instantaneous one (no retardation), which is equivalent to the Hartree-Fock approximation [51, 113]. In the frequency domain, the Markovian approximation means that the correlation function does not depend on frequencies. This is easily understood, because the Fourier transformed correlation function is $G(\omega) = g_0 + i g'$ under the Markovian approximation. Inversely speaking, if we take into account the real exciton-exciton interaction correlation, $G(\omega)$ can depend on frequency.

Now, the question is what is the more realistic form of the interaction correlation function $G(\omega)$? Fortunately, several state of the arts theoretical works provide the shape of $G(\omega)$ based on microscopic calculations based on T-matrix theory [33, 51, 53, 52, 72]. In Fig. 8.2, we redraw the real and imaginary parts of the correlation function $G(\omega)$ of exciton-exciton interaction with parallel spins in a GaAs single quantum well from [114]. The real and imaginary parts respectively contribute the energy shift and EID. The imaginary part of the full correlation function indicates the enhancement of the EID strength as the increase of the frequency. It is probable that this frequency dependence of the EID strength explains the higher EID strength in the upper-polariton branch in the narrow band pump-probe results (Fig. 8.1). In the Markovian approximation, we approximate the full correlation as a frequency independent function, which is the origin of the constants g_0 and g' (See the right side of Fig. 8.2).

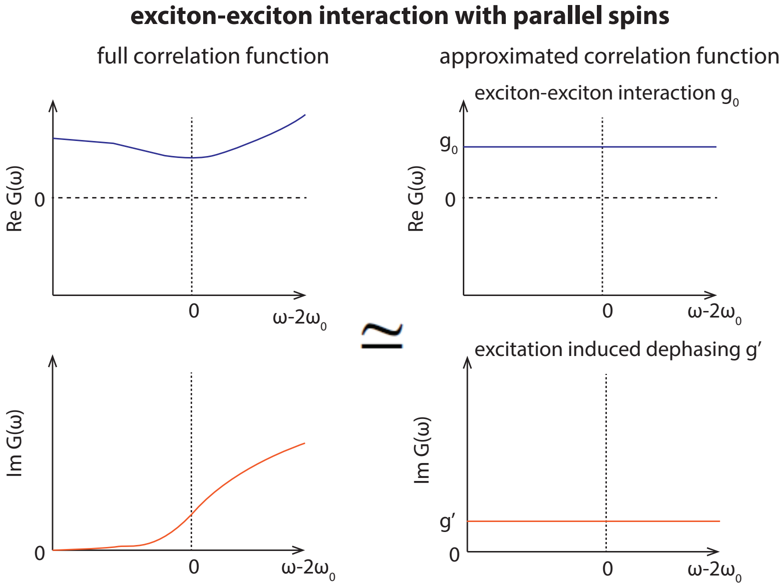

Figure 8.2: Schematic representation of the correlation function of the exciton-exciton interaction with parallel spins in a GaAs single quantum well. The real and imaginary parts of the full correlation function is redrawn from [52] (left side). The right side is the Markovian approximation of the full correlation function. ω_0 is the frequency of the exciton resonance.

Furthermore, the full correlation function of exciton-exciton interaction with anti-parallel spins provides a new view point to the two-channel model and the background interaction employed in Chapter 6. As shown in Fig. 8.3 [114], the imaginary part of the correlation function has a peak coming from the contribution of the bound biexciton. However, we should note that in the full correlation there is a background contribution even without the biexciton, which is similar to the parallel spins configuration. The contribution without the biexciton effect is sometimes called “scattering continuum" [114, 115]. Focusing on the real part of the full correlation (the left side of Fig. 8.3), we find that the dispersive shape originating from the biexciton is shifted to downward due to the scattering continuum. In Chapter 6, we approximated the full correlation as two contributions: frequency independent Markovian part and discrete biexciton state (See the right side of Fig. 8.3) [116]. The former corresponds to the attractive background interaction phenomenologically introduced as the constant g_{+-}, while the latter is the discrete biexciton state represented by $\hat{\boldsymbol{\psi}}_B$ with energy $\epsilon_B (= \hbar\omega_B)$. Additionally, in this approximation, the dephasing effect (the imaginary part of the correlation) is introduced as the large dephasing rate of the biexciton. In this sense, the two-channel model used in Chapter 6 is the simplest model that can include the “non-Markovian" effect, where the retardation is taken into account by the discrete biexciton state [116].

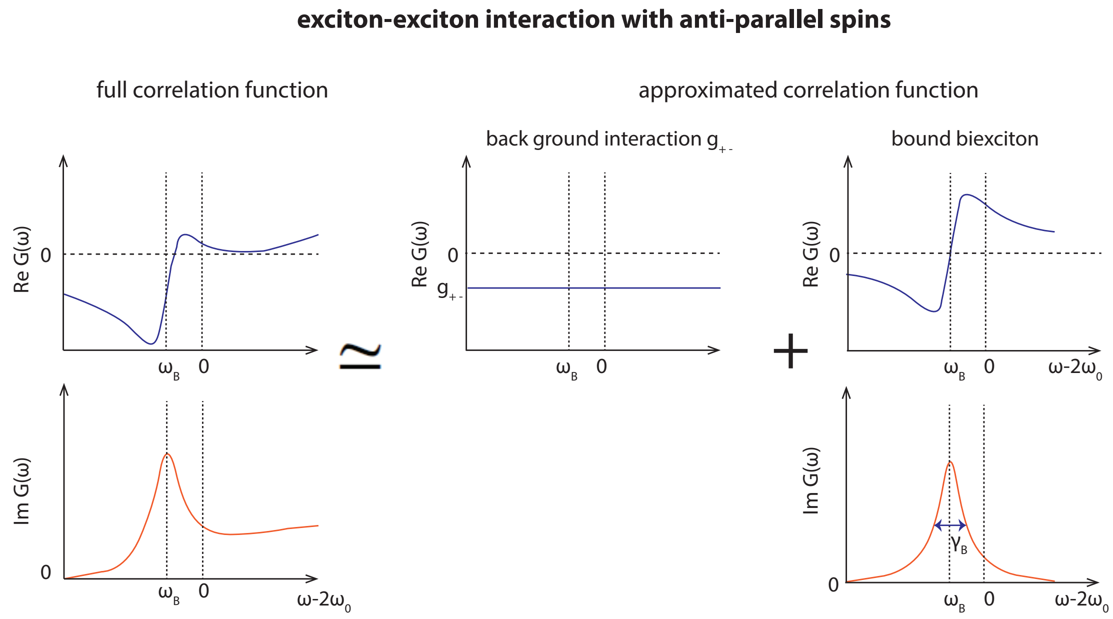

Figure 8.3: Schematic representation of the correlation function of the exciton-exciton interaction with anti-parallel spins in a GaAs single quantum well. The real and imaginary parts of the full correlation function are redrawn from [114] (left side). The right side is the approximation of the full correlation function. ω_0 and ω_B are respectively exciton and biexciton frequencies. The biexciton frequency ω_B is located below the exciton one due to the binding energy.

Finally, we comment on the possibility of the inclusion of the incoherent exciton and biexciton populations in the exciton-biexciton coupling. Since the discussion above based on the coherent limit, it is impossible to explicitly include the incoherent exciton population in a unique way. In [35], the formation of biexcitons from incoherent exciton population is investigated experimentally and the theorical model succeeded in describing it, but the creation of biexcitons from the coherent exciton is neglected because a pump-probe delay employed in the experiment is much longer than the coherence time of excitons. Here, one probable solution to include both coherent and incoherent exciton in the biexciton formation is to use the Brownian oscillator model of dephasing (Chapter 7) [109, 61, 110]. The advantage of the Brownian oscillator model is that the equation itself is same as that of coherent limit and the dephasing effect appears as an ensemble average. Therefore, we can directly use the coherent exciton-biexciton coupling equations in Chapter 6.

In summary, the experiment with the spectrally narrowband pump is the starting point of a deeper understanding of the many-body correlation effects of the exciton-exciton interaction. In parallel to this, the development of an advanced theory is expected in the future to interpret the experimental results.

9 Conclusion

In this thesis, the polariton interaction in semiconductor microcavities has been investigated through nonlinear spectroscopies. A semiconductor microcavity is a system composed of a quantum well embedded between two Bragg mirrors. The strong coupling between an exciton in the quantum well and a photon confined in the microcavity gives rise to a new quasiparticle called a polariton. The polariton is a superposition state of an exciton and a photon. The polariton-polariton interaction results from the excitonic component. The various aspects of the polariton interaction have been experimentally studied by two different types of nonlinear spectroscopies: two-dimensional Fourier transform (2DFT) four-wave mixing and pump-probe spectroscopy.

Two-demensional Fourier (2DFT) transform spectroscopy is a powerful nonlinear spectroscopy usually used in quantum chemistry to investigate vibrational states of molecules. 2DFT spectra provide us the mutual anharmonicity of different vibrational states. In Chapter 5, this technique has been applied to a semiconductor microcavity in order to probe the lower-lower (upper-upper) polariton self-interactions and lower-upper polariton cross interaction. The self and cross interactions have been presented respectively as diagonal and off-diagonal peaks in 2D spectra. The obtained 2D spectra have been firstly analysed by a double-sided Feynman diagrams based on a third-order perturbation theory, followed by a non-perturbative numerical simulation based on Gross-Pitaevskii equations written in the polariton basis. Through numerical simulations, the fine structure found in 2DFT spectra is identified as originating from the polariton energy-momentum dispersion and the polariton-polariton interaction.

Since a polariton has two spin projections, spin-up and -down, the polariton-polariton interaction depends on this spin configuration, and is called spinor polariton interaction. In Chapter 6, the measurement of the spinor polariton interaction has been performed using pump-probe spectroscopy with co- and counter-circularly polarization configuration. The strength of interaction is measured via the meanfield energy shift of the transmitted probe spectrum in presence of the pump beam. As a result, we have probed the spin anisotropic nature of the polariton spinor interaction, repulsive and attractive interaction respectively for polaritons with parallel and anti-parallel spins. Especially, for the polariton interaction with anti-parallel spins, the exciton bound molecule called biexciton carries an important role. By controlling the lower-polariton energy with the cavity detuning, the coupling between lower-polariton and biexciton has been shown to enhance the attractive polariton interaction with anti-parallel spins when the energy of two lower-polariton reaches the biexciton energy. Then at this resonance, the nature of the interaction switches from attractive to repulsive. In addition to the modification of the polariton interaction, a strong loss of the injected probe polaritons has been observed in the vicinity of the biexciton energy. We identify both features as a scattering resonance of two lower-polaritons via a biexciton and named it polaritonic Feshbach resonance. These experimental results have been examined based on the Gross-Pitaevskii equations including biexciton states.

In Chapter 7, we have investigated the decoherence process in exciton-polaritons. Focusing on the delay time dependence of the femtosecond pump-probe spectra, we have experimentally proved that the decoherence induced by the excitation induced dephasing (EID) separates the dynamics of the coherent exciton polarization and incoherent exciton population. The experimental observation has been confirmed by an excitonic Bloch equations (EBE), which can describe the dynamics of the incoherent population of excitons explicitly. These findings of the incoherent exciton population could be linked with an inactive exciton reservoir.

Finally, we have sketched some future perspectives of the research, on going pump-probe experiments with a narrow spectral band pump pulse. The preliminary experimental results are very promising to shed light on the role of the self and cross polariton interactions. Additionally, they open the way in the implementation of an advanced theory which takes into account the many-body correlation effects in the exciton interactions. The experiments and theoretical interpretations are still underway.

In summary, we have experimentally studied the polariton interactions through the nonlinear spectroscopy technique and compared the experimental results with different theoretical models. The investigations in this thesis are just the starting points of a deep understanding of the exciton-polariton physics, which is interesting also in terms of future applications of semiconductor microcavity devices.

10 Appendix A: Phase correction

In this appendix, we explain the two steps of the phase correction process required for 2DFT spectroscopy [42]. The first one is the phase correction for N times acquisition at a given delay. The second one concerns the phase change associated with the motion of the delay stage.

10.1 Phase correction after an acquisition sequence

We acquire a FWM signal 20 times at each given delay τ_0 and calculate the average. Now, let us consider a phase drift during the 20 acquisitions. Since the FWM signal includes phase information, in the worst case, the phase drift will average out the FWM signal. Thus, we have to consider a correction process for the phase drift. Firstly, we define the FWM signal for n^{th} acquisition as

$$S_n(\epsilon_t). \tag{10.1}$$

Since the delay is fixed at τ_0 in this process, we abbreviate the delay dependence. Before performing the phase correction, we apply a filter $\chi(\epsilon)$ to $S^n(\epsilon)$ as

$$S'_n(\epsilon) = S_n(\epsilon)\chi(\epsilon). \quad \text{with } \chi(\epsilon) \in [1,0] \tag{10.2}$$

The value of $\chi(\epsilon)$ is 0 or 1. If the deviation of the amplitude $|S'_n(\epsilon)|$ from the mean value over 20 acquisitions $\mu = \overline{|S'_n(\epsilon)|}$ is larger than the third of standard deviation 3σ, we consider it as noise and discard it. Using the filtered signals, the absolute phase of the initial acquisition ϕ_0 is calculated as

$$Ae^{i\phi_0} = \int S'_0(\epsilon)\,d\epsilon \tag{10.3}$$

The absolute phase ϕ_0 is used as a reference phase. The phase drift of the n^{th} acquisition $\Delta\phi_n$ is evaluated as

$$A' e^{i\Delta\phi_0} = \int S'_n(\epsilon) \cdot (S'_0(\epsilon))^* \, d\epsilon \tag{10.4}$$

Finally for the signal of n^{th} acquisition, the phase drift is corrected as

$$S_n^{\text{pc}}(\epsilon) = S'_n(\epsilon) e^{-i\Delta\phi_0}, \tag{10.5}$$

where $S_n^{\text{pc}}(\epsilon)$ is the phase corrected signal for n^{th} acquisition. An example of the phase drift correction is displayed in Fig. 10.1. We find that the phase drift during the 20 times acquisition is corrected after this numerical process. The signal for a given delay τ_0 is calculated as

$$S(\epsilon_t, \tau_0) = \frac{1}{N} \sum_{n=N} S_n^{\text{pc}}(\epsilon). \tag{10.6}$$

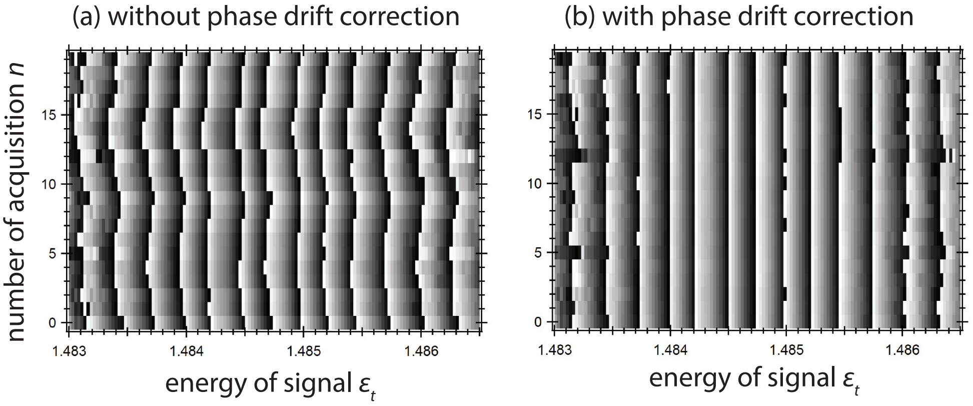

Figure 10.1: FWM signal before (a) and after (b) the phase drift correction process from [42]. The number of the acquisition is 20. A single shot measurement takes 100 ms. We find that the phase drift is indeed corrected after the numerical correction process.

10.2 Phase correction for 2DFT

Here, we explain the second phase correction step. As stated in Chapter 5, even if the phase is stabilized at a given delay position, the phase changes when the delay stage moves (See Fig. 10.2 (a)). Therefore, we apply a numerical phase correction to the FWM signal $S_{\mathrm{cor}}(\epsilon_t, \epsilon_\tau)$ [64, 68]. Phase correction is performed as $S_{\mathrm{cor}}(\epsilon_t, \tau) = S(\epsilon_t, \tau)\exp\left(\frac{i}{\hbar}(\epsilon_{\mathrm{cor}}\tau - \arg[S(\epsilon_{\mathrm{cor}}, \tau)])\right)$, where ϵ_{cor} represents a phase correction frequency. The examples of $S(\epsilon_t, \tau)$ and $S_{\mathrm{cor}}(\epsilon_t, \tau)$ are respectively presented in Fig. 10.2 (a) and (b). In Chapter 5, we chose the upper polariton energy as the phase correction energy. For example, in Fig. 5.4 (cavity detuning is δ=-0.38 meV), the phase correction energy ϵ_{cor} is equal to 1.4883 eV.

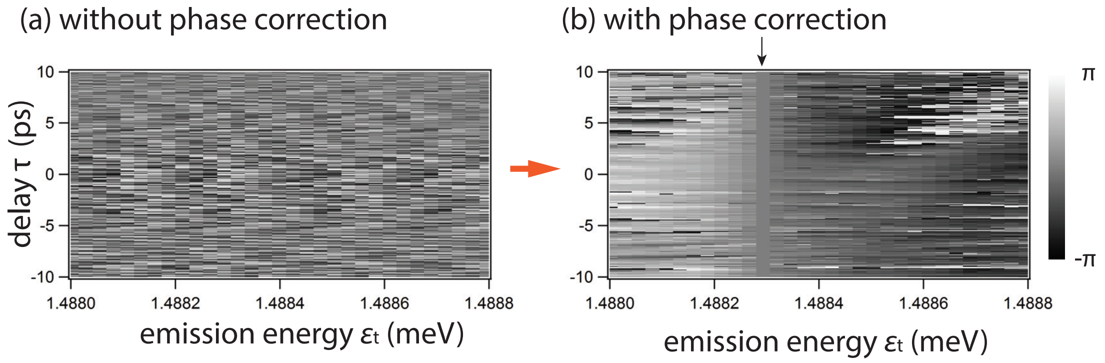

Figure 10.2: Before (a) and after (b) the phase correction with respect to the delay axis. The arrow represent the phase correction energy ϵ_{cor}=1.4883eV.

We display experimental and simulated two-quantum 2D spectra with different phase correction energies in Fig. 10.3. The energy of the normal branch (NB) of the upper-polariton is used as a reference in Fig. 10.3 (b,d), while the energy of the virtual branch (VB) of the lower-polariton is employed as the reference in Fig. 10.3 (c,e). Form the simulated and experimental spectra, we find that the phase correction process mainly shifts the ϵ_τ axis and affects the amplitude of 2D spectrum, however, it does not change the fine structure of the peaks.

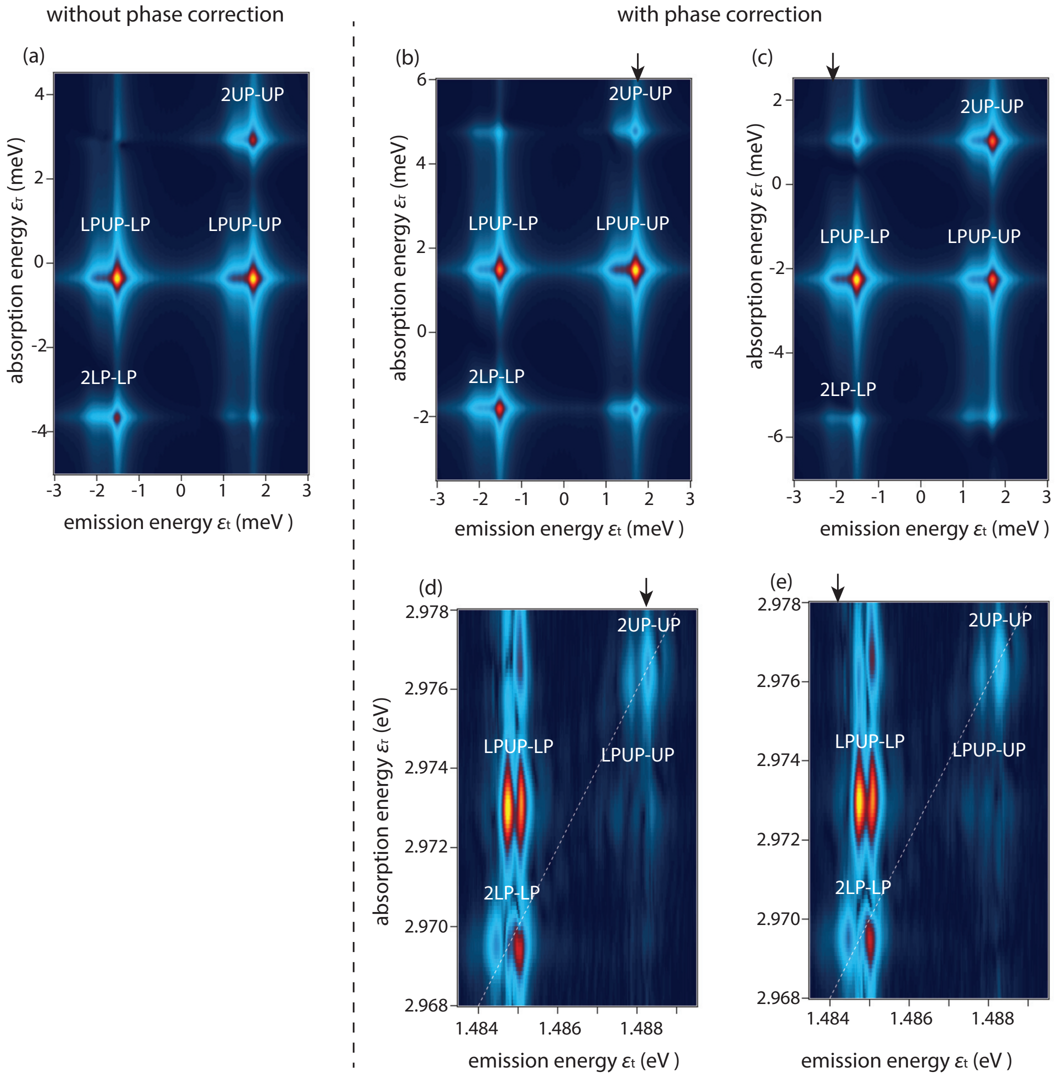

Figure 10.3: Simulated two-quantum 2DFT spectra $|S(\epsilon_t, \epsilon_\tau)|$ without (a) and with phase correction (b,c). Meanwhile, (d) and (c) are experimental 2DFT spectra. The energy of the normal branch (NB) of the upper-polariton is used as a reference in (b,d). On the other hand, the energy of the virtual branch (VB) of the lower-polariton is employed as the reference in (c,e). Arrows represent the phase correction energies ϵ_{cor}.

11 Appendix B: Third-order perturbation theory of 2DFT spectroscopy

In this Appendix, we explain the third-order perturbation theory of 2DFWM and introduce the description of the double-sided Feynman diagrams. Indices A, B, C, O and P representing Liouville-space pathways corresponding to those used for LP-LP and 2LP-LP groups in the Chapter. 5 (See Fig. 5.5 and Fig. 5.6).

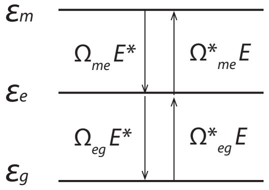

Figure 11.1: An exciton system is represented as an ideal three-level system weakly coupled to a classical electric field with a coupling constant Ω. g, e, and m respectively represent ground state, first, and second excited state.

We consider an exciton system (harmonic oscillator) weakly interacting with a classical electric field E and take into account only three levels (Fig. 11.1). The ground state $|g\rangle$, the first $|e\rangle$ and the second $|m\rangle$ excited states respectively represent one-exciton and two-exciton states. Now, we construct 3×3 density matrix as following:

$$\rho = \begin{pmatrix} \rho_{gg} & \rho^*_{eg} & \rho^*_{mg} \\ \rho_{eg} & \rho_{ee} & \rho^*_{me} \\ \rho_{mg} & \rho_{me} & \rho_{mm} \end{pmatrix}. \tag{11.1}$$

The Hamiltonian of the system H is composed of an eigen Hamiltonian H_0 and coupling Hamiltonian with electric fields μ: $H = H_0 + \mu$. H_0 and μ are given by,

$$H_0 = \begin{pmatrix} \epsilon_g & 0 & 0 \\ 0 & \epsilon_e & 0 \\ 0 & 0 & \epsilon_m \end{pmatrix}. \tag{11.2}$$

and

$$\mu = \begin{pmatrix} 0 & \Omega_{eg}E^* & 0 \\ \Omega_{eg}^*E & 0 & \Omega_{me}E^* \\ 0 & \Omega_{me}^*E & 0 \end{pmatrix}. \tag{11.3}$$

Since the eigen Hamiltonian can be written as $\hat{H}_0 = \epsilon_0 \hat{\psi}_x^\dagger \hat{\psi}_x$, we find that $\epsilon_e = \langle e|\hat{H}_0|e\rangle = \langle 1|\hat{H}_0|1\rangle = \epsilon_0$ and $\epsilon_m = \langle m|\hat{H}_0|m\rangle = \langle 2|\hat{H}_0|2\rangle = 2\epsilon_0$. The Hamiltonian describing the linear coupling between the electric field and exciton is given by $\hat{\mu} = \Omega_0(E^*\hat{\psi}_x + \hat{\psi}_x^\dagger E)$. Since $\langle g|\hat{\mu}|e\rangle = \langle 0|\hat{\mu}|1\rangle = \Omega_0 E^*$ and $\langle e|\hat{\mu}|m\rangle = \langle 1|\hat{\mu}|2\rangle = \sqrt{2}\Omega_0 E^*$, $\Omega_{me} = \sqrt{2}\Omega_{eg}$ holds in a linear (harmonic) system. The time evolution of the density matrix ρ follows the Liouville-von Neumann equation $i\hbar\dot{\rho} = [H,\rho] = H\rho - \rho H$. The equations of motion of 6 elements of the density matrix can be explicitly listed as

$$\begin{aligned}
i\hbar\dot{\rho}_{mm} &= -i\Gamma_m\rho_{mm} + \Omega_{me}E\rho_{me}^* - \Omega_{me}^*E^*\rho_{me} \\
i\hbar\dot{\rho}_{me} &= (\epsilon_m - \epsilon_e - i\gamma)\rho_{me} + \Omega_{me}^*E(\rho_{ee} - \rho_{mm}) - \Omega_{eg}E^*\rho_{mg} \\
i\hbar\dot{\rho}_{mg} &= (\epsilon_m - \epsilon_g - i\gamma)\rho_{mg} + \Omega_{me}^*E\rho_{eg} - \Omega_{eg}^*E\rho_{me} \\
i\hbar\dot{\rho}_{ee} &= -i\Gamma_e\rho_{ee} + (\Omega_{eg}^*E\rho_{eg}^* - \Omega_{eg}E^*\rho_{eg}) - (\Omega_{me}^*E\rho_{me}^* - \Omega_{me}E^*\rho_{me}) \\
i\hbar\dot{\rho}_{eg} &= (\epsilon_e - \epsilon_g - i\gamma)\rho_{eg} + \Omega_{eg}^*E(\rho_{gg} - \rho_{ee}) + \Omega_{me}E^*\rho_{mg} \\
i\hbar\dot{\rho}_{gg} &= -(\Omega_{eg}^*E\rho_{eg}^* - \Omega_{eg}E^*\rho_{eg}).
\end{aligned} \tag{11.4}$$

Here, Γ_e and Γ_m are respectively phenomenological decay rates of the population of the first and second excited states. γ is the decay rate of the polarization. In the two-level system, Γ_e and γ respectively correspond to the inverse of the lifetime T_1 and the coherence time T_2. Since the above coupled equations cannot be solved analytically, we perturbatively expand the density matrix into Taylor series of incident electric fields as

$$\rho_{ij} = \rho_{ij}^{(0)} + \rho_{ij}^{(1)} + \rho_{ij}^{(2)} + \rho_{ij}^{(3)} + \ldots \tag{11.5}$$

The first, second and third-order density matrices can be written as

$$\begin{aligned}
i\hbar\dot{\rho}_{eg}^{(1)} &= (\epsilon_e - \epsilon_g - i\gamma)\rho_{eg}^{(1)} + \Omega_{eg}^*E\rho_{gg}^{(0)} \\
\\
i\hbar\dot{\rho}_{gg}^{(2)} &= -(\Omega_{eg}^*E\rho_{eg}^{(1)*} - \Omega_{eg}E^*\rho_{eg}^{(1)}) \\
i\hbar\dot{\rho}_{ee}^{(2)} &= -i\Gamma_e\rho_{ee} + (\Omega_{eg}^*E\rho_{eg}^{(1)*} - \Omega_{eg}E^*\rho_{eg}^{(1)}) \\
i\hbar\dot{\rho}_{mg}^{(2)} &= (\epsilon_m - \epsilon_g - i\gamma)\rho_{mg}^{(2)} + \Omega_{me}^*E\rho_{eg}^{(1)} \\
\\
i\hbar\dot{\rho}_{eg}^{(3)} &= (\epsilon_e - \epsilon_g - i\gamma)\rho_{eg}^{(3)} + \Omega_{eg}^*E(\rho_{gg}^{(2)} - \rho_{ee}^{(2)}) + \Omega_{me}E^*\rho_{mg}^{(2)} \\
i\hbar\dot{\rho}_{me}^{(3)} &= (\epsilon_m - \epsilon_e - i\gamma)\rho_{me}^{(3)} + \Omega_{me}^*E\rho_{ee}^{(2)} - \Omega_{eg}E^*\rho_{mg}^{(2)}
\end{aligned} \tag{11.6}$$

We then iteratively solve these perturbative equations in an analytical way. Before doing that, we take into account phase-matching conditions associated with momenta and classify them into “pathways". Considering three momentum channels: pump ($k_2 = 0$), trigger ($k_1 = k$), and idler ($k_{FWM} = -k$), the density matrix and incident electric field can be expressed as

$$\rho_{ij}^{(n)}(t) = \rho_{ij,p}^{(n)}(t) + \rho_{ij,t}^{(n)}(t)e^{ikx} + \rho_{ij,i}^{(n)}(t)e^{-ikx} \text{ and } E = E_p(t) + E_t(t)e^{ikx}. \tag{11.7}$$

Notice that, in a strict sense, when including three wave-vector channels, the density matrix is extended to 9×9 matrix instead of 3×3. The density matrix is composed of 9 basis states: $|g, j\rangle$, $|e, j\rangle$, and $|m, j\rangle$ ($j = p, t, i$). On the pathways, we consider two cases: “one-quantum" and “two-quantum" regimes. The former is the regime where the trigger pulse ($k_1 = k$) arrives before the pump one ($k_2 = 0$), which is also called negative delay, while the latter is the regime where the pump pulse ($k_2 = 0$) arrives before the trigger one, which is also referred to as positive delay. Firstly, in the one-quantum regime (negative delay), the pathways are

$$\begin{aligned}
i\hbar\dot{\rho}_{eg,t}^{(1)} &= (\epsilon_e^t - \epsilon_g^t - i\gamma)\rho_{eg,t}^{(1)} + \Omega_{eg}^* E_t \rho_{gg}^{(0)} \\
i\hbar\dot{\rho}_{gg,i}^{(2)} &= -\Omega_{eg}^* E_p \rho_{eg,t}^{(1)*} \\
i\hbar\dot{\rho}_{ee,i}^{(2)} &= -i\Gamma_e \rho_{ee,i}^{(2)} + \Omega_{eg}^* E_p \rho_{eg,t}^{(1)*} \\
i\hbar\dot{\rho}_{eg,i}^{(3)} &= (\epsilon_e^i - \epsilon_g^i - i\gamma)\rho_{eg,i}^{(3)} + \Omega_{eg}^* E_p (\rho_{gg,i}^{(2)} - \rho_{ee,i}^{(2)}) \\
i\hbar\dot{\rho}_{me,i}^{(3)} &= (\epsilon_m^i - \epsilon_e^i - i\gamma)\rho_{me,i}^{(3)} + \Omega_{me}^* E_p \rho_{ee,i}^{(2)}.
\end{aligned} \tag{11.8}$$

Here, ϵ^p, ϵ^t, and ϵ^i respectively represent eigen energies of the pump, trigger, and idler. Secondly, the two-quantum regime (positive delay), the pathways are

$$\begin{aligned}
i\hbar\dot{\rho}_{eg,p}^{(1)} &= (\epsilon_e^p - \epsilon_g^p - i\gamma)\rho_{eg,p}^{(1)} + \Omega_{eg}^* E_p \rho_{gg}^{(0)} \\
i\hbar\dot{\rho}_{mg,p}^{(2)} &= (\epsilon_m^p - \epsilon_g^p - i\gamma)\rho_{mg,p}^{(2)} + \Omega_{me}^* E_p \rho_{eg,p}^{(1)} \\
i\hbar\dot{\rho}_{eg,i}^{(3)} &= (\epsilon_e^i - \epsilon_g^i - i\gamma)\rho_{eg,i}^{(3)} + \Omega_{me} E_t^* \rho_{mg,p}^{(2)} - \Omega_{eg} E_t^* \rho_{mg,p}^{(2)}
\end{aligned} \tag{11.9}$$

Finally, the third order polarization can be calculated as

$$\begin{aligned}
P^{(3)} + c.c. &= Tr[\rho_i^{(3)}\mu] \\
&= \Omega_{eg}\rho_{eg,i}^{(3)} + \Omega_{me}\rho_{me,i}^{(3)} + c.c.
\end{aligned} \tag{11.10}$$

In the next section, we perform analytical calculations of the third-order polarization for delta-function pump and trigger pulses.

11.1 one-quantum regime (negative delay)

Firstly, we apply a further classification to the Eq. 11.8. The third-order density matrix of the polarization is composed of the following three pathways A, B, and C:

$$\begin{aligned}
&\text{path A}\\
&i\hbar\dot{\rho}^{(1)}_{eg,t} = (\epsilon^t_e-\epsilon^t_g-i\gamma)\rho^{(1)}_{eg,t}+\Omega^*_{eg}E_t\rho^{(0)}_{gg,p}\\
&i\hbar\dot{\rho}^{(2)}_{gg,i} = -\Omega^*_{eg}E_p\rho^{(1)*}_{eg,t}\\
&i\hbar\dot{\rho}^{(3),A}_{eg,i} = (\epsilon^i_e-\epsilon^i_g-i\gamma)\rho^{(3),A}_{eg,i}+\Omega^*_{eg}E_p\rho^{(2)}_{gg,i}
\end{aligned} \tag{11.11}$$

$$\begin{aligned}
&\text{path B}\\
&i\hbar\dot{\rho}^{(1)}_{eg,t} = (\epsilon^t_e-\epsilon^t_g-i\gamma)\rho^{(1)}_{eg,t}+\Omega^*_{eg}E_t\rho^{(0)}_{gg,p}\\
&i\hbar\dot{\rho}^{(2)}_{ee,i} = -i\Gamma_e\rho^{(2)}_{ee,i}+\Omega^*_{eg}E_p\rho^{(1)*}_{eg,t}\\
&i\hbar\dot{\rho}^{(3),B}_{eg,i} = (\epsilon^i_e-\epsilon^i_g-i\gamma)\rho^{(3),B}_{eg,i}-\Omega^*_{eg}E_p\rho^{(2)}_{ee,i}
\end{aligned} \tag{11.12}$$

$$\begin{aligned}
&\text{path C}\\
&i\hbar\dot{\rho}^{(1)}_{eg,t} = (\epsilon^t_e-\epsilon^t_g-i\gamma)\rho^{(1)}_{eg,t}+\Omega^*_{eg}E_t\rho^{(0)}_{gg,p}\\
&i\hbar\dot{\rho}^{(2)}_{ee,i} = -i\Gamma_e\rho^{(2)}_{ee,i}+\Omega^*_{eg}E_p\rho^{(1)*}_{eg,t}\\
&i\hbar\dot{\rho}^{(3),C}_{me,i} = (\epsilon^i_m-\epsilon^i_e-i\gamma)\rho^{(3),C}_{me,i}+\Omega^*_{me}E_p\rho^{(2)}_{ee,i}
\end{aligned} \tag{11.13}$$

We integrate Eqs. 11.11, 11.12, and 11.13 in an analytical way by taking the pump and trigger pulses as

$$E_p(t) = \widetilde{E}_p(t)e^{-(i/\hbar)\epsilon_{pu}(t-\tau_p)} \text{ and } E_t(t) = \widetilde{E}_t(t)e^{-(i/\hbar)\epsilon_{tr}(t-\tau_t)}. \tag{11.14}$$

$\widetilde{E}_p(t)$ and $\widetilde{E}_t(t)$ respectively represent the pump and trigger pulse envelopes. For the analytical integration, we assume delta-function pulse envelopes:

$$\widetilde{E}_p(t) = \widetilde{E}^0_p\delta(t-\tau_p) \text{ and } \widetilde{E}_t(t) = \widetilde{E}^0_t\delta(t-\tau_t). \tag{11.15}$$

Let us consider the path A. Using Eq. 11.14 and 11.15, we can directly integrate Eq. 11.11 in the following way.

$$\begin{aligned}
\rho^{(1)}_{eg,t}(t) &= \frac{1}{i\hbar}\Omega^*_{eg}e^{-(i/\hbar)(\epsilon^t_e-\epsilon^t_g-i\gamma)t}e^{(i/\hbar)\epsilon_{tr}\tau_t}\int_{-\infty}^{t}dt'\widetilde{E}_t(t')e^{(i/\hbar)(\epsilon^t_e-\epsilon^t_g-i\gamma-\epsilon_{tr})t'}\rho^{(0)}_{gg,p}\\
&= \frac{1}{i\hbar}\Omega^*_{eg}e^{-(i/\hbar)(\epsilon^t_e-\epsilon^t_g-i\gamma)t}e^{(i/\hbar)\epsilon_{tr}\tau_t}\int_{-\infty}^{t}dt'\widetilde{E}^0_t\delta(t'-\tau_t)e^{(i/\hbar)(\epsilon^t_e-\epsilon^t_g-i\gamma-\epsilon_{tr})t'}\rho^{(0)}_{gg,p}\\
&= \frac{1}{i\hbar}\Omega^*_{eg}\widetilde{E}^0_t e^{-(i/\hbar)(\epsilon^t_e-\epsilon^t_g-i\gamma)(t-\tau_t)}\rho^{(0)}_{gg,p}
\end{aligned} \tag{11.16}$$

$$\begin{aligned}
\rho^{(2)}_{gg,i}(t) &= -(\frac{1}{i\hbar})\Omega^*_{eg}e^{(i/\hbar)\epsilon_{pu}\tau_p}\int_{-\infty}^{t} dt'\widetilde{E}_p(t')e^{(i/\hbar)(-\epsilon_{pu})t'}\rho^{(1)*}_{eg,t}(t') \\
&= -(\frac{1}{i\hbar})\Omega^*_{eg}e^{(i/\hbar)\epsilon_{pu}\tau_p}\int_{-\infty}^{t} dt'\widetilde{E}^0_p\delta(t'-\tau_p)e^{(i/\hbar)(-\epsilon_{pu})t'}\rho^{(1)*}_{eg,t}(t') \\
&= -(\frac{1}{i\hbar})\Omega^*_{eg}\widetilde{E}^0_p\,\rho^{(1)*}_{eg,t}(\tau_p) \\
&= (\frac{1}{i\hbar})^2|\Omega_{eg}|^2\widetilde{E}^0_p\widetilde{E}^{0*}_t\,e^{(i/\hbar)(\epsilon^t_e-\epsilon^t_g+i\gamma)(\tau_p-\tau_t)}\rho^{(0)*}_{gg,p} \qquad (11.17)
\end{aligned}$$

$$\begin{aligned}
\rho^{(3),A}_{eg,i}(t) &= (\frac{1}{i\hbar})\Omega^*_{eg}e^{-(i/\hbar)(\epsilon^i_e-\epsilon^i_g-i\gamma)t}e^{(i/\hbar)\epsilon_{pu}\tau_p}\int_{-\infty}^{t} dt'\widetilde{E}_p(t')e^{(i/\hbar)(\epsilon^i_e-\epsilon^i_g-i\gamma-\epsilon_{pu})t'}\rho^{(2)}_{gg,i}(t') \\
&= (\frac{1}{i\hbar})\Omega^*_{eg}e^{-(i/\hbar)(\epsilon^i_e-\epsilon^i_g-i\gamma)t}e^{(i/\hbar)\epsilon_{pu}\tau_p}\int_{-\infty}^{t} dt'\widetilde{E}^0_p\delta(t'-\tau_p)e^{(i/\hbar)(\epsilon^i_e-\epsilon^i_g-i\gamma-\epsilon_{pu})t'}\rho^{(2)}_{gg,i}(t') \\
&= (\frac{1}{i\hbar})\Omega^*_{eg}\widetilde{E}^0_p e^{-(i/\hbar)(\epsilon^i_e-\epsilon^i_g-i\gamma)(t-\tau_p)}\rho^{(2)}_{gg,i}(\tau_p) \\
&= (\frac{1}{i\hbar})^3\Omega^*_{eg}|\Omega_{eg}|^2\widetilde{E}^0_p\widetilde{E}^0_p\widetilde{E}^*_t\,e^{-(i/\hbar)(\epsilon^i_e-\epsilon^i_g-i\gamma)(t-\tau_p)}e^{(i/\hbar)(\epsilon^t_e-\epsilon^t_g+i\gamma)(\tau_p-\tau_t)}\rho^{(0)*}_{gg,p} \\
&= (\frac{1}{i\hbar})^3\Omega^*_{eg}|\Omega_{eg}|^2\widetilde{E}^0_p\widetilde{E}^0_p\widetilde{E}^*_t\,e^{-(i/\hbar)(\epsilon^i_e-\epsilon^i_g-i\gamma)t_3}e^{(i/\hbar)(\epsilon^t_e-\epsilon^t_g+i\gamma)t_1}\rho^{(0)*}_{gg,p} \qquad (11.18)
\end{aligned}$$

In the last line, the times t_1 and t_3 are respectively defined as

$$t_1 = \tau_p - \tau_t \text{ and } t_3 = t - \tau_p. \qquad (11.19)$$

We note that times t_1 and t_3 respectively correspond to τ and t in Chapter 5. Remembering Eq. 11.10, the contribution of the path A to the polarization is given by

$$P^{(3),A}(t_3, t_1) = \Omega_{eg}\rho^{(3),A}_{eg,i}(t_3, t_1). \qquad (11.20)$$

Similarity, the contribution of the path B and C to the polarization is given by

$$P^{(3),B}(t_3, t_1) = \Omega_{eg}\rho^{(3),B}_{eg,i}(t_3, t_1) \qquad (11.21)$$

and

$$P^{(3),C}(t_3, t_1) = \Omega_{me}\rho^{(3),C}_{me,i}(t_3, t_1). \qquad (11.22)$$

After Fourier transformation in terms of times t_1 and t_3, we obtain 2DFT spectrum associated with the path A.

$$S^{(3),A}(\epsilon_3,\epsilon_1) \propto P^{(3),A}(\epsilon_3,\epsilon_1) = |\Omega_{eg}|^4\widetilde{E}^0_p\widetilde{E}^0_p\widetilde{E}^{0*}_t\cdot\frac{1}{i(\epsilon_3-\epsilon^i_e+\epsilon^i_g)-\gamma}\cdot\frac{1}{i(\epsilon_1+\epsilon^t_e-\epsilon^t_g)-\gamma}$$

Repeating similar calculations for $\rho^{(3),B}_{eg,i}$ and $\rho^{(3),C}_{eg,i}$, $P^{(3),B}(t_3,t_1)$ and $P^{(3),B}(t_3,t_1)$ now read,

$$S^{(3),B}(\epsilon_3,\epsilon_1) \propto P^{(3),B}(\epsilon_3,\epsilon_1) = |\Omega_{eg}|^4 \widetilde{E}^0_p \widetilde{E}^0_p \widetilde{E}^{0*}_t \cdot \frac{1}{i(\epsilon_3 - \epsilon^i_e + \epsilon^i_g) - \gamma} \cdot \frac{1}{i(\epsilon_1 + \epsilon^t_e - \epsilon^t_g) - \gamma}$$

$$S^{(3),C}(\epsilon_3,\epsilon_1) \propto P^{(3),B}(\epsilon_3,\epsilon_1) = -|\Omega_{me}|^2 |\Omega_{eg}|^2 \widetilde{E}^0_p \widetilde{E}^0_p \widetilde{E}^{0*}_t \cdot \frac{1}{i(\epsilon_3 - \epsilon^i_m + \epsilon^i_e) - \gamma} \cdot \frac{1}{i(\epsilon_1 + \epsilon^t_e - \epsilon^t_g) - \gamma}$$

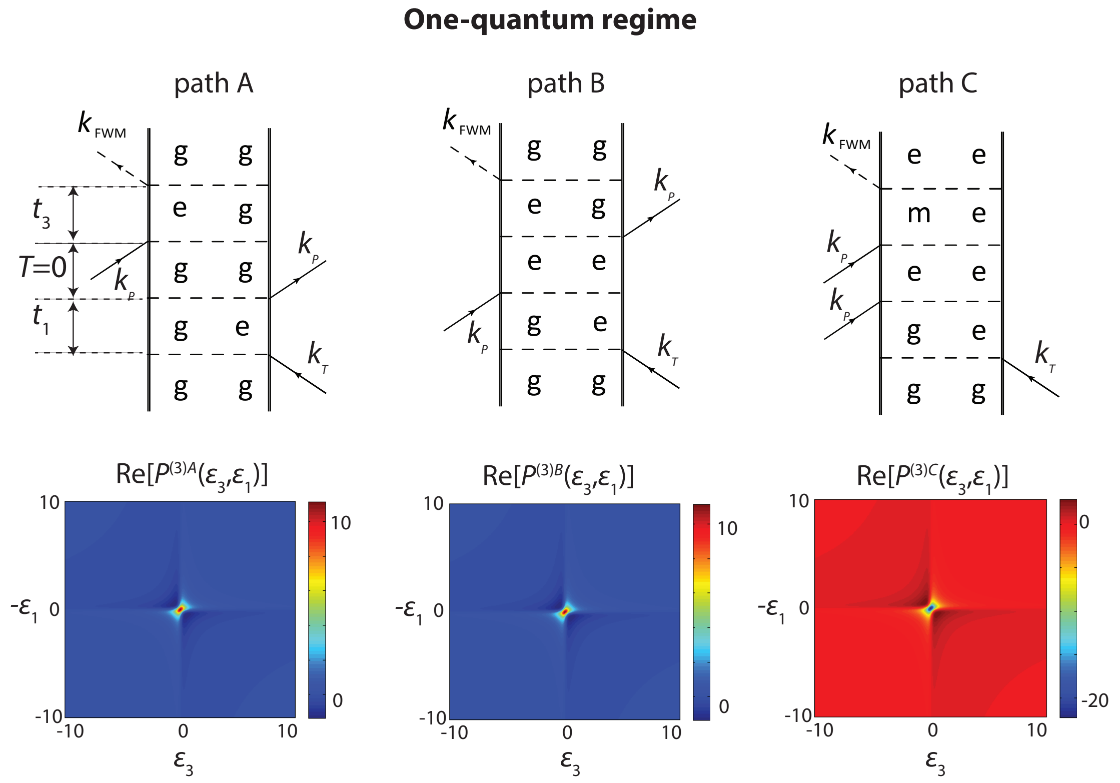

Figure 11.2: Double sided Feynman diagrams in one-quantum regime representing three different Liouville-space pathways: path A, B, and C. Below the double-sided Feynman diagrams, we plot a signal corresponding to each diagram. Absorption ϵ_1 and emission energies ϵ_3 respectively correspond to the Fourier transform counterpart of the time t_1 and t_3. Notice that if there is no non-linearity, the FWM signal from path A+B cancels the signal path C.

In Fig. 11.2, we plot double-sided Feynman diagram for paths A, B, and C and the real part of $S^{(3),A}$, $S^{(3),B}$, and $S^{(3),C}$. Finally, the 2DFT signal in the one-quantum regime that can be calculated as a sum of the path A, B, and C: $S_{1Q} = S^{(3),A} + S^{(3),B} + S^{(3),C}$. In the linear (harmonic) system the relation $\epsilon_m = 2\epsilon_e$ and $\Omega_{me} = \sqrt{2}\Omega_{eg}$ exist. Therefore, we can easily find that, in this linear system, the path $S^{(3),A} + S^{(3),B}$ cancels $S^{(3),C}$ and the FWM signal is zero ($S_{1Q}(\epsilon_3, \epsilon_1) = 0$). This consequence is intuitive because the FWM signal is associated with the existence of nonlinearities and should not appear in the linear case. Generally, the nonlinearity (aharmonicity) is introduced in two ways: with a saturation and with an energy-shift. The saturation effect is the reduction of the exciton-photon coupling in the higher excited state Ω_{me} compared to the lower one Ω_{eg} ($\Omega_{me} < \Omega_{eg}$). A special example of the saturation effect is that of two-level system. In this case, Ω_{me} is zero and only paths A and B exist. In the case of excitons in semiconductor quantum wells, the saturation effect appears due to the Fermionic nature of excitons (the photon-assisted exchange scattering). We can say that a finite-level system is intrinsically nonlinear. On the other hand, the energy-shift is defined as $\epsilon_m \neq 2\epsilon_e$. Namely, the repulsive (attractive) interaction of excitons induces the blue-(red) shift of the energy of the two-exciton state ϵ_m. In quantum well excitons with parallel spins, the repulsive interaction between excitons introduces a blue-shift of the two-excitons state ($\epsilon_m > 2\epsilon_e$). We plot the real and absolute value of $S_{1Q}(\epsilon_3, \epsilon_1)$ in Fig 11.3.

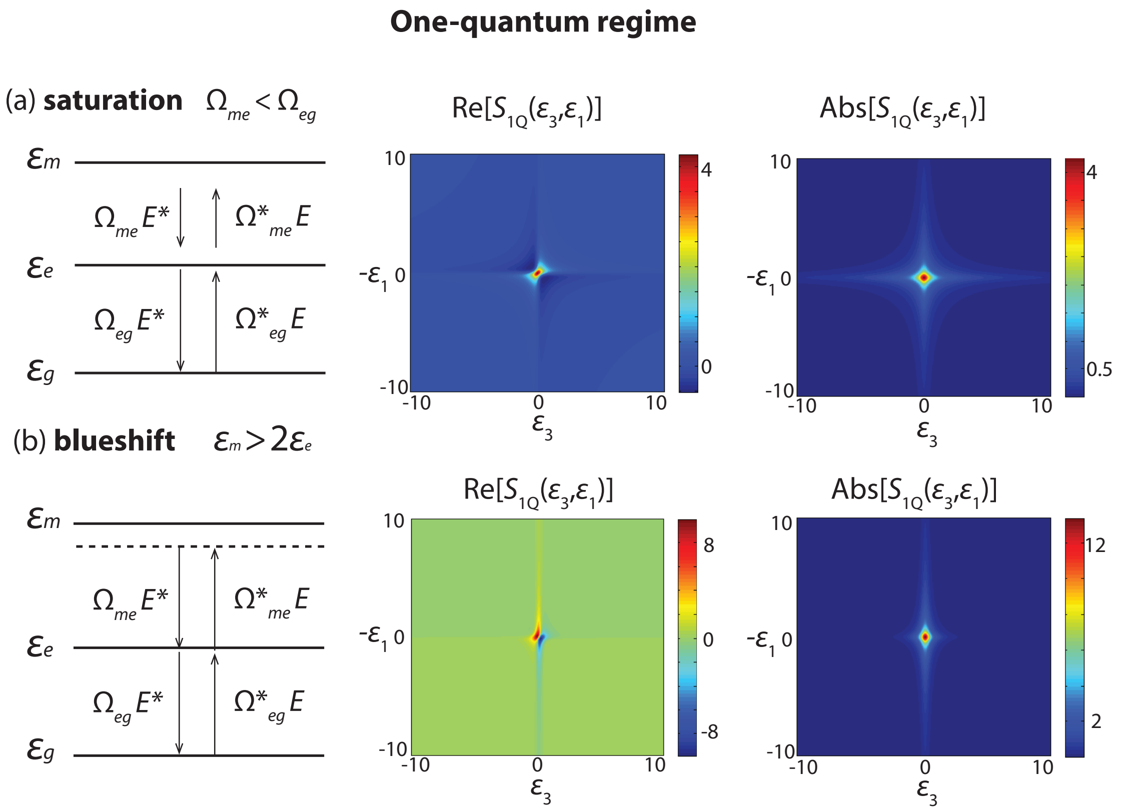

Figure 11.3: The real and absolute value of 2DFT spectrum in one-quantum regime as a summation of the path A, B, and C for two types of non-linearities: saturation (a) and blue-shift (b). A striking difference appears in real parts of 2DFT spectra. While the blue-shift type non-linearity displays dispersive shape in the real part, it does not appear in the saturation type non-linearity.

11.2 two-quantum regime (positive delay)

At positive delays (the trigger pulse arrives after the pump one), there are two Liouville-space pathways:

$$\begin{array}{l} \text{path O} \\ i\hbar\dot{\rho}^{(1)}_{eg,p} = (\epsilon^p_e - \epsilon^p_g - i\gamma)\rho^{(1)}_{eg,p} + \Omega^*_{eg}E_p\rho^{(0)}_{gg,p} \\ i\hbar\dot{\rho}^{(2)}_{mg,p} = (\epsilon^p_m - \epsilon^p_g - i\gamma)\rho^{(2)}_{mg,p} + \Omega^*_{me}E_p\rho^{(1)}_{eg,p} \\ i\hbar\dot{\rho}^{(3),O}_{eg,i} = (\epsilon^i_e - \epsilon^i_g - i\gamma)\rho^{(3),O}_{eg,i} + \Omega_{me}E^*_t\rho^{(2)}_{mg,p} \end{array} \tag{11.23}$$

$$\begin{array}{l} \text{path P} \\ i\hbar\dot{\rho}^{(1)}_{eg,p} = (\epsilon^p_e - \epsilon^p_g - i\gamma)\rho^{(1)}_{eg,p} + \Omega^*_{eg}E_p\rho^{(0)}_{gg,p} \\ i\hbar\dot{\rho}^{(2)}_{mg,p} = (\epsilon^p_m - \epsilon^p_g - i\gamma)\rho^{(2)}_{mg,p} + \Omega^*_{me}E_p\rho^{(1)}_{eg,p} \\ i\hbar\dot{\rho}^{(3),P}_{me,i} = (\epsilon^i_m - \epsilon^i_e - i\gamma)\rho^{(3),P}_{me,i} - \Omega_{eg}E^*_t\rho^{(2)}_{mg,p} \end{array} \tag{11.24}$$

We directly integrate the Eq. 11.23. The explicit calculations of the first, second and third-order density matrices are the following.

$$\begin{aligned} \rho^{(1)}_{eg,p}(t) &= \frac{1}{i\hbar}\Omega^*_{eg}e^{-(i/\hbar)(\epsilon^p_e-\epsilon^p_g-i\gamma)t}e^{(i/\hbar)\epsilon_{pu}\tau_p}\int_{-\infty}^{t}dt'\widetilde{E}_p(t')e^{(i/\hbar)(\epsilon^p_e-\epsilon^p_g-i\gamma-\epsilon_{pu})t'}\rho^{(0)}_{gg,p} \\ &= \frac{1}{i\hbar}\Omega^*_{eg}e^{-(i/\hbar)(\epsilon^p_e-\epsilon^p_g-i\gamma)t}e^{(i/\hbar)\epsilon_{pu}\tau_p}\int_{-\infty}^{t}dt'\widetilde{E}^0_p\delta(t'-\tau_p)e^{(i/\hbar)(\epsilon^p_e-\epsilon^p_g-i\gamma-\epsilon_{pu})t'}\rho^{(0)}_{gg,p} \\ &= \frac{1}{i\hbar}\Omega^*_{eg}\widetilde{E}^0_p e^{-(i/\hbar)(\epsilon^p_e-\epsilon^p_g-i\gamma)(t-\tau_p)}\rho^{(0)}_{gg,p} \end{aligned} \tag{11.25}$$

$$\begin{aligned} \rho^{(2)}_{mg,p}(t) &= \frac{1}{i\hbar}\Omega^*_{me}e^{-(i/\hbar)(\epsilon^p_m-\epsilon^p_g-i\gamma)t}e^{(i/\hbar)\epsilon_{pu}\tau_p}\int_{-\infty}^{t}dt'\widetilde{E}_p(t')e^{(i/\hbar)(\epsilon^p_m-\epsilon^p_g-i\gamma-\epsilon_{pu})t'}\rho^{(1)}_{eg,p}(t') \\ &= \frac{1}{i\hbar}\Omega^*_{me}e^{-(i/\hbar)(\epsilon^p_m-\epsilon^p_g-i\gamma)t}e^{(i/\hbar)\epsilon_{pu}\tau_p}\int_{-\infty}^{t}dt'\widetilde{E}^0_p\delta(t'-\tau_p)e^{(i/\hbar)(\epsilon^p_m-\epsilon^p_g-i\gamma-\epsilon_{pu})t'}\rho^{(1)}_{eg,p}(t') \\ &= \frac{1}{i\hbar}\Omega^*_{me}\widetilde{E}^0_p e^{-(i/\hbar)(\epsilon^p_m-\epsilon^p_g-i\gamma)(t-\tau_p)}\rho^{(1)}_{eg,p}(\tau_p) \\ &= (\frac{1}{i\hbar})^2\Omega^*_{me}\Omega^*_{eg}\widetilde{E}^0_p\widetilde{E}^0_p\; e^{-(i/\hbar)(\epsilon^p_m-\epsilon^p_g-i\gamma)(t-\tau_p)}\rho^{(0)}_{gg,p} \end{aligned} \tag{11.26}$$

$$\begin{aligned} \rho^{(3),O}_{eg,i}(t) &= (\frac{1}{i\hbar})\Omega_{me}e^{-(i/\hbar)(\epsilon^i_e-\epsilon^i_g-i\gamma)t}e^{(i/\hbar)\epsilon_{tr}\tau_t}\int_{-\infty}^{t}dt'\widetilde{E}^*_t(t')e^{(i/\hbar)(\epsilon^i_e-\epsilon^i_g-i\gamma-\epsilon_{tr})t'}\rho^{(2)}_{mg,p}(t') \\ &= (\frac{1}{i\hbar})\Omega_{me}e^{-(i/\hbar)(\epsilon^i_e-\epsilon^i_g-i\gamma)t}e^{(i/\hbar)\epsilon_{tr}\tau_t}\int_{-\infty}^{t}dt'\widetilde{E}^{0*}_t\delta(t'-\tau_t)e^{(i/\hbar)(\epsilon^i_e-\epsilon^i_g-i\gamma-\epsilon_{tr})t'}\rho^{(2)}_{mg,p}(t') \\ &= (\frac{1}{i\hbar})\Omega_{me}\widetilde{E}^{0*}_t e^{-(i/\hbar)(\epsilon^i_e-\epsilon^i_g-i\gamma)(t-\tau_t)}\rho^{(2)}_{mg,p}(\tau_t) \end{aligned}$$

$$
\begin{aligned}
&= (\frac{1}{i\hbar})^3 |\Omega_{me}|^2 \Omega_{eg}^* \widetilde{E}_t^{0*} \widetilde{E}_p^0 \widetilde{E}_p^0 \, e^{-(i/\hbar)(\epsilon_e^i - \epsilon_g^i - i\gamma)(t-\tau_t)} e^{-(i/\hbar)(\epsilon_m^p - \epsilon_g^p - i\gamma)(\tau_t - \tau_p)} \rho_{gg,p}^{(0)} \\
&= (\frac{1}{i\hbar})^3 |\Omega_{me}|^2 \Omega_{eg}^* \widetilde{E}_t^{0*} \widetilde{E}_p^0 \widetilde{E}_p^0 \, e^{-(i/\hbar)(\epsilon_e^i - \epsilon_g^i - i\gamma) t_3} e^{-(i/\hbar)(\epsilon_m^p - \epsilon_g^p - i\gamma) t_1} \rho_{gg,p}^{(0)} \qquad (11.27)
\end{aligned}
$$

In the last line, times t_1 and t_3 are respectively defined as

$$t_1 = \tau_t - \tau_p \text{ and } t_3 = t - \tau_t. \qquad (11.28)$$

In the same way as in the one-quantum regime, t_1 and t_3 respectively correspond to τ and t in Chapter 5.

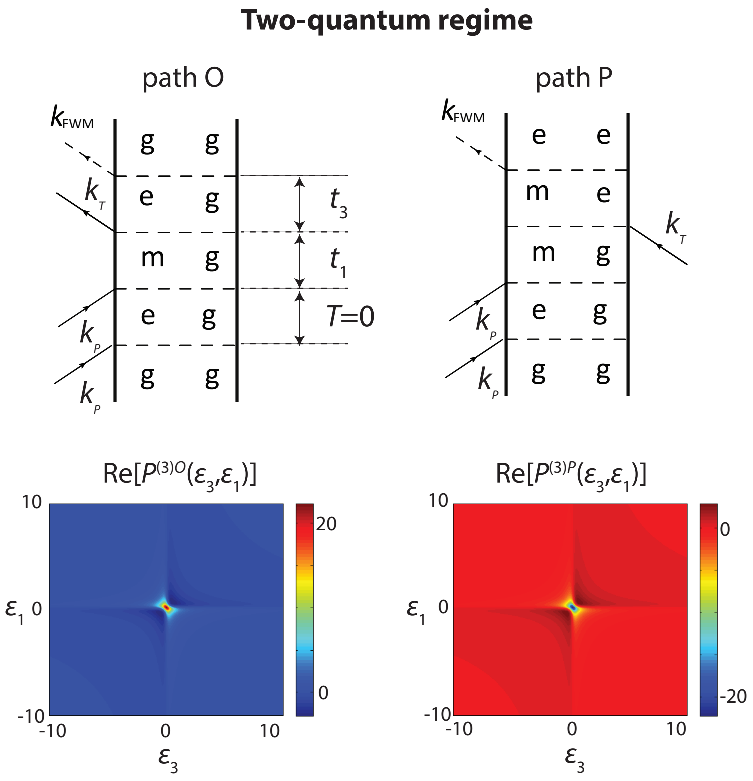
Two-quantum regime
path O
path P
k_FWM
k_T
k_P
k_P
g g
e g
m g
e g
g g
t_3
t_1
T=0
k_FWM
e e
m e
m g
e g
g g
k_T
k_P
k_P
Re[P^(3)O(ε_3,ε_1)]
Re[P^(3)P(ε_3,ε_1)]
10
ε_1 0
-10
-10
0
10
ε_3
20
0
-20

Figure 11.4: Double sided Feynman diagrams in the two-quantum regime representing two different Liouville-space pathways: path O and P. Below the double-sided Feynman diagrams, we plot the signal corresponding to each diagram. Absorption ϵ_1 and emission ϵ_3 energies respectively correspond to the Fourier transform counterpart of the time t_1 and t_3.

The contributions of the paths O and E to the polarization are given by

$$P^{(3),O}(t_3, t_1) = \Omega_{eg} \rho_{eg,i}^{(3),O}(t_3, t_1) \text{ and } P^{(3),P}(t_3, t_1) = \Omega_{me} \rho_{me,i}^{(3),P}(t_3, t_1). \qquad (11.29)$$

The FWM signal resulting from $P_i^{(3),D}(t_3,t_1)$ is

$$S^{(3),O}(\epsilon_3,\epsilon_1) \propto P^{(3),O}(\epsilon_3,\epsilon_1) = |\Omega_{me}|^2|\Omega_{eg}|^2|\widetilde{E}_t^{0*}\widetilde{E}_p^0\widetilde{E}_p^0 \cdot \frac{1}{i(\epsilon_3-\epsilon_e^i+\epsilon_g^i)-\gamma} \cdot \frac{1}{i(\epsilon_1-\epsilon_m^p+\epsilon_g^p)-\gamma}.$$

In a similar way to the path O, $P_i^{(3),E}(t_3,t_1)$ is calculated as

$$S^{(3),P}(\epsilon_3,\epsilon_1) \propto P^{(3),P}(\epsilon_3,\epsilon_1) = -|\Omega_{me}|^2|\Omega_{eg}|^2\widetilde{E}_t^{0*}\widetilde{E}_p^0\widetilde{E}_p^0 \cdot \frac{1}{i(\epsilon_3-\epsilon_m^i+\epsilon_e^i)-\gamma} \cdot \frac{1}{i(\epsilon_1-\epsilon_m^p+\epsilon_g^p)-\gamma}.$$

The double-sided Feynman diagrams of paths O and P and real values of $S^{(3),O}$ and $S^{(3),P}$ are presented in Fig. 11.4. In the same way as the one-quantum region, paths O and P cancel out each other and the total signal $S_{2Q} = S^{(3),O} + S^{(3),P}$ vanishes in the linear (harmonic) system. However, the important difference from the one-quantum region is that energy-shift type nonlinearity is required for the appearance of the signal $S_{2Q}(\epsilon_3,\epsilon_1)$. In other words, $S_{2Q}(\epsilon_3,\epsilon_1) = 0$ takes place even when the saturation type non-linearity exists ($\Omega_{eq} \neq \Omega_{me}$). Therefore, two level systems such as atoms and quantum dots emit a FWM signal only in the one-quantum region (negative delay). Actually the FWM signal in the two-quantum regime (positive delay) is an evidence of energy-shift associated with exciton-exciton interactions. Figure. 11.5 is the plot of the real and absolute value of $P^{(3),2Q} = 0$ in the system with blue-shift non-linearity

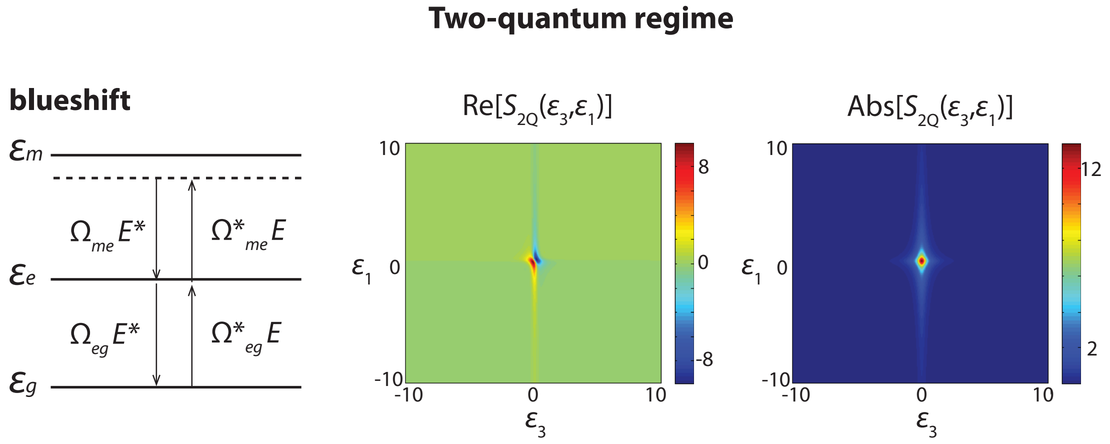

Figure 11.5: Real and absolute value of 2DFT spectrum in two-quantum regime as a summation of the path O and P for blue-shift type non-linearity. The blue-shift type non-linearity displays dispersive shape in the real part of the spectrum. Since with a saturation type non-linearity, paths O and P cancel out and no signal appears.

Finally, It is important to note that the electric field is weakly coupled to the exciton in this system, thus there is no feedback action from the exciton to electric field. This situation completely changes when the electric field is confined inside a microcavity and strongly coupled to the exciton. In the exciton-photon strong coupling system such as a semiconductor microcavity, the new polariton eigenstates are good eigenstate and we need quasi-mode formalism in order to map polariton system into the weak coupling formalism, which is addressed in Chapter 5.

12 Appendix C: Giant oscillator strength model

In this appendix, we review the giant oscillator strength model. As explained in Chapter 6, we can consider two different types of biexciton creation mechanism: the bipolariton model (x-x-B) [81, 50] and the giant oscillator strength model (x-c-B) [117, 118]. In Chapter 6, we used the bipolariton model. Here, we review the idea and possibility of using the giant oscillator strength model. We will show that the giant oscillator strength model also models the experiment in a reasonable way. In the bipolariton model, the biexciton is formed from two excitons with opposite spins through the Coulomb interaction. On the other hand, in the giant oscillator strength model, the biexciton is created from an exciton and a photon with opposite spins through the oscillator strength of the biexciton.

12.0.1 Hamiltonian

Firstly, the Hamiltonian of the giant oscillator model is given by [118]

$$\hat{H}_{\text{giant}} = \sum_{\sigma=\{\uparrow\downarrow\}} \int d\mathbf{x}\, \frac{1}{2} g_{\Omega} \left(\hat{\boldsymbol{\psi}}_B \hat{\boldsymbol{\psi}}^{\dagger}_{x,\sigma} \hat{\boldsymbol{\psi}}^{\dagger}_{c,-\sigma} + \hat{\boldsymbol{\psi}}_{x,\sigma} \hat{\boldsymbol{\psi}}_{c,-\sigma} \hat{\boldsymbol{\psi}}^{\dagger}_B \right). \tag{12.1}$$

The constant g_{Ω} represents the strength of the exciton-photon-biexciton coupling. We schematically present the Hamiltonian of the giant oscillator strength model in Fig. 12.1. By replacing the bipolariton model with the giant oscillator strength model in the Hamiltonian in Chapter 6 (See Eq. 6.1), we calculate the equations of motion of exciton, photon, and biexciton wave-functions as follows:

$$\begin{aligned} i\hbar\dot{\psi}_{x,\uparrow} &= (\epsilon_x + g|\psi_{x,\uparrow}|^2 + g_{+-}|\psi_{x,\downarrow}|^2 - i\gamma_x)\psi_{x,\uparrow} \\ &\quad + \frac{1}{2} g_{\Omega} \psi_B \psi^{*}_{c,\downarrow} + (\Omega - 2g_{\text{pae}}|\psi_{x,\uparrow}|^2)\psi_{c,\uparrow} \end{aligned} \tag{12.2}$$

$$i\hbar\dot{\psi}_{c,\uparrow} = (\epsilon_c - \frac{\hbar^2}{2m_c}\nabla^2 - i\gamma_c)\psi_{c,\uparrow} + \frac{1}{2} g_{\Omega} \psi_B \psi^{*}_{x,\downarrow} + (\Omega - g_{\text{pae}}|\psi_{x,\uparrow}|^2)\psi_{x,\uparrow} - f_{\text{ext},\uparrow} \tag{12.3}$$

$$i\hbar\dot{\psi}_B = (\epsilon_B - i\gamma_B)\psi_B + \frac{1}{2}g_\Omega(\psi_{x,\uparrow}\psi_{c,\downarrow} + \psi_{c,\uparrow}\psi_{x,\downarrow}). \tag{12.4}$$

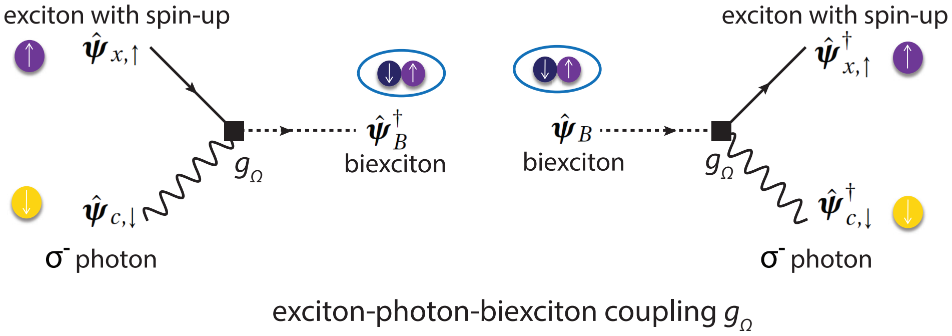
exciton with spin-up
$\hat{\psi}_{x,\uparrow}$
$\hat{\psi}_{c,\downarrow}$
σ- photon
g_Ω
$\hat{\psi}^\dagger_B$
biexciton
$\hat{\psi}_B$
biexciton
g_Ω
exciton with spin-up
$\hat{\psi}^\dagger_{x,\uparrow}$
$\hat{\psi}^\dagger_{c,\downarrow}$
σ- photon
exciton-photon-biexciton coupling g_Ω

Figure 12.1: Schematic representation of the exciton-photon-biexciton coupling g_Ω in the giant oscillator strength model. The solid and wavy lines respectively represent an exciton and a photon. The dashed lines are biexcitons. In this figure, we present only the creation process of the biexciton from exciton with spin-up and σ^- photon. However, the biexcion is also formed from exciton with spin-down and σ^+ photon.

Since the biexciton is involved only in an exciton-photon pair with opposite spins, we consider only counter-circular polarization configuration in this appendix. In the same way as in Chapter. 6, defining the vector of spin-down probe wavefunctions as $\vec{u} = (\psi^{pr}_{x\downarrow}, \psi^{pr}_{c\downarrow}, \psi_B)$, the dynamics of the vector $\vec{u}$ reads,

$$i\hbar\frac{d}{dt}\vec{u} = M^{+-}_\Omega\vec{u} - \vec{F}^{pr}_\uparrow. \tag{12.5}$$

The matrix M^{+-} is given by

$$M^{+-}_\Omega = \begin{pmatrix} \epsilon_x + g_{+-}|\psi^{pu}_{x,\downarrow}|^2 - i\gamma_x & \Omega & \frac{1}{2}g_\Omega\psi^{pu*}_{c\downarrow} \\ \Omega & \epsilon_c - i\gamma_c & \frac{1}{2}g_\Omega\psi^{pu*}_{x,\downarrow} \\ \frac{1}{2}g_\Omega\psi^{pu}_{c,\downarrow} & \frac{1}{2}g_\Omega\psi^{pu}_{x,\downarrow} & \epsilon_B - i\gamma_B \end{pmatrix}. \tag{12.6}$$

The dynamics of the pump wave functions are independently calculated as following,

$$i\hbar\dot{\psi}^{pu}_{x\downarrow} = (\epsilon_x + g|\psi^{pu}_{x,\downarrow}|^2 - i\gamma_x)\psi^{pu}_{x,\downarrow} + \Omega\psi^{pu}_{c,\downarrow} \tag{12.7}$$

$$i\hbar\dot{\psi}^{pu}_{c,\downarrow} = (\epsilon_c - i\gamma_c)\psi^{pu}_{c,\downarrow} + \Omega\psi^{pu}_{x,\downarrow} - f^{pu}_\downarrow. \tag{12.8}$$

In contrast with the bipolariton model, the photonic component of the polarion is required to form the biexciton. Similarly to Fig. 6.6 in Chapter 6, we try to fit the experimental data by finding the values of g_{+-} and g_Ω. The comparison between the simulation and experiment is shown in Fig. 12.2, where we display the fitting of the experiment based on the giant oscillator strength model with $g_{++} = 2/n_0, g_{+-} = -0.65/n_0, and g_\Omega = 1.3/\sqrt{n_0}$ meV.

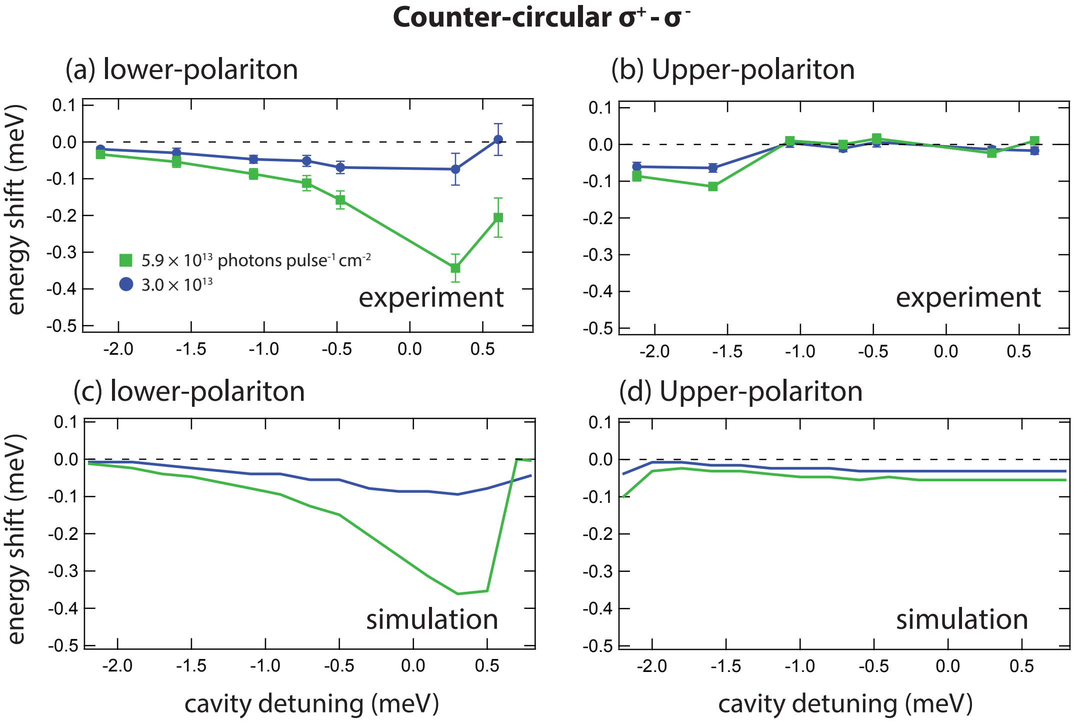

Figure 12.2: Same as Fig. 6.6 in Chapter 6 but concidering the giant oscillator strength model as a biexciton formation process. The parameters for the simulations are $g_{++} = 2/n_0$, $g_{+-} = -0.65/n_0$, $g_{bx} = 1.3/\sqrt{n_0}$ meV.

12.0.2 Lower-polariton basis

Similarly to the discussion in Chapter 6, we derive lower-polariton interaction constants α_1 and α_2 in the framework of the giant oscillator strength model. The Hamiltonian is rewritten in the lower-polariton basis as,

$$\sum_{\sigma=\{\uparrow\downarrow\}} \int d\mathbf{x} - \frac{1}{2} g_\Omega X_\mathbf{0} |C_\mathbf{0}| \left(\hat{\boldsymbol{\psi}}_B \hat{\boldsymbol{\psi}}^\dagger_{L,\sigma} \hat{\boldsymbol{\psi}}^\dagger_{L,-\sigma} + \hat{\boldsymbol{\psi}}_{L,\sigma} \hat{\boldsymbol{\psi}}_{L,-\sigma} \hat{\boldsymbol{\psi}}^\dagger_B \right), \tag{12.9}$$

Le us note that, in the lower-polariton basis, no qualitative difference between the two models (Compare Eq. 12.9 and Eq. 6.44.) is found except for the Hopfield coefficient in front of the coupling constant between the lower-polariton and biexciton. Defining the probe and

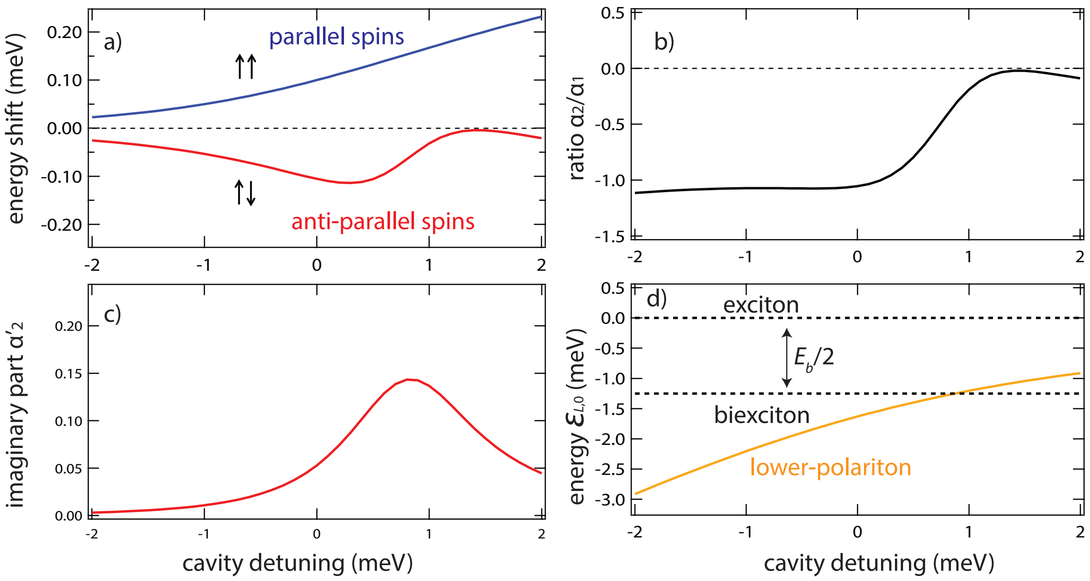

Figure 12.3: Same as Fig. 6.7 but concidering the giant oscillator strength model as the biexciton creation process.

biexciton wave-functions $\vec{u}$:

$$\vec{u}(t) = \left(\psi^{pr}_{L,\uparrow}(t), \psi_B(t)\right). \tag{12.10}$$

The equation of motion for the vector $\vec{u}$ follows

$$i\hbar \frac{d}{dt}\vec{u} = M_L^{+-}\,\vec{u} - \vec{F}^{pr}_{\uparrow}. \tag{12.11}$$

The matrix M is defined as

$$M_L^{+-} = \begin{pmatrix} \epsilon_{L,0} + g_{+-}X_{\mathbf{0}}^4|\psi^{pu}_{L,\downarrow}|^2 - i\gamma_L & -g_\Omega X_{\mathbf{0}}|C_{\mathbf{0}}|\psi^{pu*}_{L,\downarrow} \\ -g_\Omega X_{\mathbf{0}}|C_{\mathbf{0}}|\psi^{pu}_{L,\downarrow} & \epsilon_B - i\gamma_B \end{pmatrix}, \tag{12.12}$$

The analytical solution of $\psi^{pr}_{L,\uparrow}(\epsilon)$ is given by

$$\psi^{pr}_{L,\uparrow}(\epsilon) = \left[\epsilon_{L,0} - \epsilon \;+\; g_{+-}X_{\mathbf{0}}^4|\psi^{pu}_{L,\downarrow}|^2 - i\gamma_L - \frac{g_\Omega^2 X_{\mathbf{0}}^2 C_{\mathbf{0}}^2|\psi^{pu}_{L,\downarrow}|^2}{\epsilon_B - \epsilon_{L,0} - \epsilon - i\gamma_B}\right]^{-1}. \tag{12.13}$$

The approximate interaction constant of the lower-polaritons with opposite spins α_2 reads,

$$\alpha_2 \simeq g_{+-}X_{\mathbf{0}}^4 - \frac{g_{bx}^2 X_{\mathbf{0}}^2 C_{\mathbf{0}}^2(\epsilon_B - 2\epsilon_{L,0})}{(\epsilon_B - 2\epsilon_{L,0})^2 + \gamma_B^2}. \tag{12.14}$$

The imaginary part of the interaction (decay associated with the biexciton coupling) is given by

$$\alpha_2' \simeq \frac{g_\Omega^2 X_{\mathbf{0}}^2 C_{\mathbf{0}}^2 \gamma_B^2}{(\epsilon_B - 2\epsilon_{L,0})^2 + \gamma_B^2}. \tag{12.15}$$

The interaction constants α_1, α_2, and α_2' are displayed in Fig. 12.3. In the bipolariton model the polariton-biexciton coupling behaves as $|X|^4$, while in the giant oscillator strength model, it has a $|C|^2|X|^2$ detuning dependence. This is why the enhancement of the α_2 interaction constant with the increase of the cavity detuning is weaker than that in the bipolariton model.

12.0.3 Feshbach resonance

Moreover, we also fit the Feshbach resonance in Fig. 6.11 based on the giant oscillator strength model using the following effective Hamiltonian,

$$\hat{H}_{\text{eff}} = \begin{bmatrix} \hat{\psi}_{x,\uparrow} & \hat{\psi}_{c,\uparrow} & \hat{\psi}_B \end{bmatrix}^\dagger \begin{bmatrix} \epsilon_x + g_{+-} n_{x,\downarrow} - i\gamma_x & \Omega & \frac{1}{2} g_\Omega \sqrt{n_{c,\downarrow}} \\ \Omega & \epsilon_c - i\gamma_c & \frac{1}{2} g_\Omega \sqrt{n_{x,\downarrow}} \\ \frac{1}{2} g_\Omega \sqrt{n_{c,\downarrow}} & \frac{1}{2} g_\Omega \sqrt{n_{x,\downarrow}} & \epsilon_B - i\gamma_B \end{bmatrix} \begin{bmatrix} \hat{\psi}_{x,\uparrow} \\ \hat{\psi}_{c,\uparrow} \\ \hat{\psi}_B \end{bmatrix}, \tag{12.16}$$

The fitting of the Feshbach resonance is presented in Fig. 12.4. The giant oscillator strength model reproduces the experimental results reasonably well as far as the energy shift is concerned. However, the shape of the absorption feature deviates from the experiment for both very negative and positive detunings.

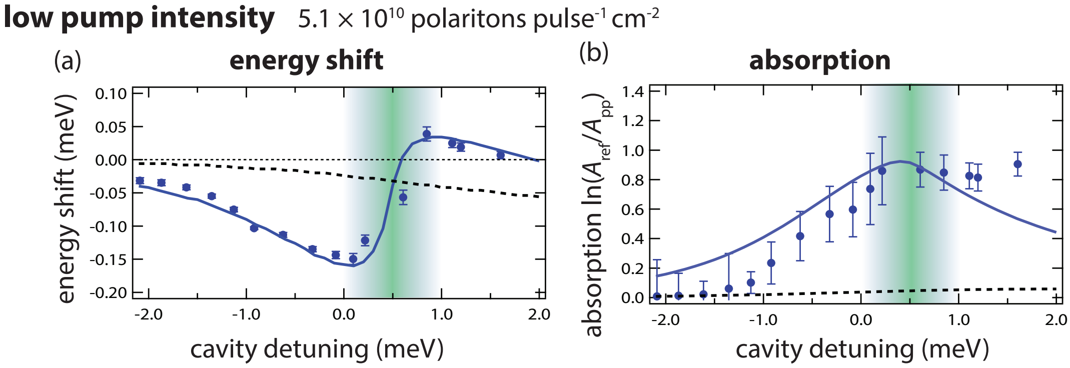

Figure 12.4: Same as Fig. 6.11 but concidering the giant oscillator strength model as the biexciton creation process. The coupling between exciton and biexciton is set to $g_\Omega = 0.21$ meV/$\sqrt{n_0}$. The background interaction is $g_{+-} = -0.06$ meV/$\sqrt{n_0}$, where n_0 is the normalized density of spin-up polaritons.

12.0.4 Summary

In this appendix, we have explained that the giant oscillator strength model also reproduces the experimental results. Actually, due to the qualitative similarity of the two models, it is difficult to determine which is more appropriate model for the biexciton formation. In Chapter 6, the bipolariton model is employed for modelling the biexciton effect based on the better fitting of the absorption of polariton Feshbach resonance (See Fig. 12.4 (b) and Fig. 6.11 (b)). Finally, we should comment on the possibility of the coexistence of the two types of couplings. The coexistence of the bipolariton model and giant oscillator strength model is difficult to consider because the two coupling pathways constructively or destructively interfere depending on the relative phase factor between them [55]. Even with an appropriate phase the resonant absorption could not be well reproduced [55]. We should therefore choose either bipolariton model or giant oscillator strength model for describing the polaritonic Feshbach resonance.

Bibliography

[1] C. Weisbuch, M. Nishioka, A. Ishikawa, and Y. Arakawa. Observation of the coupled exciton-photon mode splitting in a semiconductor quantum microcavity. *Phys. Rev. Lett.*, 69:3314–3317, Dec 1992.

[2] P. G. Savvidis, J. J. Baumberg, R. M. Stevenson, M. S. Skolnick, D. M. Whittaker, and J. S. Roberts. Angle-resonant stimulated polariton amplifier. *Phys. Rev. Lett.*, 84:1547–1550, Feb 2000.

[3] G. Messin, J. Ph. Karr, A. Baas, G. Khitrova, R. Houdré, R. P. Stanley, U. Oesterle, and E. Giacobino. Parametric polariton amplification in semiconductor microcavities. *Phys. Rev. Lett.*, 87:127403, Aug 2001.

[4] M. Saba, C. Ciuti, J. Bloch, V. Thierry-Mieg, R. André, Le Si Dang, S. Kundermann, A. Mura, G. Bongiovanni, J. L. Staehli, et al. High-temperature ultrafast polariton parametric amplification in semiconductor microcavities. *Nature*, 414(6865):731, 2001.

[5] S. Kundermann, M. Saba, C. Ciuti, T. Guillet, U. Oesterle, J. L. Staehli, and B. Deveaud. Coherent control of polariton parametric scattering in semiconductor microcavities. *Phys. Rev. Lett.*, 91:107402, Sep 2003.

[6] Wolfgang Langbein. Spontaneous parametric scattering of microcavity polaritons in momentum space. *Phys. Rev. B*, 70:205301, Nov 2004.

[7] A. Baas, J. Ph. Karr, H. Eleuch, and E. Giacobino. Optical bistability in semiconductor microcavities. *Phys. Rev. A*, 69:023809, Feb 2004.

[8] A. Amo, T. C. H. Liew, C. Adrados, R. Houdré, E. Giacobino, A. V. Kavokin, and A. Bramati. Exciton–polariton spin switches. *Nature Phot.*, 4(6):361–366, 2010.

[9] R. Cerna, Y. Léger, T. K. Paraïso, M. Wouters, F. Morier-Genoud, M. T. Portella-Oberli, and B. Deveaud. Ultrafast tristable spin memory of a coherent polariton gas. *Nature comm.*, 4, 2013.

[10] J. Kasprzak, M. Richard, S. Kundermann, A. Baas, P. Jeambrun, J. M. J. Keeling, F. M. Marchetti, M. H. Szymanska, R. André, J. L. Staehli, V. Savona, P. B. Littlewood, B. Deveaud, and Le Si Dang. Bose–einstein condensation of exciton polaritons. *Nature*, 443(7110):409, 2006.

[11] H. Deng, G. Weihs, C. Santori, J. Bloch, and Y. Yamamoto. Condensation of semiconductor microcavity exciton polaritons. *Science*, 298(5591):199–202, 2002.

[12] A. Amo, J. Lefrère, S. Pigeon, C. Adrados, C. Ciuti, I. Carusotto, R. Houdré, E. Giacobino, and A. Bramati. Superfluidity of polaritons in semiconductor microcavities. *Nature Phys.*, 5(11):805, 2009.

[13] K. G. Lagoudakis, M. Wouters, M. Richard, A. Baas, I. Carusotto, R. André, Le Si Dang, and B. Deveaud-Plédran. Quantized vortices in an exciton–polariton condensate. *Nature Phys.*, 4(9):706, 2008.

[14] S. Utsunomiya, L. Tian, G. Roumpos, C. W. Lai, N. Kumada, T. Fujisawa, M. Kuwata-Gonokami, A. Löffler, S. Höfling, A. Forchel, and Y. Yamamoto. Observation of bogoliubov excitations in exciton-polariton condensates. *Nature Phys.*, 4(9):700, 2008.

[15] V. Kohnle, Y. Léger, M. Wouters, M. Richard, M. T. Portella-Oberli, and B. Deveaud-Plédran. From single particle to superfluid excitations in a dissipative polariton gas. *Phys. Rev. Lett.*, 106:255302, Jun 2011.

[16] V. Kohnle, Y. Léger, M. Wouters, M. Richard, M. T. Portella-Oberli, and B. Deveaud. Four-wave mixing excitations in a dissipative polariton quantum fluid. *Phys. Rev. B*, 86:064508, Aug 2012.

[17] P. G. Lagoudakis, P. G. Savvidis, J. J. Baumberg, D. M. Whittaker, P. R. Eastham, M. S. Skolnick, and J. S. Roberts. Stimulated spin dynamics of polaritons in semiconductor microcavities. *Phys. Rev. B*, 65:161310, Apr 2002.

[18] A. Kavokin, P. G. Lagoudakis, G. Malpuech, and J. J. Baumberg. Polarization rotation in parametric scattering of polaritons in semiconductor microcavities. *Phys. Rev. B*, 67:195321, May 2003.

[19] W. Langbein, I. Shelykh, D. Solnyshkov, G. Malpuech, Yu. Rubo, and A. Kavokin. Polarization beats in ballistic propagation of exciton-polaritons in microcavities. *Phys. Rev. B*, 75:075323, Feb 2007.

[20] A. Kavokin, G. Malpuech, and M. Glazov. Optical spin hall effect. *Phys. Rev. Lett.*, 95:136601, Sep 2005.

[21] C. Leyder, M. Romanelli, J. Ph. Karr, E. Giacobino, T. C. H. Liew, M. M. Glazov, A. V. Kavokin, G. Malpuech, and A. Bramati. Observation of the optical spin hall effect. *Nature Phys.*, 3(9):628, 2007.

[22] A. Amo, T. C. H. Liew, C. Adrados, E. Giacobino, A. V. Kavokin, and A. Bramati. Anisotropic optical spin hall effect in semiconductor microcavities. *Phys. Rev. B*, 80:165325, Oct 2009.

[23] T. C. H. Liew, A. V. Kavokin, and I. A. Shelykh. Excitation of vortices in semiconductor microcavities. *Phys. Rev. B*, 75:241301, Jun 2007.

[24] T. C. H. Liew, Yuri G. Rubo, and A. V. Kavokin. Generation and dynamics of vortex lattices in coherent exciton-polariton fields. *Phys. Rev. Lett.*, 101:187401, Oct 2008.

[25] Yuri G. Rubo. Half vortices in exciton polariton condensates. *Phys. Rev. Lett.*, 99:106401, Sep 2007.

[26] J. J. Baumberg, A. V. Kavokin, S. Christopoulos, A. J. D. Grundy, R. Butté, G. Christmann, D. D. Solnyshkov, G. Malpuech, G. Baldassarri Höger von Högersthal, E. Feltin, J.-F. Carlin, and N. Grandjean. Spontaneous polarization buildup in a room-temperature polariton laser. *Phys. Rev. Lett.*, 101:136409, Sep 2008.

[27] N. A. Gippius, I. A. Shelykh, D. D. Solnyshkov, S. S. Gavrilov, Yuri G. Rubo, A. V. Kavokin, S. G. Tikhodeev, and G. Malpuech. Polarization multistability of cavity polaritons. *Phys. Rev. Lett.*, 98:236401, Jun 2007.

[28] T. K. Paraiso, M. Wouters, Y. Léger, F. Morier-Genoud, and B. Deveaud-Plédran. Multistability of a coherent spin ensemble in a semiconductor microcavity. *Nature mat.*, 9(8):655, 2010.

[29] M. Wouters, T. K. Paraiso, Y. Léger, R. Cerna, F. Morier-Genoud, M. T. Portella-Oberli, and B. Deveaud-Plédran. Influence of a nonradiative reservoir on polariton spin multistability. *Phys. Rev. B*, 87:045303, Jan 2013.

[30] H. Abbaspour, S. Trebaol, F. Morier-Genoud, M. T. Portella-Oberli, and B. Deveaud. Spinor stochastic resonance. *Phys. Rev. B*, 91:155307, Apr 2015.

[31] Eiichi Hanamura. Theory of many wannier excitons. i. *Journal of the Physical Society of Japan*, 37(6):1545–1552, 1974.

[32] G. Rochat, C. Ciuti, V. Savona, C. Piermarocchi, A. Quattropani, and P. Schwendimann. Excitonic bloch equations for a two-dimensional system of interacting excitons. *Phys. Rev. B*, 61:13856–13862, May 2000.

[33] Th. Östreich, K. Schönhammer, and L. J. Sham. Exciton-exciton correlation in the nonlinear optical regime. *Phys. Rev. Lett.*, 74:4698–4701, Jun 1995.

[34] M. Kuwata-Gonokami, S. Inouye, H. Suzuura, M. Shirane, R. Shimano, T. Someya, and H. Sakaki. Parametric scattering of cavity polaritons. *Phys. Rev. Lett.*, 79:1341, Aug 1997.

[35] M. Saba, F. Quochi, C. Ciuti, U. Oesterle, J. L. Staehli, B. Deveaud, G. Bongiovanni, and A. Mura. Crossover from exciton to biexciton polaritons in semiconductor microcavities. *Phys. Rev. Lett.*, 85:385–388, Jul 2000.

[36] H. Haug and S. W. Koch. *Quantum theory of the optical and electronic properties of semiconductors*, volume 5. World Scientific, 1990.

[37] I. Carusotto and C. Ciuti. Quantum fluids of light. *Reviews of Modern Physics*, 85(1):299, 2013.

[38] R. P. Stanley, R. Houdré, U. Oesterle, M. Gailhanou, and M. Ilegems. Ultrahigh finesse microcavity with distributed bragg reflectors. *Appl. Phys. Lett.*, 65(15):1883, 1994.

[39] Anthony Mark Fox. *Optical properties of solids*, volume 3. Oxford university press, 2001.

[40] Y. Peter and M. Cardona. *Fundamentals of semiconductors: physics and materials properties.* Springer Science & Business Media, 2010.

[41] C. Ciuti, V. Savona, C. Piermarocchi, A. Quattropani, and P. Schwendimann. Role of the exchange of carriers in elastic exciton-exciton scattering in quantum wells. *Phys. Rev. B*, 58:7926–7933, Sep 1998.

[42] Verena Kohnle. Nonliear spectrosocpy of a dissipative polariton quantum fluid. *PhD thesis, EPFL*, 1, 2011.

[43] S. Savasta, R. Saija, A. Ridolfo, O. Di Stefano, P. Denti, and F. Borghese. Nanopolaritons: Vacuum rabi splitting with a single quantum dot in the center of a dimer nanoantenna. *ACS Nano*, 4(11):6369–6376, 2010. PMID: 21028780.

[44] A. Kavokin, J. J. Baumberg, G. Malpuech, and F. P. Laussy. *Microcavities.* Oxford University Press, 2007.

[45] L. Pitaevskii and S. Stringari. Bose-einstein condensation (international series of monographs on physics), 2003.

[46] B. Deveaud, A. Quattropani, and P. Schwendimann. *Quantum Coherence in Solid State Systems*, volume 171. IOS Press, 2009.

[47] Y. Yamamoto and A. Imamoglu. Mesoscopic quantum optics. *Mesoscopic Quantum Optics, published by John Wiley & Sons, Inc., New York, 1999.*, 1, 1999.

[48] Govind Agrawal. *Nonlinear fiber optics.* Academic press, 2007.

[49] C. Ciuti, P. Schwendimann, B. Deveaud, and A. Quattropani. Theory of the angle-resonant polariton amplifier. *Phys. Rev. B*, 62:R4825, Aug 2000.

[50] Michiel Wouters. Resonant polariton-polariton scattering in semiconductor microcavities. *Phys. Rev. B*, 76:045319, Jul 2007.

[51] V. M. Axt, K. Victor, and T. Kuhn. The exciton–exciton continuum and its contribution to four-wave mixing signals. *physica status solidi (b)*, 206(1):189–196, 1998.

[52] N. H. Kwong, R. Takayama, I. Rumyantsev, M. Kuwata-Gonokami, and R. Binder. Evidence of nonperturbative continuum correlations in two-dimensional exciton systems in semiconductor microcavities. *Phys. Rev. Lett.*, 87:027402, Jun 2001.

[53] R. Takayama, N. H. Kwong, I. Rumyantsev, M. Kuwata-Gonokami, and R. Binder. T-matrix analysis of biexcitonic correlations in the nonlinear optical response of semiconductor quantum wells. *The Eur. Phys.Jour. B*, 25(4):445, 2002.

[54] Th. Östreich, K. Schönhammer, and L. J. Sham. Theory of exciton-exciton correlation in nonlinear optical response. *Phys. Rev. B*, 58:12920–12936, Nov 1998.

[55] N. Takemura, S. Trebaol, M. Wouters, M. T. Portella-Oberli, and B. Deveaud. Polaritonic feshbach resonance. *Nature Physics*, 10:500–504, 2014.

[56] N. Takemura, S. Trebaol, M. Wouters, M. T. Portella-Oberli, and B. Deveaud. Heterodyne spectroscopy of polariton spinor interactions. *Phys. Rev. B*, 90:195307, Nov 2014.

[57] K. L. Hall, G. Lenz, E. P. Ippen, and G. Raybon. Heterodyne pump-probe technique for time-domain studies of optical nonlinearities in waveguides. *Opt. Lett.*, 17(12):874, Jun 1992.

[58] Nick S. Jones and T. M. Stace. Photon frequency-mode matching using acousto-optic frequency beam splitters. *Phys. Rev. A*, 73:033813, Mar 2006.

[59] N. Takemura, S. Trebaol, M. D. Anderson, V. Kohnle, Y. Léger, D. Y. Oberli, M. T. Portella-Oberli, and B. Deveaud. Two-dimensional fourier transform spectroscopy of exciton-polaritons and their interactions. *Phys. Rev. B*, 92:125415, Sep 2015.

[60] O. Golonzka, M. Khalil, N. Demirdöven, and A. Tokmakoff. Vibrational anharmonicities revealed by coherent two-dimensional infrared spectroscopy. *Phys. Rev. Lett.*, 86:2154–2157, Mar 2001.

[61] P. Hamm and M. Zanni. *Concepts and methods of 2D infrared spectroscopy*. Cambridge University Press, 2011.

[62] X. Li, T. Zhang, C. N. Borca, and S. T. Cundiff. Many-body interactions in semiconductors probed by optical two-dimensional fourier transform spectroscopy. *Phys. Rev. Lett.*, 96:057406, Feb 2006.

[63] K. W. Stone, K. Gundogdu, D. B. Turner, X. Li, S. T. Cundiff, and K. A. Nelson. Two-quantum 2d ft electronic spectroscopy of biexcitons in gaas quantum wells. *Science*, 324(5931):1169–1173, 2009.

[64] J. Kasprzak, B. Patton, V. Savona, and W. Langbein. Coherent coupling between distant excitons revealed by two-dimensional nonlinear hyperspectral imaging. *Nature Photonics*, 5(1):57–63, 2011.

[65] G. Nardin, G. Moody, R. Singh, T. M. Autry, H. Li, F. Morier-Genoud, and S. T. Cundiff. Coherent excitonic coupling in an asymmetric double ingaas quantum well arises from many-body effects. *Phys. Rev. Lett.*, 112:046402, Jan 2014.

[66] P. Wen, G. Christmann, J. J. Baumberg, and K. A. Nelson. Influence of multi-exciton correlations on nonlinear polariton dynamics in semiconductor microcavities. *New Journal of Physics*, 15(2):025005, 2013.

[67] M Khalil and A Tokmakoff. Signatures of vibrational interactions in coherent two-dimensional infrared spectroscopy. *Chemical Physics*, 266(2):213–230, 2001.

[68] F. Albert, K. Sivalertporn, J. Kasprzak, M. Strauß, C. Schneider, S. Höfling, M. Kamp, A. Forchel, S. Reitzenstein, E. A. Muljarov, et al. Microcavity controlled coupling of excitonic qubits. *Nature communications*, 4:1747, 2013.

[69] Shaul Mukamel. *Principles of nonlinear optical spectroscopy*, volume 29. Oxford University Press New York, 1995.

[70] L. Yang, I. V. Schweigert, S. T. Cundiff, and S. Mukamel. Two-dimensional optical spectroscopy of excitons in semiconductor quantum wells: Liouville-space pathway analysis. *Phys. Rev. B*, 75:125302, Mar 2007.

[71] P. G. Savvidis, C. Ciuti, J. J. Baumberg, D. M. Whittaker, M. S. Skolnick, and J. S. Roberts. Off-branch polaritons and multiple scattering in semiconductor microcavities. *Phys. Rev. B*, 64:075311, Jul 2001.

[72] S. Savasta, O. Di Stefano, and R. Girlanda. Many-body and correlation effects on parametric polariton amplification in semiconductor microcavities. *Phys. Rev. Lett.*, 90:096403, Mar 2003.

[73] M. Combescot, M. A. Dupertuis, and O. Betbeder-Matibet. Polariton-polariton scattering: Exact results through a novel approach. *EPL (Europhysics Letters)*, 79(1):17001, 2007.

[74] K. V. Kavokin, P. Renucci, T. Amand, X. Marie, P. Senellart, J. Bloch, and B. Sermage. Linear polarisation inversion: A signature of coulomb scattering of cavity polaritons with opposite spins. *phys. status solidi (c)*, 2(2):763, 2005.

[75] M. Vladimirova, S. Cronenberger, D. Scalbert, K. V. Kavokin, A. Miard, A. Lemaître, J. Bloch, D. Solnyshkov, G. Malpuech, and A. V. Kavokin. Polariton-polariton interaction constants in microcavities. *Phys. Rev. B*, 82:075301, Aug 2010.

[76] L. Ferrier, E. Wertz, R. Johne, D. D. Solnyshkov, P. Senellart, I. Sagnes, A. Lemaître, G. Malpuech, and J. Bloch. Interactions in confined polariton condensates. *Phys. Rev. Lett.*, 106:126401, Mar 2011.

[77] P. Borri, W. Langbein, U. Woggon, J. R. Jensen, and J. M. Hvam. Biexcitons or bipolaritons in a semiconductor microcavity. *Phys. Rev. B*, 62:R7763–R7766, Sep 2000.

[78] T. Baars, G. Dasbach, M. Bayer, and A. Forchel. Biexciton states in semiconductor microcavities. *Phys. Rev. B*, 63:165311, Apr 2001.

[79] M. Kuwata-Gonokami, T. Aoki, C. Ramkumar, R. Shimano, and Yu. P. Svirko. Role of exciton-exciton interaction on resonant third-order nonlinear optical responses. *Journal of Luminescence*, 87–89(0):162 – 167, 2000.

[80] A. L. Ivanov and H. Haug. Self-consistent theory of the biexciton optical nonlinearity. *Phys. Rev. B*, 48:1490–1504, Jul 1993.

[81] A. L. Ivanov, M. Hasuo, N. Nagasawa, and H. Haug. Two-photon generation of excitonic molecules in cucl: An exactly solvable bipolariton model and high-precision experiments. *Phys. Rev. B*, 52:11017–11033, Oct 1995.

[82] C. Schindler and R. Zimmermann. Analysis of the exciton-exciton interaction in semiconductor quantum wells. *Phys. Rev. B*, 78:045313, Jul 2008.

[83] S. Inouye, M. R. Andrews, J. Stenger, H.-J. Miesner, D. M. Stamper-Kurn, and W. Ketterle. Observation of feshbach resonances in a bose-einstein condensate. *Nature*, 392(6672):151–154, March 1998.

[84] E. Timmermans, P. Tommasini, R. Côté, M. Hussein, and A. Kerman. Rarified liquid properties of hybrid atomic-molecular bose-einstein condensates. *Phys. Rev. Lett.*, 83:2691–2694, Oct 1999.

[85] D. Sarchi and V. Savona. Long-range order in the bose-einstein condensation of polaritons. *Phys. Rev. B*, 75:115326, Mar 2007.

[86] M. Grassi Alessi, F. Fragano, A. Patanè, M. Capizzi, E. Runge, and R. Zimmermann. Competition between radiative decay and energy relaxation of carriers in disordered $\mathrm{in}_x\mathrm{ga}_{1-x}\mathrm{As/GaAs}$ quantum wells. *Phys. Rev. B*, 61:10985–10993, Apr 2000.

[87] I. Carusotto and C. Ciuti. Probing microcavity polariton superfluidity through resonant rayleigh scattering. *Phys. Rev. Lett.*, 93:166401, Oct 2004.

[88] H. H. Yaffe, Y. Prior, J. P. Harbison, and L. T. Florez. Polarization dependence and selection rules of transient four-wave mixing in gaas quantum-well excitons. *J. Opt. Soc. Am. B*, 10(4):578–583, Apr 1993.

[89] M. Theis, G. Thalhammer, K. Winkler, M. Hellwig, G. Ruff, R. Grimm, and J. Hecker Denschlag. Tuning the scattering length with an optically induced feshbach resonance. *Phys. Rev. Lett.*, 93:123001, Sep 2004.

[90] E. A. Donley, N. R. Claussen, S. L. Cornish, J. L. Roberts, E. A. Cornell, and C. E. Wieman. Dynamics of collapsing and exploding bose–einstein condensates. *Nature*, 412(6844):295–299, 2001.

[91] M. Greiner, C. A. Regal, and D. S. Jin. Emergence of a molecular bose–einstein condensate from a fermi gas. *Nature*, 426(6966):537–540, 2003.

[92] B. L. Wilmer, F. Passmann, M. Gehl, G. Khitrova, and A. D. Bristow. Multidimensional coherent spectroscopy of a semiconductor microcavity. *Phys. Rev. B*, 91:201304, May 2015.

[93] C. Cohen-Tannoudji and D. Guéry-Odelin. *Advances in atomic physics*. World Scientific, Singapore, 2011.

[94] M. Vladimirova, S. Cronenberger, D. Scalbert, M. Nawrocki, A. V. Kavokin, A. Miard, A Lemaître, and J. Bloch. Polarization controlled nonlinear transmission of light through semiconductor microcavities. *Phys. Rev. B*, 79:115325, Mar 2009.

[95] D. Wang and M. Dignam. Excitonic approach to the ultrafast optical response of semiconductor quantum wells. *Phys. Rev. B*, 79:165320, Apr 2009.

[96] Jagdeep Shah. *Ultrafast spectroscopy of semiconductors and semiconductor nanostructures*, volume 115. Springer Science & Business Media, 1999.

[97] M. Kira and S. W. Koch. Many-body correlations and excitonic effects in semiconductor spectroscopy. *Progress in quantum electronics*, 30(5):155–296, 2006.

[98] H. Wang, H. Q. Hou, and B. E. Hammons. Coherent dynamics of excitonic nonlinear optical response in the nonperturbative regime. *Phys. Rev. Lett.*, 81:3255–3258, Oct 1998.

[99] S. S. Demirchyan, I. Yu. Chestnov, A. P. Alodjants, M. M. Glazov, and A. V. Kavokin. Qubits based on polariton rabi oscillators. *Phys. Rev. Lett.*, 112:196403, May 2014.

[100] L. Dominici, D. Colas, S. Donati, J. P. Restrepo Cuartas, M. De Giorgi, D. Ballarini, G. Guirales, J. C. López Carreño, A. Bramati, G. Gigli, E. del Valle, F. P. Laussy, and D. Sanvitto. Ultrafast control and rabi oscillations of polaritons. *Phys. Rev. Lett.*, 113:226401, Nov 2014.

[101] K. G. Lagoudakis, F. Manni, B. Pietka, M. Wouters, T. C. H. Liew, V. Savona, A. V. Kavokin, R. André, and B. Deveaud-Plédran. Probing the dynamics of spontaneous quantum vortices in polariton superfluids. *Phys. Rev. Lett.*, 106:115301, Mar 2011.

[102] M. De Giorgi, D. Ballarini, P. Cazzato, G. Deligeorgis, S. I. Tsintzos, Z. Hatzopoulos, P. G. Savvidis, G. Gigli, F. P. Laussy, and D. Sanvitto. Relaxation oscillations in the formation of a polariton condensate. *Phys. Rev. Lett.*, 112:113602, Mar 2014.

[103] T. Yajima and Y. Taira. Spatial optical parametric coupling of picosecond light pulses and transverse relaxation effect in resonant media. *Journal of the Physical Society of Japan*, 47(5):1620–1626, 1979.

[104] D. B. Turner, P. Wen, D. H. Arias, and K. A. Nelson. Coherent two-exciton dynamics measured using two-quantum rephasing two-dimensional electronic spectroscopy. *Phys. Rev. B*, 84:165321, Oct 2011.

[105] A. Honold, L. Schultheis, J. Kuhl, and C. W. Tu. Collision broadening of two-dimensional excitons in a gaas single quantum well. *Phys. Rev. B*, 40:6442–6445, Sep 1989.

[106] F. Quochi, G. Bongiovanni, A. Mura, J. L. Staehli, B. Deveaud, R. P. Stanley, U. Oesterle, and R. Houdré. Strongly driven semiconductor microcavities: From the polariton doublet to an ac stark triplet. *Phys. Rev. Lett.*, 80:4733–4736, May 1998.

[107] F. Quochi, C. Ciuti, G. Bongiovanni, A. Mura, M. Saba, U. Oesterle, M. A. Dupertuis, J. L. Staehli, and B. Deveaud. Strong coherent gain from semiconductor microcavities in the regime of excitonic saturation. *Phys. Rev. B*, 59:R15594–R15597, Jun 1999.

[108] M. Saba, F. Quochi, C. Ciuti, D. Martin, J. Staehli, B. Deveaud, A. Mura, and G. Bongiovanni. Direct observation of the excitonic ac stark splitting in a quantum well. *Phys. Rev. B*, 62:R16322–R16325, Dec 2000.

[109] S. Schmitt-Rink, S. Mukamel, K. Leo, J. Shah, and D. S. Chemla. Stochastic theory of time-resolved four-wave mixing in interacting media. *Phys. Rev. A*, 44:2124–2129, Aug 1991.

[110] R. Kubo, M. Toda, and N. Hashitsume. *Statistical physics II: nonequilibrium statistical mechanics*, volume 31. Springer Science & Business Media, 2012.

[111] G. Nardin, K. G. Lagoudakis, M. Wouters, M. Richard, A. Baas, R. André, Le Si Dang, B. Pietka, and B. Deveaud-Plédran. Dynamics of long-range ordering in an exciton-polariton condensate. *Phys. Rev. Lett.*, 103:256402, Dec 2009.

[112] F. Manni, K. G. Lagoudakis, T. C. H. Liew, R. André, V. Savona, and B. Deveaud. Dissociation dynamics of singly charged vortices into half-quantum vortex pairs. *Nature communications*, 3:1309, 2012.

[113] V. M. Axt, T. Kuhn, B. Haase, U. Neukirch, and J. Gutowski. Estimating the memory time induced by exciton-exciton scattering. *Phys. Rev. Lett.*, 93:127402, Sep 2004.

[114] N. H. Kwong, R. Takayama, I. Rumyantsev, M. Kuwata-Gonokami, and R. Binder. Third-order exciton-correlation and nonlinear cavity-polariton effects in semiconductor microcavities. *Phys. Rev. B*, 64:045316, Jun 2001.

[115] V. M. Axt, B. Haase, and U. Neukirch. Influence of two-pair continuum correlations following resonant excitation of excitons. *Phys. Rev. Lett.*, 86:4620–4623, May 2001.

[116] Yu. P. Svirko and M. Kuwata-Gonokami. Signatures of the excitonic memory effects in four-wave mixing processes in cavity polaritons. *Phys. Rev. B*, 62:6912–6915, Sep 2000.

[117] Eiichi Hanamura. Giant two-photon absorption due to excitonic molecule. *Solid State Communications*, 12(9):951–953, 1973.

[118] I. Carusotto, T. Volz, and A. Imamoğlu. Feshbach blockade: Single-photon nonlinear optics using resonantly enhanced cavity polariton scattering from biexciton states. *EPL (Europhysics Letters)*, 90(3):37001, 2010.

Naotomo Takemura

Personal Data

Date of Birth	April 18, 1985
Address	Avenue de l'Eglise Anglaise 10 #509, Lausanne, CH-1006, Switzerland
Gender	Male
Phone	+41 21 69 37630
E-Mail	naotomo.takemura@epfl.ch
Nationality	Japanese

Education

- *Dec. 2011-present* **PhD student in Photonics**, **Laboratory of Quantum Optoelectronics, École Polytechnique Fédérale de Lausanne (EPFL), Switzerland**
  Topic: Study on polariton interactions in semiconductor microcavities using nonlinear spectroscopies (Supervisors: Professor Benoît Deveaud, Dr Marcia Portella Oberli)

- *Apr. 2010-Oct. 2011* **Department of Physics, The University of Tokyo, Japan**
  Topic: Photon statistics measurement of Vertical Cavity Surface Emitting Lasers (VCSELs) using a streak camera (Supervisor: Professor Makoto Gonokami)

- *Apr. 2008-Mar. 2010* **Master of Science, Department of Physics, The University of Tokyo, Japan**
  Topic: Development of a 461nm laser system for MOT of Sr atoms and study on evaporative cooling of ^{85}Rb atoms (Supervisor: Associate Professor Yoshio Torii)
  Master thesis: “Evaporative Cooling of ^{85}Rb toward Bose-Einstein Condensation”

- *Apr. 2004-Mar. 2008* **Bachelor of Science, Department of Physics, The University of Tokyo, Japan**

Skills

- **Technical skills**: lasers (CW and pulse) and optics, vacuum technique, cryogenics, ulatrafast spectroscopy, streak camera, design of SHG cavity
- **Computing**: Matlab, Igor, C++, Fortran, LaTeX, Illustrator, Microsoft Office

Languages

- **Japanese**: Mother tongue
- **English**: Full proficiency
- **French**: A2
- **German**: Basic

Hobbies

- Skiing, cycling, traveling, literature and poetry

Selected Conference Contributions

- **FIRST Quantum Information Processing Project General Meeting 2010** Atami, Japan, 2010: **Poster presentation** with the title “Photon Correlation Measurement Using a Streak Camera”
- **Quantum Information Processing Summer School 2011**, Kyoto, Japan, 2011: **Poster presentation** with the title “Photon Statistics Measurement of Vertical Cavity Surface Emitting Lasers (VCSELs)”
- **PHYSICS SCHOOL POLATOM** Toledo, Spain, 2012
- **ICPS 2012** Zurich, Switzerland, 2012
- **POLATOM 2012** Cambridge, UK, 2012
- **PLMCN 2013** Crete, Greece, 2013: **Oral presentation** with the title “Tuning of Spinor Interaction in Polariton Gas”
- **OECS13** Rome, Italy, 2013: **Oral presentation** with the title “Biexcitonic Feshbach resonance in spinor polariton gas”
  N. Takemura, S. Trebaol, M. Wouters, M. T. Portella-Oberli, and B. Deveaud
- **PLMCN** Montpellier, France, 2014: **Oral presentation** with the title “Lower and upper polariton-polariton interactions”
  N. Takemura, S. Trebaol, M. Wouters, M. T. Portella-Oberli, and B. Deveaud
- **CLEO2015** Munich, Germany, 2015: **Poster presentation** with the title “Lower-Upper Polariton Interactions Proved with Two-Dimensional Fourier Transform (2DFT) Spectroscopy in Semiconductor Microcavity”

Publications

- Takatoshi Aoki, Kotaro Umezawa, Yuki Yamanaka, Naotomo Takemura, Yasuhiro Sakemi, and Yoshio Torii "A 461 nm Laser System and Hollow-Cathode Lamp Spectroscopy for Magneto-Optical Trapping of Sr Atoms" *Journal of the Physical Society of Japan* **81**, 034401 (2012)

- Naotomo Takemura Junko Omachi and Makoto Kuwata-Gonokami “Fast periodic modulations in the photon correlation of single-mode vertical cavity surface emitting lasers," *Physical Review A* **85**, 053811 (2012)

- A. Lebreton, I. Abram, N. Takemura, M. Kuwata-Gonokami, I. Robert-Philip and A. Beveratos "Stochastically sustained population oscillations in high-β nanolasers" *New Journal of Physics* **15**(3), 033039 (2013)

- N. Takemura, S. Trebaol, M. Wouters, M. T. Portella-Oberli, and B. Deveaud “Polaritonic Feshbach Resonance” *Nature Physics.* **10**, 500 (2014).

- N. Takemura, S. Trebaol, M. Wouters, M. T. Portella-Oberli, and B. Deveaud “Heterodyne Spectroscopy of Polariton Spinor Interactions”, *Physical Review B* **90**, 195307 (2014)

- N. Takemura, S. Trebaol, M. D. Anderson, V. Kohnle, Y. Léger, D. Y. Oberli, M. T. Portella-Oberli, and B. Deveaud "Two-dimensional Fourier transform spectroscopy of exciton-polaritons and their interactions", *Physical Review B* **92**, 125415 (2015) -Editors’ Suggestion

- N. Takemura, S. Trebaol, M. D. Anderson, S. Biswas, D. Y. Oberli, M. T. Portella-Oberli, and B. Deveaud “Dephasing effects on coherent exciton-polaritons and the breaking of the strong coupling regime” accepted to *Physical Review B*